WAVELET DOMAIN BILATERAL FILTERING FOR DENOISING MR IMAGES

C. Shyam Anand

WAVELET DOMAIN BILATERAL FILTERING FOR DENOISING MR IMAGES

A

Thesis submitted

for the award of the degree of

DOCTOR OF PHILOSOPHY

By

C. SHYAM ANAND

DEPARTMENT OF ELECTRONICS AND ELECTRICAL ENGINEERING

INDIAN INSTITUTE OF TECHNOLOGY GUWAHATI

GUWAHATI - 781 039, ASSAM, INDIA

MARCH 2013

vakra tuNDa mahA kAya
sUrya kOTi sama prabha
nirvighnam kuru mE dEva
sarva kAryEshu sarvadA

Dedicated to My Beloved Wife

Certificate

This is to certify that the thesis entitled "**WAVELET DOMAIN BILATERAL FILTERING FOR DENOISING MR IMAGES**", submitted by **C. Shyam Anand** (06610201), a research scholar in the *Department of Electronics and Electrical Engineering, Indian Institute of Technology Guwahati*, for the award of the degree of **Doctor of Philosophy**, is a record of an original research work carried out by him under my supervision and guidance. The thesis has fulfilled all requirements as per the regulations of the institute and in my opinion has reached the standard needed for submission. The results embodied in this thesis have not been submitted to any other University or Institute for the award of any degree or diploma.

Dated:
Guwahati.

Dr. J. S. Sahambi
Associate Professor
Dept. of Electronics and Electrical Engg.
Indian Institute of Technology Guwahati
Guwahati - 781 039, Assam, India.

Acknowledgements

This dissertation would not have been possible without the guidance and the help of several individuals who in one way or another contributed and extended their valuable assistance in the preparation and completion of this work. First and foremost, I feel it as a great privilege in expressing my deepest and most sincere gratitude to my supervisor Dr. J. S. Sahambi, for his excellent guidance throughout my study. His guidance helped me in all the time of research and writing of this thesis. I could not have imagined having a better advisor and mentor for my Ph.D. study. My heartfelt thanks to you sir, for the unlimited support and patience you have for me. I am sure that finishing my degree in a proper and timely manner was only possible because of his support, suggestions and advices.

I am also very thankful to my doctoral committee members Prof. P. K. Bora, Prof. S. Dandapat, Prof. S. R. M. Prasanna and Dr. A. Mitra for their encouragement, insightful comments, and hard questions. I owe my deepest gratitude to the Head of the Department and the other faculty members for their kind help in carrying out this work. I would like to express my sincere thanks to Dr. M. K. Bhuyan my administrative guide. I am also grateful to all the members of the research and technical staff of the department without whose help I could not have completed this thesis.

My special thanks to Mr. Sanjib Das for providing excellent computing facilities and various resources that were useful for the research work. I thank my fellow research scholars: Dakua, Himanshu, Rupaban, Kuntel, Nagesh, Ashish, Rajib, Debadatta Pati and Utkal for the stimulating discussions, for the sleepless nights we were working together before seminar deadlines, and for all the fun we have had in the last four years.

I would like to convey my gratitude to Dr. Baijayanta Saharia of Guwahati Neurological Research Centre (GNRC) for providing the MRI data and also for giving his opinion on the diagnostic details of the denoised images. I wish to thank my best friends, Dr. P. Krishnamoorthy and Dr. D. Senthil Kumar for helping me get through the difficult times and for all the emotional support and care. In addition, grateful acknowledgement to my friends Govind, Kannan, Anantharaj, Satheesh, Santosh and Lakshmanan for their constant support and unconditional help.

All my other friends have also helped me in several ways and so, I would like to say a big thank you to all of them for their friendship and support. I would like to extend my sincere thanks to Mrs. Sahambi for her constant support and care towards me and my wife.

My deepest gratitude goes to my parents for their continuous love and support throughout my studies. The opportunities that they have given me and their unlimited sacrifices are the reasons where I am and what I have accomplished so far.

Finally, I believe this research experience will greatly benefit my career in the future.

C. Shyam Anand

Abstract

Noise removal from magnetic resonance (MR) images is an important area of research that progresses towards developing efficient denoising methods that are also capable of preserving the structural details in the MR image. In this thesis, a novel wavelet domain bilateral filter (WD-BF) framework is proposed for noise reduction in MR images. The method implements bilateral filtering in the undecimated wavelet domain and so exploits the advantages of non-linear spatial filters and the wavelet transform. Adopting the wavelet thresholding techniques in the WD-BF framework improved the denoising efficiency and also ensured feature preservation. Therefore, an efficient approach using the NeighShrink wavelet thresholding in the WD-BF framework is proposed for feature preserved MR image denoising. One of the potential issues identified in the WD-BF framework was the choice of the bilateral filter parameters. It demanded several experiments to find its optimal values. Hence, a pixel-wise automatic parameter selection strategy based on the local statistics of the image is proposed. This new adaptive bilateral filter provides significant improvement over the standard bilateral filter.

Further improvements in the WD-BF framework are attained by exploiting the properties of bilateral filter for denoising the detail sub-bands of the wavelet decomposition. The first method proposed is the *Adaptive VisuShrink* and it is formulated by adapting the universal threshold based on the spatial context of the wavelet coefficients. The spatial context information of the coefficient is computed using the range component of the bilateral filter. The adaptive universal threshold value is optimal than other conventional threshold selection methods. The second approach projects *bilateral filtering as an effective alternative to the wavelet thresholding.* The performance of the technique is better than wavelet thresholding methods based on the inter-scale and intra-scale dependencies. The proposed WD-BF and its variations improves the denoising efficiency and are effective in preserving the desired structural details of the MR image.

Contents

List of Figures

List of Tables

List of Acronyms

ARNLM	Adaptive Rician Non-Local Means
ABF	Adaptive Bilateral Filter
ADF	Anisotropic Diffusion Filtering
AVREC	Averaging Reconstructed Images
BF	Bilateral Filter
BC	Bhattacharrya Coefficient
CSF	Cerebrospinal Fluid
CNR	Contrast-to-Noise Ratio
DWT	Discrete Wavelet Transform
DCE-MRI	Dynamic Contrast Enhanced MRI
DNLM	Dynamic Non-Local Means
EM	Expectation Maximization
FFT	Fast Fourier Transform
FID	Free Induction Decay
GGD	Generalized Gaussian Distributed
GE	Gradient Echo
GNRC	Guwahati Neurological Research Center
HVS	Human Visual System
IDWT	Inverse Discrete Wavelet Transform
LLSE	Linear Least Square Error
LMMSE	Linear Minimum Mean Square Error
MRI	Magnetic Resonance Imaging
MRF	Markov Random Field
ML	Maximum Likelihood

MDF	Measurement Dependent Filtering
MAD	Median Absolute Deviation
MNLM	Multi-component Non-Local Means
MRMSE	Multi-component Root Mean Square Error
MS	Multiple Sclerosis
MRA	Multi-Resolution Analysis
NLM	Non-Local Means
NMR	Nuclear Magnetic Resonance
NEX	Number of Excitations
NSA	Number of Signal Averages
OMNLM	Optimized MNLM
OWT	Orthogonal Wavelet Transform
PDE	Partial Differential Equations
PCA	Principle Component Analysis
pdf	Probability Distribution Function
QMF	Quadrature Mirror Filters
QILV	Quality Index based on Local Variance
RF	Radio Frequency
ROI	Region of Interest
RNRAD	Rician Noise Reducing Anisotropic Diffusion
RMSE	Root Mean Square Error
SNR	Signal-to-Noise Ratio
SFA	Singularity Function Analysis
SRAD	Speckle Reducing Anisotropic Diffusion
SE	Spin Echo
SWT	Stationary Wavelet Transform
SURE	Steins Unbiased Risk Estimate
SSIM	Structural Similarity Index
TE	Echo Time
TR	Repetition Time

TV	Total Variation
UDWT	Undecimated Wavelet Transform
UNLM	Unbiased Non-Local Means
WD-BF	Wavelet Domain Bilateral Filter
WD-all-band-BF	Wavelet Domain all Band Bilateral Filter

List of Symbols

α_p	Type 1 error function
B_0	External magnetic field
$\#$	Cardinality
η	Noise
$\epsilon(.)$	Unit step heaviside function
$E(.)$	Expected value
$\|.\|$	Norm
$|.|$	Absolute value
$f(.)$	Noise-free MR image
$g(.)$	Noisy MR image
γ	Gyromagnetic ratio
$\Gamma(.)$	Gamma function
$h_{\psi}(.)$	Wavelet function coefficients
$h_{\varphi}(.)$	Scaling function coefficients
$I_n(.)$	n^{th} order modified Bessel function
λ	Universal threshold
λ_{adap}	Adaptive universal threshold
λ_{bayes}	Bayes threshold
R_{neigh}	Kernel width of bilateral filter
σ_n	Standard deviation of noise
σ_n^2	Variance of noise
σ_d	Standard deviation of domain component in BF
σ_r	Standard deviation of range component in BF
$\{,\}$	Set

$\hat{\theta}_m$	Estimate of noise free data
V_m	Approximation subspace
$\psi_{a,b}(.)$	Wavelet basis function
$\varphi_{m,n}(.)$	Scaling function
W_d	Domain component of bilateral filter
W_r	Range component of bilateral filter
W_r^A	Adaptive range component in bilateral filter
$W_\psi(.)$	Discrete detail coefficients of wavelet transform
$W_\varphi(.)$	Discrete approximation coefficients of wavelet transform
W_m	Wavelet subspace

1

Introduction

Contents

1.1 Denoising in Magnetic Resonance Imaging

Allied development in the fields of physics and medical imaging has spawned a productive imaging modality known as the magnetic resonance imaging (MRI). The imaging method is used to generate magnetic resonance (MR) images of the internal body parts and thus aids in studying the structural features and the functional behavior (functional magnetic resonance imaging - fMRI) of human body.

The diagnostic and the visual quality of the MR images are affected by the noise added while acquisition [2]. Therefore, post-acquisition image filtering techniques are employed to improve the image quality. However, the difficulty in restoring the salient structures and the subtle tissue boundaries leads to increasing demand for accurate image filtering or estimation methods. These methods can be referred as feature-preserving denoising methods [3]. In this context, denoising methods utilizing non-linear spatial filtering procedures and wavelet transform have evolved as efficient tools for feature preserving denoising.

The non-linear filtering methods [4] are based on the local spatial activity and hence, adapt to the spatial context in the image resulting in good denoising. In spite of this property, the performance of these methods rely on the optimal choice of the control parameter values that has to be obtained empirically or through extensive training. The wavelets provide an appropriate basis for differentiating the noisy samples from the image samples and hence, offer accurate noise estimation procedures for denoising. Three main properties of wavelets [5] are *sparsity, locality* and *multi-resolution*. These properties promote the utility of the correlation between the pixels within and across the resolution scales and directs towards novel advancement in feature preserving denoising techniques.

In this research work a wavelet domain non-linear filtering approach is proposed for improving denoising efficiency. Accordingly, the work adopts the principles of non-linear filtering in wavelet subbands to improve the existing threshold selection schemes. A comprehensive study and exploitation of the proposed approach lead to novel wavelet domain non-linear filtering strategies for efficient feature preserving denoising.

1.2 Motivation for the Present Work

The noise in MR image is signal dependent with its mean depending on the local intensities of the image [6]. The wavelet based filtering techniques can automatically adapt to spatial variations in the noise distribution and preserve important image features. Despite of this, the conventional methods utilizing discrete wavelet transform (DWT) produces distinct artifacts such as low frequency noise and edge ringing. Hence, this work opts for a non-decimated wavelet transform reducing the technique to redundant sub-band decomposition. The method is referred as undecimated wavelet transform (UDWT).

The bilateral filter proposed in [7] is a non-linear filter and is shown to be an effective alternative to wavelet thresholding in image denoising applications [8]. MR image denoising using the non-linear spatial filtering methods like anisotropic diffusion [9] and non-local means filtering [10] preserve the dominant edge features. However, these methods completely smoothen the small structural details and also reduce the contrast as the noise level increases which can be verified from the evaluation results given in the chapters to follow in this thesis.

Unlike wavelet transform, these filtering methods do not exhibit properties that enable to highlight the features of interest (e.g. edges) from the noise pixels. In other words, they do not have individual access to the different frequency components of a signal. Conversely, the wavelet basis functions are independent of the spatial context in the image. Hence, if the wavelet filters are modified to adapt to the local spatial activity around a pixel as in non-linear filters, it can be expected to have better feature preserving capability.

Hence, our research was motivated towards developing a UDWT based denoising framework that utilizes bilateral filter to exploit the intra-scale dependencies of the scaling and the wavelet coefficients. The proposed work associates the local spatial interaction with the wavelet properties to result in good feature preserving denoising.

1.3 Contributions of the Thesis

Motivated towards developing a new feature-preserved denoising scheme for MRI, this research work has proposed

(i) A novel wavelet domain bilateral filtering framework for Rician noise removal in MRI.

(ii) Coefficient-based automatic parameter selection for the bilateral filter.

(iii) An adaptive universal threshold selection scheme based on the spatial context.

(iv) Bilateral filtering of wavelet coefficients as an efficient alternative to traditional wavelet thresholding approaches.

1.4 Organization of the Thesis

This thesis presents the proposed wavelet domain bilateral filtering strategies that exploit the neighborhood dependency of the wavelet coefficients within the sub-bands. The efficiency of the proposed methods are validated and compared with some of the existing MR image denoising techniques.

The organization of the thesis is as follows

Chapter 2 explains the fundamentals of MR image formation and its characteristics. It discusses about the essential imaging parameters and its influence on the quality of the output MR data. The chapter concludes by providing the basis for considering noise reduction as a principle issue in MRI.

Chapter 3 presents in detail about the characteristics of noise in MR images. It also summarizes about the noise estimation techniques that are used for MR image denoising.

Chapter 4 gives the overview of spatial and wavelet filters used for denoising MR images. It presents a thorough review on the existing spatial and wavelet domain filtering methods established for noise reduction in MRI. The chapter concludes with the proposal for combining the properties of wavelets and the non-linear spatial filters for improved MR image denoising.

Chapter 5 and 6 elaborates the proposed wavelet domain bilateral filtering method for reducing noise in MRI. It discusses the influence of bilateral filter parameters and the experiments performed for optimal choice of these parameters. The experimental results validating the efficiency of the proposed technique over the other denoising procedures are presented.

Chapter 7 explains the proposed method for adaptive and automatic selection of bilateral filter parameters and hence, presents the improved wavelet domain bilateral filtering approach.

Chapter 8 discusses about the wavelet thresholding techniques and its improvements based on the bilateral filter. It details the proposed method for pixel wise universal threshold selection. The improvement in the performance of wavelet thresholding schemes utilizing the proposed threshold over the conventional threshold selection strategies is analyzed. Another important denoising method based on bilateral filtering of wavelet coefficients is proposed as an effective alternative to wavelet thresholding. The choice of bilateral filter parameters based on the sub-band coefficients is explained. The experimental results validate the efficiency of this approach.

Chapter 9 concludes this thesis, with the scope for future directions in the improvement of wavelet domain bilateral filtering strategies.

2

Principles of MRI

Contents

The imaging principle of the MRI scanner is based on the magnetic properties of the tissues that constitute the human body. The anomalies in the mechanism creates image artifacts and hence, reduces the visual and the diagnostic quality of the resultant MR data. Therefore, image processing algorithms are usually employed for removing these artifacts and to improve the MR image quality. As the imaging procedure strongly influences the output image characteristics, an insight in to MR image formation is important for improving the versatility of the image processing methods.

2.1 Basics of MR Image formation

The basics about the physics of MRI and the essential information on imaging mechanisms are explained proficiently in [11–18]. They have also dealt in detail about the fundamentals of MR image formation and the imaging parameters that influence the quality of the resulting MR image. From these references, this section presents concisely the MR imaging modality and the factors influencing the characteristics of MR image.

The essential component of a MRI scanner is the hollow bore containing the primary magnet. The magnet produces a very strong, static and homogeneous magnetic field (B_0). Besides the main magnet, other important coils located inside the bore are [11, 13, 14]

- Shimming coils - These are used to maintain/increase the homogeneity of the applied external magnetic field (B_0).

- Radio frequency (RF) coils - They usually act as both transmitter and receiver. Therefore, it is responsible for transmitting RF pulses in to the subject for magnetic excitation and collecting the response of the excitation. These coils usually conform to the contour of the body part being imaged.

- Gradient coils - These coils induce additional field to B_0 and causes the field strength to vary so as to achieve spatial localization.

2.1.1 Magnetization phenomenon

The human body is basically composed of large concentration of hydrogen atoms [11–13]. The nucleus of an hydrogen atom consists of a single proton that possess a spin (rotate about its axis) and hence, it always induces a magnetic field. For these reasons MRI principally images the signal from the hydrogen nuclei. The nuclei density variation among different tissues in the body affects the magnetization [14, 16]. As a result they attain different intensity levels in the resultant image. The body tissues that can be perceived distinctly in an MR image are [17, 19, 20]

- ***Fluids*** - cerebro-spinal fluid (CSF), oedema and synovial fluid.
- ***Water based tissues*** - cartilage, grey matter in brain, kidney, muscle.
- ***Fat based tissues*** - bone marrow, fat, white matter in brain.

Therefore, MR data is a result of the electromagnetic signals generated by these body tissues in response to the magnetic excitation.

2.1.1.1 Nuclei alignment

The magnetic field of the spins in the body have random orientations and hence, the net magnetization is zero. Under the influence of a strong external magnetic field (B_0), the spins orient themselves parallel/anti-parallel to B_0. The proton pairs with opposing orientation gets canceled, resulting in zero magnetic moments. A slightly large proportion of spins aligned parallel to B_0 *precess* about the axis of B_0 with the frequency ω_0. The precession frequency is directly proportional to B_0 and is defined by the Larmor equation as [14–16]

$$\omega_0 = \gamma B_0, \tag{2.1}$$

where γ is the gyromagnetic ratio. For hydrogen atoms $\gamma = 42.56\, MHz/Tesla$. In an MRI scanner with $B_0 = 1.5\, Tesla$, the precession frequency of the hydrogen protons is $63.84\, MHz$.

Figure 2.1 illustrates the alignment process. Consider a three dimensional ($3D$) space in which the field B_0 is oriented along the $z-$axis. The magnetic moments of the precessing protons induce a net magnetization M_z in the $z-$direction. As this magnetization is in direction longitudinal to the external magnetic field, it is also called *longitudinal magnetization*.

2.1.1.2 RF excitation

The precessing protons are excited by a RF pulse of short duration. The pulse is applied at 90° to B_0 and its frequency is same as the precession frequency. This causes the hydrogen nuclei to resonate (energy absorption from RF pulse) and flips the spin from parallel to anti-parallel state [11, 14, 17]. As a result the magnetization vector M_z moves down towards the $x - y$ plane. The $x - y$ plane is perpendicular to B_0 and is also referred as the *transverse plane*.

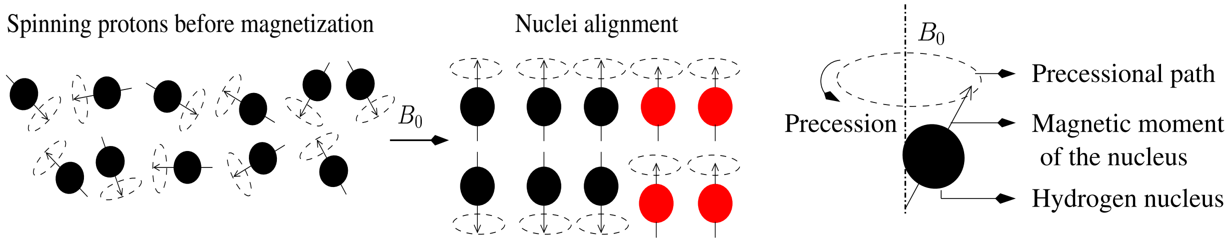

(a) (b)

Figure 2.1: Illustration of (a) *Nuclei alignment:* Initially the protons rotate about their axes in random direction. Under the influence of a strong external magnetic field (B_0), slightly more protons align parallel to B_0 and produce ***longitudinal magnetization***. (b) the hydrogen nucleus precessing along the direction of B_0. *Precession:* The spinning proton under the influence of an strong magnetic field begins to wobble (like an spinning top). This type of movement is called precession.

The angle of rotation towards the $x-y$ plane is defined as the flip angle (α) and is a function of the strength and duration of the RF pulse. At $\alpha = 90°$ the spins get oriented along the transverse plane and continue to precess in phase with each other. This phase coherence results in a magnetization vector M_{xy} and is known as the *transverse magnetization.* The RF pulse producing 90° flip angle is referred as the 90° RF pulse [16].

2.1.1.3 T1 relaxation

The RF pulse is removed after achieving the transverse magnetization. As a consequence, the nuclei emits the absorbed energy and the orientation of the spins reconvenes parallel to B_0. Therefore, the net magnetization increases in the longitudinal direction inducing longitudinal magnetization. This relaxation process is called *T1 recovery* or *spin-lattice relaxation* and the time taken for relaxation is referred as T1 [11, 14, 16].

The energy emitted during the relaxation is the desired MR signal with frequency same as the precession frequency. The MR image reconstructed from the *T1* recovery signal is known as the *T1 weighted* image.

2.1.1.4 T2 decay

Prior to the *T1* recovery, the transverse magnetization decays due to the dephasing of nuclei. The dephasing process is known as *T2 decay* and occurs due to two main reasons. They are

- interactions of intrinsic magnetic fields of the adjacent nuclei result in spin to spin energy transfer and is known as *spin-spin interaction* [11, 14, 16].

- inhomogeneities of the external magnetic field.

The dephasing with respect to time reduces the strength of the MR signal in the transverse direction and the signal received during this phenomenon is called the *free induction decay* (FID) [11,12,14–16]. The time taken for the decay of transverse magnetization is referred as T2. Therefore, in order to produce images from the transverse magnetization, additional pulse sequences are applied to rephase the spins and compensate for magnetic field inhomogeneities [21].

The diagrams in Fig. 2.3 illustrates the entire magnetization phenomenon responsible for T1 recovery and T2 decay.

2.1.2 Pulse sequence mechanisms

A pulse sequence is a series of RF pulses and gradient magnetic fields that are required to bring the protons in phase coherence. Two of the most representative pulse sequences for structural imaging include the spin and gradient echo.

2.1.2.1 Spin echo sequence

At time $t = \tau$ after the RF excitation, another short duration RF pulse at 180° to the transverse magnetization vector is applied. The 180° RF pulse reverses the direction of the transverse magnetization in such a way that the net magnetization vector is aligned in the $-z$ direction. As a result, the spins will rotate over to the opposite axis and will begin to rephase. Hence, it is known as 180° *rephasing pulse*. After the time $t = 2\tau$ the precessing protons come in phase coherence and the transverse magnetization $M_{xy'}$ becomes strong [12, 14, 16]. The MR signal received at this instant is known as the *echo signal* and the RF sequences are called *spin echo (SE) sequences.*

2.1.2.2 Gradient echo sequence

In this pulse sequence, a magnetic field gradient is induced instead of the 180° pulse. The magnetic field gradient is switched ON for a short time. This results in even larger magnetic field inhomogeneities and causes the protons to dephase faster [14, 16].

As the transverse magnetization reach to a minimum, the gradient is turned back ON with the same strength, but in opposite direction. As a result, the protons in phase-lead becomes phase-lag and vice versa (similar to SE sequence). At a particular time, the precessing protons gets in phase and the transverse magnetization M_{xy} increases and hence, the MR signal [16]. The MR signal received

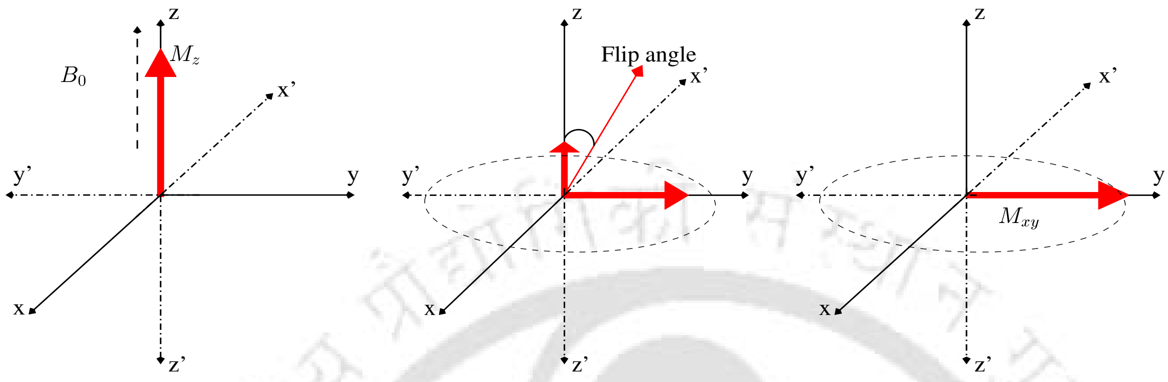

(a) Longitudinal magnetization (b) RF excitation (c) Transverse magnetization

Figure 2.2: Illustration of the magnetization processes within a 3D coordinate system. (a) The object being imaged lie on the $x-y$ plane. The field B_0 is applied along the $z-$axis and hence, the resultant magnetization is also parallel to $z-$axis. (b) An RF pulse tips the magnetization vector towards the transverse plane by an angle. This angle is known as flip angle. The flip angle should be 90°, to induce a large transverse magnetization M_{xy}. (c) Due to the 90° RF pulse, the magnetic field of the nuclei align perpendicular to B_0 and result in transverse magnetization.

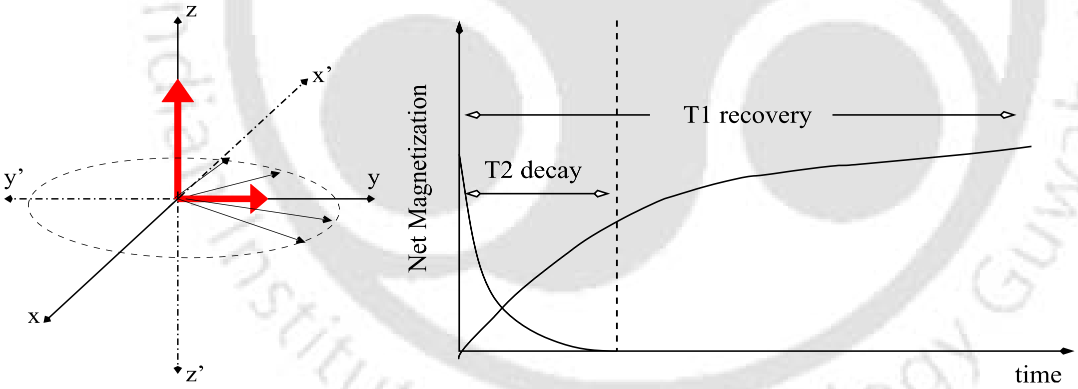

(a) Relaxation process (b) Relaxation curves with respect to time

Figure 2.3: (a) Occurrence of spin-lattice and spin-spin relaxation, after the RF pulse is removed. In the absence of RF pulse, the spins get out of phase decreasing M_{xy} and involves energy transfer between the neighboring spins. Hence, the name spin-spin relaxation. As the spins regain M_z, the absorbed energy is dissipated to the surroundings (lattice) leading to spin-lattice relaxation. During the relaxation process M_{xy} decreases and M_z increases. (b) T2 is the time taken by the spins to dephase in the transverse plane returning the transverse magnetization to its equilibrium value, zero. T1 is the time taken by the spins to realign with the magnetic field B_0. T2 is always shorter than T1 [1].

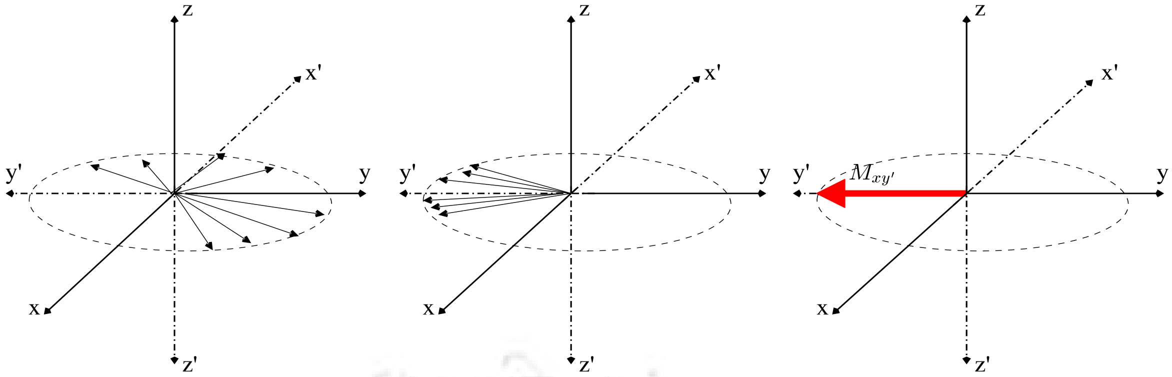

(a) Dephasing of Nuclei (b) Nuclei Rephasing (c) Recovery of transverse magnetization

Figure 2.4: Illustration of nuclei rephasing through spin reversal in the spin echo sequence. (a) Dephasing of spins occurs due to the variation in the magnetic susceptibility of the tissues. (b) Inducing the 180° pulse or gradient pulse causes the spins to precess in phase. (c) The spin echo pulse causes spin reversal and induces the magnetization $M_{xy'}$. The gradient pulse does not cause spin reversal and hence, results in magnetization M_{xy}.

is the echo signal and the RF sequences are called *gradient echo* (GE) *sequences.* The dephasing and the rephasing of nuclei using the echo sequences is shown in Fig. 2.4.

Echo time (TE) is defined as the time from the center of the initial excitation of RF pulse to the time where the signal (echo) reaches maximum. The time gap between two consecutive 90° RF pulses is defined as the repetition time (TR) [22].

Thus, the pulse sequences serve to eliminate the effects of static magnetic field inhomogeneities. As a result the signal from transverse magnetization is strong. This signal due to echo pulses is defined as the *echo signal.* The MR image reconstructed from the echo signal in transverse direction is known as the *T2 weighted* image. However, the inhomogeneities due to spin-spin interaction causes the magnetization decay, but at a slow rate. This decay builds up the longitudinal magnetization. Therefore, the SE and GE sequences are used to generate both the T1 and T2 weighted MR images [12].

2.1.3 Spatial encoding using gradients

A gradient imposes the magnetic field B_0 to vary linearly with distance from the center of the magnet. As a result, each point in the $3D$ plane experiences a different magnetic field strength. It implies that the spins exposed to higher magnetic field strength precess faster than the spins in the center, while spins on the other side exposed to lower magnetic field strength precess at a slow pace. Therefore, by inducing a RF pulse of certain precession frequency, the desired point can be excited to

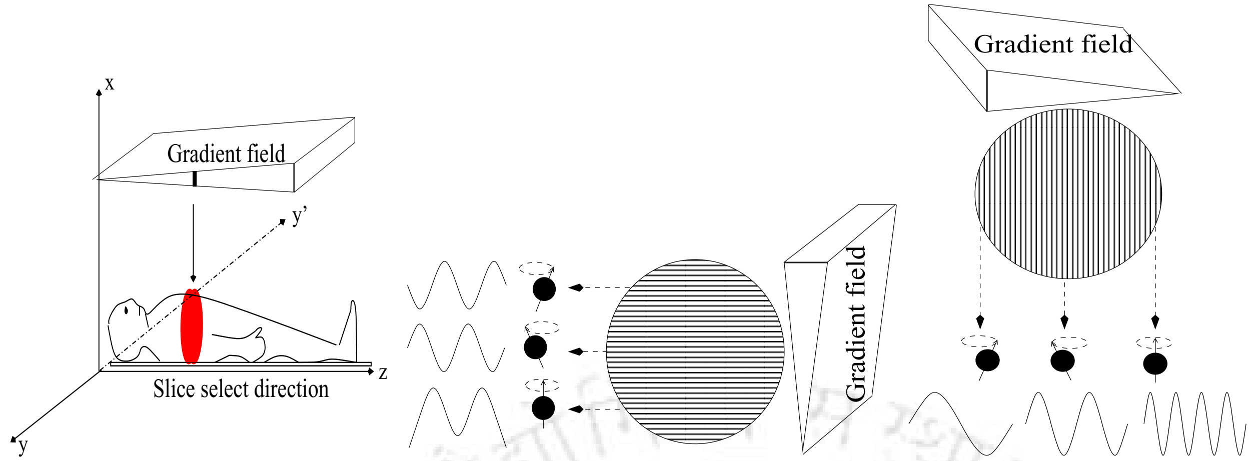

(a) Slice selection in axial direction (b) Phase encoding (c) Frequency encoding

Figure 2.5: Spatial encoding of MR signals using the gradients. (a) Slice selection is achieved in axial direction by temporarily inducing a linear magnetic field gradient along $z-$axis. The nuclei in each slice along z axis have different precession frequencies. The excited slice is considered as a $2D$ object. Each point on the slice is spatially localized in $x-y$ plane using phase and frequency encoding gradients (b) Phase encoding is achieved by creating a magnetic field gradient along y axis. The nuclei in each row is identified by a unique phase. (c) Frequency encoding is achieved by creating a magnetic field gradient along x axis. The nuclei in each column process with different frequency. Each point on the slice is represented by a unique phase and frequency.

receive the MR signal [12, 14, 16, 17].

Based on this principle, the MRI system uses three gradient coils for spatial localization. The procedure for spatial encoding that is illustrated through Fig. 2.5 is explained as follows.

2.1.3.1 Slice selection

A gradient field known as slice select gradient is used to select a cross section or slice of the object being imaged. This causes the spins to precess with different frequencies along the gradient. Therefore, RF pulses with different frequencies are used to excite each slice respectively. The slice selecting gradient fields can be superimposed either in transverse or longitudinal direction [23]. Hence, the choice for imaging the human body in axial, sagittal and coronal planes is made possible.

2.1.3.2 Phase and frequency localization

Having selected the slice, the two dimensional ($2D$) spatial image is generated from a $2D$ map known as the *k-space*. The k-space is the $2D$ Fourier space formed by organizing the $1D$ MR signals [12, 14, 16]. *The* $1D$ *MR signals received as a response for varying the frequency and the phase of the excited spins with in the slice constitutes each row of the k-space.* Hence, k-space is a $2D$ data with the phase values along the rows and frequency values along the columns. The dynamics in the frequency and the phase characteristics of the spins are generated using the frequency and phase encoding gradients respectively.

It is important to understand that these gradients are not used to selectively excite the protons, but to encode the spatial information of the already excited protons in terms of the frequencies and phases.

The phase encoding gradient is turned ON before the application of 180° RF pulse. The frequency encoding gradient is switched ON for the duration when the echo signal is received.

(i) *Phase encoding :* The gradient is used to locate the signals along the shortest axis of the slice being imaged [12, 17]. As the phase encoding gradient is turned ON, the phase of the magnetic moment of each nucleus changes and so, the precession frequency. The degree of phase shift in a nucleus depends on its distance from the center of the gradient. When the gradient is turned OFF, the nuclei returns to the precession frequency but their phase shift remains. The nuclei in each row precess at different phase. This phase shift relative to the position in the gradient gives signal localization along one dimension of the image.

(ii) *Frequency encoding :* The spatial localization along the longest axis of the slice is achieved through the frequency gradient [12, 17]. The gradient applied in this direction alters the precession frequency of the spins relative to its distance from the center of the gradient. As a result, the nuclei in each column exhibits different frequency. This process is called frequency encoding and the frequency shift of the nuclei is used for signal localization along one dimension of the image.

The slope of the gradients determines the resolution of the output MR image. Steeper gradients cause large number of frequency and phase shifts resulting in more frequency and phase encoding steps respectively [12, 14].

2.1.3.3 k-space encoding

The output measured is a composite time signal consisting of the sum of all frequency responses. The response received for each encoding step is stored in a line or row of k-space. The frequency and phase encoding procedure is repeated several times to fill the k-space. At each repetition, the amplitude and the polarity of the phase encoding gradient has to be changed in order to encode all the rows in the k-space. As a result, each nucleus along the row undergoes a unique phase shift depending on the strength of the gradient magnetic field. It is known that frequency is the rate of change of phase. Hence, the phase shifts in phase encoding can also be interpreted as different frequencies along the row. The row of k-space to be encoded depends on the amplitude and the polarity of the gradients. The polarity depends on the direction of the current through the gradient coil. The basic principle for encoding the rows of k-space is as follows [12, 14]

(i) The amplitude of phase encoding gradient gives the distance between the center of the k-space and the row positioned above or below along the vertical axis.

(ii) The amplitude of frequency encoding gradient determines the distance to be traversed from the center of the k-space to its left and \ or right along the horizontal axis.

(iii) The polarity of the gradients define the direction traveled through the k-space.

  (a) If the frequency encoding gradient is positive, the k-space is traversed from left to right.

  (b) For negative value of frequency encoding gradient, the k-space is traversed from right to left.

  (c) If the phase encoding gradient is positive, the upper half of the k-space is encoded.

  (d) For negative value of phase encoding gradient, the lower half of the k-space is encoded.

Therefore, it can be understood that phase encoding gradients with shallow slopes are used to fill the central row and the lines close to the central row. These encoding slopes do not produce a large phase shift and therefore the output signal has a large amplitude. The steepness of the slope increases as the rows deviate far from the central line. The outer lines are filled using the steep phase encoding slopes resultant in signal of small amplitude. With respect to frequency encoding, the center of k-space is encoded from the echo signal and hence, has the maximum signal amplitude. The rephasing and dephasing portions of the echo are mapped to the left and the right of the frequency axis respectively.

Thus, the center of k-space contains data with the highest signal amplitude along both the phase and frequency axis. The outer portions of k-space contain data with the lowest signal amplitude along both the phase and frequency axis. The resultant k-space contains $2D$ frequency encoded information of the excited slice [12]. The desired MR image is obtained through inverse Fourier transform of the k-space data. Figures 2.6 and 2.7 illustrates the k-space traversal and reconstruction of MR image from the k-space data respectively.

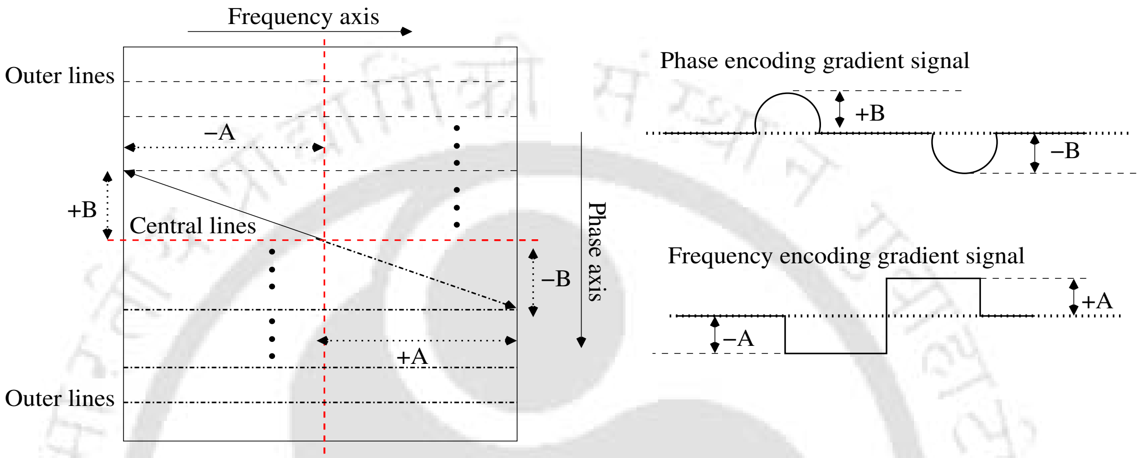

Figure 2.6: Illustration of k-space filling for the phase and frequency encoding gradient signals shown in right. The k-space filling always starts from the centre. $+A$ and $+B$ are the positive amplitudes ($-A$ and $-B$ are the negative amplitudes) of the phase and frequency encoding gradient signals respectively.

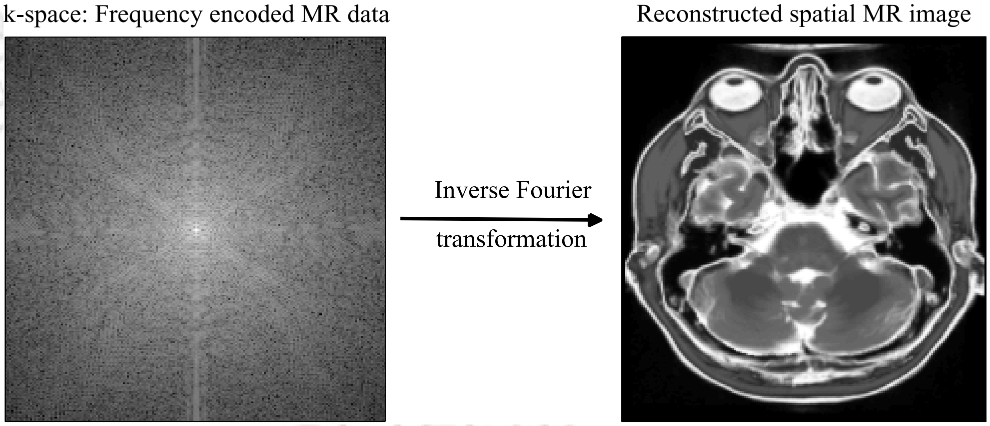

Figure 2.7: Schematic representation of the MR image reconstructed from the k-space data using $2D$ inverse fast Fourier transform.

2.2 MR Image Characteristics

The spatial MR image reconstructed from the k-space is a grey scale image and is composed of regions with three distinct intensity values. These regions correspond to the tissues that intensify the human body. The signal intensity on the MR image is determined by: proton density, T1-relaxation time, T2-relaxation time and flow. Long TR and short TE help in getting the proton density images. Proton-density weighted images are not often required in MRI; the proton density does not differ very much from one tissue to the next, and the contrast between tissues is low. The diagnostic and the perceptual quality of the MR data are characterized in terms of [14]

- Contrast
- Spatial resolution
- Signal-to-noise ratio

The important parameters influencing these image characteristics are the TR and the TE timings which eventually guide the T1 recovery and the T2 decay phenomena [14, 16, 17].

2.2.1 Contrast

The image contrast is the fundamental and the most essential characteristic of the MR image. It entirely depends on the T1 recovery and the T2 decay characteristics of the tissues.

Basically, the fluids possess the longest recovery and the decay times. The T1 and T2 for the water based tissues are comparatively less than the fluids. The fat based tissues experience short T1 and its T2 time is comparatively less than the water based tissues [17]. Accordingly, the grey level distribution and the contrast characteristics are different for T1 weighted and T2 weighted MR images.

(i) *T1 weighted MR image:*

The contrast of a T1 weighted image is controlled by the repetition time (TR). When the TR between the RF pulses is long, all the tissues would have regained its longitudinal magnetization. Hence, the difference between the signal strengths emitted from the tissues are very small resulting in poor contrast. In the case of short TR, the tissues with short T1 regain most of its longitudinal magnetization, resulting to higher intensity values [14]. Those tissues with longer T1 attains less longitudinal magnetization resulting in small intensity values.

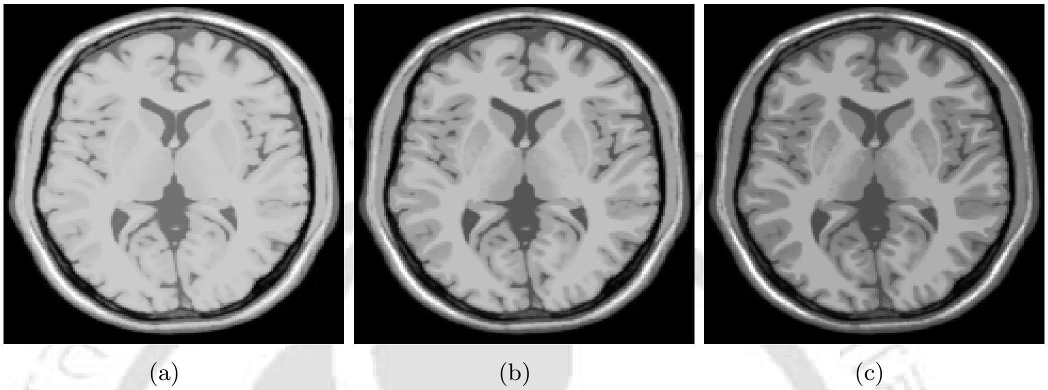
(a) (b) (c)

Figure 2.8: Effects of TR and TE on the contrast of T1 weighted brain MR images. Illustration using the images acquired using spin echo sequence with the parameters (a) TR=1100 ms,TE=10 ms (b) TR=650 ms,TE=10 ms. (c) TR=200 ms,TE=10 ms. By comparing these images, it can be inferred that the tissue contrast of the T1 weighted image is good for the choice TR=200 ms,TE=10 ms. The Typical parameters are: TR-300 to 600 ms and TE-10 to 30 ms.

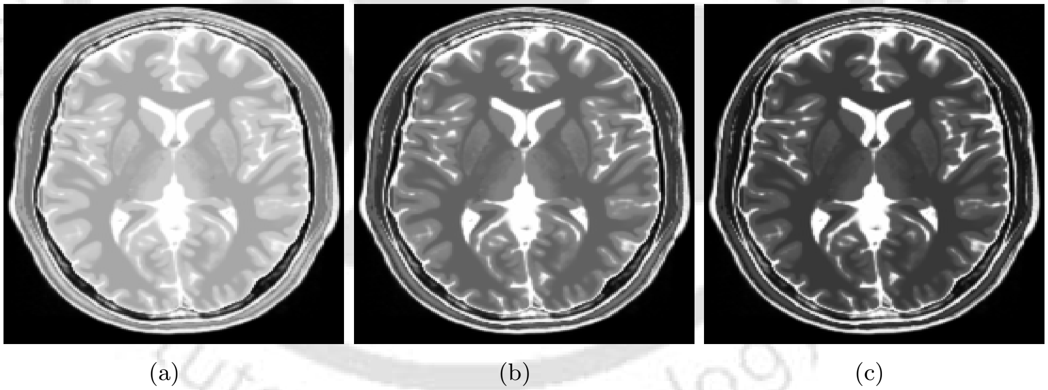
(a) (b) (c)

Figure 2.9: Effects of TR and TE on the contrast of T2 weighted images. Illustration using the images acquired using spin echo sequence with the parameters (a) TR=2000 ms,TE=70 ms (b) TR=2000 ms,TE=120 ms. (c) TR=2000 ms,TE=170 ms. By comparing these images, it can be inferred that the tissue contrast of the T2 weighted image in (c) is superior to (a) and (b). The Typical parameters are: TR> 2000 ms and TE> 70 ms.

Therefore, in a T1 weighted MR image the fluids appear dark, water and fat based tissues appear grey. However, fat based tissues are brighter than the water based tissues [17].

(ii) *T2 weighted MR image:*

The contrast of a T2 weighted image depends on the echo time (TE). When TE is short, tissues with short T2 decays faster and those with long T2 would not have completely decayed. Hence, the contrast of the resulting image will be poor. If TE is long, the tissues with long T2 would have completely decayed and appear brighter [14].

In the T2 weighted MR image the fluids appear brighter, while the other tissues attain grey values, such that fat based tissues are darker than the water based tissues [17].

The details in the T1 and T2 weighted images for different values of TR and TE are illustrated through Fig. 2.8 and 2.9. Also, the dynamic range of grey values in T2 weighting is greater than the T1 weighting. This can be verified by comparing the histogram of the T1 and T2 weighted images as shown in Fig. 2.10.

The tissue boundaries are very distinct in the T1 weighted images and hence, are particularly used to study the anatomical details. The T1 weighted images are also known as *anatomy scans*. The pathological details are very distinctively acquired in the T2 weighted images. Hence, they are also known as *pathology scans* [17].

2.2.2 Spatial resolution

The spatial resolution of a MR image is the ability to distinguish two points as separate and distinct [14]. Images with increased spatial resolution produces more details, those are diagnostically very significant.

The resolution is increased by employing steeper gradients for slice selection, phase and frequency encoding [14]. As a result, improved resolution in slice select direction and in-plane resolution is achieved.

2.2.3 Signal-to-noise ratio

Noise is an inevitable component that adds to the MR signal while acquisition. The level of noise in the acquired data is measured in terms of signal-to-noise ratio (SNR). The noise induced in MRI are due to the [16]

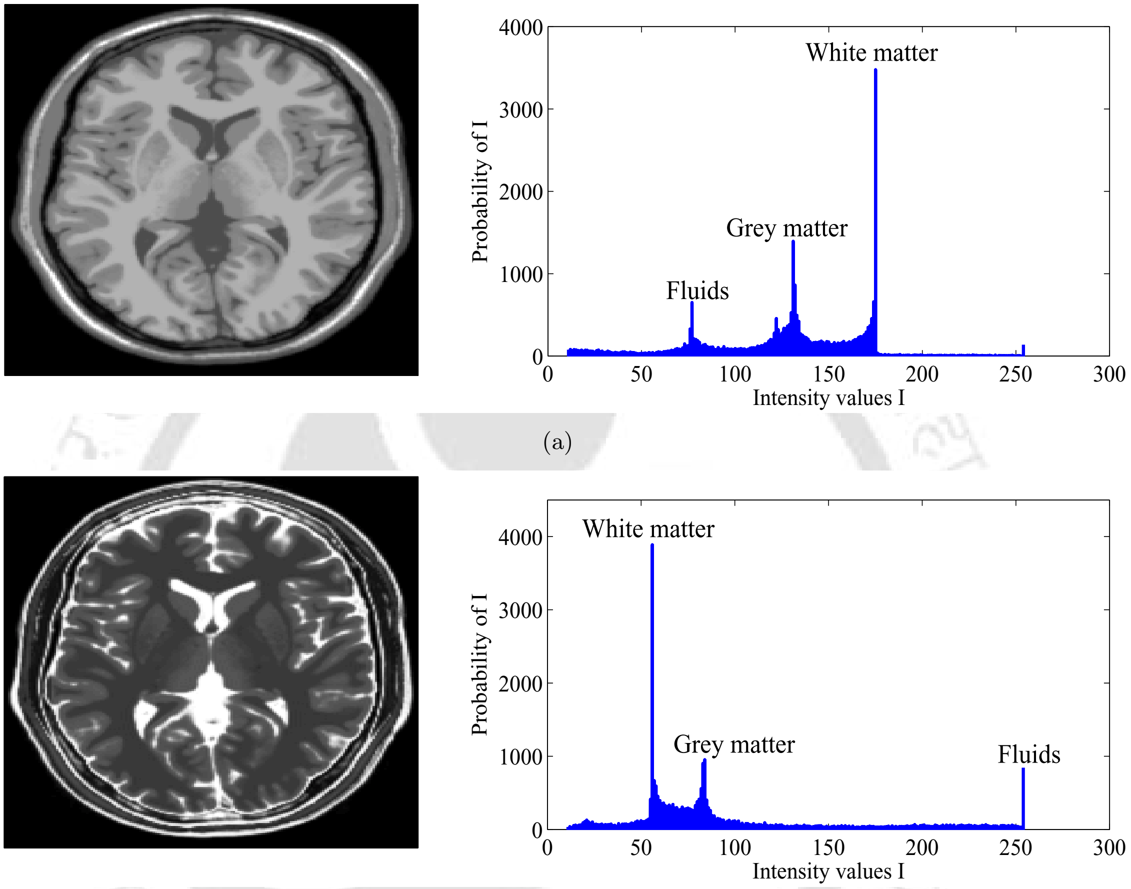

(a)

(b)

Figure 2.10: Human Brain is composed of cerebro-spinal fluid (CSF), white matter and grey matter. CSF is a fluid, white matter has higher fat concentration and grey matter has higher water concentration. Comparison of (a) T1 weighted brain MR image and the histogram representing its grey level distribution. with (b) T2 weighted brain MR image and the histogram representing its grey level distribution. The contrast between grey and white matter in T1 weighting is better than T2 weighting. Hence, T1 images are generally used to study the anatomical details. The CSF appears bright in T2 weighting and hence the dynamic range of grey levels in T2 weighting with respect to these three tissues is larger. The pathological tissues appear brighter in T2 weighting and has better contrast than in T1 weighting. Hence, T2 weighted images are used to study the pathologies. The darkest regions in T1 and T2 weighting are the no signal regions which correspond to air (background) and tissues with very little or no hydrogen like bones.

(i) random motion of electrons in the RF coils and the amplifiers.

(ii) magnetic field inhomogeneities caused by the gradient coils.

(iii) ions such as sodium, potassium and chloride present in the tissues. These ions generate fluctuating magnetic fields which induce a noise voltage in the receiver coil.

The level of thermal noise in a MRI system is constant throughout and its value depends on the area under examination and the inherent noise of the system [12]. Noise occurs at all frequencies and is random in time [12]. Conversely, the MR signal level is adaptable and it depends mainly on the imaging parameters. The signal is therefore increased or decreased relative to the noise. The increase in signal level increases the SNR and hence, the image quality. The imaging factors that affect the SNR are the [14, 17]: field strength, coil type, TR, TE timings and flip angle.

2.2.3.1 Field strength

The SNR increases with the magnetic field strength. If the external field B_0 is large, the net magnetization increases thereby increasing the strength of the MR signal emitted during the relaxation processes [1].

2.2.3.2 Coil type

Small RF coils result in high SNR. However, such coils provide less coverage restricting the cross section being imaged. Conversely, larger coils provide more coverage but results in reduced SNR [16].

Therefore, phased array coils comprising of multiple small RF coils are used to increase both the SNR and the coverage area. The MR signal collected from these coils are combined to produce an image. This sytem is known as *multi-coil imaging system.*

2.2.3.3 TR

The signal level increases if there is large longitudinal magnetization. Hence, increasing the TR results in more longitudinal and transverse magnetization. When the TR is short, the magnetization decreases yielding less MR signal [24].

2.2.3.4 TE

The SNR increases, if the rate of dephasing in transverse plane is less. This requires TEs of short duration. As the TE is large, the rate of dephasing increases reducing the signal emitted during T2 relaxation [24].

2.2.3.5 Flip angle

The flip angle determines the amount of longitudinal magnetization being flipped to transverse plane. Larger flip angle results in more transverse magnetization and thus, high SNR [14].

2.2.4 Significance of SNR and its trade-offs

The contrast and the resolution of the image can be directly improved by proper choice of imaging parameters. Conversely, achieving the desired SNR is very complicated as it influences the contrast and the resolution. For this reason SNR improvement is considered as one of the major issues in MR imaging.

From the discussion on MR image characteristics, it can be understood that the signal level increases for higher values of TR. However, large TR results in poor contrast T1 images. The T2 weighted images require long TEs for good contrast, but result in reduced SNR. Since short TE improves the signal level, T1 weighted images are acquired with short TR and TE. This results in good contrast and better SNR than the T2 weighted images. Additionally, the MR signal from the tissues with low proton density are less and, hence, SNR in these regions are low [14].

The spatial resolution of the MR image is increased by using steeper gradient field which results in more magnetic field inhomogeneities, that increase the noise level in the MR signal. However, reducing the resolution conceals small details and subtle contrast changes.

Considering the discussion above, imaging parameters are not sufficient to ensure high SNR in MRI. Hence, signal averaging based acquisition and image denoising algorithms are developed to reinstate the signal values.

Signal averaging based acquisition involves increasing the number of excitations (NEX) [14,16,17]. It is also referred as the number of signal averages (NSA). This parameter defines the number of times frequencies in the signal are sampled with the same slope phase encoding gradient [14]. The resultant MR signal is the average of these excitations. Hence, the received signal level increases and the level of thermal noise decreases due to its random characteristic. Doubling the number of signals to calculate the average, increase the SNR only by $\sqrt{2}$ and proportionally increases the scan time [12, 16]. Therefore, post acquisition image denoising methods became essential for MR images affected by thermal noise [25].

Research and advancements in the field of MR image denoising has made post acquisition image denoising a most versatile approach to improve the SNR. Also, the technique absolves the restriction on imaging parameters and facilitates MR image acquisition with good contrast and high spatial resolution.

2.3 Summary

In this chapter, the principles behind the MR image formation are briefly discussed. The acquisition parameters influencing the characteristics of the T1 and T2 weighted MR images are explained in detail. In MRI applications, there is an intrinsic trade-off between signal-to-noise ratio (SNR), contrast-to-noise ratio (CNR), and resolution. Depending on specific diagnostic tasks, high spatial resolution and high contrast may be required. But for precise diagnosis and further image processing operations like segmentation, a high SNR is usually necessary because most of the algorithms are very sensitive to noise [24]. Thus, the estimation and reduction of noise in MR images becomes a mandatory procedure.

3

Noise in MRI

Contents

3.1 Introduction

The MR data acquired from the scanner is complex in nature and is represented in k-space (frequency domain). Hence, inverse Fourier transformation of the k-space data is performed to obtain the MR image in spatial domain. Due to the linearity of the Fourier transform, the resultant MR image in the spatial domain is also complex.

Consider the k-space data $s(m,n)$ defined over a grid of size $N \times N$, such that $m = \{0, 1, \cdots N-1\}$ and $n = \{0, 1, \cdots N-1\}$. The MR data $s(m,n)$ is complex and hence it can be represented as

$$s(m,n) = s_{re}(m,n) + i\, s_{im}(m,n) \tag{3.1}$$

where $i = \sqrt{-1}$ is the imaginary number. The complex MR image in spatial domain $f(x,y)$ for $x = \{0, 1, \cdots N-1\}$ and $y = \{0, 1, \cdots N-1\}$, is obtained by computing the inverse discrete Fourier transform of $s(m,n)$. Therefore,

$$f(x,y) = \frac{1}{N^2} \sum_{m=0}^{N-1} \sum_{n=0}^{N-1} \left(s_{\mathrm{re}}(m,n) + i\, s_{\mathrm{im}}(m,n)\right) \exp\left(\frac{i2\pi xm}{N}\right) \exp\left(\frac{i2\pi yn}{N}\right) \tag{3.2}$$

The above equation can be simplified as

$$f(x,y) = \frac{1}{N^2} \sum_{x=0}^{N-1} \sum_{y=0}^{N-1} s(m,n) \cos\left(\frac{2\pi (xm + yn)}{N}\right) + i\, s(m,n) \sin\left(\frac{2\pi (xm + yn)}{N}\right) \tag{3.3}$$

By assuming the right-hand side of the Eq. (3.3) as $p(x,y) + i\, q(x,y)$, we can generalize as

$$f(x,y) = p(x,y) + i\, q(x,y)\,. \tag{3.4}$$

p and q are the real and imaginary parts of the spatial domain complex MR signal f. The magnitude of the complex MR image used in practice is obtained as

$$|f(x,y)| = \sqrt{p(x,y)^2 + q(x,y)^2} \tag{3.5}$$

The noise added to the complex k-space data during acquisition is modeled as zero mean Gaussian noise with variance σ_n^2. The Gaussian noise model is a good approximation for the noise in each of the real and imaginary channels. The characteristics of noise upon inverse transformation do not change because of the linearity and orthogonality of the Fourier transform. However, computing the magnitude of the complex MR image alters the intensity distribution of the magnitude data. The characteristics of the noisy MR image are also influenced by the number of RF coils used in acquiring the MR signal. Therefore, estimation of the noise variance is an important factor in developing noise removal algorithms for MR images [26]. This chapter presents in detail the characteristics of the noisy MR images and the review of existing noise variance estimation methods.

3.2 Characteristics of Noisy MR image

This section deals with the characteristics of noise in MR images acquired using both single and multiple coil systems. The noise characteristics are analyzed based on the probability distribution function (pdf) of the signal and the noise. The knowledge of the pdf is vital for estimating the noise variance [27].

3.2.1 Characteristics of noise in single coil system

The noise-free MR data represented in Eq. (3.6) can be generalized as

$$f = p + iq. \tag{3.6}$$

The noise added to the complex raw data is zero mean Gaussian noise with variance σ_n^2. The distribution of noise is given by $N(0, \sigma_n^2)$. Therefore,

$$\begin{aligned} g &= f + (\eta_{re} + i\eta_{im}) \\ g &= (p + iq) + (\eta_{re} + i\eta_{im}) \\ g &= (p + \eta_{re}) + i(q + \eta_{im}) \end{aligned} \tag{3.7}$$

where g is the noisy MR image, η_{re} and η_{im} are the real and the imaginary components of noise. From Eq. (3.7) it is clear that noise in the image domain is still additive and Gaussian. In real time, complex MR images are transformed to magnitude and phase images. Since the computation of magnitude (or phase) image is a non-linear operation, the pdf of the MR image changes to Rician [28]. The magnitude of the noisy MR image is computed as

$$|g| = \sqrt{(p + \eta_{re})^2 + (q + \eta_{im})^2} \tag{3.8}$$

As mentioned earlier, the complex MR image is Gaussian distributed [29]. Due to the square-root operation performed for computing the magnitude image the pdf of $|g|$ becomes Rician [29–31] and is represented :

$$p(g|f,\sigma_n) = \frac{g}{\sigma_n^2} e^{\frac{-(g^2+f^2)}{2\sigma_n^2}} I_0\left(\frac{fg}{\sigma_n^2}\right)\epsilon(g) \tag{3.9}$$

where I_0 denotes the 0^{th} order modified Bessel function of the first kind. The unit step heaviside function $\epsilon(.)$ is used to indicate that the expression for the pdf of g is valid only for non-negative values of g. This distribution function does not give the distribution of noise in the image, it gives the distribution of the observed pixel intensities in the presence of noise [32].

If the ratio $\frac{f}{\sigma_n}$ is zero, the Rician pdf given in Eq. (3.9) leads to Rayleigh distribution and it is defined as follows

$$p(g|\sigma_n) = \frac{g}{\sigma_n^2} e^{\frac{-(g^2)}{2\sigma_n^2}} \epsilon(g). \tag{3.10}$$

Thus, we infer that noise in the image regions with no nuclear magnetic resonance (NMR) signal is Rayleigh distributed. The image regions with large signal intensity approximates to Gaussian pdf [29] and the distribution function is given by

$$p(g|\sigma_n) = \frac{1}{\sqrt{2\pi\sigma_n^2}} e^{\frac{-(g-\sqrt{f^2+\sigma_n^2})^2}{2\sigma_n^2}} \epsilon(g) \tag{3.11}$$

Therefore noise in MR images behaves to be Gaussian distributed when the SNR is high and Rayleigh distributed for low SNR. Hence it can be considered that the noise depends on the local intensity in the image. Fig. 3.1 gives the illustration for the behavior of noisy MR images.

Similar to magnitude image, the phase MR image is also obtained through non-linear operation. The formulation for obtaining the phase MR image is defined as

$$\Phi_{x,y} = \arctan\left(\frac{q(x,y)}{p(x,y)}\right) \tag{3.12}$$

Therefore Φ denotes the desired phase MR image. Since, the arctangent operation is a non-linear function the distribution of phase MR image also tends to be Rician [29, 33].

3.2.2 Characteristics of noise in multi-coil system

In case of multiple coil MR acquisition system, the acquired signal in each coil can be modeled as the original signal corrupted by zero mean and equal variance additive Gaussian noise. The complex MR data in the coil l is given as,

$$g_l = (p_l + iq_l) + (\eta_{l_{re}} + i\eta_{l_{im}}) \tag{3.13}$$

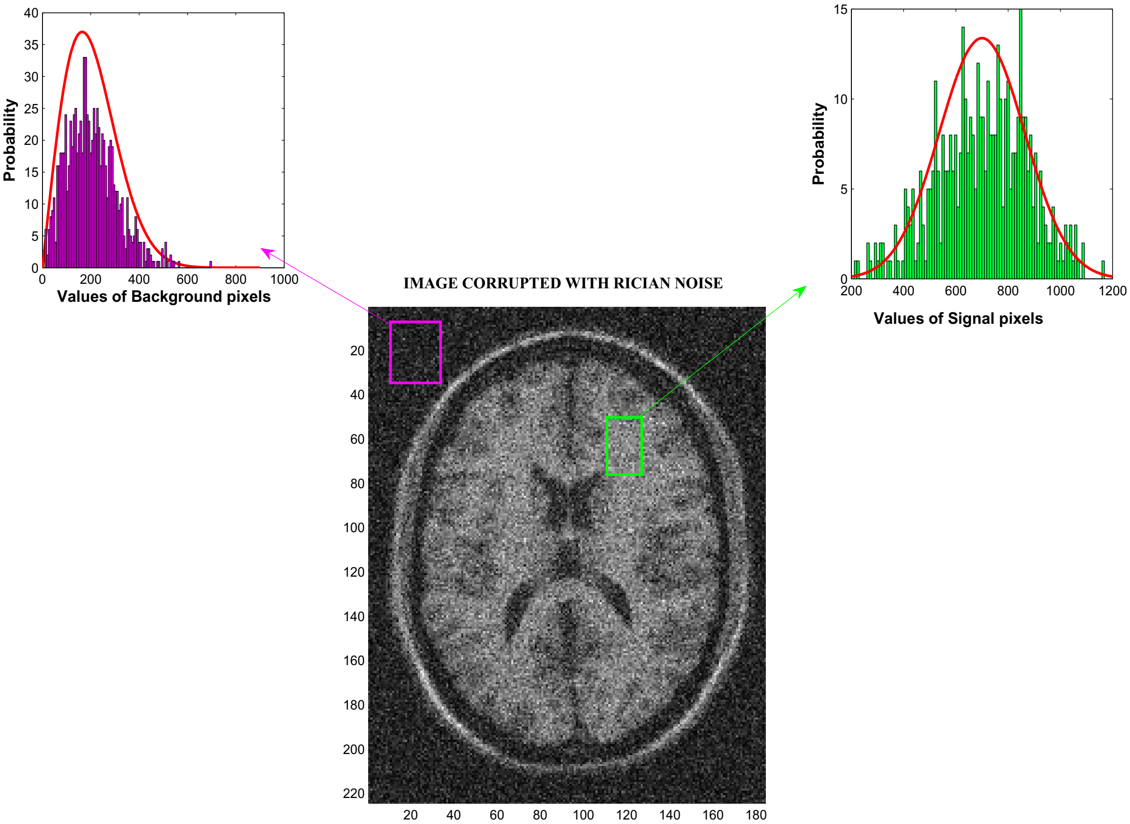

Figure 3.1: The distribution of noise in MR image obtained using single-coil MRI scanner.

where $l = (1, 2, ..., L)$ and L represents the maximum number of coils. The magnitude image $g_{_L}$ is obtained using the sum of squares method [34],

$$g_{_L} = \sqrt{\sum_{l=1}^{L} |g_{_l}|^2}. \tag{3.14}$$

accordingly we can write the original image as

$$f_{_L} = \sqrt{\sum_{l=1}^{L} |f_{_l}|^2}. \tag{3.15}$$

Considering the noise to be independent and identically distributed, the pdf of the magnitude signal $g_{_L}$ is a non-central chi-squared distribution. The distribution is given as [35] below

$$p(g_{_L}\,|f_{_L}, \sigma_n, L) = \frac{f_{_L}^{1-L}}{\sigma_n^2} g_{_L}^L\, e^{-\frac{g_L^2+f_L^2}{2\sigma_n^2}}\, I_{L-1}\left(\frac{f_{_L} g_{_L}}{\sigma_n^2}\right) \epsilon\,(g_{_L}) \tag{3.16}$$

In regions with no NMR signal (background), the above distribution revises to a central chi-square distribution and it is given as,

$$p(g_L\,|\sigma_n, L) = \frac{2^{1-L}}{\Gamma(L)}\frac{g_L^{2L-1}}{\sigma_n^{2L}}e^{-\frac{g_L^2}{2\sigma_n^2}}\epsilon(g_L). \tag{3.17}$$

where $\Gamma(L)$ is the gamma function. For $L = 1$ the formulations of multi-coil system is same as the single-coil system.

3.3 Noise Variance Estimation

The performance of the image denoising algorithms depends on the characteristics of noise. Hence, it is essential to know the variance of the noise in the underlying signal. There are several methods for estimating the noise variance from the noisy MR image. Most of these techniques rely on the characteristics of the MR image. A complete survey of the noise estimation methods for single-coil and multi-coil MRI systems is presented in [36]. This section presents the method proposed in [37], for estimating the noise variance from the background regions of MR image.

Nowak [37] has shown that estimation of noise from the magnitude MR image is biased and it is signal dependent. Hence, he proposed a noise estimation technique based on squared magnitude MR images. Squaring the magnitude MR image makes the bias additive and signal independent. The square of the noisy magnitude MR image $|g|$ in Eq. (3.7)is written as

$$|g|^2 = (p + \eta_{re})^2 + (q + \eta_{im})^2 \tag{3.18}$$

Taking expectation of (3.18) yields,

$$E[g^2] = E[(p + \eta_{re})^2 + (q + \eta_{im})^2] \tag{3.19}$$

The above equation can be simplified as

$$E[g^2] = E[p^2] + E[q^2] + 2\sigma_n^2 \tag{3.20}$$

Therefore the bias in square magnitude domain is $2\sigma_n^2$. In the absence of NMR signal for which $p = 0$ and $q = 0$ the expected value in Eq. (3.20 becomes

$$E[g^2] = 2\sigma_n^2 \tag{3.21}$$

This implies

$$\sigma_n = \sqrt{\frac{E[g^2]}{2}} \tag{3.22}$$

Under this condition, $E[g^2]$ specifies the mean value in the absence of signal. Generally, the background regions of the MR image does not contain any NMR signal. Therefore by considering $E[g^2]$ as the mean value μ computed from a portion of the background region, the noise standard deviation is estimated as

$$\sigma_n = \sqrt{\frac{\mu}{2}} \tag{3.23}$$

In all our denoising methods to be presented hereafter, the noise variance is estimated from the background regions of the MR image using equation Eq. (3.23).

3.4 Summary

In this chapter, the characteristics of noisy MR images and their influence on single and multi-coil MR imaging systems are discussed. The signal dependent characteristics of noise in MR images makes it difficult to be estimated through simple procedures. An efficient method for estimating the noise variance as proposed in [37] was presented.

4

Review of MR Image Denoising Methods

Contents

4.1 Introduction

In this chapter, we discuss about the existing state-of-art methods for MR image denoising. Noise reduction techniques for MR images can be categorized into two types: acquisition-based noise reduction methods and post- acquisition image filtering. Acquisition-based methods generally utilize longer scan times, averaging over repeated measurements, enlarging the voxel volume that is being employed or improvements in hardware [38–40]. Beside hardware improvements, these methods either increase image acquisition time or sacrifice spatial resolution [38]. Hence, post-acquisition image filtering is an inexpensive and effective alternative [39, 40] and will be discussed in detail. The vast literature of MR image denoising algorithms can be widely classified under spatial domain and wavelet domain methods. Spatial domain refers to the image plane, and techniques under this category are based on direct manipulation of pixels in an image. The wavelet domain denoising methods can be termed as transform domain point processing techniques. Popularity of wavelet domain methods in denoising applications is mainly due to the energy compaction property [5] of the wavelet transform.

4.2 Basics of Spatial Filtering

Spatial domain filtering, involves convolving the original image with a mask that represents a low-pass filter or a smoothing function. Low-pass filtering of an image is essentially a spatial averaging operation. Low-pass filtering attenuates the high frequency contents in the signal and is equivalent to integrating the signal [41]. The output image is a smooth version of the original image, without the high frequency contents of the image. Considering an additive noise model,

$$g(x,y) = f(x,y) + \eta(x,y) \tag{4.1}$$

where $g(x,y)$ is the noisy image, $f(x,y)$ the original image and $\eta(x,y)$ is the noise. The output image obtained using the spatial filter is given as,

$$\hat{g}(x,y) = \sum_{(m,n)\in W}\sum h(m,n)f(x-m,y-n) \tag{4.2}$$

where W is the neighborhood around the pixel and $h(m,n)$ is the filter. The weights in the spatial averaging filters are assigned equal values. The output of the spatial averaging filter is given as,

$$\hat{g}(x,y) = \frac{1}{N}\sum_{(m,n)\in W}\sum f(x-m,y-n) + \hat{\eta}(x,y) \tag{4.3}$$

where N is the number of pixels in the neighborhood W and $\hat{\eta}(x, y)$ is the spatial average of the noise component. Spatial averaging the noisy image reduces the noise power by a factor equal to N [41]. The filter weights used in spatial filtering approaches are independent of the contents of the image. Thus, all the regions of the image are uniformly affected. This leads to over smoothing of edges and features of interest in the denoised image.

The spatial filtering techniques can be divided into two types, linear filtering and non-linear filtering. Gaussian filter is an example for linear filtering technique. Gaussian smoothing of images, though suppresses the noise also causes blurring of edges [9]. Non-linear filtering techniques are more popular for denoising applications because of their better denoising capability and edge preserving characteristics. Median filter [42], is a best example for non-liner filters. Advantage of non-linear filter is that they are able to discriminate the high frequency components of signal and noise.

4.3 Spatial Filtering Techniques for MRI Denoising

In this section, we will discuss about the existing spatial filtering methods specific to MR images.

4.3.1 Gaussian filtering

Henkelman *et al.* [43] was the first to discuss the characteristics of noise in the Fourier transformed MR images and the effects of spatial and temporal filtering on the MR images. Noise considered in their study was a normally distributed white noise mainly due to the RF receiver noise in the MR system. The spatial domain filtering of MR images was done by convolving the original image with a smoothing function. This resulted in elimination of high spatial frequency content of the image. Convolution of the Fourier transformed image may also cause some artifacts to arise in the denoised image [43]. The noise power spectrum of the noisy image is used to determine the shape of the smoothing function. A simple low-pass filter with a frequency response similar to Gaussian was used in spatial filtering. The temporal filters control the bandwidth of the sampled data. This choice of the temporal filter depends on the sampling interval. An optimum temporal filter must be able to reduce aliasing, caused due to the overlapping of the data. The authors concluded that spatial filtering was not sufficient to remove the noise and artifacts completely and that the estimation of noise from the background region is valid.

4.3.2 Measurement dependent filtering

Brosnan *et al.* [44] have proposed a noise reduction technique based on measurement-dependent filtering (MDF) applicable to multiple measurement systems. MDF combines the information from multiple measurements and gives a single image suitable for human interpretation and analysis. MDF algorithm is formulated by considering two images: g_l and g_h. g_l is a low SNR image with desired structures and g_h a high SNR image of the same region. The image g_l can be expressed in terms of signal and noise as,

$$g_l = f_l + \eta_l \tag{4.4}$$

where f_l and η_l represent the signal and noise respectively. The estimate of g_l using the Wiener filter is given as,

$$\hat{g}_l = g_l * h \tag{4.5}$$

where h is the filter function. The Fourier transformed expression of h is,

$$H = \frac{P_{f_l}}{P_{f_l} + P_{\eta_l}} \tag{4.6}$$

where P_{f_l} and P_{η_l} represent the power spectrum of signal and noise respectively. Incorporating the information from the image g_h improves the solution obtained in Eq. (4.5). The low spatial frequencies of g_l are combined with the high spatial frequencies in g_h as,

$$\hat{g}_l = g_{ll} + C g_{hh} \tag{4.7}$$

where C is the control function and $\hat{g}_l$ the denoised version of g_l. The subscripts l, h represent the low and high pass filters respectively. The low pass filter reduces the noise and the control function determines the amount of high frequency information to be added to restore the edges in the estimated image $\hat{g}_l$. The control function is determined using the statistical approaches. The value of C based on the linear least square approach is obtained as,

$$\hat{C} = \frac{\sum\limits_{i \in W} g_{lh}(i)\hat{g}_{hh}(i)}{\sum\limits_{i \in W} \hat{g}_{hh}(i)\hat{g}_{hh}(i)} \tag{4.8}$$

where $g_l h$ is the high pass filter output of image g_l and $\hat{g}_{hh}$ the estimated high pass filtered result of the image g_h. W is the local region within which the local statistical estimation is done. The optimal choice of g_h highly impacts the performance of MDF. The filtered output has the high-spatial frequency information preserved and shows improvement in SNR. The authors have shown the diagnostic utility of the denoised images using this method. The major disadvantage of this technique is the need for multiple measurements of the same image.

4.3.3 PDE based denoising

Second order partial differential equations (PDE) have been widely used in denoising applications [45]. Frequently used PDE based denoising technique is the anisotropic diffusion filtering (ADF) [9,46] method, which aids in suppressing noise and in preserving the image features such as edges and lines. Anisotropic diffusion is a non-linear and space-variant transformation of the original image [47]. ADF is based on the multiscale representation of the image. The idea behind this filter is to embed the original image in a family of derived images $f(x, y, \sigma)$, obtained by convolving the original image $f_0(x, y)$ with a Gaussian kernel $G(x, y, \sigma)$ of variance σ^2, expressed as

$$f(x, y, \sigma) = f_0(x, y) * G(x, y, \sigma). \tag{4.9}$$

The family of derived images can be represented as a solution of the heat diffusion equation,

$$f_\sigma = c\nabla^2 f(x, y) \tag{4.10}$$

The initial conditions are $f(x, y, 0) = f_0(x, y)$, where c is a constant known as conduction coefficient. In [9], the conduction coefficient was considered as scale and space varying, which enables the diffusion process to preserve the boundaries of the image. Thus, the anisotropic diffusion equation is given as,

$$\begin{aligned} f_\sigma &= \mathrm{div}(c(x, y, \sigma)\nabla f(x, y, \sigma)) \\ &= c\nabla^2 f + \nabla c \nabla f \end{aligned} \tag{4.11}$$

The two conduction coefficients given by Perona *et al.* [9] are,

$$c\,(x, y, \sigma) = e^{-\left(\frac{||\nabla f||}{\kappa}\right)^2} \tag{4.12}$$

and

$$c\,(x, y, \sigma) = \frac{1}{1 + \left(\frac{||\nabla f||}{\kappa}\right)^2}. \tag{4.13}$$

From Eq. (4.12, 4.13), c tends to be small when the gradient of the image is large yielding less smoothing near the edges. The parameter κ, known as the diffusion constant controls the sensitivity of the edges and is chosen experimentally. If the gradient magnitude of the image (∇f) is greater than κ, then the corresponding edge is enhanced and if it is less than κ then the homogeneous regions are smoothened. In this section, we will discuss about the various ADF based MR image denoising techniques in detail.

Gerig *et al.* [38] have proposed a MRI filtering algorithm based on ADF. Smoothing is expressed as a diffusive process, performed over intra-regions and restricted at the region boundaries. The filtering approach works on the assumption that the MR image data consists of smooth regions separated by discontinuities. Two main functions that effectively control the performance of this technique are: number of iterations and the diffusion function. The number of iterations required is determined on visual comparison of the different filtered results. The parameter κ, in Eq. (4.12) depends on the noise level and the strength of the edges. The optimal value of κ was found to lie within a range $1.5\sigma_n < \kappa < 2\sigma_n$. In this work, the number of iterations has been prefixed to be within three to five iterations. This method has been made applicable to $3D$ MR data. The optimal parameters of the diffusion function have to be determined manually, which is a notable disadvantage to this method.

Sijbers *et al.* [48] have proposed an adaptive anisotropic filtering method based on the local intensity orientation and a measure to control the shape and extent of filter kernel. This method works on the assumption that MR images consist of many regions in which the signal is stationary and ergodic in the mean and variance [49]. The authors modified the anisotropic diffusion filtering [50] for filtering magnitude MR images. Relationship between the local orientation direction and the Eigen vectors are obtained, which enable in controlling the shape and extent of the filter kernel. This algorithm ensures the preservation of corners and junctions by stopping the smoothing process when the value of conduction coefficient (c) is large. The knowledge of Rician distribution of noise in magnitude MR images are used in this approach to reduce the bias. The filter parameters are obtained using the ML [51] estimation method. The bias reduction helps in retaining the spatial resolution of the denoised image.

A new method called confidence based anisotropic diffusion for denoising MR images was proposed in [39]. The conductance function proposed in [9] tends to completely remove fine structures in low SNR images. Determining a better conductance function using knowledge-based approach [52] has been under research. In this work, a new method for determining the conductance function using a priori knowledge and a scale selection has been discussed. This mechanism assumed that any pixel in a image lies either in a homogeneous region or on a slope of an edge. Diffusion should he high in homogeneous regions $(c(x,y,\sigma) \simeq 1)$ and moderate on a slope of a blurred edge $(c(x,y,\sigma) \simeq 0)$. The gradient of an image is used as a feature to derive the confidence of a pixel being in a homogeneous region. Since, the significant features in an image exists over multiple scales, a multiscale approach is used in gradient calculation. The minimum reliable scale at each pixel in an image is obtained using local scale control [53], based on the prior knowledge about the noise. The gradient is estimated using a steerable Gaussian first derivative filters given as:

$$\begin{aligned} G_x(x,y,\sigma_1) &= -\tfrac{x}{2\pi\sigma_1^4} e^{-\frac{(x^2+y^2)}{2\sigma_1^2}} \\ G_y(x,y,\sigma_1) &= -\tfrac{y}{2\pi\sigma_1^4} e^{-\frac{(x^2+y^2)}{2\sigma_1^2}} \end{aligned} \tag{4.14}$$

where, σ_1 represents the scale of the Gaussian kernel. The gradient of the image is given by,

$$\nabla f = \cos(\theta) f_x(x,y,\sigma_1) + \sin(\theta) f_y(x,y,\sigma_1) \tag{4.15}$$

where, θ is the gradient vector direction at (x,y). The functions $f_x(x,y,\sigma_1)$ and $f_y(x,y,\sigma_1)$ are defined as,

$$\begin{aligned} f_x(x,y,\sigma_1) &= G_x(x,y,\sigma_1) * f(x,y) \\ f_y(x,y,\sigma_1) &= G_y(x,y,\sigma_1) * f(x,y). \end{aligned} \tag{4.16}$$

The effect of noise in images, leads to a nonzero value of gradients in the homogeneous regions. Hence, the gradient response of noise has to be estimated. The pdf of noise gradient is [53],

$$p_{|\nabla f|}(\eta) = \frac{\eta}{s_1} e^{-\frac{\eta^2}{2s_1^2}} \tag{4.17}$$

and s_1 is expressed as:

$$s_1 = \frac{\sigma_n}{2\sqrt{2\pi}\sigma_1^2} \tag{4.18}$$

where, σ_n is the standard deviation of the noise. From the pdf of the gradient of noise the critical threshold function is defined as,

$$T(\sigma_1) = \frac{\sigma_n}{2\sigma_1^2} \sqrt{\frac{-\ln(\alpha_p)}{\pi}} \tag{4.19}$$

where, α_p is the type 1 error function defined as,

$$\alpha_p = \int_T^\infty \frac{\eta}{s_1^2} e^{-\frac{\eta^2}{2s_1^2}} d\eta \tag{4.20}$$

T represents the gradient threshold to determine the edge. $T(\sigma_1)$ is directly proportional to the standard deviation of noise (σ_n). The critical threshold map $(C(x,y))$ is represented using the gradient response of $f(x,y)$,

$$C(x,y) = \max\{T(\sigma_1) : |\nabla f| \geq T(\sigma_1)\}. \tag{4.21}$$

This critical threshold map is obtained from the scaled space technique [54], in which the white region correspond to high threshold which indicates edges and black region corresponds to low threshold indicating homogeneous region. The conductance function of the anisotropic diffusion is defined using the critical threshold map (4.21),

$$c(x,y,\sigma_1) = \frac{T(\min(\sigma_1)) - C(x,y)}{T(\min(\sigma_1))}. \tag{4.22}$$

For values of the gradient response of a point, less than the critical threshold function, it is assumed to be a homogeneous region and a conductance function of one is assigned to the point.

A new noise adaptive anisotropic diffusion filter was presented in [55] for denoising MR images with spatially varying noise levels, where the conventional ADF [38] does not yield optimal results. The noise adaptive characteristic of the filter is due to the priori knowledge of the spatial dependency of the noise inducted in to it. The diffusion constant (κ) in the conductance coefficient has to be chosen based on the image noise properties. An ideal ADF should reduce the enhancement of the noise and at the same time minimize the smoothing of the anatomical structure boundaries. In [9] the value of κ is chosen as constant for spatially uniform noise levels. Such an assumption in MR images, yields optimal results. Two neighboring pixels u and v with intensities f_u and f_v and predetermined variance of σ_u^2 and σ_v^2 are chosen. Let, the difference between the two pixels be given as $\Delta_{uv} = f_v - f_u$. If, both the pixels belong to the same tissue, the distribution of Δ_{uv} is Gaussian, given by

$$\Delta_{uv} \in N(0, \sigma_{uv}) = \sqrt{\sigma_u^2 + \sigma_v^2}. \tag{4.23}$$

The difference Δ_{uv}^e across a tissue boundary is considered as an outlier as it is formed by values from different population ($\Delta_{uv}^e \notin N(0, \sigma_{uv})$). The value of the threshold for the rejection of such outliers are chosen as the population standard deviation $\sigma_e = \sigma_{uv}$. The local conductance parameter is given as,

$$c_{uv} = k\sqrt{\sigma_u^2 + \sigma_v^2} \tag{4.24}$$

where, k is a constant. The value of k is found to be $\sqrt{2}$, thus c is made dependent on the local noise properties. Experimental results prove that the new method produces a high SNR compared to the traditional anisotropic filtering.

An automatic selection of optimal parameters for denoising MR images using anisotropic diffusion filter for denoising MR images was proposed in [56]. The optimization of the two main parameters: number of iterations and diffusion function is done iteratively using a feedback output from an evaluation method. This automatic parameter selection method consists of three modules: the denoising filters, the evaluation method and the adjustment rules. The denoising filter module uses the biased ADF proposed in [57] and estimates the position of edges as described in [58]. The main component of this method is the evaluation module, it gives feedback about the improvement or degradation of the image during the processing. The feedback is done by using the noise information from the residual image obtained by subtracting the original and the processed image. The evaluation module consists of three steps: local variance operator, histogram and evaluation function. The local variance operation measures the variance in a 3×3 neighborhood. The histogram, extracts the distribution information from the variance image. The evaluation function analyzes the histogram obtained and yields higher values when the histogram is closer to a Gaussian distribution, which reflects uniform distribution of the local variance values. Finally, the adjustment rule module helps to optimize the parameters diffusion constant and the number of iterations to be finally used in filtering the image. The authors validate that this method performs well in comparison to the median and k-nearest neighbor filters.

A new Rician noise specific MR image denoising using an extended speckle reducing anisotropic diffusion (SRAD) was proposed in [59], represented as Rician noise reducing anisotropic diffusion (RNRAD) filter. SRAD [60] is a combination of the linear minimum mean square error (LMMSE) estimation method [61,62] and the anisotropic diffusion filtering (ADF) [9]. This method demands an accurate estimation of the standard deviation of noise. The noise variance estimated using the local sample variance is given as,

$$\hat{\sigma}_n^2 = \text{mode}\{\text{Var}(W(xy))\} \tag{4.25}$$

where $(W(xy))$ is the local sample region. In this work, the authors have extended the PDE to use a diffusion matrix which helps in better noise reduction at the contour location. The use of LMMSE method to estimate the noise at each level of iteration helps in effectively reducing the total diffusion time of the filter and in faster convergence of the filtering approach. This method does not depend on the norm of the gradient for filtering as in the traditional ADF [9]. The advantage of the proposed filtering method is that it does not require manual intervention in making the choice of contrast parameter for the edges of the structures. The matrix extension of the SRAD filter [63], is based on the local orientation of the structures of the image. In this method [59], the matrix extension is based on the statistical properties of the local structures in the image. To validate the performance of this method the authors have compared it with the following techniques: conventional approach (CA) [64], Koays method [65], wavelet domain denoising [66], ADF [9], NLM [67], unbiased NLM [68] using structural similarity index (SSIM) [69] and quality index based on local variance (QILV) [70] as the quality metrics.

Image smoothing using a fourth order partial differential equation (PDE) model was proposed in [25]. The proposed approach is similar to total variation (TV) norm filters [71]. The parameters of the PDE model used are adapted from [72]. The advantage of the proposed method is, it overcomes the staircase effect present in the TV norm filter and it processes signals with a smooth change in intensity value. Experiments performed over MR images, considering additive noise characteristics at very low SNR provides good noise suppression without any harm to the anatomical details of the image.

4.3.4 Neighborhood based filtering

A new multidimensional non-linear filter for restoration and enhancement of MR images was proposed in [73]. The filter utilizes both temporal (interframe) and spatial (intraframe) information to remove additive noise and preserve the partial volume information in MR image sequences. This filtering algorithm begins by choosing a square neighborhood around the pixel to be estimated. The Euclidean distance between each pixel vector in the neighborhood region with the center pixel is estimated. Based on a fixed threshold (η), if the distance is less than the threshold that pixel vector is considered for pixel estimation else it is not used to estimate the center pixel. The value of λ depends on the standard deviation of noise σ_n in the image sequences. After, the estimation of pixel vectors two methods: averaging and ML estimation has been used for estimation of the contributing pixel vectors. The average of several estimates is obtained for a particular pixel vector to find the filtered output of that pixel vector. The performance of the proposed filter depends on the noise power, the contrast-to-noise (CNR) ratio between the tissues, the neighborhood size and the number of images in the sequence. Depending upon on the choice of the neighborhood size the computational complexity of this method varies. This method proposes a filter which has been used as a pre-processing step for Eigen image filtering [74]. The authors have also compared the performance of their proposed method with the existing spatial filtering methods and have observed that their method is superior.

In [75], the authors have employed a local shape adaptive template filtering for improving SNR in MR images. Instead of using a fixed template as in conventional filtering methods, various template shapes are considered and an optimal shape chosen based on its similarity to the locally constant region of the pixel under consideration. The local standard deviation of the templates is obtained and is categorized as plain templates and edge templates based on a threshold. The filter coefficients are obtained using the 2-D adaptive linear least square error (LLSE) filters [76] after an optimal template is chosen. This method enables the minimization of edge blurring and an increase in SNR.

4.3.5 Bayesian denoising

Awate *et al.* [3] proposed a feature preserving MRI denoising based on Bayesian [77] denoising technique. The proposed method performs by inferring the prior knowledge of the uncorrupted image statistics, from the noisy input and the knowledge of the Rician noise model. The method models the prior using a nonparametric Markov random field (MRF) [78] and then optimizes it using the expectation maximization (EM) [79] algorithm. The results obtained by the proposed method illustrated that the images denoised has all the important features preserved. Quantitative comparison in terms of RMSE with other denoising algorithms [66, 80] depicts the advantage of this method. A natural limitation associated with this nonparametric method, degrades the performance if the image regions does not have many continual patterns.

4.3.6 Wiener filtering

Fernandez *et al.* [81] have proposed three different sequential Wiener filters [82], that is, isotropic, orientation and anisotropic filter for denoising $3D$ MRI data. In the isotropic version of the filter the neighborhoods used to estimate the local sample mean are of different orientations. Isotropic Wiener filter is similar to the classical Wiener filter [83] used in a sequence over the data. The isotropic filter performs well in homogeneous region of the image where local variance is less compared to the noise variance (σ_n^2), in regions of an image where there is a discontinuity the filter just returns the original values without any change. Orientation Wiener filter depends on the oriented neighbors to estimate the structure orientation present at each volume elements (voxel), thus helps in reducing the noise in the regions with discontinuity. The anisotropic Wiener filter is a combination of the isotropic and orientation Wiener filter. All the three filters are performed iteratively over the $3D$ data using a regularization parameter. The results obtained, demonstrate that the anisotropic Wiener filter is found to be the optimum one for both denoising and segmentation approaches as it preserves the boundaries and suppresses the noise.

4.3.7 AVREC based filtering

Luo *et al.* [84] have proposed a denoising approach based on averaging reconstructed images (AVREC). The spectrum of the image to be denoised is divided in to different parts and from each partial spectrum an image is reconstructed using a $2D$ singularity function analysis (SFA) model [85,86]. SFA is a mathematical tool used for both correcting and reconstructing images. Each of these reconstructed images are expressed as sum of a single noise-free image and various small noise. The denoising is obtained by averaging these reconstructed images. This method helps in recovering the useful high frequency components and thus, yields images of good quality.

4.3.8 Non-local means filtering

Non-local means (NLM) filter based denoising of MR images was proposed by Manjon *et al.* [87]. Introduced by Buades *et al.* [10] the NLM filter is based on the redundancy property of the images. The NLM filter of an image f is defined as,

$$NLM(f(i)) = \sum_{\forall j \in f} w(i,j) f(j), w(i,j) \in [0,1] \tag{4.26}$$

where i is the pixel being filtered and j corresponds to each one of the other pixels in the entire image. The weight function $w(i,j)$ gives the similarity between the neighborhood region of pixels i and j represented as W_i and W_j respectively. The weight function is given as,

$$\begin{aligned} w(i,j) &= \tfrac{1}{Z(i)} e^{-\frac{d(i,j)}{h^2}} \\ Z(i) &= \sum_{\forall j} e^{-\frac{d(i,j)}{h^2}} \end{aligned} \tag{4.27}$$

$Z(i)$ is the normalization constant and h is the smoothing parameter which controls the decay of the exponential function, thus it has an impact on the degree of filtering. d is a Gaussian weighted Euclidian distance of all the pixels of each neighborhood given as,

$$d(i,j) = G_i \left\| f(W_i) - f(W_j) \right\|_N^2 \tag{4.28}$$

where G_i is a normalized Gaussian weighting function with zero mean and unit standard deviation and N is the radius of the squared neighborhood window size. This function G_i helps to give more weighting to pixels near the center of the neighborhood window. The proposed method was specific to Rician nature of the noise and the experiments were conducted in the square magnitude domain of the MR images. The authors determined the optimal values of all the parameters of the NLM filter using experiments conducted on both clinical and simulated MR images.

In the denoising approach proposed in [87] the main hindrance was the computational complexity of the NLM filter and in determining the optimum value of the filter parameters. Coupe *et al.* [67] proposed a method to fully automate and optimize the performance of NLM filter for denoising $3D$ MR images. The main contributions of this work were: automating the choice of smoothing parameter h, voxel selection based on local mean and variance of the neighborhood, block-wise implementation of the algorithm and parallel computation. The $3D$ formulation of NLM filter is give as,

$$NL(f)(x_i) = \sum_{x_j \in \Omega^3} w(x_i, x_j) f(x_j), w(x_i, x_j) \in [0, 1] \tag{4.29}$$

where, $f(x_j)$ is the intensity of the voxel x_j and $w(x_i, x_j)$ is the weighting function assigned to $f(x_j)$ in the denoising of voxel x_i. $w(x_i, x_j)$ is computed as,

$$w(x_i, x_j) = \frac{1}{Z_i} e^{-\frac{\left\| f(W_i) - f(W_j) \right\|_{2,a}^2}{h^2}} \tag{4.30}$$

where W_i and W_j are the local neighborhoods of the voxels x_i and x_j respectively. Z_i is the normalization constant. The smoothing parameter h depends on the standard deviation of noise (σ_n) and the neighborhood size W_i. In [87] the Gaussian weighting Euclidean distance was used in determining the weighting function $w(i, j)$, to reduce the computational time the authors propose the use of classical Euclidean distance normalized by the neighborhood size. The modified weighting function is given as,

$$w(x_i, x_j) = \frac{1}{Z_i} e^{-\frac{\left\| f(N_i) - f(N_j) \right\|_2^2}{2\beta \hat{\sigma}_n^2 |N_i|}} \tag{4.31}$$

where, β is a constant and $\hat{\sigma}_n^2$ is the estimated standard deviation of noise. The computational complexity of the NLM filter was reduced by adapting the algorithm in [88]. To reduce the computational burden the authors have just considered the voxels inside a search volume V_i. The voxels with maximum weights inside the search volume are preferred over the voxels with lesser weights, this improves the result. This preselection of voxels was done using the local mean and variance. The choice of

$w(x_i, x_j)$ is given as,

$$w(x_i,x_j) = \begin{cases} \frac{1}{Z_i} e^{-\frac{\left\|f(W_i)-f(W_j)\right\|_2^2}{2\beta\hat{\sigma}_n^2|W_i|}} & ; \text{if } \mu_1 < \frac{\overline{f(W_i)}}{\overline{f(W_j)}} < \frac{1}{\mu_1} \text{ and } \sigma_1^2 < \frac{\text{Var}(f(W_i))}{\text{Var}(f(W_j))} < \frac{1}{\sigma_1^2} \\ 0 & ; \text{Otherwise} \end{cases} \tag{4.32}$$

where $\overline{f(W_i)}$ and $\text{Var}(f(W_i)$ is the mean and variance of the local neighborhood W_i of voxel x_i. Block-wise implementation of this algorithm is adapted from [10]. This implementation is a three step process: divide the volume into overlapping blocks, perform NLM filtering of these blocks and restore the voxel values based on the restored values of their blocks. For each block B_{i_k} the NLM filtering is performed as,

$$NL(f)(B_{i_k}) = \sum_{B_j \in V_{i_k}} w(B_{i_k}, B_j) f(B_j) \tag{4.33}$$

where, $w(B_{i_k}, B_j)$ is given as,

$$w(B_{i_k}, B_j) = \frac{1}{Z_{i_k}} e^{-\frac{\left\|f(B_{i_k})-f(B_j)\right\|_2^2}{2\beta\hat{\sigma}_n^2|W_i|}} \tag{4.34}$$

For voxel x_i included in several blocks B_{i_k}, several restored values $NL(f)(B_{i_k})$ are obtained. These estimated values are stored in a vector A_i. The final restored intensity of voxel x_i is expressed as,

$$NL(f)(x_i) = \frac{1}{|A_i|} \sum_{p \in A_i} A_i(p). \tag{4.35}$$

The optimization of the weighting function for the blockwise implementation is given as,

$$w(B_{i_k},B_j) = \begin{cases} \frac{1}{Z_{i_k}} e^{-\frac{\left\|f(B_{i_k})-f(B_j)\right\|_2^2}{2\beta\hat{\sigma}_n^2|W_i|}} & ; \text{if } \mu_1 < \frac{\overline{f(B_{i_k})}}{\overline{f(B_j)}} < \frac{1}{\mu_1} \text{ and } \sigma_1^2 < \frac{\text{Var}(f(B_{i_k}))}{\text{Var}(f(B_j))} < \frac{1}{\sigma_1^2} \\ 0 & ; \text{Otherwise} \end{cases} \tag{4.36}$$

where, $\overline{f(B_{i_k})}$ and $\text{Var}(f(B_{i_k})$ is the mean and variance of the intensity function of the block B_{i_k} centered on the voxel x_i. The non iterative nature of the NLM filter helps in executing the NLM filter on several processors. The main advantage of this filter is that its not iterative as the ADF or total variation minimization. Experimental results obtained illustrate that this method has a reduced computational complexity, but still maintains the denoising quality of the standard NLM filters.

Manjon *et al.* [89] considered the intrinsic multicomponent nature of MR images for denoising using NLM filters. The idea behind this work is, when multiple MR images acquired using various parameters are available, and then the correlated information from these images can be used for denoising. The authors, have extended the NLM filter to multicomponent denoising by proposing a multicomponent non-local means filter (MNLM). The similarity measure is obtained in this filter by combining the information from both the neighboring pixels and the different components as in color image processing [90]. Thus the multicomponent weighting function $w(x_i, x_j)$ is given as,

$$w(x_i, x_j) = \frac{1}{Z(i)} e^{-\left(\sum_{l=1}^{C} \left(d(x_i^l, x_j^l) \big/ h^{l^2} \right) \big/ C \right)} \tag{4.37}$$

where C is the number of components and h^l is the smoothing parameter related to standard deviation of noise in each image component. $Z(i)$ is the normalization function expressed as,

$$Z(i) = \sum_{\forall j} e^{-\left(\sum_{l=1}^{C} \left(d(x_i^l, x_j^l) \big/ h^{l^2} \right) \big/ C \right)}. \tag{4.38}$$

The radius of the search window is restricted to a local window $\Omega = 10$ as in [67], to reduce the computational burden. The radius of the neighborhood window is chosen as 3×3. The smoothing parameter h was set to be $\sigma_{nl}\sqrt{2}$, where σ_{nl} is the standard deviation of noise in each image component. In this work the authors have proposed a pixel preselection criteria based on the local image moments [91] to reduce the complexity of the algorithm. The optimized weighting function is given as,

$$w(x_i, x_j) = \begin{cases} \frac{1}{Z(i)} e^{-d(i,j)^*}; \ \text{if} \left(|\mu_{il} - \mu_{jl}| < k\sigma_{nl}/\sqrt{m} \right), \forall l \in [1, C] \\ 0 \qquad\qquad ; \ \text{Otherwise} \end{cases} \tag{4.39}$$

where, k is a constant and m is the number of pixels used to compute the mean. The Euclidean distance $d(i,j)^*$ is expressed as,

$$d(i,j)^* = \max \left(\frac{\sum_{l=1}^{C} d(x_i^l, x_j^l) \big/ h^{l^2}}{C} - 1, 0 \right) \tag{4.40}$$

This modification to the MNLM method is named as optimized MNLM (OMNLM). A principal component analysis (PCA) [92] approach is used to remove noise using the information from the inter-component domain. Thus, using the PCA as a post-processing approach after the OMNLM has been applied helps in reducing the noise using both spatial and intercomponent domain. This OMNLM-PCA approach yields better results in terms of RMSE and multicomponent RMSE (MRMSE) in comparison to the MNLM and OMNLM approaches.

Manjon *et al.* [93] proposed a new method for denoising MR images based on the Rician nature of the data and the spatially varying noise levels, referred as adaptive Rician non-local means filter with wavelet mixing (ARNLM). In this work, the optimized NLM method has been made adaptive to the spatially varying noise levels of the image. The preselection approach used in Eq. (4.36), is based on the local mean which is intensity sensitive. To avoid such differences, in this method the preselection is based on the original and the inverted means. The inverted mean is obtained as:

$$\mathrm{Inv}(f(B_{i_k})) = \max(f) - f(B_{i_k}) \tag{4.41}$$

The proposed preselection method, leads to a modified weighting function given as,

$$w(B_{i_k}, B_j) = \begin{cases} \frac{1}{Z_{i_k}} e^{-\frac{\left\| f(B_{i_k}) - f(B_j) \right\|_2^2}{2\beta \hat{\sigma}_n^2 |W_i|}} & ;\ \text{if } \mu_1 < \frac{\mathrm{Inv}(f(B_{i_k}))}{\mathrm{Inv}(f(B_j))} < \frac{1}{\mu_1} \text{ and } \sigma_1^2 < \frac{\mathrm{Var}(f(B_{i_k}))}{\mathrm{Var}(f(B_j))} < \frac{1}{\sigma_1^2} \\ 0 & ;\ \text{Otherwise} \end{cases} \tag{4.42}$$

In making the NLM approach used in this method adaptive to Rician noise characteristics of MR images the authors adapted the method used in [94], to restore the unbiased intensity values. The NLM restoration of the voxel x_i is given as,

$$NL(f)(x_i) = \sqrt{\max\left(\left(\sum_{x_j \in V_i} w(x_i, x_j) f(x_j)^2\right) - 2\sigma_n^2, 0\right)} \tag{4.43}$$

Wavelet mixing [95] is used to optimize the denoising over all the frequencies of the image. The main advantage of this method is that it does not require a noise parameter to be estimated as it has been made in-built in to the algorithm and it adapts itself to varying noise levels. Experimental results using the proposed method exhibit good denoising results with the anatomical features of the denoised image being well preserved.

A modified NLM based approach for denoising dynamic contrast enhanced MR images (DCE-MRI) was proposed in [96]. This approach represented as the dynamic NLM (DNLM) is used in DCE-MRI which consists of a volume of MR images acquired during and after the contrast agent has been injected in to the imaging region. This technique utilizes the redundancy of information in the temporal sequences of the images. The reason for modifying the traditional NLM [10] is: the similarity metric used does not account for local changes in intensity due to contrast enhancement and the non-local property of the algorithm might eliminate the diagnostically important details of the MR images. In the proposed variation the similarity metric is expressed as,

$$\begin{aligned}\bar{d}(V_1, V_2) &= d(V_1, C(V_1, V_2) \cdot V_2) \\ &= \| V_1 - C(V_1, V_2) \cdot V_2 \|_{2,a}^{\,2}\end{aligned} \tag{4.44}$$

where, V_1 and V_2 are the vectors from the temporal components t_1 and t_2 respectively. $C(V_1, V_2)$ is given as,

$$C(V_1, V_2) = \begin{cases} \frac{E(V_1)}{E(V_2)}; \;\; t_1 \neq t_2 \text{ and } |E(V_1) - E(V_2)| > \sigma_n \\ 1; \qquad\quad \text{Otherwise} \end{cases} \tag{4.45}$$

where $E(V)$ denotes the expected value and σ_n is the estimated noise in the image. The weighting function $w(i, j)$ is represented as,

$$w(i, j) = \frac{C(f(W_i, W_j))}{Z(i)} \cdot e^{-\bar{d}(f(W_i), f(W_j))/h^2} \tag{4.46}$$

The algorithm is compared with other denoising methods such as Gaussian filtering, NLM, ADF, traditional wavelet thresholding and adaptive multiscale product thresholding method. The proposed method is evaluated both qualitatively as well as quantitatively.

4.4 Theory of Wavelet Transform

Wavelet transform in signal and image processing perspective has evolved from combining the wavelet theory with the multi-resolution analysis. Wavelets are originally developed for representing the signals in time-frequency domain. The compact support of the wavelets provides good time-frequency localization and hence, are used for analyzing non-stationary signals [97].

Multi-resolution analysis involves exploring the properties of the image in more than one resolution or scale. The representation at each scale is an approximation of the original image. However, the information contained in the approximations at each scale characterize different physical structures of the image [98]. At low resolution levels, these details correspond to the large structures or the overall image context. The details in the high resolution levels characterize individual regions contained in the image [42].

Multi-resolution methods that exist prior to wavelet decomposition are the Gaussian and the Laplacian pyramids [99]. The Gaussian pyramid provides approximations at multiple scales, using simple low-pass filtering and decimation techniques. The Laplacian pyramid provides a coarse representation of the image as well as a set of detail images at different scales. These pyramidal representations are over-complete and lack sufficient methods for modeling the correlations between the data at successive scales [99].

The wavelet representation introduced by Mallat [98] is a complete, orthogonal multi-scale decomposition technique. The image is decomposed into sub-bands, that includes an approximation image and the detail images obtained at different orientations in each scale. The basics of wavelets and the formulation of wavelet transformation in multi-resolution point of view is presented in this section.

4.4.1 Wavelets and wavelet transform

A wavelet $\psi(t)$ is a wave function of finite duration, compact support and zero mean value. Therefore, for a period of time $t_1 \leq t \leq t_2$

$$\int_{t_1}^{t_2} \psi(t)\, dt = 0 \tag{4.47}$$

Representation of a signal as the linear combination of the set of basis functions derived from $\psi(t)$ is known as the ***wavelet transform***.

The wavelet bases are obtained through time-scalings and translations of the original function $\psi(t)$ and are represented as

$$\psi_{a,b}(t) = \frac{1}{\sqrt{a}} \psi\left(\frac{t-b}{a}\right) \tag{4.48}$$

where a is the scaling parameter, b is the translation parameter and $\frac{1}{\sqrt{a}}$ is the normalization constant. In general, $\psi(t)$ is referred as the *mother wavelet.*

The wavelet transform of a signal $f(t)$ in the continuous domain is defined as

$$W_f(a,b) = \frac{1}{\sqrt{a}} \int_{-\infty}^{\infty} f(t)\, \psi^*\left(\frac{t-b}{a}\right) dt \tag{4.49}$$

Using the orthogonality of the wavelet bases, the inverse continuous wavelet transform is computed as

$$f(t) = \frac{1}{C_\psi} \int_{0}^{\infty} \int_{-\infty}^{\infty} W_f(a,b)\, \psi\left(\frac{t-b}{a}\right) \frac{da}{a^2} db \tag{4.50}$$

where, $C_\psi = \int_{-\infty}^{\infty} \frac{|\psi(\omega)|^2}{\omega} d\omega$

$\psi(\omega)$ is the Fourier transform of $\psi(t)$. The constant C_ψ has to be finite for the validity of the wavelet transform. Hence, $C_\psi < \infty$ is called the admissibility condition that implies

$$\psi(\omega) = 0 \text{ for } \omega = 0 \text{ and } \psi(\omega) \to 0 \text{ as } \omega \to \infty$$

Equation (4.50) implies that the continuous wavelet transform is an over-complete representation and hence, it is highly redundant. The redundancy is reduced by using discrete values of a and b. The parameters are chosen as

$$a = a_0^m \text{ and } b = nb_0a_0^m$$

where a_0 and b_0 are the positive constants and $a_0 > 1$. m and n are integers.

By substituting the values of a and b in Eq. (4.48), the discrete wavelet bases can be written as

$$\psi_{m,n}(t) = a_0^{-\frac{m}{2}}\psi\left(a_0^{-m}t - nb_0\right) \tag{4.51}$$

The wavelet bases defined through Eq. (4.51) forms a set of orthonormal basis functions if $a_0 = 2$ and $b_0 = 1$. Therefore,

$$\psi_{m,n}(t) = 2^{-\frac{m}{2}}\psi\left(2^{-m}t - n\right) \tag{4.52}$$

The choice of $a_0 = 2$ is known as the *dyadic scaling*. Given that m is an integer, the wavelet bases can be redefined as

$$\psi_{m,n}(t) = 2^{\frac{m}{2}}\psi\left(2^{m}t - n\right) \tag{4.53}$$

4.4.2 Wavelets as filters

The filter bank implementation of wavelet transform is possible through realizing wavelets as bandpass filters [100]. The wavelet transform defined in Eq. (4.49) can be rewritten by replacing t with τ and b with t. Therefore,

$$W_f(a,t) = \frac{1}{\sqrt{a}}\int_{-\infty}^{\infty} f(\tau)\,\psi^*\left(\frac{\tau - t}{a}\right)d\tau \tag{4.54}$$

The above equation can be written in terms of convolution as

$$W_f(a,t) = f(t) * \left\{\frac{1}{\sqrt{a}}\psi^*\left(\frac{-t}{a}\right)\right\} \tag{4.55}$$

Assuming, $h_a(t) = \frac{1}{\sqrt{a}}\psi\left(\frac{t}{a}\right)$ the above equation is written as

$$W_f(a,t) = f(t) * h_a^*(-t) \tag{4.56}$$

Therefore, wavelet transform can be considered as filtering the signal $f(t)$ with a bank of filters having the impulse response $h_a(-t)$. Taking the Fourier transform of Eq. (4.56) gives

$$W_f\left(a,\omega\right) = F\left(\omega\right) * H_a\left(\omega\right) \tag{4.57}$$

$$\text{and } \; H_a\left(\omega\right) = \sqrt{a}\psi\left(a\omega\right)$$

The support of the wavelet within its domain varies as a function of a. Accordingly, the center frequency and the bandwidth of $h_a(t)$ also varies.

Let $\omega_0 = 2\pi f_0$ be the center frequency of the mother wavelet $\psi(t)$. Then, the center frequency ω_a of the scaled wavelet bases is given by

$$\omega_a = \frac{\omega_0}{a} \tag{4.58}$$

Similarly, if Δf_0 is the bandwidth of $\psi(t)$, the bandwidth of the wavelet bases is

$$\Delta f_a = \frac{\Delta f_0}{a} \tag{4.59}$$

For $a < 1$, the wavelet is compressed in time and it acts as the high pass filter. For $a > 1$, the wavelet is expanded in time and it passes the low frequency components. Therefore, the wavelet bases acts as bandpass filters with center frequency ω_a and bandwidth Δf_a [100].

4.4.3 Formulation of Discrete Wavelet Transform

For representing a signal\image through wavelet transform, the filter $H_a(\omega)$ must span the whole frequency space of the image. Since, the wavelet filters are either high-pass or bandpass, the low frequency information of the image at different scales is obtained using a low-pass filter. The time domain response of the low-pass filter is represented by the scaling functions. This framework leads to multi-resolution analysis (MRA) using wavelet transform [98].

In MRA, a scaling function is employed to obtain a series of approximations of the function or image, each differing by a factor of 2 from its adjacent scales. The difference in information between the approximations at adjacent scales are encoded using the wavelets [42].

4.4.3.1 Scaling functions

A scaling function (or approximation function) $\varphi(t) \in L^2(\mathbb{R})$, is defined to generate a nested sequence of subspaces $\{V_m\}_{m\in\mathbb{Z}}$ of $L^2(\mathbb{R})$ such that

$$\cdots \subset V_{-3} \subset V_{-2} \subset V_{-1} \subset V_0 \subset V_1 \subset V_2 \subset V_3 \cdots \tag{4.60}$$

$$\bigcup_{m\in\mathbb{Z}} V_m = L^2\left(\mathbb{R}\right) \tag{4.61}$$

$$\bigcap_{m\in\mathbb{Z}} V_m = \{0\} \tag{4.62}$$

The subspace V_m represents the coarse resolution and V_{m+1} denotes the fine resolution. For MRA, the signal $f(t)$ is represented by its projections on the function space $L^2(\mathbb{R})$ spanned by the set of scaling functions $\{\varphi_{m,n}\left(t\right)\}$. $\{\varphi_{m,n}\left(t\right)\}$ is obtained through integer translations and scalings of $\varphi(t)$, as given below

$$\varphi_{m,n}\left(t\right) = 2^{\frac{m}{2}}\varphi\left(2^m t - n\right) \tag{4.63}$$

At scale $m = 0$, the subspace V_0 is spanned by $\varphi(t-n)$. It means that $\varphi(t)$ is in V_0. Hence, V_0 is considered as the basic multi-resolution space.

The condition in Eq. (4.60) explains the *containment property* of MRA [101]. It states that the subspaces spanned by the scaling function at low resolution scales (V_m) are nested within those spanned at the higher scales (V_{m+1}). Intuitively, it implies that if $\varphi(t) \in V_m$, then $\varphi(2t) \in V_{m+1}$. Therefore, the expansion functions of the subspace V_m can be expressed as the weighted sum of the expansion functions of the subspace V_{m+1} and it is computed as

$$\varphi_{m,n}\left(t\right) = \sum_{k\in\mathbb{Z}} h_\varphi\left(k\right)\varphi_{m+1,k}\left(t\right) \tag{4.64}$$

The coefficients $h_\varphi(k)$ are called the *scaling function coefficients*. By expanding the scaling functions, Eq. (4.64) can be written as

$$\varphi_{m,n}\left(t\right) = \sum_{k} h_\varphi\left(k\right) 2^{\frac{(m+1)}{2}}\varphi\left(2^{(m+1)}t - k\right) \tag{4.65}$$

For $m = 0$ and $n = 0$, the above relation becomes

$$\varphi\left(t\right) = \sum_{k} h_\varphi\left(k\right)\sqrt{2}\varphi\left(2t - k\right) \tag{4.66}$$

Equation (4.66) is fundamental to multi-resolution analysis and is called the *refinement equation* or the *dilation equation* [42].

4.4.3.2 Wavelet functions

The wavelet function $\psi(t)$ with its integer translates and scalings are defined to span the difference between any two adjacent scaling subspaces V_m and V_{m+1}. The set of wavelet functions generated from the mother wavelet $\psi(t)$ is given by

$$\psi_{m,n}(t) = 2^{\frac{m}{2}} \psi\left(2^m t - n\right) \tag{4.67}$$

When the projections progress from the subspace V_{m+1} to V_m, certain details are lost due to the reduction in resolution. As $V_m \subset V_{m+1}$, the lost details remain conserved in the orthogonal complement of the subspace V_m [102]. This orthogonal complement is called the *wavelet subspace* 'W_m'. Therefore, the higher resolution subspace V_{m+1} can be related as

$$V_{m+1} = V_m \oplus W_m \tag{4.68}$$

'$\oplus$' denotes the union of the spaces. For any $(m, n, k) \in \mathbb{Z}^3$, the orthogonality condition is stated as

$$\left\langle \varphi_{m,n}(t)\, \psi_{m,k}(t) \right\rangle = 0 \tag{4.69}$$

The wavelet spaces reside within the spaces spanned by the next higher resolution scaling functions. Therefore, the wavelet function at scale m can be expressed in terms of the scaling function at scale $m + 1$ as

$$\psi_{m,n}(t) = \sum_k h_\psi(k)\, \varphi_{m+1,k}(t) \tag{4.70}$$

For $m = 0$ and $n = 0$, the wavelet function in basic multi-resolution space becomes

$$\psi(t) = \sum_k h_\psi(k) \sqrt{2}\varphi(2t - k) \tag{4.71}$$

$h_\psi(k)$ are called the *wavelet function coefficients.* The coefficients of the wavelet function are related to the scaling coefficients as

$$h_\psi(k) = (-1)^k h_\varphi(1 - k) \tag{4.72}$$

4.4.3.3 Wavelet series expansions

The properties of MRA in Eq. (4.60) and (4.61) implies [100, 101]

$$L^2(\mathbb{R}) = \cdots \oplus V_{-2} \oplus V_{-1} \oplus V_0 \oplus V_1 \oplus V_2 \oplus \cdots \tag{4.73}$$

Substituting Eq. (4.68) in (4.73) gives

$$L^2(\mathbb{R}) = V_{-\infty} \oplus W_{-\infty} \oplus \cdots \oplus W_{-3} \oplus W_{-2} \oplus W_{-1} \oplus W_0 \oplus W_1 \oplus W_2 \oplus \cdots \oplus W_{(\infty-1)} \tag{4.74}$$

It implies that, any function in the space $L^2(\mathbb{R})$ can be represented using an approximation at the lowest subspace and all the wavelet functions. Therefore, the wavelet series expansion of the signal $f(t) \in L^2(\mathbb{R})$ is formulated as

$$f(t) = \sum_n c_{m_0}(n)\, \varphi_{m_0,n}(t) + \sum_{m=m_0}^{\infty} \sum_n d_m(n)\, \psi_{m,n}(t) \tag{4.75}$$

where m_0 is the arbitrary starting scale, c_{m_0} are called the *approximation coefficients* and d_m are the *detail coefficients*. These expansion coefficients are calculated as

$$c_{m_0}(n) = \langle f(t), \varphi_{m_0,n}(t) \rangle = \int f(t)\varphi_{m_0,n}(t)\, dt \tag{4.76}$$

and

$$d_m(n) = \langle f(t), \psi_{m,n}(t) \rangle = \int f(t)\psi_{m,n}(t)\, dt \tag{4.77}$$

$\varphi_{m_0,n}(t)$ and $\psi_{m,n}(t)$ are defined in Eq. (4.63) and (4.67) respectively. These functions can be recursively computed using the relations stated in Eq. (4.64) and (4.70).

4.4.3.4 Discrete wavelet transform

Wavelet series expansions of the discrete function is known as the *discrete wavelet transform* (DWT). The DWT representation of the discrete signal $f(x)$ of length M defined for $x = \{0, 1 \cdots M-1\}$ is given by

$$f(x) = \frac{1}{\sqrt{M}} \sum_n W_\varphi^{m_0}(n)\, \varphi_{m_0,n}(x) + \frac{1}{\sqrt{M}} \sum_{m=m_0}^{\infty} \sum_n W_\psi^{m}(n)\, \psi_{m,n}(x) \tag{4.78}$$

W_φ and W_ψ are the approximation and detail coefficients for the discrete representation respectively.

$$W_\varphi^{m_0}(n) = \frac{1}{\sqrt{M}} \sum_{x=0}^{M-1} f(x)\, \varphi_{m_0,n}(x) \tag{4.79}$$

$$W_{\psi}^{m}\left(n\right)=\frac{1}{\sqrt{M}}\sum_{x=0}^{M-1}f\left(x\right)\psi_{m,n}\left(x\right) \tag{4.80}$$

Conventionally, the minimum scale m_0 is chosen as 0. If the number of decomposition level is fixed as J, maximum scale is $J-1$. Therefore, $m=\{0,1\cdots J-1\}$ and length of the signal M must be chosen as 2^J.

4.4.4 Filter bank implementation of DWT

Mallat [98] exploited the relationship between the DWT coefficients of adjacent scales and proposed the iterative filtering scheme for computationally efficient implementation of DWT. This realization is known as the *fast wavelet transform* and it resembles the subband filtering technique [42].

The inter-scale relation between the coefficients is derived using the refinement equation. The dilation equation defined for the discrete variable x is given as

$$\varphi\left(x\right)=\sum_{k}h_{\varphi}\left(k\right)\sqrt{2}\varphi\left(2x-k\right) \tag{4.81}$$

By substituting x as 2^jx-n, Eq. (4.81) becomes

$$\varphi\left(2^mx-n\right)=\sum_{k}h_{\varphi}\left(k\right)\sqrt{2}\varphi\left(2\left(2^mx-n\right)-k\right) \tag{4.82}$$

Letting $r=2n+k$ gives

$$\varphi\left(2^mx-n\right)=\sum_{r}h_{\varphi}\left(r-2n\right)\sqrt{2}\varphi\left(2^{m+1}x-r\right) \tag{4.83}$$

Similarly, the recursive wavelet equation can be derived as

$$\psi\left(2^mx-n\right)=\sum_{r}h_{\psi}\left(r-2n\right)\sqrt{2}\varphi\left(2^{m+1}x-r\right) \tag{4.84}$$

Substituting Eq. (4.83) in

$$W_{\varphi}^{m}\left(n\right)=\frac{1}{\sqrt{M}}\sum_{x=0}^{M-1}f\left(x\right)2^{\frac{m}{2}}\varphi\left(2^mx-n\right)$$

gives

$$W_{\varphi}^{m}\left(n\right)=\sum_{r}h_{\varphi}\left(r-2n\right)\left[\frac{1}{\sqrt{M}}\sum_{x=0}^{M-1}f\left(x\right)2^{\frac{m+1}{2}}\varphi\left(2^{m+1}x-r\right)\right] \tag{4.85}$$

Hence,

$$W_{\varphi}^{m}\left(n\right)=\sum_{r}h_{\varphi}\left(r-2n\right)W_{\varphi}^{m+1}\left(r\right) \tag{4.86}$$

Therefore, the approximation coefficients at scale m are computed by convolving the approximation coefficients at scale $m+1$ with the scaling function $h_{\varphi}(-n)$ and down-sampling the results.

Similarly, substituting Eq. (4.84) in

$$W_{\psi}^{m}(n) = \frac{1}{\sqrt{M}} \sum_{x=0}^{M-1} f(x)\, 2^{\frac{m}{2}} \psi(2^{m}x - n)$$

and simplifying gives,

$$W_{\psi}^{m}(n) = \sum_{r} h_{\psi}(r-2n)\, W_{\varphi}^{m+1}(r) \tag{4.87}$$

Therefore, the wavelet coefficients at the low resolution scale are obtained by filtering the high resolution approximation coefficients with the wavelet filter $h_{\psi}(-n)$ followed by two-fold decimation.

The filter bank realization for the two level forward and inverse DWT is shown in Fig. 4.1(a) and 4.1(b) respectively. The filters employed for wavelet decomposition $h_{\varphi}(-n)$ and $h_{\psi}(-n)$ are known as the *analysis filters*. The decomposition coefficients computed using these analysis filters can be consolidated as

$$W_{\varphi}^{m}(n) = h_{\varphi}(-k) * W_{\varphi}^{m+1}(k)\big|_{k=2n,\, n\geqslant 0} \tag{4.88}$$

$$W_{\psi}^{m}(n) = h_{\psi}(-k) * W_{\varphi}^{m+1}(k)\big|_{k=2n,\, n\geqslant 0} \tag{4.89}$$

Conventionally, h_{φ} and h_{ψ} are known as the low-pass and the high-pass filters respectively. These filters are quadrature mirror filters (QMF) such that [100]

$$h_{\psi}(n) = (-1)^{n}\, h_{\varphi}(1-n) \tag{4.90}$$

The above equation in the frequency domain is given by

$$H_{\psi}(\omega) = e^{-j\omega} H_{\varphi}^{*}(\omega+\pi) \tag{4.91}$$

Similar to the forward transform, the inverse DWT is realized using the synthesis filter bank. For perfect reconstruction, the synthesis filters are chosen to be time-reversed versions of the corresponding analysis filters [100]. Therefore, the synthesis filters for reconstruction $\tilde{h}_{\varphi}(n)$ and $\tilde{h}_{\psi}(n)$ are given by

$$\tilde{h}_{\varphi}(n) = h_{\varphi}(n) \tag{4.92}$$

$$\tilde{h}_{\psi}(n) = h_{\psi}(n) \tag{4.93}$$

Fig. 4.1(b), details the structure of the synthesis filter bank. The approximation coefficients at

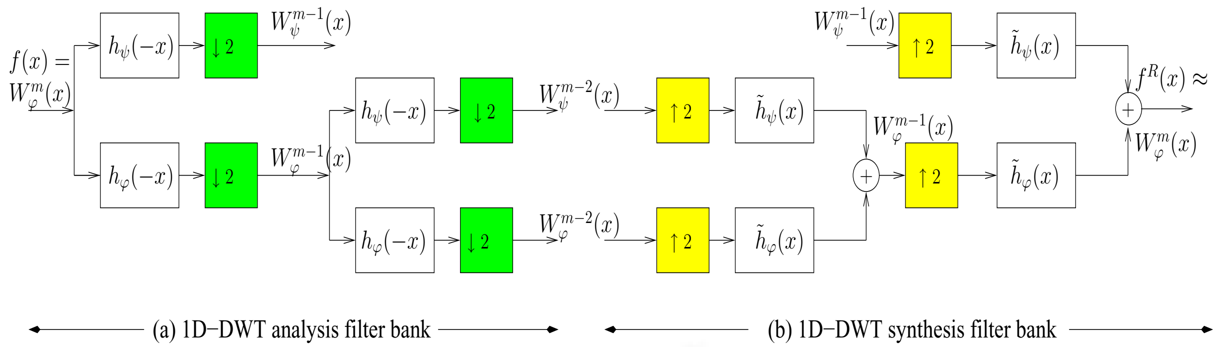

(a) 1D−DWT analysis filter bank

(b) 1D−DWT synthesis filter bank

Figure 4.1: Filter bank representation of two level decomposition of the signal $f(x)$ using 1D-DWT. (a) Analysis filter bank corresponding to the forward DWT (b) Synthesis filter bank corresponding to the inverse DWT. $f^R(x)$ denotes the signal reconstructed from the transform coefficients. m denotes the higher scale that contains the high resolution image and lower scales ($< m$) contains the low resolution decompositions of the input $f(x)$.

the high resolution level $m+1$ are reconstructed by up-sampling the approximation and the detail coefficients at resolution level m and convolving with the synthesis filters. The formulation is defined as

$$W_\varphi^{m+1}(n) = \sum_r W_\varphi^m(r)\, h_\varphi(n-2r) + \sum_r W_\psi^m(r)\, h_\psi(n-2r) \tag{4.94}$$

The above equation can be written in terms of convolution as

$$W_\varphi^{m+1}(n) = \tilde{h}_\varphi(n) * W_\varphi^m(n)_{\uparrow 2} + \tilde{h}_\psi(n) * W_\psi^m(n)_{\uparrow 2} \tag{4.95}$$

$W_\varphi^m(n)_{\uparrow 2}$ and $W_\psi^m(n)_{\uparrow 2}$ denotes up-sampling of the decomposition coefficients $W_\varphi^m(n)$ and $W_\psi^m(n)$ respectively.

4.4.5 Two dimensional DWT

Using the separability property, the $1D$ scaling and the wavelet functions can be easily extended for representing the two dimensional functions [42, 98]. The scaling function in $2D$ is defined as

$$\varphi(x,y) = \varphi(x)\varphi(y) \tag{4.96}$$

Therefore,

$$\varphi_{m,n,k}(x,y) = 2^{\frac{m}{2}}\varphi\left(2^m x - n, 2^m y - k\right) \tag{4.97}$$

Similarly, the $2D$ wavelet functions are formulated as

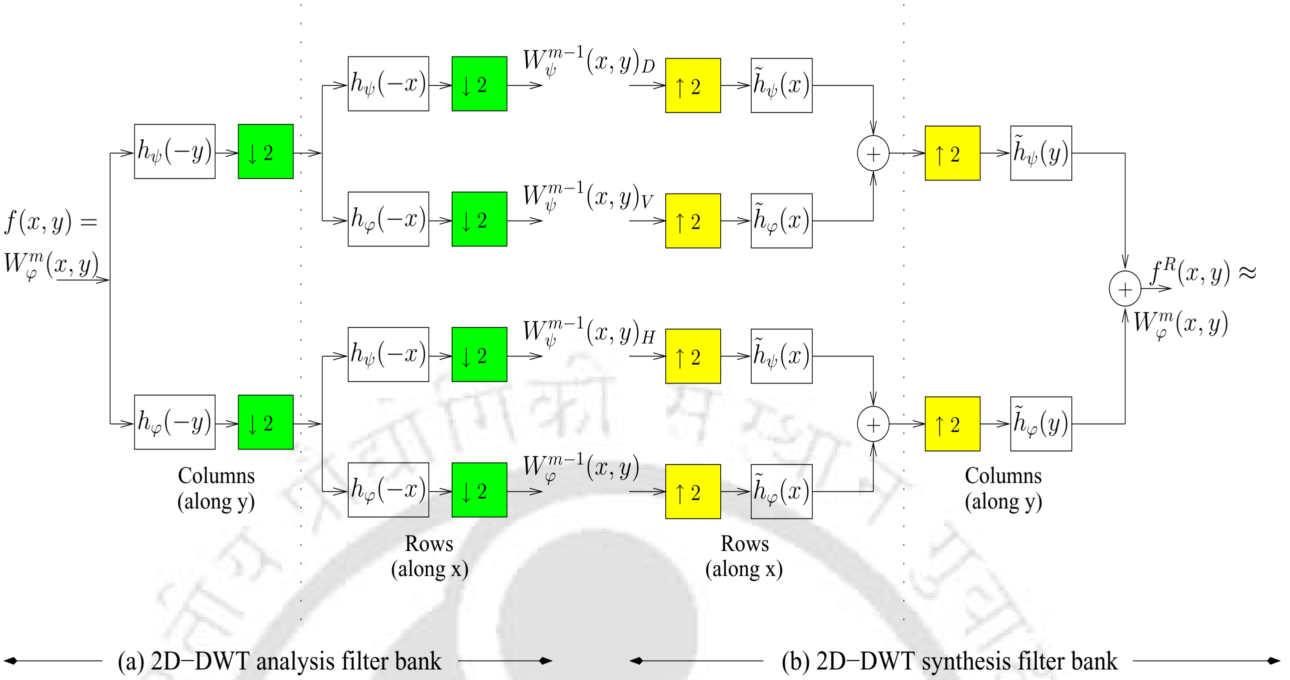

Figure 4.2: Filter bank representation of two level decomposition of the image $f(x, y)$. Using the separability property of the basis functions, the $2D$ filter bank realization is possible through performing column-wise and row-wise 1D filtering. $f^R(x, y)$ denotes the reconstructed image.

$$\psi^H(x,y) = \psi(x)\varphi(y) \tag{4.98}$$

$$\psi^V(x,y) = \varphi(x)\psi(y) \tag{4.99}$$

$$\psi^D(x,y) = \psi(x)\psi(y) \tag{4.100}$$

and hence,

$$\psi^L_{m,n,k}(x,y) = 2^{\frac{m}{2}}\psi^L(2^m x - n, 2^m y - k) \tag{4.101}$$

$L = \{H, V, D\}$ identifies the directionality of the wavelets. The $2D$ wavelet measures functional variations along three different directions. ψ^H measures variations in the horizontal direction, ψ^V responds to variations in the vertical direction and ψ^D corresponds to the variations along the diagonals. Therefore, the $2D$ wavelet coefficients are capable of individually representing the horizontal, vertical and diagonal edges of the image. This directional sensitivity is the natural consequence of the separability and it does not increase the computational complexity of the $2D$ wavelet transform [42]. Given the basis function, the discrete wavelet transform of a $2D$ image $f(x, y)$ of size $M \times N$ defined at $x = \{0, 1, \cdots M-1\}$ and $y = \{0, 1, \cdots N-1\}$ is computed as

$$W_{\varphi}^{m_0}(n,k) = \frac{1}{\sqrt{MN}} \sum_{x=0}^{M-1} \sum_{y=0}^{N-1} f(x,y) \varphi_{m_0,n,k}(x,y) \tag{4.102}$$

$$W_{\psi}^{m}(n,k)_L = \frac{1}{\sqrt{MN}} \sum_{x=0}^{M-1} \sum_{y=0}^{N-1} f(x,y) \psi_{m,n,k}^{L}(x,y) \tag{4.103}$$

Therefore, the $2D$ inverse discrete wavelet transform is

$$\begin{aligned} f(x,y) = {} & \tfrac{1}{\sqrt{MN}} \sum_{n} \sum_{k} W_{\varphi}^{m_0}(n,k)\, \varphi_{m_0,n,k}(x,y) \\ & + \tfrac{1}{\sqrt{MN}} \sum_{L=H,V,D} \sum_{m=m_0}^{\infty} \sum_{n} \sum_{k} W_{\psi}^{m}(n,k)_L\, \psi_{m,n,k}^{L}(x,y) \end{aligned} \tag{4.104}$$

The filter bank realizations for the $2D$ forward and inverse discrete wavelet transform are shown in Fig. 4.2.

4.4.6 Modifications of DWT

Two useful adaptations of the DWT contributing to the development in the various fields of image processing are the (i) Translation invariant wavelet transforms and the (ii) Wavelet packets. These adaptations improve the efficiency of wavelet based algorithms in applications such as compression, edge detection, pattern matching, and image denoising [99].

(i) **Translation invariant wavelet transforms:**

The conventional DWT produces different wavelet coefficients for the translates of the input signal. Hence, it is not translation invariant. The translation invariance is achieved by retaining all the coefficients at each level of decomposition. The existing translation invariant methods are discussed in chapter 5.

(ii) **Wavelet packets:**

Wavelet packets are formulated to produce more sparser representation of the input signal. In DWT, only the approximation coefficients are iteratively filtered. Conversely, in wavelet packets both the approximation and the detail coefficients are iteratively filtered. It means that the detailed coefficients are also passed through the low-pass and the high-pass filters at each level.

4.5 Wavelet based MRI denoising

The DWT decomposes the image in terms of its low and high frequency contents. The low frequency components can be considered as the local signal averages and hence, it is an approximation of the original image. The high frequency components characterize the singularities in the image such as the edges, texture and the noise. Thus, the wavelet decomposition decorrelates the image and leads to a sparse representation [5]. This decorrelating property allows to define a threshold that shrinks the noisy coefficients within the detail sub-bands. For, this reason wavelet denoising is commonly referred as wavelet thresholding [5, 103].

Further, the decomposition at several scales is useful in distinguishing the regular signal components from the noise pixels. The magnitude of the wavelet coefficients corresponding to the image singularities increases with the level of decomposition. Conversely, the noise pixels are uncorrelated and hence, the magnitude of the transformed coefficients representing the noise singularities decrease with the decomposition level [5, 103, 104].

Therefore, several wavelet thresholding methods based on these properties of the wavelet transform are proposed for noise removal in MRI. In this section, the wavelet based MR image denoising techniques will be discussed briefly.

Weaver *et al.* [105] were the first to propose the filtering of MR images using wavelet transform as an alternative to Fourier transform. The wavelet transform used in this method is adapted from [98]. The maximum noise at each scale is obtained from the absolute value of the wavelet transform of five lines at the edge of the image. This method was quite effective in reducing noise without eliminating edges. Estimating the level of noise to eliminate from the signal in the wavelet transform was a difficult task. The choice of this level was made in a trail and error means. Automating the choice of this level, depending on the spatial characteristics will improve the performance of this method. The disadvantage of this method is it tends to eliminate small structures of the image that are similar in size to the noise pixels. Wavelet packet [106] based denoising of MR images was proposed in [107]. The Gaussian characteristic of noise in the complex MR images is used in this method. The wavelet packet denoising algorithm employed in this method is adapted from [108]. The three main steps of this algorithm are: wavelet packet transformation, best basis selection and coefficient thresholding. Coiflet wavelets were used for the wavelet packet transformation step. The best basis selection is based on the minimum entropy criterion. Thresholding of the coefficients was done by ranking the wavelet coefficients in terms of their power level and choosing an optimum value as threshold [109] which eliminates the noise from the signal. This approach was tested over both magnitude and complex MR images. In low SNR images complex image denoising produced better preservation of edges compared to the magnitude image denoising.

A study of wavelet domain denoising for filtering Rician noise in magnitude MR images was proposed in [37]. Two wavelet domain methods for denoising MR images in both high and low SNR instances were presented. In high SNR images, the Rician characteristics are well approximated to be Gaussian in nature. Hence, the standard discrete wavelet transform (DWT) based denoising of MR images is performed. Haar wavelet is preferred over the other wavelets as it preserves fine image details. In low SNR images, the wavelet and the scaling coefficients are biased and in turn, it affects the contrast of the image. To remove the bias the author proposed a novel idea of denoising the MR images in its squared magnitude domain. It is shown that the bias becomes independent of the underlying signal in the squared domain. As a result, unbiased estimates of the noise-free images are obtained. The authors also developed a new wavelet domain filter α_I which is data adaptive. The filter is expressed as,

$$\alpha_I = \left(\frac{W_\psi^2(I) - 3\sigma_I^2}{W_\psi^2(I)} \right)_+ \tag{4.105}$$

where $I \in \mathbb{Z}$ and $W_\psi(I)$ is the I^{th} wavelet coefficient and σ_I^2 is its variance. The thresholding operation given in Eq. (4.105) operates by altering the square magnitude wavelet coefficients ($W_\psi^2(I)$) with values less than three times the estimated variance to zero and the larger values are unaltered. This filtering operation has been effectively used in similar applications [110, 111]. Experiments were performed on both clinical and simulated MR images with high and low SNR characteristics. The denoised output from this method tends to preserve the vital image features, suppresses noise and also maintains the contrast of the image. The proposed method has been efficiently used in the denoising of other MR image modalities like magnetic resonance angiography (MRA) [112, 113].

A wavelet domain MR denoising algorithm based on the complex MR images was proposed in [6, 114]. Since, the characteristic of noise in complex MR image domain is Gaussian it is easier to adapt any method that assumes an additive noise model. A shift invariant wavelet domain Wiener type denoising algorithm similar to the one proposed in [37] was developed. The standard deviation of noise was estimated using the MAD method [115]. The proposed method tends to effectively reduce the noise in the background (no signal) region of the image. This method has the advantage over separately denoising the real and imaginary parts as it reduces the phase and amplitude distortions that occurs in the output images. The two main parameters of the algorithm: the level of wavelet decomposition and the threshold has to be determined manually by the user. The adaptation of this method to denoise MR image time sequences was discussed in [116]. Zaroubi *et al.* [117] proposed a complex denoising method for MR images. In this method, the denoising is done separately over the two orthogonal components of a complex MR image. Noise reduction is done by applying the soft thresholding rule [118] over the wavelet coefficients obtained using DWT. The basic Gaussian noise assumptions in MR images are satisfied in this approach. This complex denoising method improves the SNR and contrast-to-noise ratio (CNR) compared to the magnitude domain denoising.

Pizurica *et al.* [66] proposed a versatile wavelet domain filtering technique for medical images. The performance of this method can be varied using a single parameter, which depends on the preference of the medical expert analyzing the image. This parameter helps in controlling the degree of smoothing and the preservation of relevant features of the image. This algorithm is applicable to any type of noise in images as it does not rely on the prior knowledge of its distribution. A shift invariant wavelet transform with equal number of coefficients at each level of decomposition is used in order to exploit the inter-scale and intra-scale correlation [119] among the wavelet coefficients. The inter-scale correlation among the wavelet coefficients is used to classify the coefficients to be either in the signal of interest or noise.

The non-decimated wavelet decomposition of the image using the spline wavelet bases is obtained. For the wavelet coefficients W_ψ^m at level m and of length N, let $k = \{1, 2...N\}$ and $W_\psi^m = \{w_{1,m}, ., ., ., \hat{w}_{N,m}\}$. For the wavelet coefficients corresponding to each detail sub-bands, a mask $\hat{X}_m = \{\hat{x}_{1,m}, ., ., ., \hat{x}_{N,m}\}$ is computed as [120],

$$\hat{x}_{k,m} = \begin{cases} 0, if\; w_{k,m}|\hat{f}_{k,m+1} < (K\hat{\sigma}_m)^2 \\ 1, if\; w_{k,m}|\hat{f}_{k,m+1} \geq (K\hat{\sigma}_m)^2 \end{cases} \tag{4.106}$$

where $\hat{\sigma}_m$ is an estimate of the standard deviation of noise in the detail image W_ψ^m, $\hat{f}_{k,m+1}$ is the estimate of the unknown noiseless wavelet coefficient and K is the tunable control parameter.

The estimate of the wavelet coefficient $\hat{f}_{k,m}$ from the mask $\hat{X}_m$ uses the conditional probabilities $p_{W_\psi^m|X_m}(w_{k,m}|1)$ which represents the wavelet coefficients with the signal of interest and $p_{W_\psi^m|X_m}(w_{k,m}|0)$ representing the wavelet coefficients corresponding to the absence of the signal of interest. Therefore, $\hat{f}_{k,m}$ is given as,

$$\hat{f}_{k,m} = \frac{\xi_{k,m}\mu_{k,m}}{1+\xi_{k,m}\mu_{k,m}} w_{k,m} \tag{4.107}$$

Assuming $S^m_\psi = |W^m_\psi|$ such that $s_{k,m} = |w_{k,m}|$ the following are defined.

$$\begin{aligned} \xi_{k,m} &= \frac{P_{S^m_\psi|X_m}(s_{k,m}|1)}{P_{S^m_\psi|X_m}(|s_{k,m}||0)} \\ \mu_{k,m} &= \frac{P(X_m=1)}{P(X_m=0)} \frac{P_{E_m|X_m}(e_{k,m}|1)}{P_{E_m|X_m}(e_{k,m}|0)}. \end{aligned} \tag{4.108}$$

$E_m = \{e_{1,m}, ., ., ., \hat{e}_{N,m}\}$ and $e_{k,m}$ denotes the local spatial activity of the k^{th} wavelet coefficient at scale m and it is calculated over the neighborhood of $w_{k,m}$ as [121],

$$e_{k,m} = \frac{1}{2l+1} \sum_{t=k-l}^{k+l} |w_{t,m}| \tag{4.109}$$

l specifies the size of the neighborhood. This method has been applied to MR image denoising in the square magnitude domain. The value of K was determined to be equal to two for MR images in terms of the SNR. Pizurica *et al.* [122] have given a review of wavelet based denoising techniques and their application in ultrasound and MR imaging. The shift invariant wavelet transform was employed along with the thresholding technique given in [66].

Bao *et al.* [104] proposed a edge preserved denoising technique for MR images using the wavelet based multiscale product thresholding scheme. This technique exploits the interscale dependencies of the wavelet coefficients to enhance the important features and to suppress noise [123, 124]. An orthogonal wavelet transform (OWT) has been employed in this approach. Wavelet used in this technique is the MZ wavelet adapted from [125] which approximates the first derivative of Gaussian. The smoothing function $\theta(x)$ is a cubic spline, which also approximates a Gaussian function. The DWT obtained using these two wavelet and scaling function acts like a Canny edge detector. The authors have considered an additive noise model,

$$g(x,y) = f(x,y) + \eta \tag{4.110}$$

where $g(x,y)$ is the noisy image, $f(x,y)$ is the original image and η is the noise. The expression of wavelet transformation of Eq. (4.110) is given as,

$$W^d_m g(x,y) = W^d_m f(x,y) + W^d_m \eta \tag{4.111}$$

where $d = \{x, y\}$. The multiscale product of the wavelet coefficients for an noisy image $g(x, y)$ is given as two components,

$$\begin{aligned} P_m^x g(x,y) &= W_m^x g(x,y).W_{m+1}^x g(x,y) \\ P_m^y g(x,y) &= W_m^y g(x,y).W_{m+1}^y g(x,y) \end{aligned} \tag{4.112}$$

where $W_m g(x, y)$ and $W_{m+1} g(x, y)$ are the wavelet coefficients at the decomposition level m and $m+1$ respectively. The estimated wavelet coefficients from the multiscale products after thresholding are given by,

$$\hat{W}_m^d g(x,y) = \begin{cases} W_m^d g(x,y), & P_m^d g(x,y) \geq t_p^d(m) \\ 0, & P_m^d g(x,y) < t_p^d(m) \end{cases} \tag{4.113}$$

where $m = 1, ...M$ and $t_p^d(m)$ is the adaptive threshold function. Thresholding is done on the multiscale products compared to other wavelet based denoising techniques where the thresholding is applied directly on the wavelet coefficients. The authors analyzed the distribution of the multiscale products and developed the thresholding function $(t_p^d(m))$ to remove the noise. The noise η is considered to be Gaussian and its wavelet transform representation is given as,

$$U_m^d = W_m^d \eta(x,y). \tag{4.114}$$

The multiscale products of noise is

$$V_m^d = U_m^d.U_{m+1}^d \tag{4.115}$$

The adaptive threshold function is given as,

$$t_p^d(m) = 5\kappa_m \left(1 + \frac{\mu_\eta^d(m)}{\mu_f^d(m)}\right) \tag{4.116}$$

where $\mu_f^d(m)$ and $\mu_\eta^d(m)$ are expressed as,

$$\mu_f^d(m) = \mu_g^d(m) - \mu_\eta^d(m);\ \mu_\eta^d(m) = \rho_{m+1,m}\sigma_m\sigma_{m+1} \tag{4.117}$$

and κ_m is the standard deviation of V_m^d obtained from,

$$\kappa_m = \sqrt{1 + 2\rho_{m+1,m}^2}.\sigma_m\sigma_{m+1} \tag{4.118}$$

The parameters μ_g^d, μ_f^d and μ_η^d are expressed as expected value of the multiscale products of the noisy image , the original image and the noise respectively. In Eq. (4.117, 4.118) the parameter $\rho_{m+1,m}$

represents the correlation coefficient of U_m^d and U_{m+1}^d given by,

$$\rho_{m+1,m} = \frac{\iint \psi_m(x,y).\psi_{m+1}(x,y)dxdy}{\sqrt{\iint \psi_m^2(x,y)dxdy.\iint \psi_{m+1}^2(x,y)dxdy}} \tag{4.119}$$

and σ_m is the standard deviation of noise. The adaptive threshold value varies depending upon the ratio of $\mu_\eta^d(m)/\mu_f^d(m)$ in Eq. (4.116).

4.6 Summary

In this chapter, a review of the various denoising methodologies applicable to MR images has been discussed. The denoising methods are categorized into two types: spatial domain and wavelet domain methods. The non-linear spatial filtering techniques are based on the local spatial activity and hence, adapt to the spatial context in the image resulting in good denoising. In spite of this property, the performance of these methods rely on the optimal choice of the control parameter values that have to be obtained empirically or through extensive training which makes these algorithms computationally complex. The wavelet based filtering techniques can automatically adapt to spatial variations in the noise distribution and preserve important image features. The DWT based denoising technique leads to artifacts such as edge ringing. The stationary wavelet transform based approaches tend to over-smoothen the image because of their multi-resolution characteristics. Therefore, in order to exploit the advantages of both the methods in a single framework, a denoising approach based on the non-linear spatial filters and the wavelet decomposition can be formulated to yield good feature preserved denoising results.

5

Framework of Wavelet Domain Bilateral Filter and its Validity

Contents

5.1 Introduction

The objective of this chapter is to introduce the proposed wavelet domain bilateral filter (WD-BF) strategy and validate its applicability for MR image denoising. The detail coefficients of the wavelet decomposition are denoised by wavelet thresholding. The proposed technique is validated by comparing the denoising results of WD-BF representation with other existing wavelet decompositions that includes DWT and translation-invariant wavelet transform. Also, this chapter includes the discussion on a bias factor that affects signal estimation and suggests denoising the squared magnitude MR image for bias removal.

5.2 Translation Invariant Wavelet Decompositions

The advantage of wavelet denoising methods over the spatial filtering techniques is due to their spatial-frequency representation and multi-scale decomposition [126]. The wavelet decomposition divides the input signal spectrum into its sub-spectra or sub-band. Hence, the image structures like edges are reorganized in to a set of detail coefficients at different scales and orientations. Each sub-band is processed individually such that the signal details localized within each frequency band are well preserved. Despite these advantages, an important factor limiting the extent of denoising in the DWT domain is its *translation dependance*. It means that the translations of input signal results in different transform coefficients.

The translation dependency is an effect of down-sampling the coefficients at each scale. Conventionally, decimation allows only the even samples to advance to the next level of decomposition. As a result, some of the image structures get weakly defined and it may introduce artifacts in the reconstructed image. This leads to the evolution of translation invariant wavelet transforms. These methods are extensively utilized for developing efficient image denoising approaches.

The translation invariance is obtained through simple modifications in the DWT framework. The main idea is to retain all the coefficients at each level of decomposition. Hence, such representations are over-complete or redundant and are also referred as *redundant wavelet transforms*. The basic algorithms utilized for constructing the redundant transforms are the (i) undecimated algorithm (ii) à trous algorithm and the (iii) cycle-spinning algorithm [100].

(i) **Undecimated algorithm:**

In the DWT, only the even samples of the transform coefficients are iteratively filtered. The undecimated algorithm adopts the DWT for both the even and the odd samples individually. Therefore, the transform coefficients at lower resolution level are computed separately from the even and the odd samples of the approximation coefficients at the preceding higher resolution level [127, 128]. Thus, it preserves the multi-resolution character of the transform.

The reconstruction is achieved by computing IDWT of the even and the odd samples and averaging their results. The analysis and the synthesis filter bank representations of the undecimated method are shown in Fig. 5.1 and 5.3. The inverse or reconstruction illustrated through Fig. 5.3 is known as the *average basis inverse* method [129]. It is evident that the approach is more complicated. However, the forward transform can be implemented efficiently using the à trous algorithm [130].

(ii) **à trous algorithm:**

The translation invariance is achieved by omitting the down-sampling and the up-sampling procedures. Instead of splitting the coefficients in to even and odd samples, the multi-resolution is achieved by up-sampling the filters at each decomposition level [129–131]. For each level of decomposition the filters are up-sampled by inserting zeros between the non-zero filter coefficients [131]. Algorithms in which the filters are up-sampled are called à trous filters which means " with holes" [1,118]. Hence, the name à trous algorithm [131, 132].

There are different approaches for constructing the inverse of the à trous method [129, 131]. However, the *average basis inverse* method of the undecimated algorithm as explained by Nason and Silverman [129] is the common implementation in practice [131]. Their formulation of the redundant transform is known as the *stationary wavelet transform* (SWT).

(iii) **Cycle-spinning algorithm:**

The cycle-spinning method proposed by Coifman [133] is to improve the denoising performance of the conventional DWT by suppressing the visual artifacts that occur due to translation dependency. The idea is to average out the translation dependance by computing DWT for more than one shifted versions of the original signal. The cycle-spinning procedure is summarized as follows:

(a) Given a signal $f(x)$ of length M, generate n number of circulant shifts of $f(x)$. Therefore, for $k = \{0, 1 \cdots n-1\}$ the shifted sequence $f^k(x)$ is defined as $f\left((x+k) \bmod M\right)$.

(b) Perform DWT decomposition of each sequence $f^k(x)$ and denoise the transform coefficients independently. Let us denote the set of denoised transform coefficients as $\mathbf{T}^k(f)$.

(c) Unshift the coefficients $\mathbf{T}^k(f)$ corresponding to $f^k(x)$.

(d) Compute the average of the unshifted coefficients $\mathbf{T}^k(f)$ as given below

$$\mathbf{T}(f) = \frac{1}{n}\sum_{k=0}^{n-1} \mathbf{T}^k(f) \tag{5.1}$$

(e) Reconstruct the signal $f(x)$ by taking IDWT on the average $\mathbf{T}(f)$.

Cycle-spinning over all the possible circulant shifts of the original signal is equivalent to denoising using the stationary wavelet transform [133].

5.2.1 Stationary wavelet transform

As mentioned earlier, the translation invariance is achieved by omitting the decimation and the up-sampling steps. The multi-resolution property is preserved by up-sampling the filters h_φ and h_ψ at each scale by a factor of 2^{J-1-m}. It is given by

$$h_\varphi^m(n) = \begin{cases} h_\varphi^m\left(\frac{n}{2^{J-1-m}}\right) & : \text{ if } n \text{ is an integer multiple of } 2^{J-1-m} \\ 0 & : \text{ Otherwise} \end{cases} \tag{5.2}$$

where J denotes the maximum level of decomposition and $m = \{0, 1 \cdots J-1\}$. Therefore, the filters at lower scale m can be directly obtained by two-fold upsampling of the filters at higher scale $m+1$.

$$h_\varphi^m(n) = \begin{cases} h_\varphi^{m+1}\left(\frac{n}{2}\right) & : \text{ if } n \text{ is an integer multiple of } 2 \\ 0 & : \text{ Otherwise} \end{cases} \tag{5.3}$$

The above definitions also apply for the wavelet filter h_ψ. The up-sampling in time domain reduces the bandwidth of the filters by a factor of two between subsequent resolution levels. The SWT representation is consistent with the DWT, in the sense that all the decimated coefficients are contained in it [5]. The decomposition coefficients computed recursively using the analysis filters $h_\varphi(-n)$ and $h_\psi(-n)$ are given by

$$W_\varphi^m(n) = \sum_r h_\varphi\left(-n + 2^{J-1-m} r\right) W_\varphi^{m+1}(r) \tag{5.4}$$

$$W_\psi^m(n) = \sum_r h_\psi\left(-n + 2^{J-1-m} r\right) W_\varphi^{m+1}(r) \tag{5.5}$$

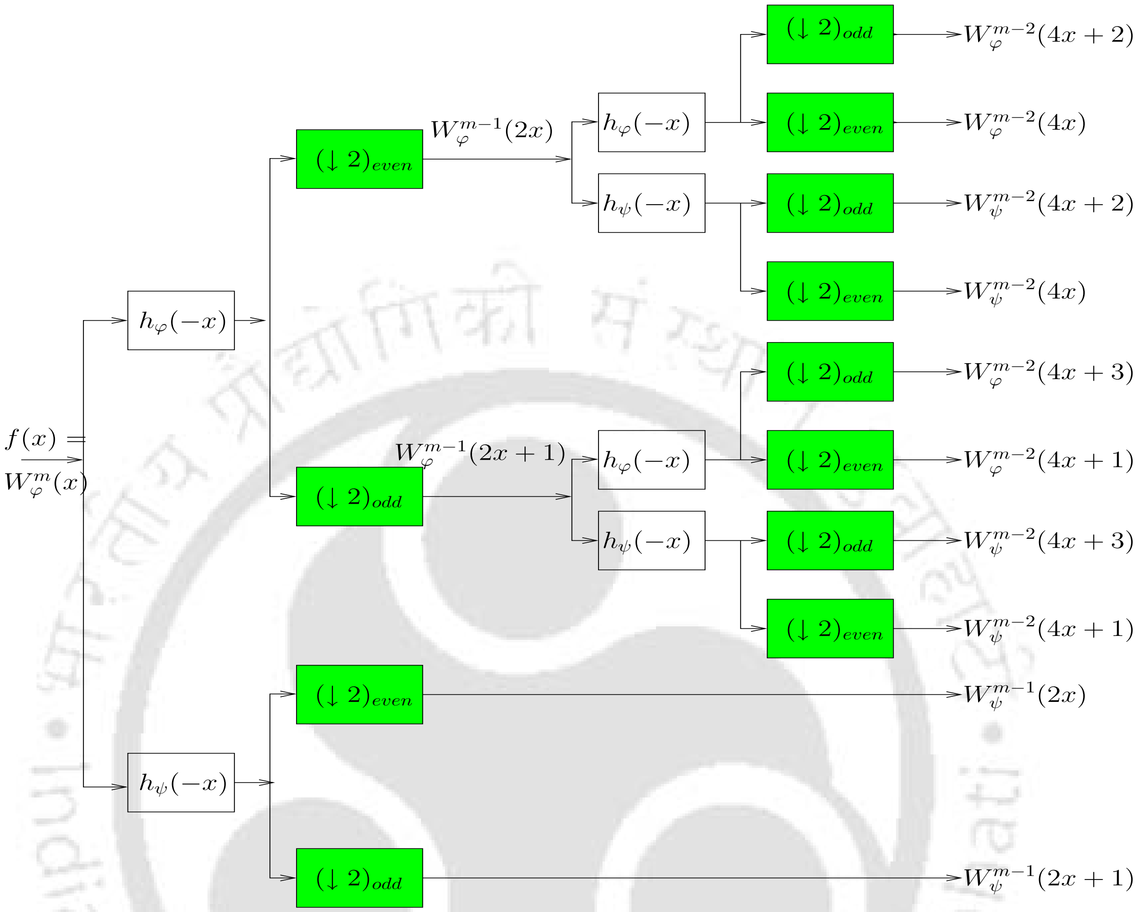

Figure 5.1: Forward transform: Undecimated algorithm

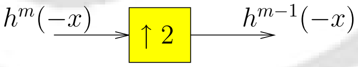

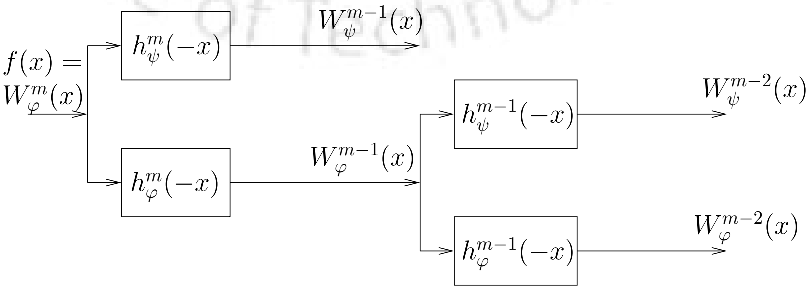

Figure 5.2: Filter bank representation of forward stationary wavelet transform (SWT)

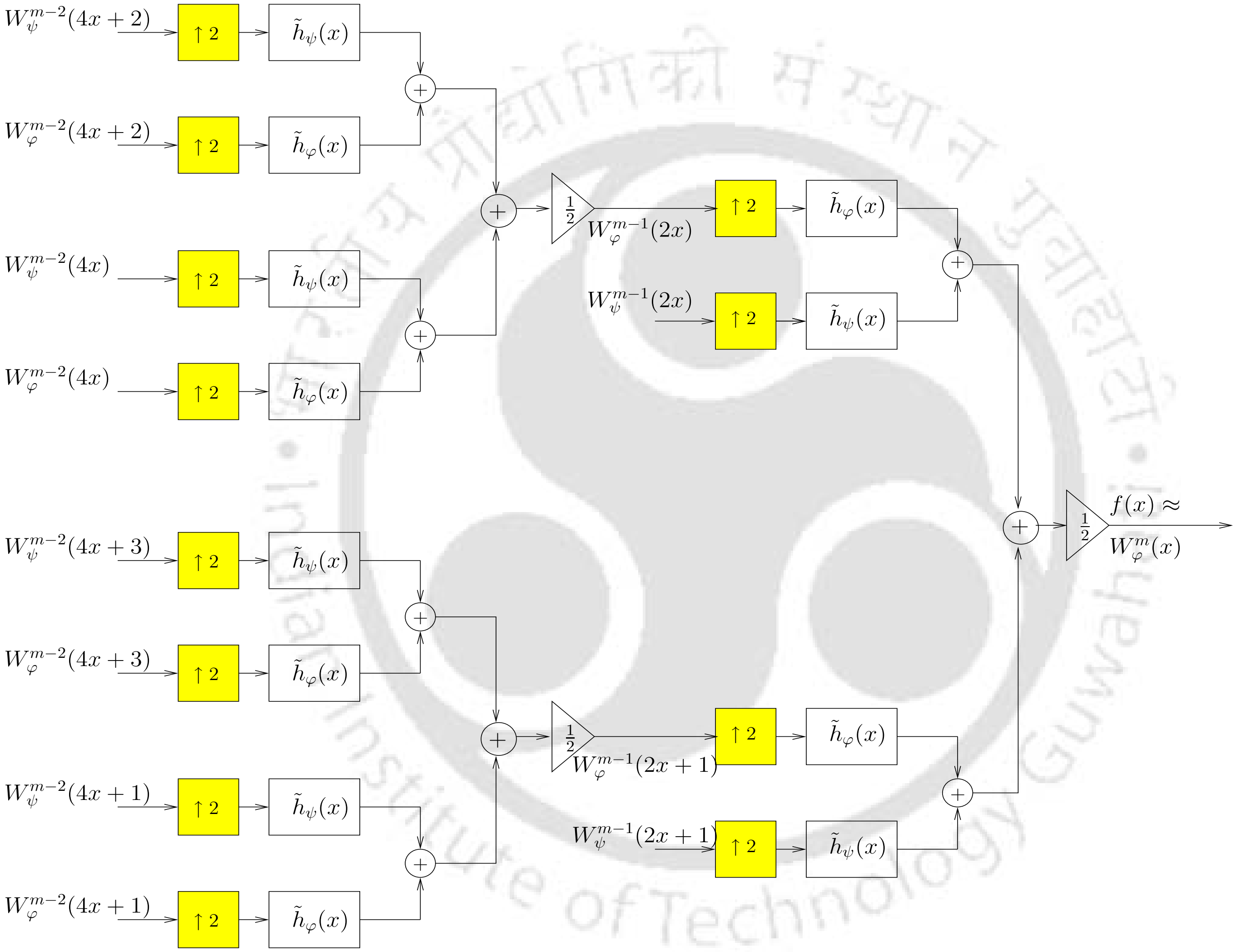

Figure 5.3: Average basis inverse method for computing the inverse of undecimated algorithm and SWT

The inverse is same as the undecimated algorithm except that the SWT coefficients must be split in to sub-sequences in order to be consistent with the number of undecimated coefficients allotted at each level of synthesis.

From the discussion, it is easy to conclude that the SWT is a comparatively efficient method for achieving translation invariance. Therefore, the reconstructed image is free from the visual artifacts like blurring and ringing. Also, the non-decimation allows the complete signal characteristics to be available at each level of decomposition. Hence, even the image structures with less spatial support (refers to the area of a homogeneous region containing pixels with similar statistical and radiometrical properties) can be well preserved. These characteristics of SWT are particularly useful in improving the wavelet based denoising algorithms.

5.2.2 Proposed wavelet domain bilateral filter

While SWT is effective for noise removal in general images, it cannot be directly adopted for denoising MR images. This is because, the MR images contain numerous structural variations and SWT tends to over-smoothen these details. The over-smoothing occurs due to up-sampling of the filters. Hence, in our method the filters are not up-sampled and the modified transform is referred as *undecimated wavelet transform*.

A new denoising framework by coalescing the undecimated wavelet transform and the bilateral filter is proposed for ensuring feature preserved MR image denoising. The decomposition is known as the wavelet domain bilateral filter (WD-BF).

5.2.2.1 Undecimated wavelet transform

The proposed undecimated wavelet transform (UDWT) is formulated by eliminating the down-sampling and the up-sampling steps as employed in DWT and SWT. Hence, UDWT is translation invariant. The filters at each level are not scaled and thus, the technique recedes to redundant sub-band decomposition. Also, this method does not sustain the multi-resolution characteristics. The transform recursively decomposes the input into one global average plus difference signals at several locations with different scales. Therefore, UDWT is a recursive filtering method. Since, the filters are quadrature mirror filters and each step is invertible; the transform satisfies the perfect reconstruction property.

Let $h_\varphi(n)$ and $h_\psi(n)$ define the low-pass (scaling) and the high-pass (wavelet) filters respectively.

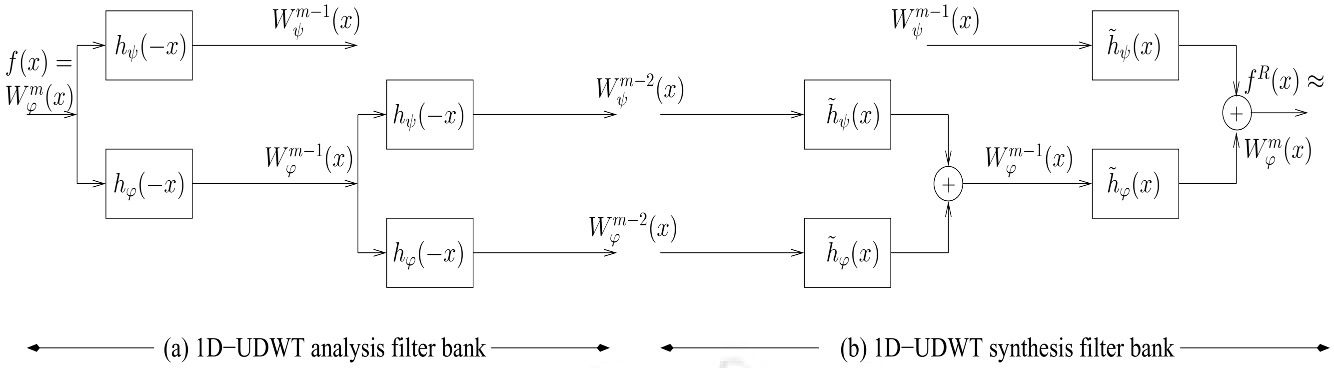

(a) 1D−UDWT analysis filter bank

(b) 1D−UDWT synthesis filter bank

Figure 5.4: Filter Bank representation of UDWT.

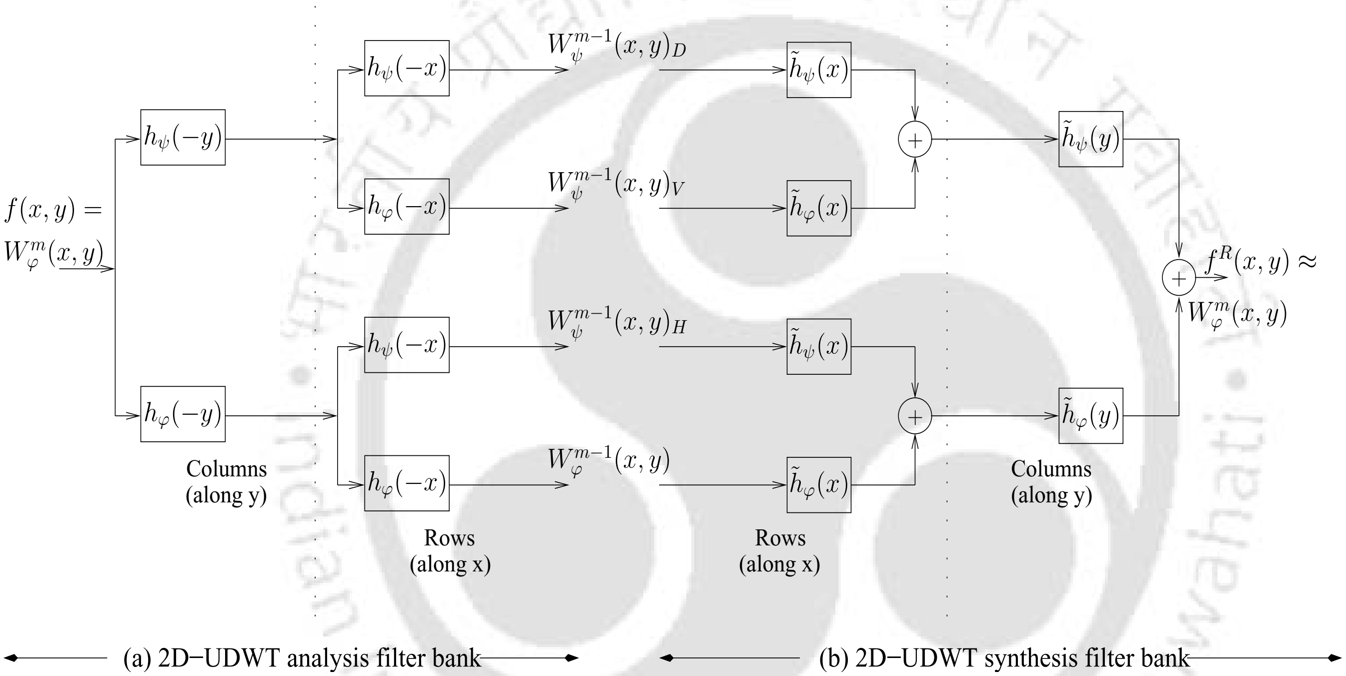

(a) 2D−UDWT analysis filter bank

(b) 2D−UDWT synthesis filter bank

Figure 5.5: Filter Bank representation of 2D-UDWT.

Then, the perfect reconstruction property is satisfied if [42]

$$H_\varphi(z^{-1})\tilde{H}_\varphi(z) + H_\psi(z^{-1})\tilde{H}_\psi(z) = 1. \tag{5.6}$$

where $H_\varphi(z)$ and $H_\psi(z)$ represent the Z-transform of $h_\varphi(n)$ and $h_\psi(n)$ respectively. The relationship between the analysis and the synthesis filters are same as discussed for DWT. The filter bank representation of UDWT is given in Fig. 5.4. The input of the system $f(x)$ is decomposed into approximation coefficient $W_\varphi^m(x)$ and detail coefficient $W_\psi^m(x)$ at each level m. The output sequence $f^R(x)$ is obtained by subsequent recombination of the decomposed coefficients. Following the theory of DWT, the relationship between the adjacent scales are obtained as

$$W_{\varphi}^{m}(x) = h_{\varphi}(-x) * W_{\varphi}^{m+1}(x) \tag{5.7}$$

$$W_{\psi}^{m}(x) = h_{\psi}(-x) * W_{\varphi}^{m+1}(x) \tag{5.8}$$

Similarly, in the inverse transform

$$W_{\varphi}^{m+1}(x) = W_{\varphi}^{m}(x) * \tilde{h}_{\varphi}(x) + W_{\psi}^{m}(x) * \tilde{h}_{\psi}(x). \tag{5.9}$$

The UDWT representation of the $1D$ signal $f(x)$ of length M and $x = \{0, 1 \cdots M-1\}$ can be written as

$$f\left(x\right) = \frac{1}{\sqrt{M}} \sum_{k} W_{\varphi}^{m_0}\left(k\right) \tilde{h}_{\varphi}\left(x-k\right) + \frac{1}{\sqrt{M}} \sum_{m=m_0}^{\infty} \sum_{k} W_{\psi}^{m}\left(k\right) \tilde{h}_{\psi}\left(x-k\right) \tag{5.10}$$

Therefore,

$$f\left(x\right) = W_{\varphi}^{m_0}\left(x\right) * \tilde{h}_{\varphi}\left(x\right) + \sum_{m=m_0}^{\infty} W_{\psi}^{m}\left(x\right) * \tilde{h}_{\psi}\left(x\right) \tag{5.11}$$

As in DWT, the separability property of the basis functions permits extension of the $1D$ UDWT for $2D$ functions. The filter bank realization of $2D$ UDWT is shown in Fig. 5.5.

In the MR images, the transitions between the tissue regions are of wide importance. The tissue regions are largely homogeneous and the transition refers to the boundary between the two homogeneous regions. The transition neighborhood represents the width of the boundary in terms of the number of pixels. The transition neighborhood between the two regions-of-interest is obtained by calculating the first order difference between the pixel values with in the desired region. The pixels that belong to the transition region will have higher gradient value relative to other pixels that lie with in the neighborhood of the homogeneous tissue regions.

An example illustrating the transition region that lie between the tissue regions in a MR image is shown in Fig. 5.6 and 5.7.

The condensed smoothing in UDWT concedes the significant noise pixels into the approximation sub-band. The magnitude of these noise pixels are different from the magnitude of the signal coefficients present with in its neighborhood. Hence, it is advantageous to have filters with adaptive weights that depend on the magnitude of the approximation coefficients within a neighborhood. However, developing orthogonal filters with adaptive coefficients is an intricate task. Therefore, we suggest to employ the non-linear filtering method for removing noise in the approximation sub-band of the

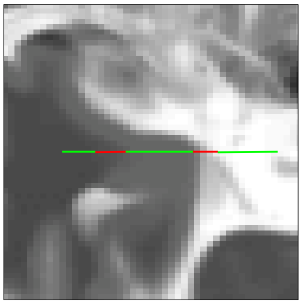

Figure 5.6: An example illustrating the transition between the tissue regions in a MR image. The transition is explained by considering few pixels that lie along the line drawn through regions in the MR image.

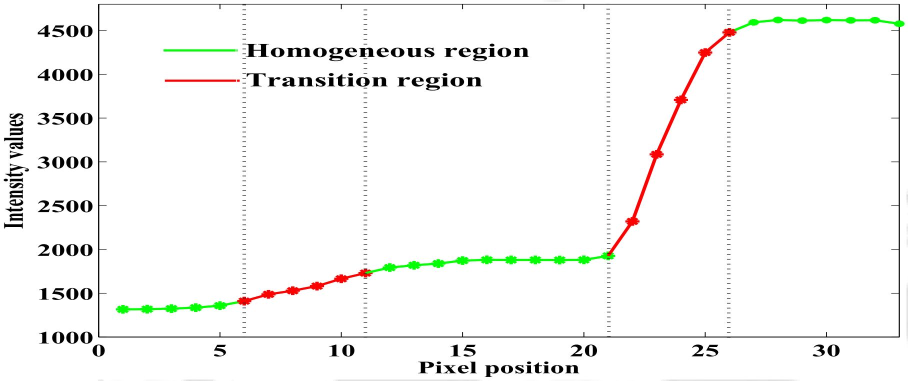

Figure 5.7: Plot of the intensity values of the pixels that lie along the line drawn in Fig. 5.6. From the plot we can infer that the gradient with respect to the pixels in the transition region are higher than the pixels in the tissue regions that lie in the neighborhood.

coarsest level. This lead to the development of WD-BF.

5.2.2.2 Bilateral filter

Bilateral filter is a non-linear filter developed by Tomasi *et al.* [7] for edge preserved denoising. The filter is a combination of the domain and the range filters. The weights of the domain filter is proportional to the spatial distance of a pixel around its neighborhood. The range filter coefficients are proportional to the radiometric (intensity) distance around the neighborhood of a pixel. The response of the bilateral filter at a pixel location $f(x, y)$ is given by

$$\hat{f}(x, y) = \frac{1}{C} \sum_{i=x-R_{neigh}}^{x+R_{neigh}} \sum_{j=y-R_{neigh}}^{y+R_{neigh}} W_d(i; x, j; y) W_r(f(i, j); f(x, y)) f(x, y) \tag{5.12}$$

where R_{neigh} is a non-negative integer such that $(2R_{neigh} + 1) \times (2R_{neigh} + 1)$ denotes the spatial neighborhood window size. W_d and W_r are the domain and range components respectively and are defined as

$$W_d(i; x, j; y) = \exp\left(-\frac{\left|(i-x)^2 + (j-y)^2\right|}{2\sigma_d^2}\right) \tag{5.13}$$

and

$$W_r(f(i,j);f(x,y)) = \exp\left(-\frac{|f(i,j)-f(x,y)|^2}{2\sigma_r^2}\right) \tag{5.14}$$

The normalization constant C is given as

$$C = \frac{1}{\sum\limits_{i=x-R_{neigh}}^{x+R_{neigh}} \sum\limits_{j=y-R_{neigh}}^{y+R_{neigh}} W_d(i;x,j;y)W_r(f(i,j);f(x,y))} \tag{5.15}$$

The weight function W_d decreases as the spatial distance between (x, y) and (i, j) increases and similarly, the function W_r decreases with the increase in the radiometric distance between intensities $f(x, y)$ and $f(i, j)$. Thus, the spatial component decreases the influence of farther pixels to reduce blurring. While, the radiometric component diminishes the influence of pixels with significantly different intensities to keep the edges of distinct image regions sharp. The parameters σ_d and σ_r control the behavior of the weights. As noise level varies, the parameters of the filter must be optimized to provide good smoothing.

For the poor choice of parameters, the bilateral filter results in undesirable cartooning effect [7]. The cartooning effect eliminates the middle gray tones and introduces abrupt changes between the gray values. In the case of MR images, the cartooning effect reduces the number of gray levels constituting the image regions and hence, results in the loss of some structural details in the MR image. However, the parameters of the bilateral filter can be optimized when the noise characteristics is well elucidated. As mentioned before, undecimated wavelet domain representation gives a well allocated set of frequency coefficients. As the noise characteristics can be studied from the detail wavelet coefficients, performance of the bilateral filter can be optimized in the wavelet domain. Hence, the combined properties of UDWT and the bilateral filter assists in reducing the noise and also prevents blurring of image features.

5.3 Wavelet Thresholding

The approximation coefficients obtained at the coarsest scale are the result of iterative low-pass filtering. Hence, it can be considered as an smoothened approximation of the original image. Unlike approximation components, the detail coefficients at each scale are the result of high-pass filtering. Therefore, the singularities like the edges and the noise at various scales and orientations are contained in the detail coefficients [134].

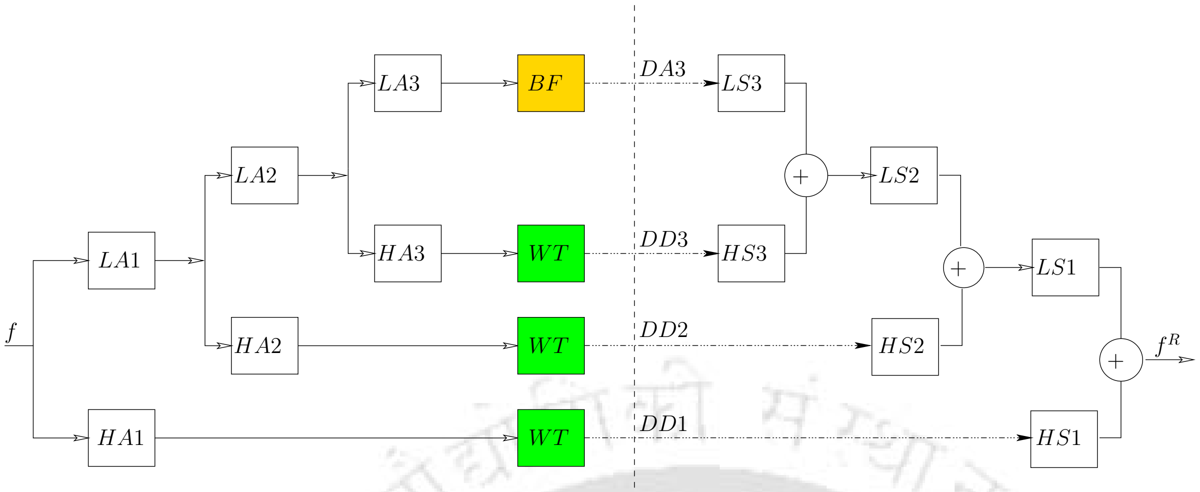

f-Input image
LA-Low-pass analysis filter
HA-High-pass analysis filter
BF-Bilateral filter
WT-Wavelet thresholding

$DA3$-Denoised approximation coefficient
DD-Denoised detailed coefficient
LS-Low-pass synthesis filter
HS-High-pass synthesis filter
f^R-Denoised image

Figure 5.8: Filter bank representation of the proposed WD-BF method.

Denoising in wavelet domain is performed by removing the noisy coefficients contained in the detail sub-band. The term *denoising* should not be considered synonymous to *smoothing* because, smoothing removes high frequencies and retains only the low frequency components. On the other hand denoising attempts to remove the noise and retains all the signal components regardless of the frequency content [134]. Hence, wavelet denoising is a thresholding operation in which the noise and the signal coefficients are identified by comparing its magnitudes against a threshold. The schematic representation of the WD-BF adopting the wavelet thresholding approach for noise removal in MR images is given in Fig. 5.8.

Considering that noise is uncorrelated with the underlying image structure, the magnitude of the wavelet coefficients corresponding to the signal will be large. Conversely, the noisy wavelet coefficients have small magnitudes and it decreases across the decomposition scale. Based on this principle, Donoho and Johnstone [115] proposed wavelet thresholding in which the signal reconstruction is achieved using only the wavelet coefficients with magnitude greater than a specified threshold value λ. This threshold is known as the *universal threshold* and is defined as

$$\lambda = \sigma_n \sqrt{2 \log (M)} \tag{5.16}$$

where M is the length of the data and σ_n is the estimated noise standard deviation. Conventionally, a good estimator for σ_n is the median of absolute deviation (MAD) from the wavelet coefficients at highest scale [135]. However, for MR images a robust estimate of noise is obtained from the background regions of the MR image as stated in Eq. (3.23).

The two basic rules of wavelet thresholding are the (i) hard thresholding and (ii) soft thresholding. **Hard thresholding** is the keep-or-kill procedure [5, 115], in which the coefficients with magnitude less than the threshold λ are set to zero. The hard thresholding of a $2D$ wavelet coefficient $W_{\psi}^{m}(x, y)$ at scale m is given by

$$\hat{\theta}^{m}(x, y) = \begin{cases} W_{\psi}^{m}(x, y) & : \left|W_{\psi}^{m}(x, y)\right| > \lambda \\ 0 & : \left|W_{\psi}^{m}(x, y)\right| < \lambda \end{cases} \tag{5.17}$$

The large noisy coefficients that pass the threshold appear as false structures in the reconstructed image and it is the major limitation of hard thresholding.

Soft thresholding reduces the wavelet coefficients with magnitude less than the threshold λ to zero and shrunk the coefficients with large magnitude by the threshold value. As a result, the false structures are eliminated in the soft thresholding method. The formulation for soft thresholding rule is as follows

$$\hat{\theta}^{m}(x, y) = \begin{cases} W_{\psi}^{m}(x, y) - \lambda & : \ W_{\psi}^{m}(x, y) > \lambda \\ 0 & : \left|W_{\psi}^{m}(x, y)\right| < \lambda \\ W_{\psi}^{m}(x, y) + \lambda & : \ W_{\psi}^{m}(x, y) < -\lambda \end{cases} \tag{5.18}$$

This soft thresholding rule is also known as *wavelet shrinkage*. The soft thresholding rule utilizing the universal threshold defined in Eq. (5.16) is known as *VisuShrink* and it is the standard method for wavelet denoising.

5.4 Bias Removal in MR images

As discussed earlier, the noisy magnitude MR image is Rician distributed. Hence, estimation in the magnitude domain introduces a bias [37]. Recalling from chapter 3, the noisy magnitude MR image is represented as

$$|g| = \sqrt{(p + \eta_{re})^2 + (q + \eta_{im})^2}.$$

where $f = p + i\,q$ is the noise-free MR image and η_{re} and η_{im} are the Gaussian random variables with $N(0, \sigma_n^2)$. The Rician distribution of the magnitude image g is as follows

$$p(g|f, \sigma_n) = \frac{g}{\sigma_n^2} e^{\frac{-(g^2+f^2)}{2\sigma_n^2}} I_0\left(\frac{fg}{\sigma_n^2}\right)$$

Using the moments of Rician distribution, the mean of $|g|$ is obtained as

$$E\left(|g|\right) = \sigma\sqrt{\frac{\pi}{2}} \exp\left(\frac{-f^2}{2\sigma_n^2}\right)\left[\left(1 + \frac{f^2}{2\sigma_n^2}\right) I_0\left(\frac{f^2}{4\sigma_n^2}\right) + \frac{f^2}{2\sigma_n^2} I_1\left(\frac{f^2}{4\sigma_n^2}\right)\right] \tag{5.19}$$

where I_0 and I_1 denote the Bessel function of the first kind of order 0 and 1 respectively. Thus, it is evident that the expected value of $|g|$ is not equal to the signal value $|f|$ [37]. The bias is signal dependent and is considerably higher in the low signal regions ($f << \sigma_n^2$). Also, it reduces the tissue contrast of the MR image as the noise level increases. Due to the dependance of bias on the signal intensity, bias removal in the magnitude domain is very complex.

Nowak in his work [37] has shown that computing the square of the magnitude MR image makes the bias constant and independent of the signal intensity. Consider the square of the noisy magnitude image $|g|$,

$$|g|^2 = (p + \eta_{re})^2 + (q + \eta_{im})^2 \tag{5.20}$$

The expected value of the squared magnitude image is

$$E\left(|g|^2\right) = E\left(p^2\right) + E\left(q^2\right) + 2\sigma_n^2 \tag{5.21}$$

since $f = p + i\,q$, the above equation can be written as

$$E\left(|g|^2\right) = |f|^2 + 2\sigma_n^2 \tag{5.22}$$

The bias term is $2\sigma_n^2$. Therefore, as stated in [37] the bias in the square magnitude domain is constant and is independent of the signal intensity. Further, it is the function of noise variance σ_n^2 and can be easily removed.

Considering the wavelet decomposition of the squared magnitude image, the wavelet basis functions are not sensitive to the constant bias term. The wavelet coefficient computed for $|g|^2$ at any particular scale and orientation is given by

$$W_\psi\left(x, y\right) = \frac{1}{\sqrt{MN}} \sum_{x=0}^{M-1} \sum_{y=0}^{N-1} |g\left(x, y\right)|^2 \psi\left(x, y\right) \tag{5.23}$$

The expected value of the wavelet coefficient $W_\psi(x,y)$ is

$$E\left(W_\psi\left(x,y\right)\right)=\frac{1}{\sqrt{MN}}\sum_{x=0}^{M-1}\sum_{y=0}^{N-1}\left|f\left(x,y\right)\right|^2\psi\left(x,y\right)+\frac{2\sigma_n^2}{\sqrt{MN}}\sum_{x=0}^{M-1}\sum_{y=0}^{N-1}\psi\left(x,y\right)\tag{5.24}$$

Using the wavelet property,

$$\sum_{x=0}^{M-1}\sum_{y=0}^{N-1}\psi\left(x,y\right)=0\tag{5.25}$$

Eq. (5.24) becomes,

$$E\left(W_\psi\left(x,y\right)\right)=\frac{1}{\sqrt{MN}}\sum_{x=0}^{M-1}\sum_{y=0}^{N-1}\left|f\left(x,y\right)\right|^2\psi\left(x,y\right)\tag{5.26}$$

Therefore, the wavelet coefficients of the squared magnitude image are unbiased estimators of $|f|^2$. Similarly, the expected value of the approximation coefficient $W_\varphi(x,y)$ of $|g|^2$ at a particular scale is given by

$$E\left(W_\varphi\left(x,y\right)\right)=\frac{1}{\sqrt{MN}}\sum_{x=0}^{M-1}\sum_{y=0}^{N-1}\left|f\left(x,y\right)\right|^2\varphi\left(x,y\right)+\frac{2\sigma_n^2}{\sqrt{MN}}\sum_{x=0}^{M-1}\sum_{y=0}^{N-1}\varphi\left(x,y\right)\tag{5.27}$$

Thus, each scaling coefficient is biased from the noise-free coefficient by a shift in the mean equal to the constant $2\sigma_n^2$. Therefore, for a J-scale wavelet decomposition the bias term is $2^{(J+1)}\sigma_n^2$ [37]. The bias is removed by subtracting the bias term from the approximation coefficients at the coarsest scale.

Therefore, noise removal in the squared magnitude MR images preserves the denoising efficiency and also restores the contrast of the MR image.

5.5 Validation of WD-BF for MRI Denoising

Following the discussions in previous section, the wavelet decomposition is performed on the squared magnitude image. The basis functions employed for wavelet representation are the *Haar wavelets*. The 1D Haar wavelet function is defined as

$$\psi\left(x\right)=\begin{cases}1 & : 0\leqslant x<\dfrac{1}{2}\\ -1 & : \dfrac{1}{2}\leqslant x<1\\ 0 & : \text{Otherwise}\end{cases}\tag{5.28}$$

The corresponding Haar scaling functions are

$$\varphi\left(x\right)=\begin{cases}1 & : 0\leqslant x<1\\ 0 & : \text{Otherwise}\end{cases}\tag{5.29}$$

The Haar wavelets have compact spatial support and are particularly useful in preserving the fine structural details. For this reason, Haar wavelets are preferred over other wavelet basis functions for denoising MR images.

For a noisy image function denoted by g, the summary of the WD-BF based denoising procedure is as follows:

(i) Compute the square of noisy MR image $|g|$ to obtain its square magnitude $|g|^2$.

(ii) Perform J-level decomposition of $|g|^2$ using UDWT to obtain the approximation and the detail coefficients. In our experiments, the maximum level of decomposition is fixed as 3.

(iii) The bias in the approximation coefficients obtained at the coarsest level J is removed by subtracting $2^{J+1}\sigma_n^2$.

(iv) These unbiased coefficients are passed through the bilateral filter.

(v) Denoise the detail coefficients using soft thresholding technique.

(vi) Compute inverse UDWT of the filtered approximation and detail coefficients to obtain the estimate of $|f|^2$.

(vii) The square root of the resultant gives the denoised magnitude MR image.

5.5.1 Validation strategies

The efficiency of the wavelet based denoising methods are verified quantitatively and qualitatively. For quantitative assessment root mean squared error and structural similarity index are evaluated. These metrics are computed with the noise-free MR image as the ground truth. Visual assessment of the residual image and the contrast measure are employed for qualitative evaluation.

(i) **Root mean squared error (RMSE):**

RMSE is the objective quality measure that quantifies the deviation of estimated values from the true value. The RMSE between the original image (f) and the denoised image $\left(\hat{f}\right)$ is measured as:

$$\text{RMSE} = \sqrt{\frac{\sum_x \sum_y \left[f(x,y) - \hat{f}(x,y)\right]^2}{M \times N}} \tag{5.30}$$

where $M \times N$ is the size of the image.

(ii) **Structural similarity index (SSIM):**

Though, RMSE is the most commonly employed similarity metric, it is not optimal with respect to the perceived quality [69]. Hence, measures that take into account the characteristics of human visual system (HVS) are of interest. SSIM is the effective alternative that improvises the error measures and is also consistent with the visual perception. As mentioned earlier, MRI consists of delicate structural details, for which RMSE is not sufficient to quantify the restored information. Therefore, SSIM is also employed to study the structural and the perceptual closeness between the denoised and the original image. The SSIM index is estimated locally over a 11×11 window, which moves pixel-by-pixel over the entire image. The final value of SSIM is the mean of the SSIM index calculated over the R local regions. The SSIM between the images f and $\hat{f}$ is evaluated from

$$\mathrm{SSIM}\left(f, \hat{f}\right)_R = \frac{\left(2\mu_f \mu_{\hat{f}} + c_1\right)\left(2\sigma_{f\hat{f}} + c_2\right)}{\left(\mu_f^2 + \mu_{\hat{f}}^2 + c_1\right)\left(\sigma_f^2 + \sigma_{\hat{f}}^2 + c_2\right)} \tag{5.31}$$

where μ is the mean intensity, σ denotes the standard deviation and c_1 and c_2 are constants chosen as given in [69].

Therefore, the mean value of SSIM index representing the overall image quality is,

$$\mathrm{SSIM}\left(f, \hat{f}\right) = \frac{1}{R}\sum_{r=1}^{R} SSIM\left(f, \hat{f}\right)_r \tag{5.32}$$

The value of SSIM lies between $[-1, 1]$. Alternately, the SSIM can also be given in percentage (%). Larger value of SSIM means high similarity between the compared images.

(iii) **Contrast:**

Contrast is a measure of the difference in pixel brightness measured between two different tissues. The contrast must be high in order to well perceive the image details. Noise in MRI, reduces the image contrast [6, 37]. Hence, it is important to ensure that the original contrast is restored or improved while denoising.

In order to verify the ability of denoising methods in preserving the contrast of the structural details, two homogeneous regions of interest (ROI) corresponding to the brightest tissue and comparatively dark tissue are considered. The MR image contrast based on the ROI's is measured as

$$C = \frac{S_{\max} - S_{\min}}{S_{\max} + S_{\min}} \tag{5.33}$$

where S_{max} is the mean value of the ROI in the brightest tissue and S_{min} is the mean value of the ROI contained within the dark tissue area.

(iv) **Residual image:**

The residual image is obtained by subtracting the denoised image from the noisy image [87]. The residual image is required to verify the traces of anatomical information removed during denoising. Hence, this reveals the excessive smoothing and the blurring of small structural details contained in the image.

5.5.2 Experiments and results

The WD-BF strategy is compared with the DWT and SWT decompositions of the squared magnitude MR image. The importance of adopting the bilateral filter in the undecimated wavelet decomposition is verified by comparing the denoising results of WD-BF with the results obtained using UDWT only. The experiments are also performed to verify the suitability of bilateral filtering in the DWT domain. The approximation coefficients of the DWT obtained at the coarsest scale are passed through the bilateral filter. The values of the bilateral filter parameters are chosen experimentally for each MR image such that it yields the optimal result in terms of the quality metrics.

Thus, the denoising approaches compared with the WD-BF includes DWT, bilateral filtering (BF) , bilateral filtering in DWT (DWT-BF), SWT and UDWT. As explained previously, the detail coefficients are denoised using soft thresholding procedure and the bias in the approximation coefficients are removed appropriately.

5.5.2.1 About the dataset

The experiments were conducted on two MRI dataset. The first dataset consists of simulated MR images obtained from the Brainweb database [136]. The second dataset consists of high and low SNR clinical MR images collected from Guwahati neurological research centre (GNRC), India. The noise levels considered for evaluation are 1%, 3%, 5%, 7% and 9%. The percentage of noise level is computed in accordance with the maximum intensity of the MR image $|f|$. For $n\%$ of noise level, the noise standard deviation is computed as

$$\sigma_n = \max(f) \times \frac{n}{100} \tag{5.34}$$

(i) **Simulated dataset:**

Simulated MR images are used collectively as the reference to evaluate and compare the validity of our technique. It evicts the data dependency enabling precise comparative studies. The dataset consists of T1 and T2 weighted MR images of resolution 217 × 181. The images were simulated using spin-echo pulse sequence. The experiments were performed on various images degraded by different noise levels. The denoising results of the following images are taken for discussion.

(a) T1 weighted brain axial MR image with large structural variations and corrupted by 5% of noise.

(b) T2 weighted brain axial MR image with less structural details and corrupted by 9% of noise.

(ii) **Clinical dataset:**

The images are acquired using Phillips 1.5 Tesla scanner. This data set consists of high SNR MR images obtained directly from the MRI scanner. The images are considered as high SNR if the noise variance estimated from their background regions are almost zero. The noisy clinical MR image is generated by adding Gaussian noise to the original data as follows [126],

$$g = \sqrt{(f + n_1)^2 + n_2^2} \tag{5.35}$$

where, f is the high SNR MR image, n_1 and n_2 is the independent identically distributed random variables with $N\left(0, \sigma_n^2\right)$. The results are discussed for the following clinical images.

(a) T2 weighted brain axial MR image containing structural variations with less spatial support and corrupted by 3% of noise.

(b) T1 weighted brain axial MR image with less tissue contrast and structural details with less spatial support. The image is corrupted by 7% noise.

(c) T2 weighted axial MR image with severe multiple-sclerosis (MS) lesions and is corrupted by 5% noise level.

5.5.2.2 Comparative evaluation

The MR images for evaluation are chosen such that it spans the entire possible structural variations contained in the MR images. As a result, it is possible to study the effects of the denoising methods in correspondence to the nature of the MR image.

The denoising results of the T1 weighted simulated MR image corrupted by 5% noise is shown in Fig. 5.9. The values of the quality metrics obtained for the denoising methods are given in Table-5.1. This image consists of large structural details and tissue areas with less spatial support. It implies that the high frequency information content is more and hence, even small loss of these details strongly degrades the quality of the denoised MR image. This is revealed in the DWT based denoising approach. Due to the multi-resolution decomposition, the structural details get poorly defined at large scales. These high frequency elements are considered as noise and are removed by wavelet thresholding. As a result, the loss of these details introduce significantly large artifacts in the denoised image. Also, BF in DWT domain, did not influence the quality of the denoised output. Conversely, in the case of SWT the details are blurred and it is due to the up-sampling of the filters at each scale.

The denoising results of BF, UDWT and WD-BF is better than DWT and SWT decomposition in reference that the structural features are well preserved. Though the UDWT based denoising preserves the structural details, the spatial support of the filters in UDWT domain is not sufficient for smoothing the noise in the constant signal regions. As a result, the noise in the background regions are not completely smoothened. Therefore, the WD-BF method combining the UDWT and BF is capable of preserving the structural details and also smoothing the noise in the constant signal regions. The RMSE and the SSIM values show that the performance of WD-BF is better than the BF and UDWT. Through visual inspection it is clearly evident that the extent of smoothing is compensated in BF in order to preserve the structural details. This introduces a grainy appearance in the denoised image.

The results show that the contrast is best preserved in the UDWT and WD-BF methods. Though, the contrast value does not reflect the actual similarity between the images, it is necessary to complement the efficiency of the denoising methods in restoring the intensity levels of the tissue regions. The residual images shown in Fig. 5.10 are used to quantify the loss in structural features and the extent of blurring along the edges. It is evident from the result that the BF has restricted the extent of smoothing along the structural details. The residuals of DWT and SWT based decompositions shows significant loss in the structural details. The residual of UDWT, shows the traces of noise still contained in the constant signal regions. The WD-BF method compensates for the noise in constant signal areas and the smoothing in edges are more than BF. However, WD-BF did not blur the edge details. The experiments on this T1 weighted simulated image is repeated for varying noise levels. The plots in Fig. 5.11 gives the values of RMSE, SSIM and contrast obtained for denoising at different noise levels. From these plots we can infer that as the noise level increase, the performance of WD-BF gets better than BF. It is expected; because as the noise level increase the spatial width of BF has to be increased and it leads to blurred edges.

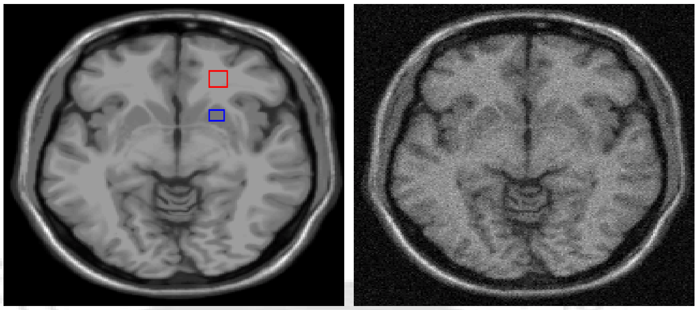

(a) Original image (b) Noisy image

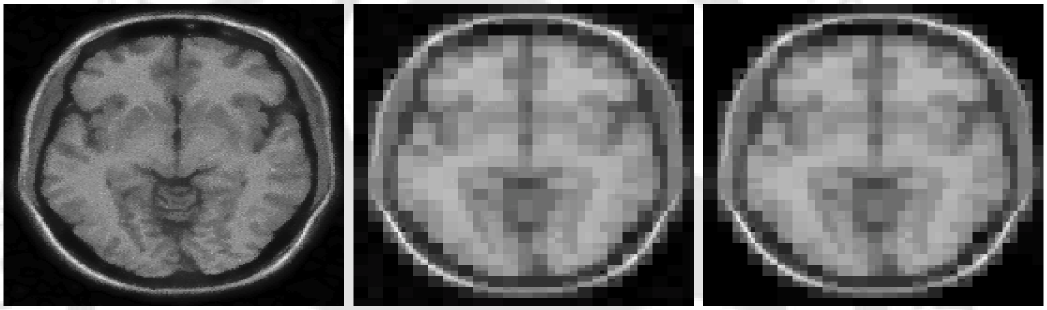

(c) Result of BF (d) Result of DWT (e) Result of DWT-BF

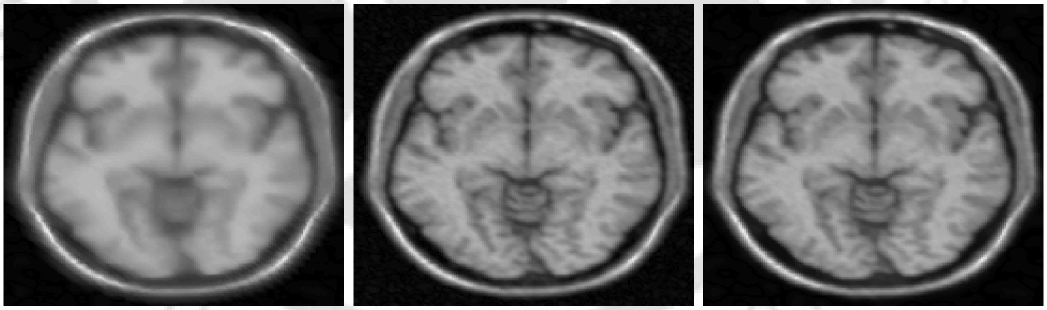

(f) Result of SWT (g) Result of UDWT (h) Result of WD-BF

Figure 5.9: Denoising results of simulated T1 weighted axial MRI corrupted by 5% noise level. The region within the boxes represent the low intensity ROI and the high intensity ROI chosen for calculating the contrast.

Table 5.1: Comparison of the denoising techniques based on the similarity metrics computed between the original and denoised T1 weighted axial MR image. The simulated noisy image contains 5% of noise.

	BF	DWT	DWT-BF	SWT	UDWT	WD-BF
RMSE	0.0533	0.1032	0.1021	0.0971	0.0527	0.0518
SSIM	0.7400	0.5434	0.5887	0.6603	0.7855	0.8101
Contrast	0.1454	0.1387	0.1375	0.1292	0.1502	0.1503

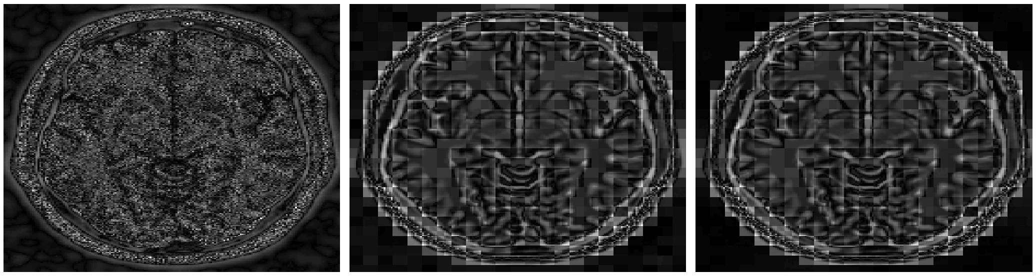

(a) Residual image of BF (b) Residual image of DWT (c) Residual image of DWT-BF

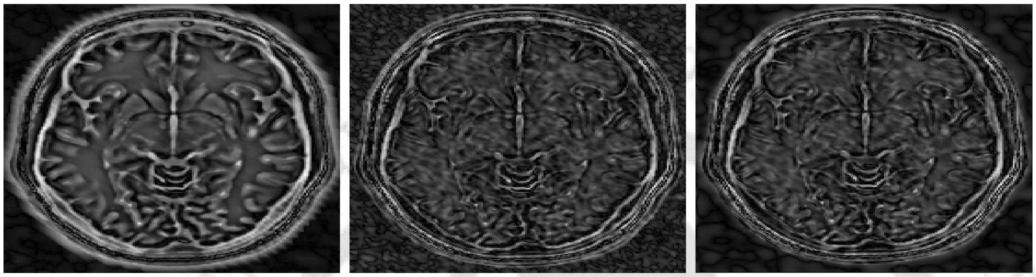

(d) Residual image of SWT (e) Residual image of UDWT (f) Residual image of WD-BF

Figure 5.10: Illustration of the extent of over-smoothing in the T1 weighted simulated image corrupted by 5% noise. The residual images are obtained by computing the absolute difference between the denoised images and the noisy MR image.

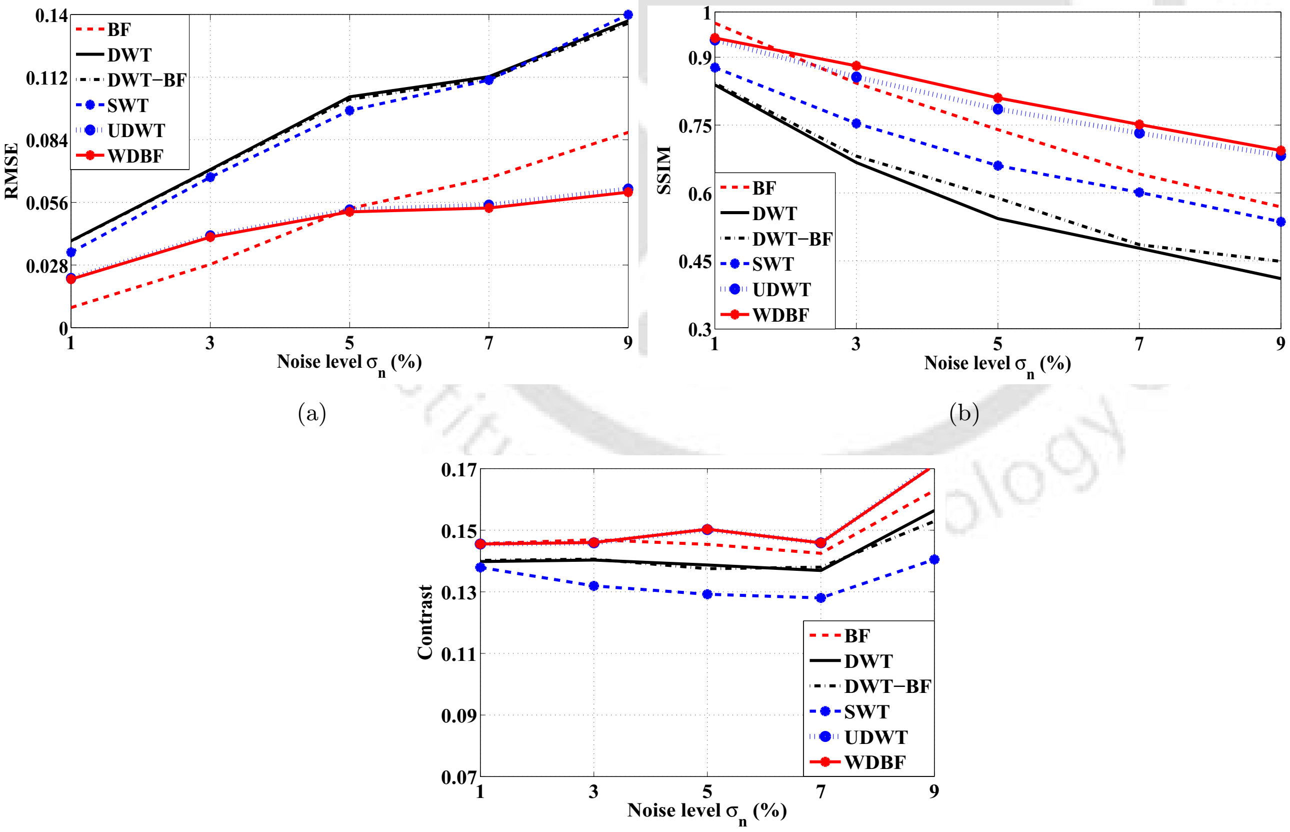

(a) (b)

(c)

Figure 5.11: Comparative plot of denoising results obtained for the T1 weighted simulated MR image at varying noise levels. (a) RMSE versus the noise level σ_n (b) SSIM versus the noise level σ_n (c) Contrast versus the noise level σ_n

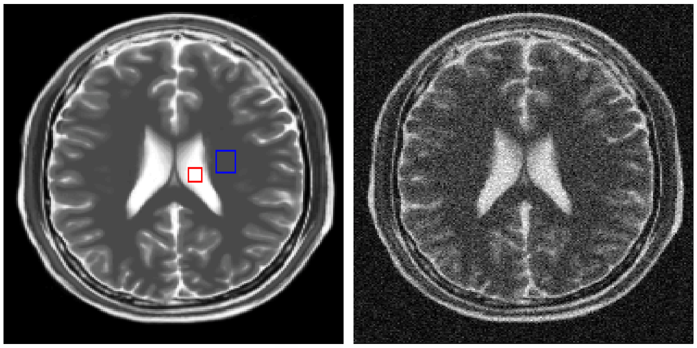

(a) Original image (b) Noisy image

(c) Results of BF (d) Results of DWT (e) Results of DWT-BF

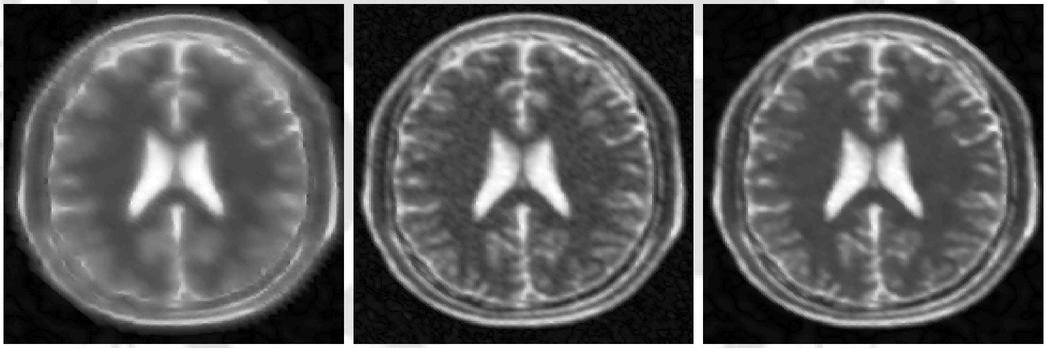

(f) Results of SWT (g) Results of UDWT (h) Results of WD-BF

Figure 5.12: Denoising results of simulated T2 weighted axial MRI corrupted by 9% noise level. The region within the boxes represent the low intensity ROI and the high intensity ROI chosen for calculating the contrast.

Table 5.2: Comparison of the denoising techniques based on the similarity metrics computed between the original and denoised T2 weighted axial MR image. The simulated noisy image contains 9% of noise.

	BF	DWT	DWT-BF	SWT	UDWT	WD-BF
RMSE	0.0918	0.1215	0.1195	0.1144	0.0808	0.0774
SSIM	0.6904	0.4722	0.5373	0.5428	0.6329	0.7101
Contrast	0.5523	0.5422	0.5339	0.5366	0.5576	0.5545

The evaluation of denoising performance on the T2 weighted simulated MR image corrupted by

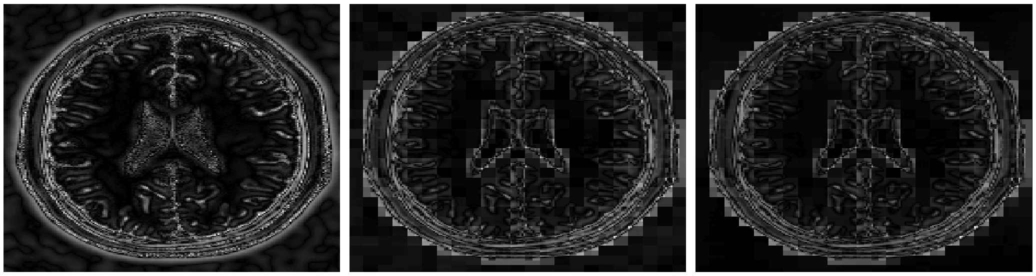

(a) Residual image of BF (b) Residual image of DWT (c) Residual image of DWT-BF

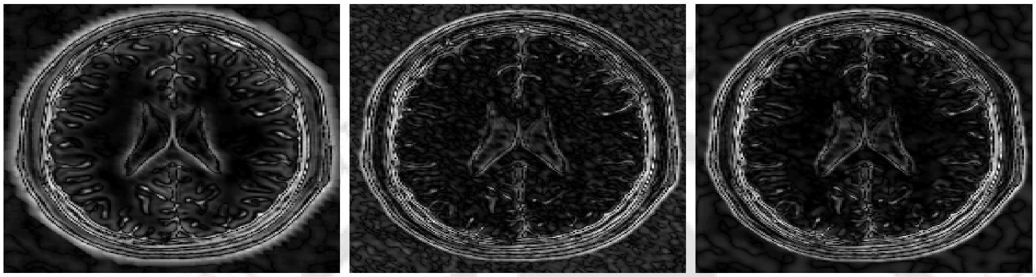

(d) Residual image of SWT (e) Residual image of UDWT (f) Residual image of WD-BF

Figure 5.13: Illustration of the extent of over-smoothing in the T2 weighted simulated image corrupted by 9% noise.

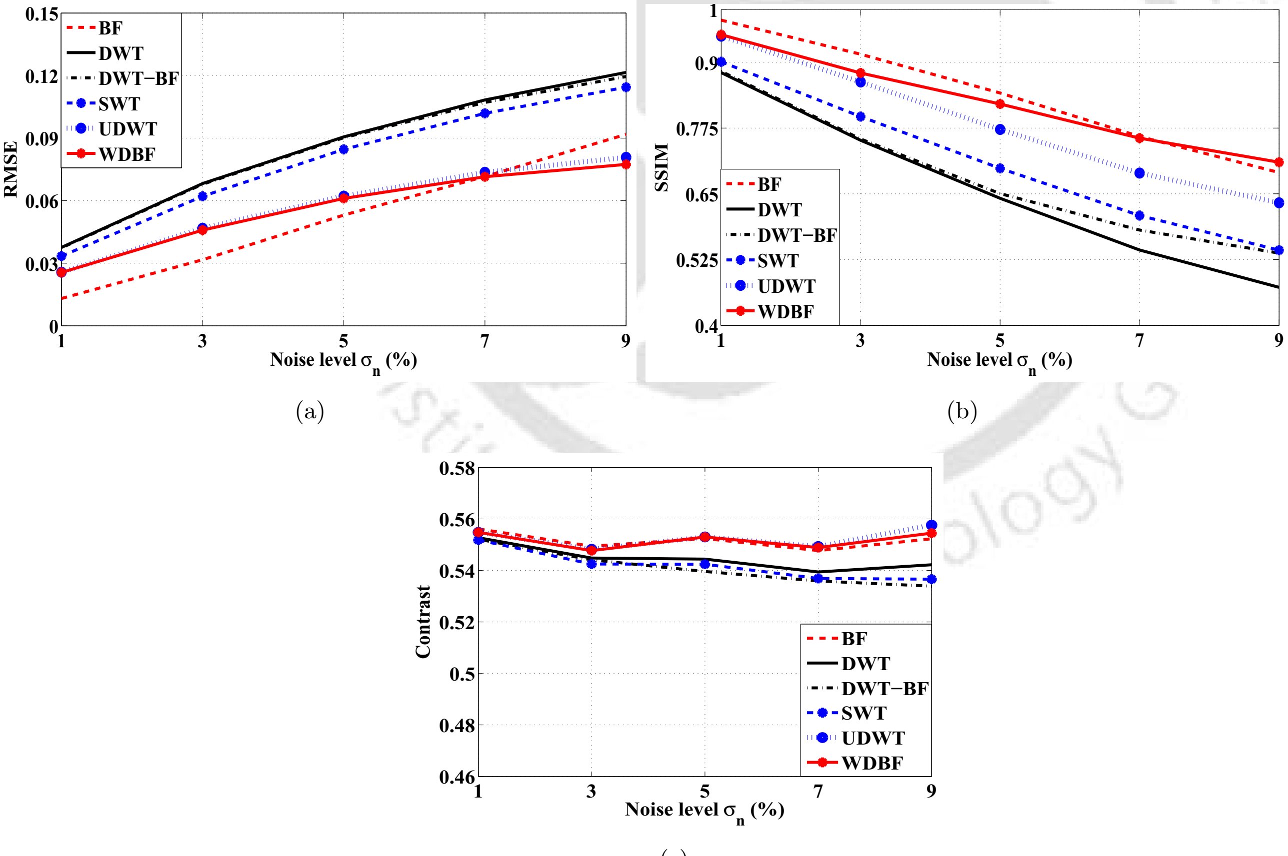

(a) (b)

(c)

Figure 5.14: Comparative plot of denoising results obtained for the T2 weighted simulated MR image at varying noise levels. (a) RMSE versus the noise level σ_n (b) SSIM versus the noise level σ_n (c) Contrast versus the noise level σ_n

9% noise is illustrated in Fig. 5.12. In comparison with the T1 weighted simulated data, this image contains less structural details and more smooth regions of constant intensity value. It can be observed that the contrast of the noisy image is reduced by the underlying noise variance. Similar to the previous denoising result, the DWT and the SWT based decompositions does not produce the optimal results. The BF has succeeded in preserving the significant edges features like the tissue boundaries. However, the small structural details corresponding to the high intensity values are blurred. Despite this smoothing effect, the grainy artifacts are still persistent in the high intensity regions. The insufficient smoothing of noise in the constant intensity areas as restricted by the spatial support of the UDWT filters are evident from the denoising result in Fig. 5.12(g). On the contrary, the denoised image obtained using WD-BF is perceptually better than the other denoising procedures. The structural features are well-preserved than the BF and the noise in the smooth regions are also removed. The values of the quality metric in Table-5.2 , confirms that the proposed WD-BF provides better denoising.

The residual images in Fig. 5.13 shows that the image details are preserved well in the WD-BF approach. The evaluations of the denoising methods on the T2 weighted simulated MR image for varying noise levels are shown in Fig. 5.14. From the RMSE and the SSIM plot, it can be observed that the error in WD-BF is more than the BF approach for noise levels $< 5\%$. Because, the structural details in this T2 weighted simulated MR are very distinct and hence the low noise levels, the BF approach is efficient in preserving these image features. The limitation of the WD-BF approach in this case is due to the wavelet threshold used for denoising the detail coefficients. However, this can be compensated by employing more robust threshold selection methods [137]. The contrast of the denoised image is properly restored in the BF, UDWT and the WD-BF approaches.

Similar to the evaluations in simulated MR images, the experiments are also performed on the diagnostically significant high SNR MR images collected from the MRI scanner.

The denoising results of a clinical T2 weighted axial MR image is presented in Fig. 5.15. The noisy MR image is simulated by adding the noise level of 3% to the high SNR image. It is observed that the denoising in the DWT domain results in artifacts which is due to the loss of signal details. Also, BF in the DWT domain is not significant in improving the denoising efficiency. The SWT results in over-smoothing and hence, blurs the edge details. The BF preserves the edge features and it also introduces grainy artifacts in the high SNR regions of the MR image. The performance of the UDWT based denoising is limited by the noise contained in the constant signal regions. Hence, the proposed WD-BF approach offers the feature preserving advantage of UDWT and also with the BF it smoothens the noise in constant signal regions. The values of the quality metrics are given in Table-5.3.

From the residual images in Fig. 5.16, we can observe that the edges are preserved in BF approach. But it also retains some of the noise pixels in the high intensity regions. If the bilateral filter width is increased for smoothing the high intensity regions, it also tends to blur the edges. Alternatively, the WD-BF approach smoothens the noise in high intensity regions and also limits the extent of smoothing in the edges. The experiments are repeated by varying the noise levels and the respective plots of the quality metrics are given in Fig. 5.17.

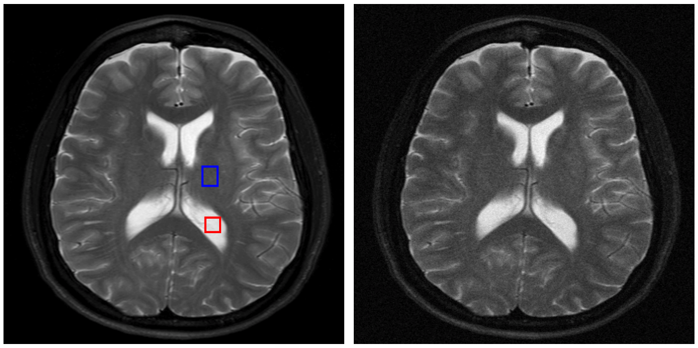

(a) Original image (b) Noisy image

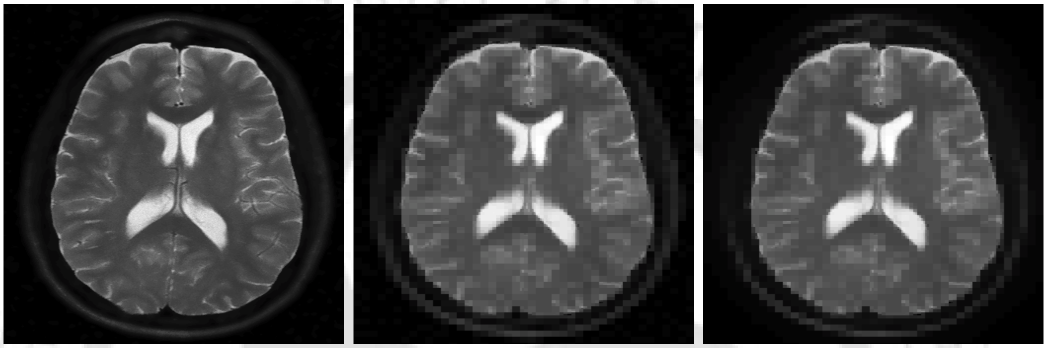

(c) Results of BF (d) Results of DWT (e) Results of DWT-BF

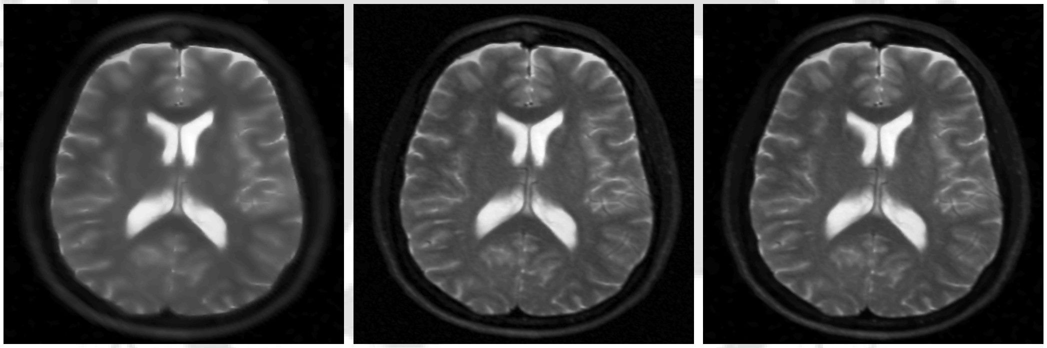

(f) Results of SWT (g) Results of UDWT (h) Results of WD-BF

Figure 5.15: Denoising results of clinical T2 weighted axial MRI corrupted by 3% noise level. The region within the boxes represent the low intensity ROI and the high intensity ROI chosen for calculating the contrast.

Table 5.3: Comparison of the denoising techniques based on the similarity metrics computed between the original and denoised T2 weighted clinical MR image. The noisy image contains 3% of noise.

	BF	DWT	DWT-BF	SWT	UDWT	WD-BF
RMSE	0.0188	0.0341	0.0339	0.0292	0.0213	0.0189
SSIM	0.8785	0.7831	0.8035	0.8403	0.8274	0.8940
Contrast	0.4823	0.4827	0.4794	0.4801	0.4830	0.4829

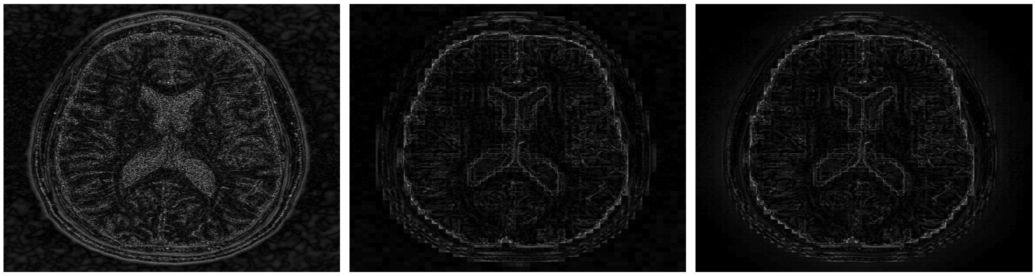

(a) Residual image of BF (b) Residual image of DWT (c) Residual image of DWT-BF

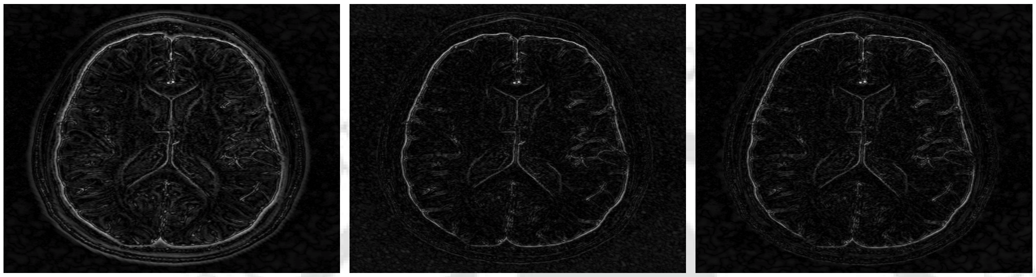

(d) Residual image of SWT (e) Residual image of UDWT (f) Residual image of WD-BF

Figure 5.16: Residual images illustrating the extent of smoothing in the clinical T2 weighted axial MR image corrupted by 3% noise.

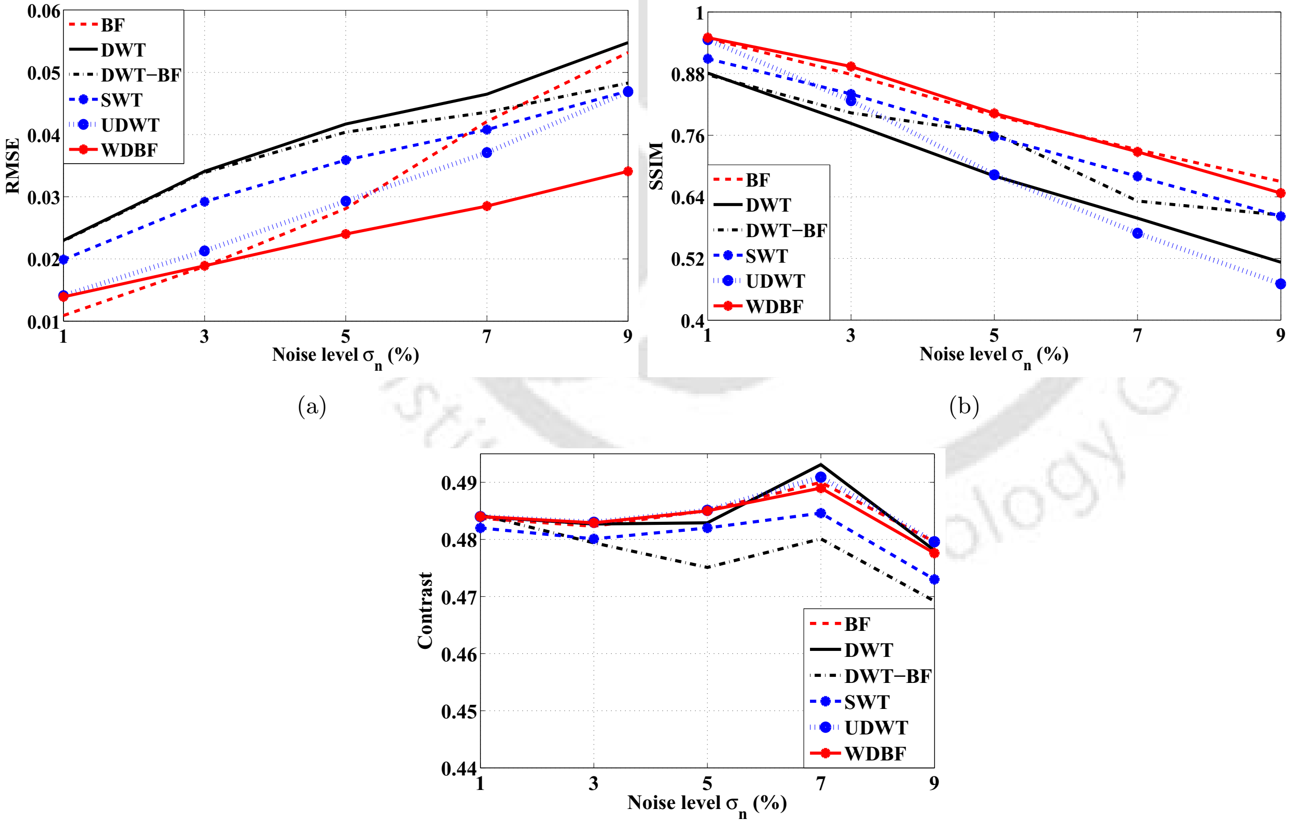

(a) (b)

(c)

Figure 5.17: Comparative plot of denoising results obtained for the T2 weighted clinical MR image at varying noise levels. (a) RMSE versus the noise level σ_n (b) SSIM versus the noise level σ_n (c) Contrast versus the noise level σ_n

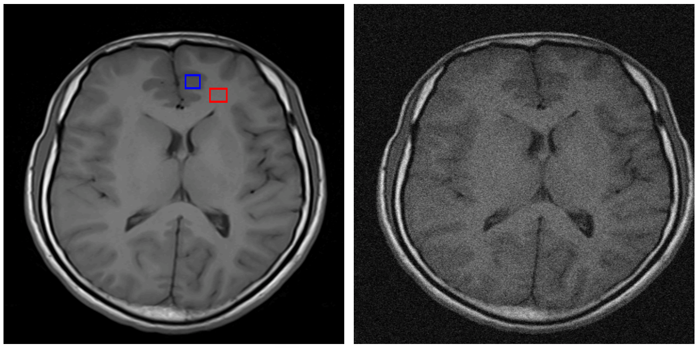

(a) Original image (b) Noisy image

(c) Results of BF (d) Results of DWT (e) Results of DWT-BF

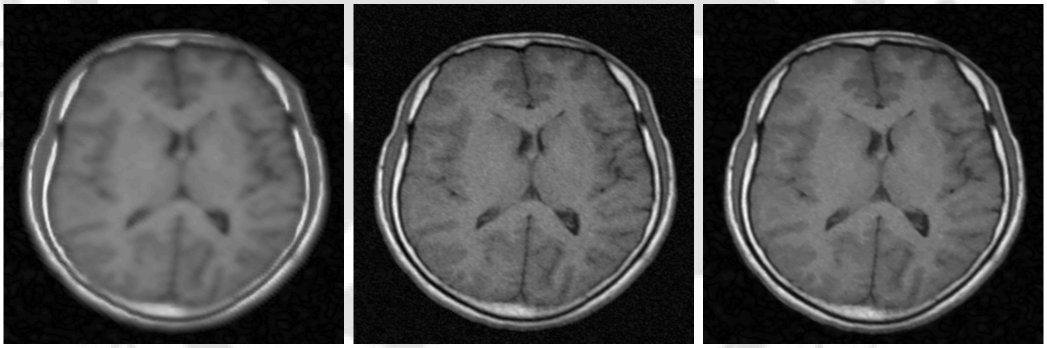

(f) Results of SWT (g) Results of UDWT (h) Results of WD-BF

Figure 5.18: Denoising results of clinical T1 weighted axial MRI corrupted by 7% noise level. The region within the blue box represents the low intensity ROI and the red box represents the high intensity ROI chosen for calculating the contrast.

Table 5.4: Comparison of the denoising techniques based on the similarity metrics computed between the original and denoised T1 weighted clinical MR image. The noisy clinical image is generated by adding 7% of noise.

	BF	DWT	DWT-BF	SWT	UDWT	WD-BF
RMSE	0.0466	0.0698	0.0672	0.0718	0.0464	0.0404
SSIM	0.8021	0.6918	0.7200	0.7644	0.6702	0.8206
Contrast	0.1565	0.1468	0.1455	0.1520	0.1599	0.1578

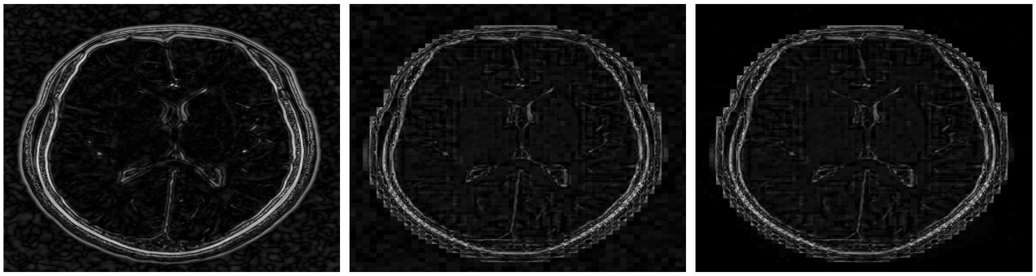

(a) Residual image of BF (b) Residual image of DWT (c) Residual image of DWT-BF

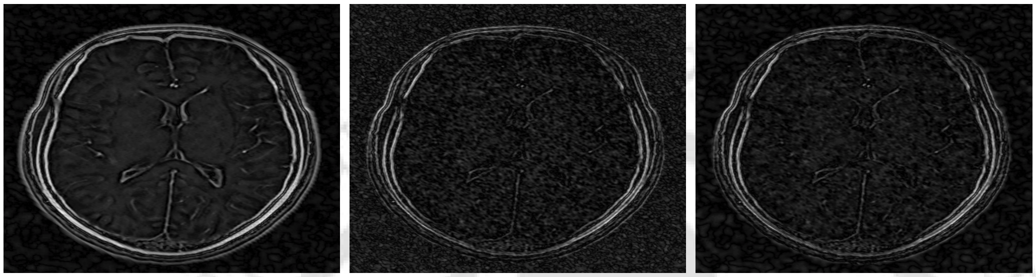

(d) Residual image of SWT (e) Residual image of UDWT (f) Residual image of WD-BF

Figure 5.19: Illustration of the extent of over-smoothing in the T1 weighted clinical MR image corrupted by 7% noise.

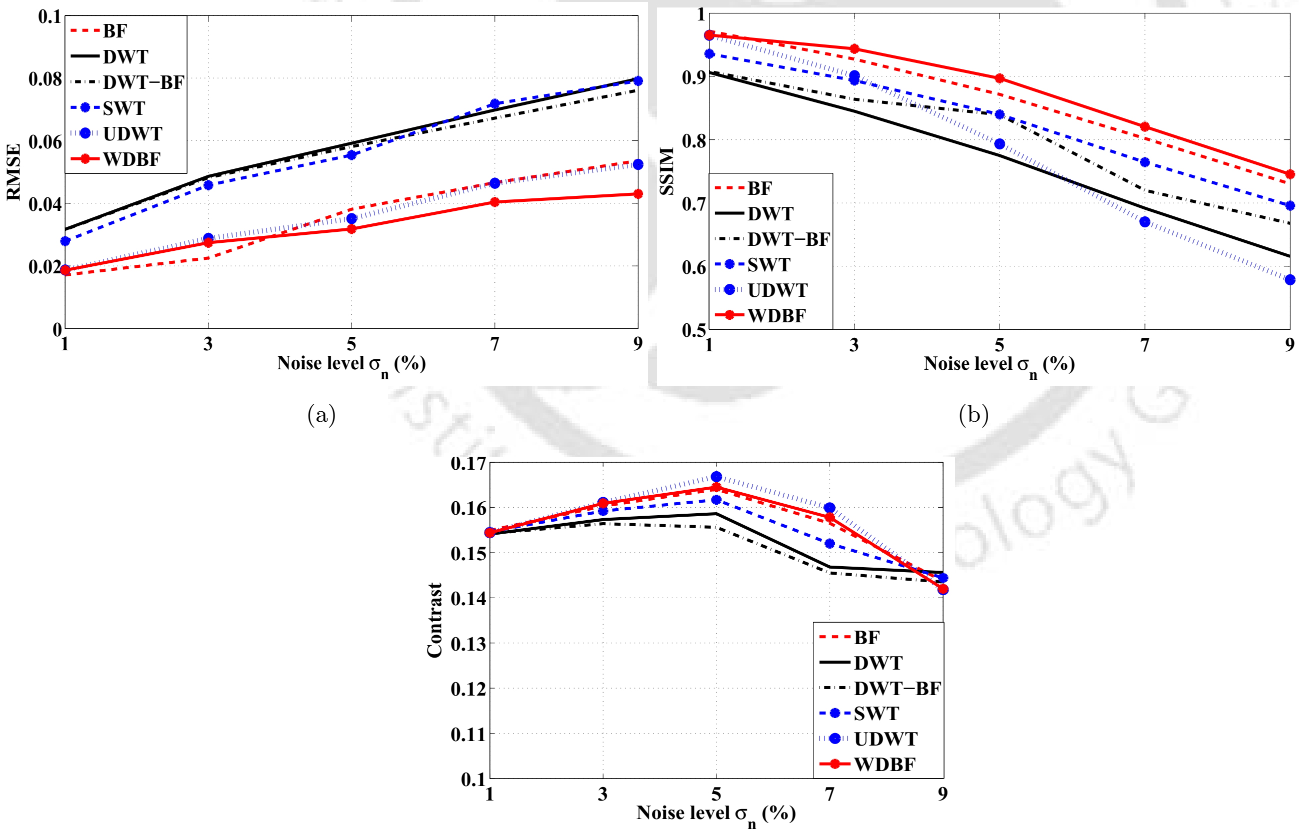

(a) (b)

(c)

Figure 5.20: Comparative plot of denoising results obtained for the T1 weighted clinical MR image at varying noise levels. (a) RMSE versus the noise level σ_n (b) SSIM versus the noise level σ_n (c) Contrast versus the noise level σ_n

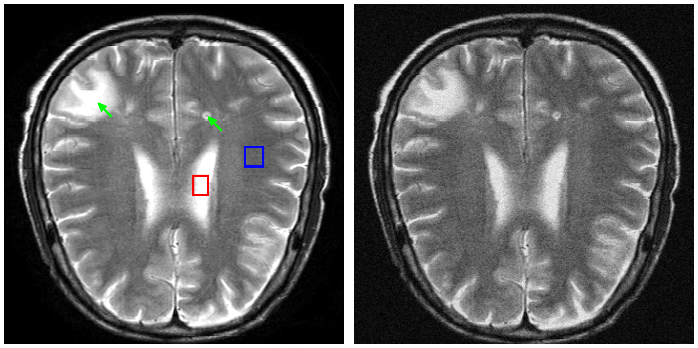

(a) Original image (b) Noisy image

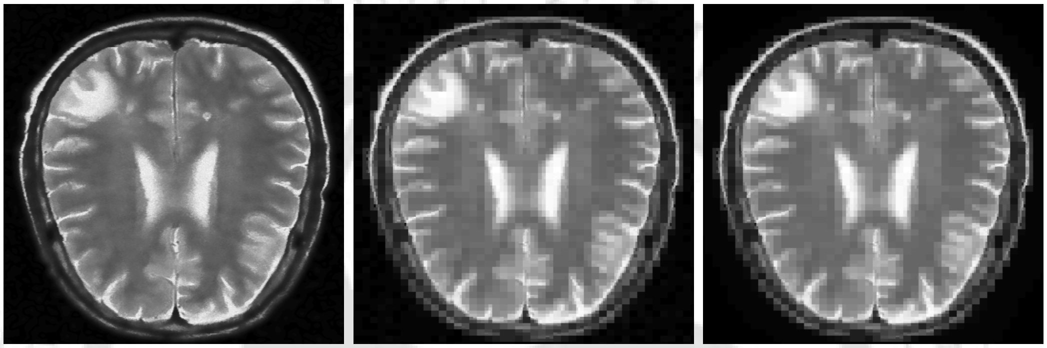

(c) Results of BF (d) Results of DWT (e) Results of DWT-BF

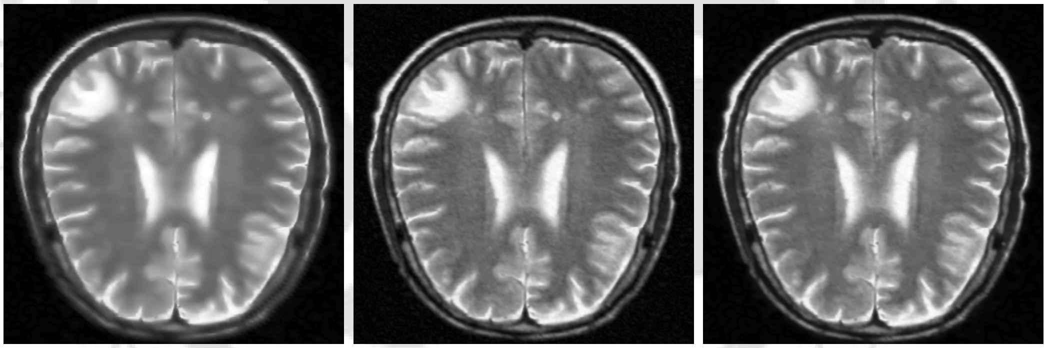

(f) Results of SWT (g) Results of UDWT (h) Results of WD-BF

Figure 5.21: Denoising results of clinical T2 weighted axial MRI consisting of pathology and is corrupted by 5% noise level. The region within the boxes represent the low intensity ROI and the high intensity ROI chosen for calculating the contrast.

Table 5.5: Comparison of the denoising techniques based on the similarity metrics computed between the original and denoised T2 weighted pathological axial MR image. The noisy image is simulated by adding 5% noise level.

	BF	DWT	DWT-BF	SWT	UDWT	WD-BF
RMSE	0.0462	0.0519	0.0499	0.0449	0.0364	0.0318
SSIM	0.7816	0.6688	0.7802	0.7391	0.6689	0.7988
Contrast	0.4236	0.4190	0.4191	0.4193	0.4221	0.4233

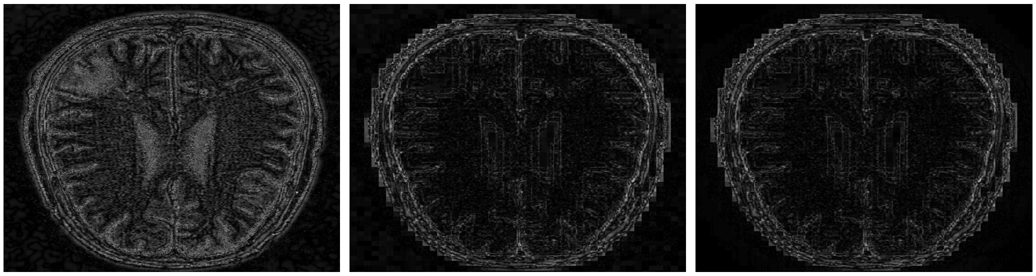

(a) Residual image of BF (b) Residual image of DWT (c) Residual image of DWT-BF

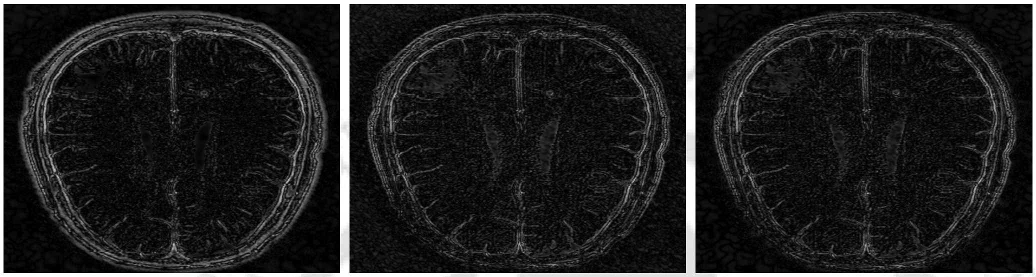

(d) Residual image of SWT (e) Residual image of UDWT (f) Residual image of WD-BF

Figure 5.22: Illustration of the extent of over-smoothing in the T2 weighted clinical MR image containing the pathology and is corrupted by 5% noise.

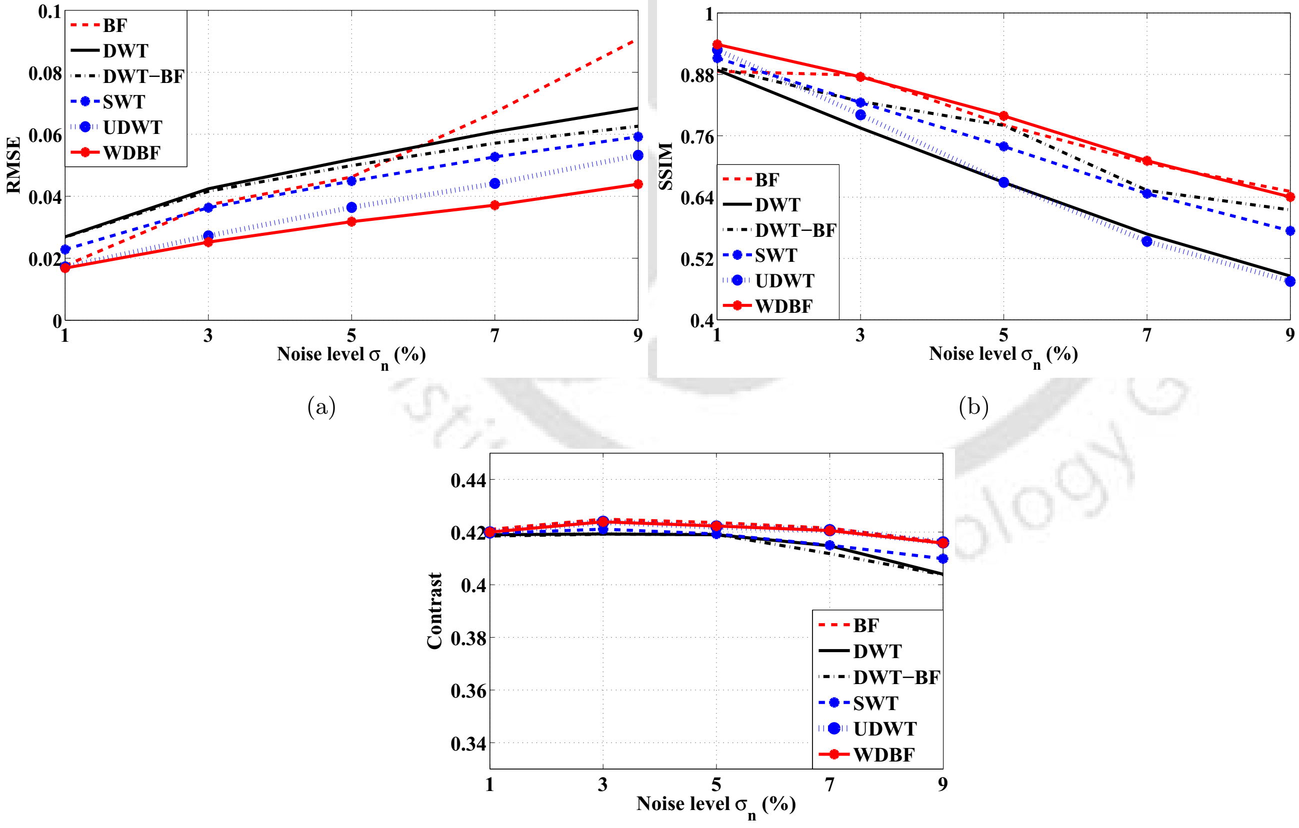

(a) (b)

(c)

Figure 5.23: Comparative plot of denoising results obtained for the pathological T2 weighted clinical MR image at varying noise levels. (a) RMSE versus the noise level σ_n (b) SSIM versus the noise level σ_n (c) Contrast versus the noise level σ_n

Another example, illustrating the denoising of a T1 weighted clinical MR image is shown in Fig. 5.18. Similar to the previous observations, the DWT and the SWT based denoising methods introduce artifacts. The considered image contains mainly regions of constant intensity value. Hence, the improved performance of BF is obtained only for large values of the filter width. As a result, the edges are blurred. In the case of UDWT, the insufficient smoothing of noise in constant intensity regions are evident. Alternatively, the WD-BF method preserves the edges as well as smoothens the noise in the constant intensity regions. The corresponding values of the quality metrics validating the denoising results are given in Table-5.4.

The residual image in Fig. 5.19, shows that the edges are well preserved in the WD-BF approach. The experiments are repeated for varying noise levels and the values of the quality metrics are given in Fig. 5.20. In comparison with the previous image denoising results, the denoising efficiency of the UDWT approach is reduced and it is due to the nature of the MR image.

The extent of denoising in affecting the pathological information contained in the MR image is verified by conducting experiments on a clinical T2 weighted axial MR image consisting of multiple sclerosis (MS) lesions. From the denoising results in Fig. 5.21, we can observe that the pathology is well preserved in the UDWT and the WD-BF methods. Also, the quality metrics in Table-5.5 confirm the validity of the denoising procedures. The applicability of UDWT is limited by its performance on the constant intensity regions. Though BF preserves the significant tissue boundaries, it retains some of the noise pixels in the high intensity regions. This can be verified from the residual images shown in Fig. 5.22. As a result, it reduces the contrast of the pathological structure which is evident through visual inspection. The DWT based methods introduce artifacts that reduce the diagnostically significant information of the MR image. The SWT based denoising results in over-smoothening of the structural details.

From these denoising results and the plots in Fig. 5.23, it is evident that WD-BF approach is more suitable for achieving feature preserved denoising in the MR images.

5.6 Summary

In this chapter a new wavelet domain bilateral filtering (WD-BF) framework is proposed for denoising MR images. The main objective of this study is to show that the combined features of wavelet transform and the non-linear bilateral filter gives better performance then the traditional wavelet filtering approaches. It is shown that the undecimated wavelet transform adapted in the WD-BF framework provides good denoising results in comparison to the DWT and SWT based filtering approaches. The approximation coefficients obtained from the UDWT is filtered using the bilateral filter and the detail coefficients are subjected to simple wavelet thresholding. Bilateral filtering of the approximation coefficients helps in preserving the edges and also reducing the noise in smooth regions. Experiments are performed on both the simulated and the clinical MR images. The residual image obtained from the denoised images depicts the good feature preserved denoising characteristics of the proposed WD-BF framework. The contrast plot obtained for all the denoised images shows that the contrast of the images are well preserved. The performance evaluation of all the techniques is obtained using SSIM and RMSE as quality metrics. The performance measures showed that the proposed method results in better denoising of MR images in comparison to the individual wavelet domain and BF approaches. The next chapter presents an adaptation of the NeighShrink thresholding in the WD-BF framework and the experimental evaluation for the optimal choice of bilateral filter parameters.

6

MR Image Denoising using WD-BF and NeighShrink Thresholding

Contents

6.1 Introduction

The MR image denoising based on the WD-BF framework is improved by applying the NeighShrink thresholding method for removing noise in the detail coefficients. The NeighShrink technique is data-driven and sub-band adaptive. As a result, it prevents excessive smoothing of the edges that is very prevalent in soft thresholding. Further improvement is obtained by automating the choice of the bilateral filter parameters. The optimal values of the filter parameters are proposed by conducting experiments on a sufficiently large number of MR images at varying noise levels.

Therefore, the improved WD-BF method is capable of achieving the desired feature preserved MR image denoising. The denoising performance of this method is compared with two of the efficient state-of-the-art techniques, the unbiased non-local means (UNLM) algorithm [87] and Pizurica's wavelet denoising method based on the inter-scale dependencies [66].

This chapter presents in detail the NeighShrink wavelet thresholding method and the choice of bilateral filter parameters for MR images. The discussion on the experiments and the results is presented to validate the efficiency of the improved WD-BF technique for feature preserved MR image denoising.

6.2 NeighShrink Wavelet Thresholding

Denoising using VisuShrink yields over-smoothened images. This is because; the universal threshold is very large due to its dependence on the data size, that is the number of samples. Hence, several other threshold selection methods were suggested to counteract the excessive smoothing in VisuShrink [5]. One of such improvement is the threshold estimation using Stein's unbiased risk estimate (SURE) [138]. The SURE threshold selection procedure basically aims in obtaining an optimal threshold value for each sub-band, such that the error is minimized.

Further improvements were achieved by exploiting the relationship between the wavelet coefficients contained within a neighborhood. The thresholding rule suggested in [139] and [137], considers the similarity between the wavelet coefficient and its corresponding neighbors. This approach is known as the NeighShrink thresholding and it employs the universal threshold. For the wavelet coefficient $W_{\psi}(x,y)$ at any scale and orientation, the estimate using NeighShrink thresholding rule is defined as

$$\hat{\theta}(x,y) = W_{\psi}(x,y)\,\beta(x,y) \tag{6.1}$$

where $\beta(x,y)$ is the shrinkage factor computed as

$$\beta(x,y) = \max\left(1 - \frac{\lambda^2}{\sum\limits_{m=x-L}^{x+L}\sum\limits_{n=y-L}^{y+L} W_\psi(m,n)^2}, 0\right) \tag{6.2}$$

$L \times L$ defines the size of the neighborhood and λ is the universal threshold. Dengwen *et al.* [135], improved the NeighShrink algorithm by using SURE to find the optimal threshold value and the neighborhood size L. The improved NeighShrink algorithm proposed by [135] is described in the following paragraphs.

For ease of notation, let us rearrange the $2D$ wavelet coefficients of size $M \times N$ at scale m as a $1D$ vector of length $N_1 = M \times N$, such that $w_m = \left\{W_\psi^m(x,y)\right\}$. For the n^{th} wavelet coefficient $w_m(n)$, let

$$S_m(n) = \sum_{r=n-L}^{n+L}\left(w_m^2(r)\right) \tag{6.3}$$

denote the sum of the squares of the wavelet coefficients within the neighborhood L. Then, the expected risk in the estimate $\hat{\theta}_m$ is given by

$$E\left\{\left\|\hat{\theta}_m - \theta_m\right\|_2^2\right\} = N_1 + E\left\{\|g(w_m)\|_2^2 + 2\nabla.g(w_m)\right\} \tag{6.4}$$

where,

$$g(w_m) = \left\{\hat{\theta}_m(n) - w_m(n)\right\}_{n=1}^{N_1} \quad \text{and} \quad \nabla.g = \sum_{n=1}^{N_1}\frac{\partial g(w_m(n))}{\partial w_m(n)}$$

are defined respectively as

$$g(w_m(n)) = \begin{cases} -\dfrac{\lambda^2}{S_m(n)}w_m(n) & : \lambda^2 < S_m(n) \\ -w_m(n) & : \text{otherwise} \end{cases} \tag{6.5}$$

$$\frac{\partial g(w_m(n))}{\partial w_m(n)} = \begin{cases} -\lambda^2\dfrac{S_m(n) - 2w_m^2(n)}{S_m^2(n)} & : \lambda^2 < S_m(n) \\ -1 & : \text{otherwise} \end{cases} \tag{6.6}$$

Thus, we can write

$$\|g(w_m(n))\|_2^2 = \begin{cases} \frac{\lambda^4}{S_m^2(n)}w_m^2(n) & : \lambda^2 < S_m(n) \\ w_m^2(n) & : \text{otherwise} \end{cases} \tag{6.7}$$

The expected loss or Stein's unbiased risk estimate for sub-band m and $L \times L$ neighborhood is defined by

$$SURE\left(w_m, \lambda, L\right) = N_1 + \sum_{n} \left\| g\left(w_m\left(n\right)\right)\right\|_2^2 + 2\sum_{n=1}^{N_1} \frac{\partial g\left(w_m\left(n\right)\right)}{\partial w_m\left(n\right)} \tag{6.8}$$

Therefore,

$$E\left\{\left\|\hat{\theta}_m - \theta_m\right\|_2^2\right\} = E\left\{SURE\left(w_m, \lambda, L\right)\right\} \tag{6.9}$$

Accordingly, the optimal threshold λ^m and neighboring window size L^m for sub-band m that minimize $SURE(w_m, \lambda, L)$ is chosen as

$$\left(\lambda^m, L^m\right) = \underset{\{\lambda, L\}}{\operatorname{argmin}}\, SURE\left(w_m, \lambda, L\right) \tag{6.10}$$

6.3 Influence of Bilateral Filter Parameters

The parameters of the bilateral filter are the (i) kernel width R_{neigh} (ii) domain component σ_d and the (iii) range component σ_r. The smoothing effect of the bilateral filter is completely influenced by the choice of these parameters.

6.3.1 Effect of R_{neigh}

The kernel width R_{neigh} specifies the size of the neighborhood within which the weighted average is computed. It can also be referred as the filter width. The width of the filter must be chosen such that it is broad enough to smooth the noise contained in the large uniform regions and should be narrower at edges in order to prevent blurring. However, in practice only the bilateral filters with fixed width are employed. Hence, the width must be chosen such that there exist a tradeoff between the extent of smoothing and the edge preservation. Also, as the filter width is large the number of computations involved also increases. Therefore, computational efficiency is also an important factor to be considered in the choice of neighborhood size.

6.3.2 Effect of σ_d

The domain component σ_d also referred as the spatial parameter is chosen based on the size of the neighborhood. In spite of this, there are no conditions specifying the relationship between σ_d and R_{neigh}. For a large neighborhood, if the σ_d value is small, only those neighborhood pixels at close proximity to the center pixel are assigned higher weights. The pixels at utmost distance within the neighborhood area does not influence the computed filter response. As a result the edges are well preserved. Conversely, for large values of σ_d the width of the domain filter increases thereby considering more distant pixels leading to excessive smoothing of edges. Thus, the domain standard deviation σ_d determines the amount of blurring.

6.3.3 Effect of σ_r

The range parameter σ_r is the most essential parameter inciting the adaptivity of the bilateral filter. This parameter characterizes the intensity similarity between the pixels with in the neighborhood and the center pixel. The weights assigned to the pixels in neighborhood decay with the intensity dissimilarity. As a result, only those pixels belonging to the same region are contained while smoothing and this prevents edge blurring.

From the dependency of the range parameter on the intensity values, it is obvious that the smoothing properties of the bilateral filter can be controlled by directly relating σ_r to the noise level σ_n. Intuitively, for low noise level the intensity dissimilarity between the pixels belonging to the same region is less and hence, the value of σ_r must be less. In the case of higher noise levels, the range parameter must be sufficiently large to ensure proper smoothing. Therefore, the value of σ_r must be chosen directly proportional to the noise standard deviation.

The smoothing effect due to the large values of R_{neigh} and σ_d is limited by the choice of range component σ_r. Thus, the range parameter enforces a strict preservation of the contours and the edges.

From this discussion it is clear that the domain component is independent of the noise level σ_n. The neighborhood size R_{neigh} must be sufficiently large to treat the higher noise levels. In the case of low noise levels, the effect of large R_{neigh} can be limited by the proper choice of σ_r. For these reasons, σ_r is considered as the most important parameter influencing the denoising efficiency of bilateral filter.

6.4 Experiments and Results

The dataset consists of T1 and T2 weighted MR images and experiments performed include images degraded by noise levels 1%, 3%, 5%, 7% and 9%. The experiments for selecting the bilateral filter parameters are conducted on a T2 weighted simulated MR volume consisting of 142 images of resolution 217×181. The denoising results of the simulated images presented in the discussion are:

- T1 weighted axial MR image of normal brain.
- T2 weighted axial MR image of normal brain.
- T2 weighted axial MR image with multiple sclerosis (MS) lesion.

The clinical images contained in the experiments are as follows:

- T1 weighted axial MR image of normal brain with resolution 256 × 256.
- T2 weighted axial MR images of normal brain and tumor pathology. The resolution of the images is 256 × 256.
- T2 weighted MR image of knee with resolution 512 × 512.

As explained in chapter 5, the denoising is performed on the squared magnitude images. Haar wavelet is used for 3-level decomposition of the MR images. The wavelet coefficients are denoised using NeighShrink thresholding.

The efficiency of this WD-BF method is compared with the unbiased non-local means (UNLM) filtering and the wavelet denoising based on inter-scale dependency proposed in [66]. Also, the improvement in adopting the NeighShrink procedure in WD-BF approach is verified by comparing with the VisuShrink approach proposed earlier.

UNLM is proved to be an efficient procedure for feature preserved denoising and they are shown to outperform existing wavelet based denoising methods [87]. Bilateral filter has similar characteristics as UNLM. However, UNLM are computationally expensive than bilateral filters.

The major advantage of UNLM is its exploitation of the intensity similarities. Similar exploitations in the wavelet domain, where the data and noise can be efficiently discriminated provide better denoising. Hence, we have compared the performance of WD-BF with UNLM. The optimal parameters of UNLM were chosen as given in [87].

The denoising technique proposed by Pizurica *et al.* [66] is one of the efficient wavelet based strategy for denoising medical images. The method classifies the signal and the noisy wavelet coefficients by exploiting the correlation between the coefficients across the resolution scales. This classification is used to empirically estimate the statistical distributions of the coefficients based on which denoising is performed. For this reason, the approach was capable of retaining the significant structural features of the MR image while denoising. Hence, this wavelet denoising method is considered for comparing with the proposed WD-BF approach.

6.4.1 Parameter selection

The optimal values of the bilateral filter parameters are determined by conducting experiments on the simulated data sets, for different noise levels.

6.4.1.1 Choice of R_{neigh}

The value of R_{neigh}, gives the radii of the neighborhood window within which the weighted average is computed. Its choice should remain a compromise between the (RMSE , SSIM) and the number of computations. Here, RMSE quantifies the prediction error and SSIM gives the structural correlation. As R_{neigh} increases, the computational complexity also increase.

The value of R_{neigh} is chosen by evaluating for various combinations of (σ_d, σ_r). The parameters are chosen as; $1 \leq \sigma_d \leq 7$, $0.1\sigma_n \leq \sigma_r \leq 7\sigma_n$ and $3 \leq R_{neigh} \leq 11$. The experiments are conducted for various noise levels.

For all the combinations of (σ_d, σ_r), the RMSE and the SSIM values are obtained. The RMSE (SSIM) reaches its minimum (maximum) within the range $7 \leq R_{neigh} \leq 11$. Also, the computed values did not vary significantly over this range. This implies that the behavior of RMSE (SSIM) with respect to R_{neigh} does not change for any values of (σ_d, σ_r). Hence, the optimal choice of R_{neigh} for a particular value of (σ_d, σ_r) can be assumed to be valid for other combinations of (σ_d, σ_r).

The average results computed from the experiments conducted on a simulated T2 weighted MRI volume are presented in Table-6.1. It gives the average values of RMSE and SSIM obtained for different choice of R_{neigh} and σ_n. From the table, it can be verified that lower RMSE value implies higher SSIM. Hence, the choice of R_{neigh} based on RMSE will hold true for SSIM.

For the values in Table-6.1, the plot of variation in the RMSE (SSIM) values along R_{neigh} for a constant σ_n is shown in Fig. 6.1. The variation in RMSE (SSIM) values is computed as the first order difference of RMSE (SSIM) with respect to R_{neigh}. This gives the rate of change in RMSE (SSIM) values as R_{neigh} increases. Thus, we can infer the critical value of R_{neigh} beyond which it does not influence the denoising performance.

Table 6.1: RMSE, SSIM values obtained for various (R_{neigh}, σ_n) and $(\sigma_d = 5, \sigma_r = 2\sigma_n)$.

σ_n \ R_{neigh}	**3**	**4**	**5**	**6**	**7**	**8**	**9**	**10**	**11**
5	0.0041, 0.9753	0.0042, 0.9746	0.0042, 0.974	0.0042, 0.9735	0.0042, 0.973	0.0042, 0.9726	0.0042, 0.9722	0.0042, 0.9719	0.0042, 0.9716
10	0.0055, 0.9497	0.0056, 0.9521	0.0056, 0.9538	0.0056, 0.9556	0.0056, 0.956	0.0056, 0.9563	0.0056, 0.9564	0.0056, 0.9565	0.0056, 0.9566
20	0.0087, 0.8819	0.0086, 0.8893	0.0085, 0.8944	0.0085, 0.8981	0.0084, 0.9006	0.0084, 0.9023	0.0084, 0.9035	0.0084, 0.9043	0.0084, 0.9048
30	0.0115, 0.8194	0.0112, 0.8326	0.011, 0.8423	0.0109, 0.85	0.0109, 0.8601	0.0108, 0.8603	0.0108, 0.8634	0.0108, 0.8636	0.0108, 0.8640
40	0.0146, 0.772	0.0141, 0.7873	0.0139, 0.7989	0.0137, 0.8075	0.0137, 0.8157	0.0136, 0.8184	0.0136, 0.822	0.0136, 0.8236	0.0136, 0.8244
50	0.0217, 0.7305	0.0212, 0.7483	0.0208, 0.7617	0.0206, 0.7718	0.0205, 0.7853	0.0204, 0.7856	0.0204, 0.7882	0.0204, 0.7906	0.0204, 0.7921
70	0.0229, 0.6503	0.0224, 0.6697	0.0223, 0.6842	0.0222, 0.6944	0.0222, 0.7050	0.0221, 0.7073	0.0221, 0.7108	0.0221, 0.7132	0.0221, 0.7148
100	0.0355, 0.5725	0.0342, 0.5926	0.0334, 0.6074	0.033, 0.6178	0.0328, 0.6249	0.0327, 0.6299	0.0327, 0.6332	0.0327, 0.6335	0.0327, 0.6338

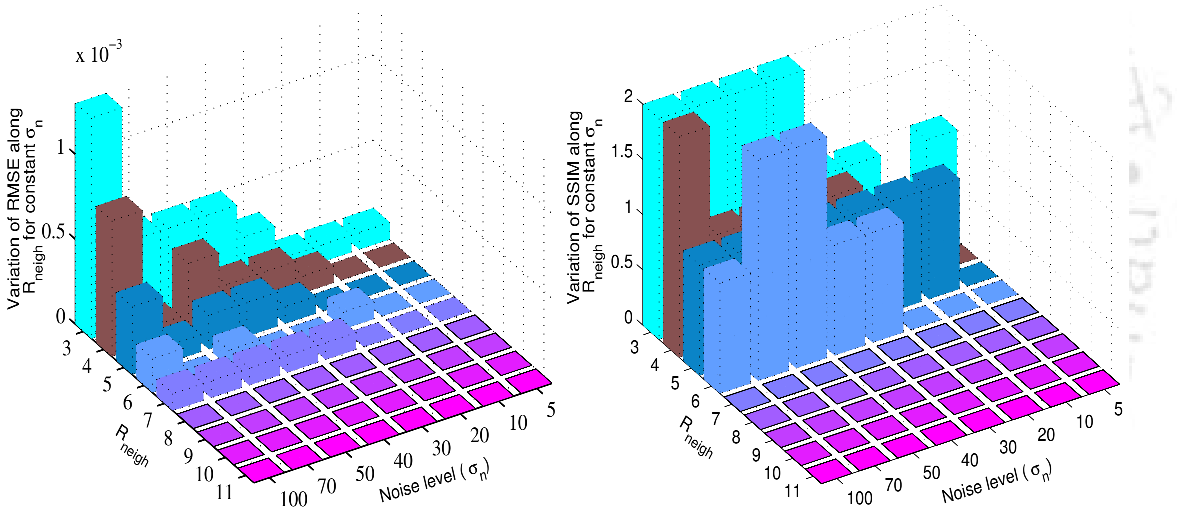

(a) (b)

Figure 6.1: Plot of variation in RMSE and SSIM for various combination of (R_{neigh}, σ_n) and $(\sigma_d = 5, \sigma_r = 2\sigma_n)$.

We can observe that the variation in R_{neigh} is not significant for lower σ_n. However, as σ_n increases, larger value of R_{neigh} is required in RMSE sense. As it is evident from Table-6.1, $R_{neigh} > 8$ is found optimal, beyond which there is no significant change in the RMSE value. It can also be verified from Fig. 6.1(a). This is because, the spatial weight w_S decreases for large R_{neigh}. In practice, the size of the window must be an odd number and hence, R_{neigh} must be 9. However, there is only negligible difference in the performance of RMSE, for the choice of $R_{neigh} = 7$ and 9. In the case of SSIM, there is no significant improvement for $R_{neigh} > 7$. Therefore, as a compromise between RMSE and computational complexity, $R_{neigh} = 7$ has been chosen.

6.4.1.2 Choice of σ_d and σ_r

The parameters (σ_d, σ_r) must be properly chosen to optimize the bilateral filter. σ_d and σ_r are the values at which the respective Gaussian weighting functions take their maximum derivatives, so they serve as rough thresholds for identifying pixels that are spatially and radiometrically close. σ_d characterizes the behavior of domain filter w_S and σ_r influences the behaviour of the range filter w_R. The optimal choice of σ_d and σ_r are evaluated by repeating the experiments for different combinations of $(\sigma_d\,,\, \sigma_r)$ for a constant σ_n. The RMSE and SSIM value for each combination is calculated. The combination of $(\sigma_d\,,\, \sigma_r)$ for which the RMSE is globally minimum (SSIM is high) under varying noise level σ_n is chosen.

Larger values of σ_d results in over-smoothing and decreases the RMSE. The experiments for various combination of (σ_d, σ_r) at different noise levels are conducted on real high SNR MR images and simulated MR images. The plots in Fig. 6.2 and 6.3 presents the results obtained for an T2 weighted axial MR image. The 2-D plot in Fig. 6.4 gives the average of RMSE and SSIM values estimated at different noise levels for the simulated T2 weighted MRI brain volume consisting of 142 image slices of thickness $1mm$.

From the plot in Fig. 6.2, we can infer that the optimal value of σ_d is 5. The choice of σ_r is directly proportional to the noise variance σ_n. If $\sigma_r < \sigma_n$, noise pixels remain unfiltered. When $\sigma_r \gg \sigma_n$, the data is over smoothened. The optimal value of σ_r is identified to lie between $(1.5\sigma_n - 2\sigma_n)$. The plot in Fig. 6.3, gives the RMSE and the SSIM values obtained at different noise levels for constant σ_d and varying σ_r.

Similarly from Fig. 6.4, we can conclude the range of σ_d and σ_r. It can be observed that, the minimum of RMSE and maximum of SSIM with respect to σ_r lies within the range $(0.9\sigma_n - 1.9\sigma_n)$ and $\sigma_d \geq 5$ respectively. However, as the noise level increase the optimal range of σ_r narrows around $1.5\sigma_n$ and $\sigma_d \geq 5$ remains optimal for all the considered noise level. Thus, the optimal values in reference to RMSE and SSIM are chosen as $\sigma_d = 5$ and $\sigma_r = 1.5\sigma_n$.

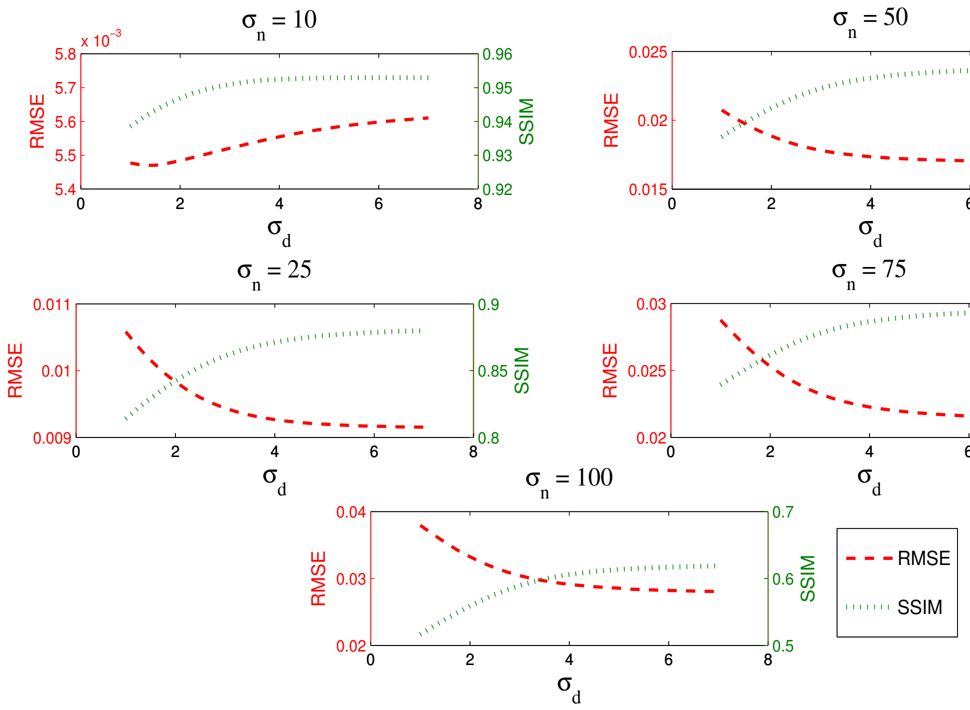

Figure 6.2: Plot of σ_d Vs. (RMSE, SSIM) for $\sigma_r = 1.5\sigma_n$ and $R_{neigh} = 7$.

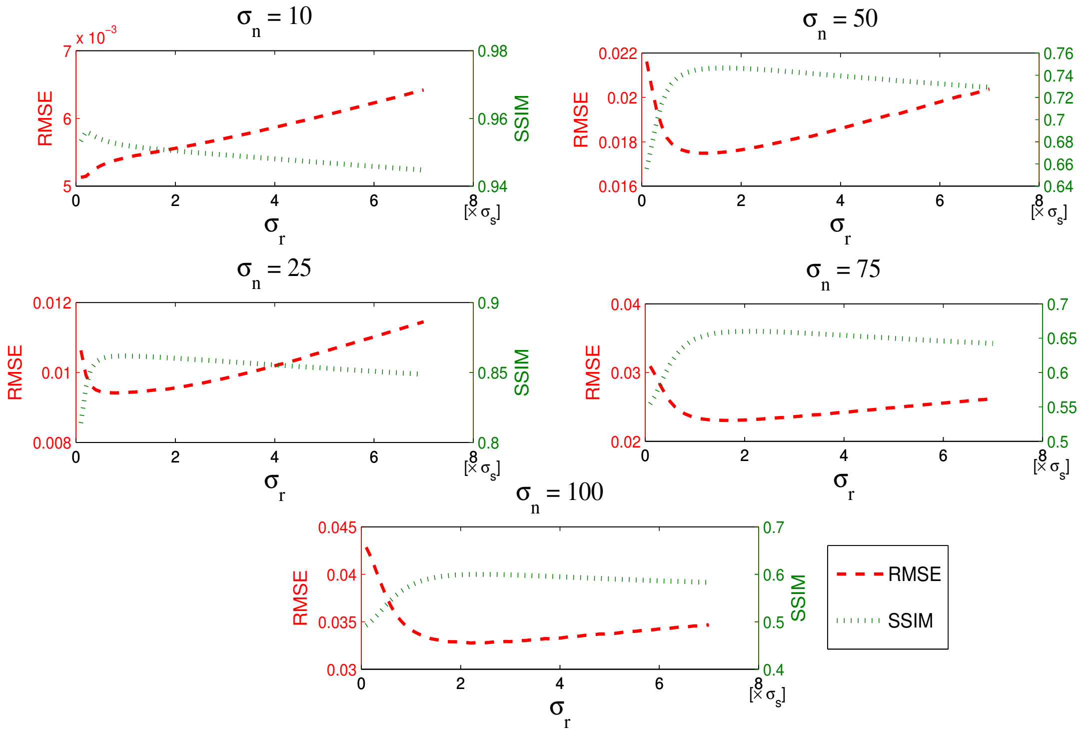

Figure 6.3: Plot of σ_r Vs. (RMSE, SSIM) for $\sigma_d = 5$ and $R_{neigh} = 7$. $\sigma_s = \sigma_n$ is the estimated noise variance.

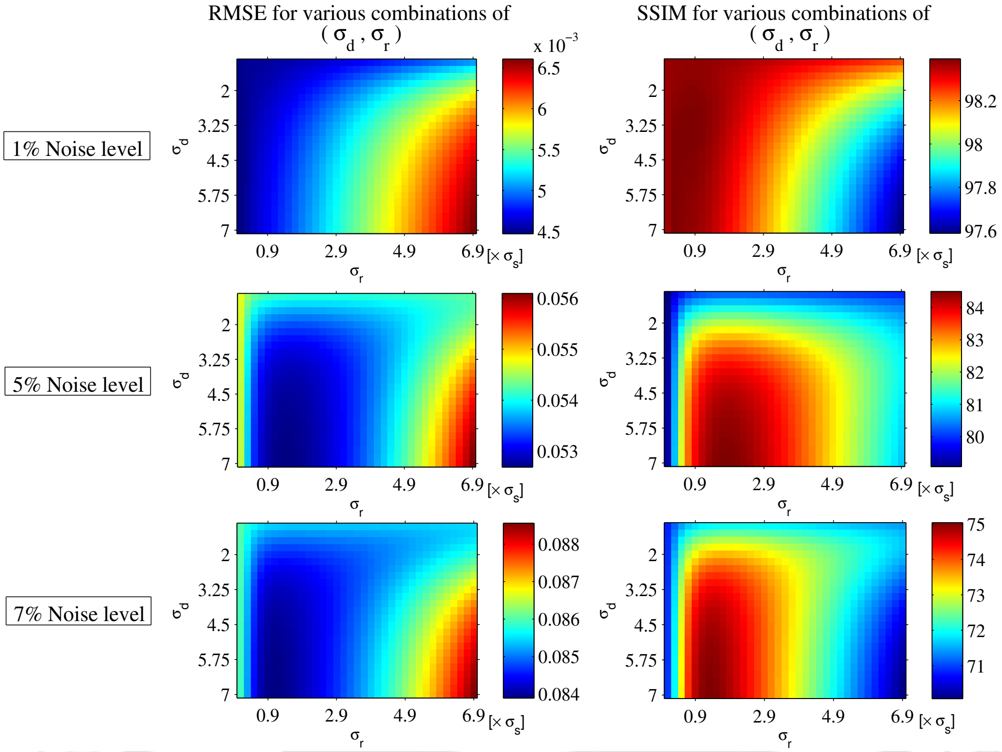

Figure 6.4: 2D plot of the average of RMSE and SSIM(%) values obtained using WD-BF for different combinations of (σ_d, σ_r). The experiments are carried on a simulated MR volume consisting of 142 images with slice thickness $1mm$. The results obtained at 1%, 5% and 7% of noise levels are displayed. σ_s denotes the estimated noise variance σ_n. The optimal range of RMSE and SSIM with respect to σ_r lies around $0.9\sigma_n$ to $1.9\sigma_n$ and for $\sigma_d \geq 5$ for all the noise levels.

6.4.2 Denoising results - A comparative validation

The performance of the denoising methods is evaluated using RMSE, SSIM, contrast and residual image. Additionally, in this chapter we introduce *Bhattacharrya coefficient* (BC) to measure the correlation between the noise-free and the denoised MR image.

(i) **Bhattacharrya coefficient (BC):**

It is a correlation measure for finding the statistical similarity between two data samples. The coefficient measures the closeness between two discrete probability distributions. In statistics, BC is a measure of the statistical separability of classes, giving an estimate of the probability of closeness. For the discrete probability distributions p and q over the same domain X, it is defined as [67, 140]

$$BC(p,q) = \sum_{x \in X} \sqrt{p(x)q(x)} \tag{6.11}$$

The range of the coefficient is $0 \leq BC \leq 1$. The value of BC closer to 1 indicates that the data samples corresponding to the distribution p and q are similar.

For an 2-D image, its histogram gives the probability of distribution of the intensity values. The correlation between two image histograms are estimated using the Bhattacharrya coefficient (BC). It implies that the BC value characterizes the similarity between the grey level distribution of the compared images. Also, spread of the histogram and the peaks in the histogram relates to the contrast of the image. Therefore, unlike RMSE and SSIM, the BC is a global measure computing the intensity similarity.

6.4.2.1 Evaluation on simulated dataset

A detailed evaluation of the denoising techniques is done by including MR images with different structural characteristics. From the results, we observed that the Pizurica's wavelet denoising method is efficient for high structural MR images. But in the case of MR image with more smooth regions, the method does not completely remove the noise in the very high intensity regions. Hence, it demands high threshold values for which the significant signal details are also removed. Alternately, the WD-BF approach based on VisuShrink performed well for MR images with large smooth regions. For the MR data containing more details or the structural variations, the method yields over-smoothened images.

The UNLM algorithm proved efficient for MR images with varying structural characteristics. However WD-BF approach with NeighShrink yields comparatively better results. The performance of UNLM decreases particularly at higher noise levels. This is because; as the noise value increase, the level of smoothing in UNLM should also increase for ensuring noise removal. But, the smoothing parameter in UNLM is not pixel adaptive and as a result it also removes the signal components. Conversely, the WD-BF method based on NeighShrink performed well for all the considered MR images and the denoising efficiency is comparatively high, as the noise level increase.

The denoising results of a simulated T1 weighted axial MR image corrupted by 5% of noise level is shown in Fig. 6.5. The values of the quality metrics corresponding to this image is given in Table-6.2. In order to ensure a comprehensive analysis, the results obtained for different noise noise levels are shown in Fig. 6.6. This T1 weighted MR image does not consist of large structural variations and for this considerably low noise level, the denoising methods preserves the significant details of the image. However, from the residual images the excessive smoothing along the edges introduced in the WD-BF (VisuShrink) approach is clearly evident. However, it does not lead to loss in details and the value of

SSIM suggest that WD-BF (VisuShrink) restored the structural details. In the Pizurica's method some of the strong noisy coefficients belonging to the high intensity regions are passed without thresholding. Though not prevalent in the denoised image, such coefficients will introduce some unwanted *blips* like artifacts in the reconstructed image. UNLM and WD-BF (NeighShrink) methods result in efficient denoising. Though, UNLM efficiently perform smoothing along the edges, the smooth regions appear over-smoothened and it also results in loss of small structural details. For these reason, WD-BF approach has yielded better SSIM than the other techniques. The advantages of NeighShrink method over the VisuShrink approach can be directly inferred from the denoising results. As we refer the BC and the contrast plots in Fig. 6.6, it is evident that WD-BF approaches are efficient in restoring the intensity distributions and thus, the contrast if the denoised image.

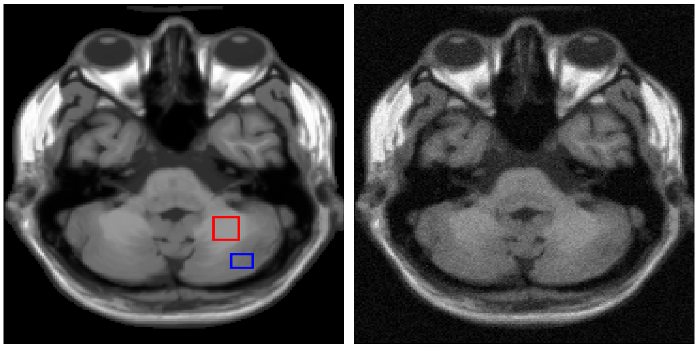

(a) Original image (b) Noisy image

DENOISED IMAGES

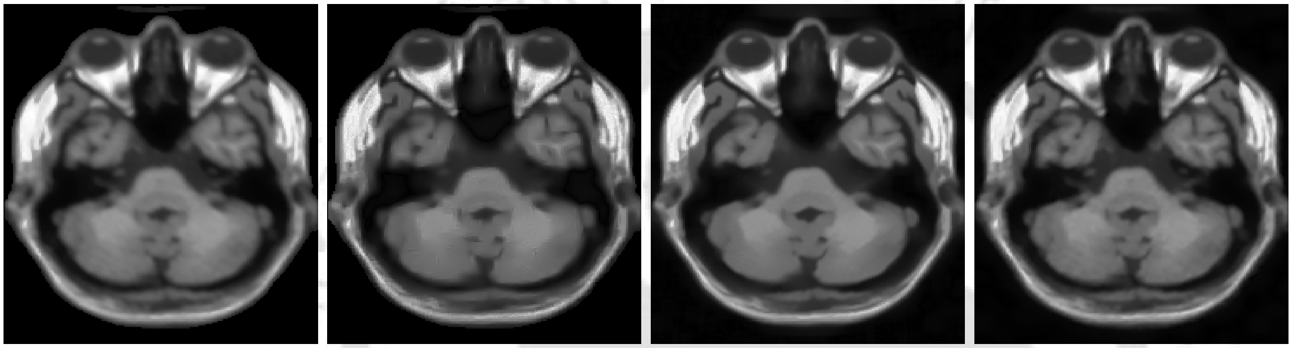

(c) WD-BF (VisuShrink) (d) Pizurica's method (e) UNLM (f) WD-BF (NeighShrink)

RESIDUAL IMAGES

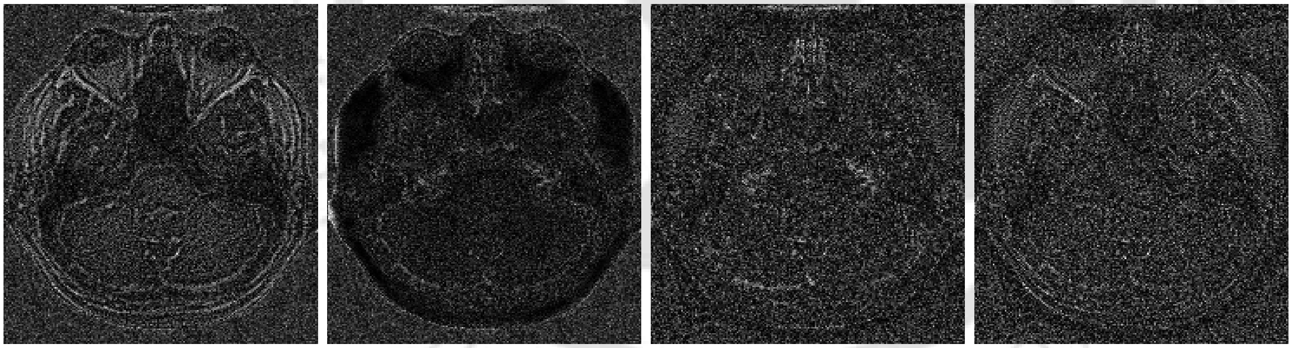

(g) WD-BF (VisuShrink) (h) Pizurica's method (i) UNLM (j) WD-BF (NeighShrink)

Figure 6.5: Denoising results of simulated T1 weighted axial image corrupted by 5% noise level. The region within the boxes represent the low intensity ROI and the high intensity ROI chosen for calculating the contrast. The computed value of contrast in the original image is 0.1608.

Table 6.2: Comparison of the denoising results based on the similarity metrics computed between the original and the denoised T1 weighted axial simulated data. The simulated noisy image contains 5% of noise.

	WD-BF (VisuShrink)	Pizurica's method	UNLM	WD-BF (NeighShrink)
RMSE	0.0253	0.0317	0.0233	0.0202
SSIM	0.9311	0.9218	0.9311	0.9517
BC	0.9810	0.9589	0.9655	0.9638
Contrast	0.1599	0.1601	0.1597	0.1603

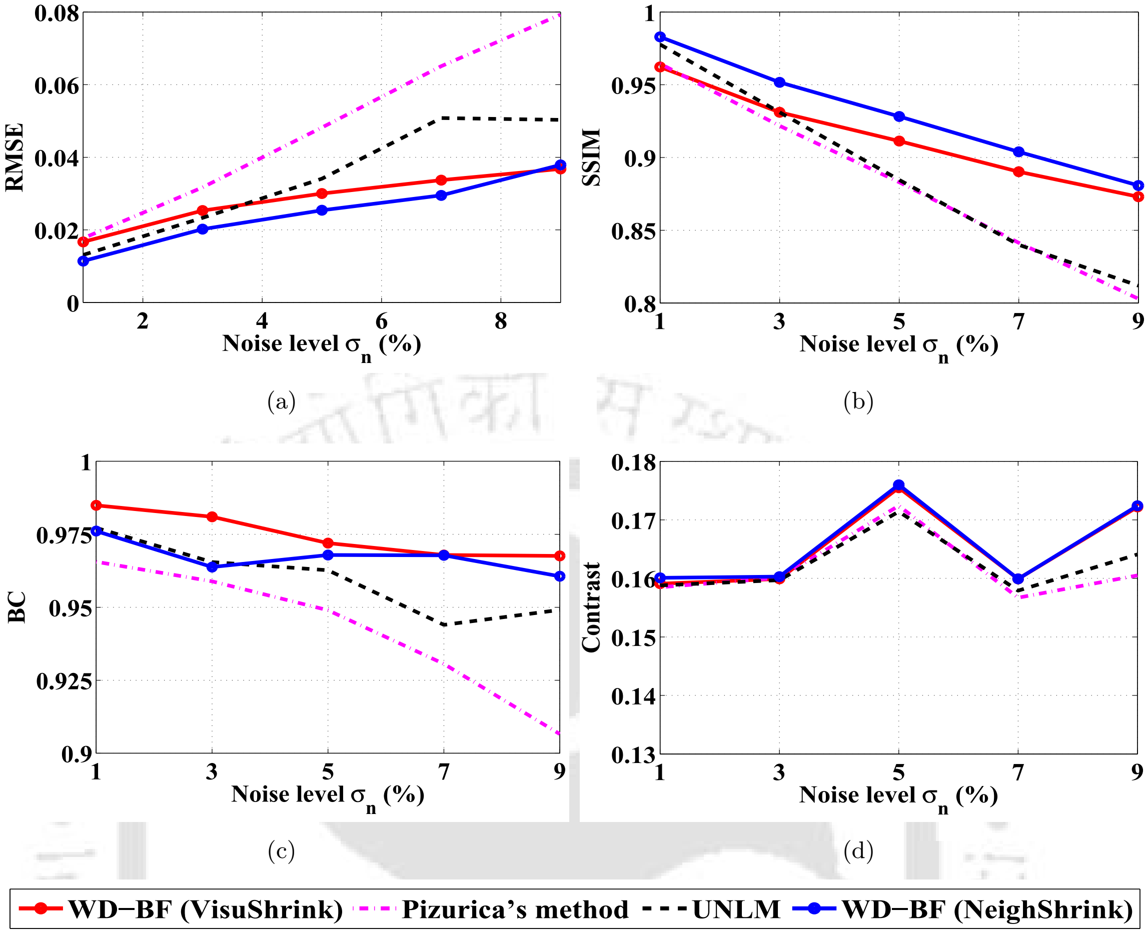

(a) (b) (c) (d)

Figure 6.6: Comparative plot of denoising results obtained for the simulated T1 weighted axial MR image at varying noise levels. (a) RMSE versus the noise level σ_n (b) SSIM versus the noise level σ_n (c) BC value versus the noise level σ_n (d) Contrast versus the noise level σ_n. Original contrast = 0.1608.

The denoising results of a simulated T2 weighted axial MR image corrupted by 5% of noise level is shown in Fig. 6.7. Except for the weighting, the axial section considered here is the same as in Fig. 6.6. The values of the quality metrics corresponding to this image is given in Table-6.3. A detailed analysis can be made from the results obtained for different noise noise levels and are shown in Fig. 6.8. This T2 weighted MR image consists of comparatively more structural variations. Hence, the degradation in the visual quality of the denoised images obtained using WD-BF (VisuShrink) is more prevalent and the results suggests that this approach performs poor even for low noise levels. The UNLM performs better conveying the significance of the technique in edge preservation. The residual images show that smoothing along edges in WD-BF (NeighShrink) is neither controlled as in UNLM nor excessive as in WD-BF (VisuShrink). The extent of smoothing is balanced and hence, the performance of WD-BF (NeighShrink) in terms of the quality metrics is better than UNLM.

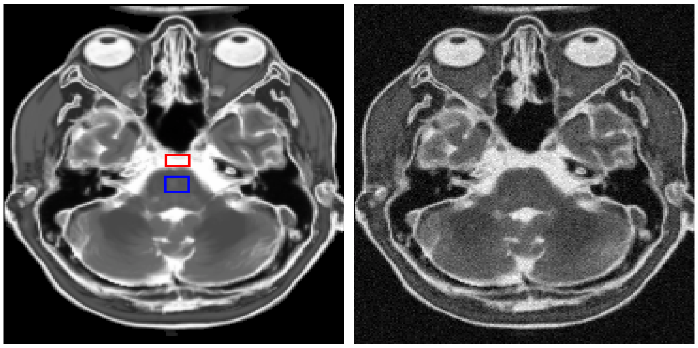

(a) Original image (b) Noisy image

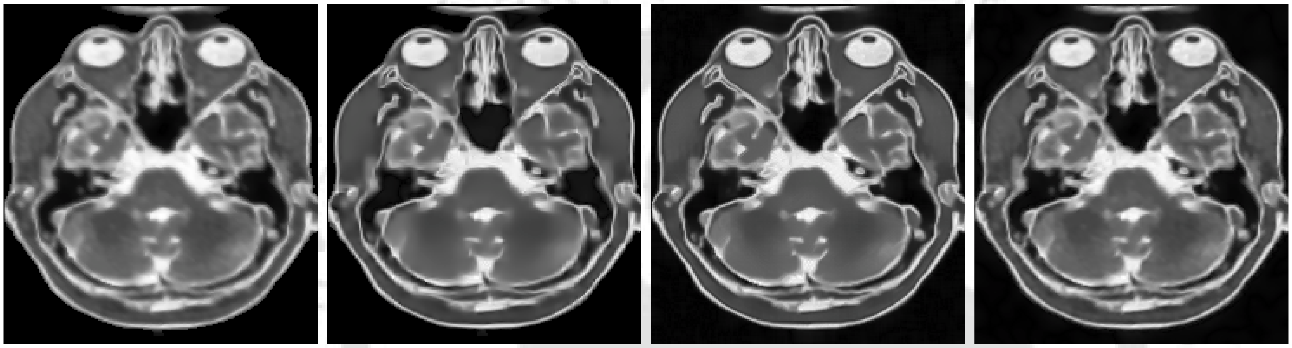

DENOISED IMAGES

(c) WD-BF (VisuShrink) (d) Pizurica's method (e) UNLM (f) WD-BF (NeighShrink)

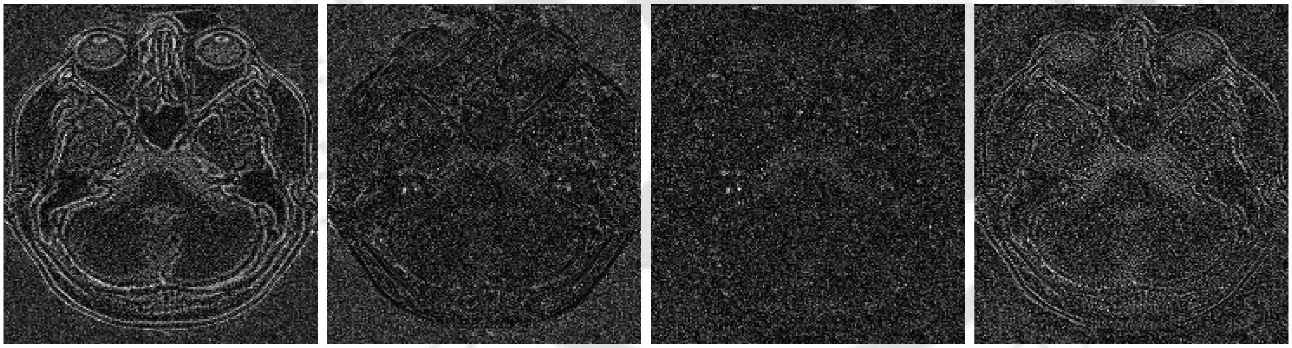

RESIDUAL IMAGES

(g) WD-BF (VisuShrink) (h) Pizurica's method (i) UNLM (j) WD-BF (NeighShrink)

Figure 6.7: Denoising results of simulated T2 weighted axial MR image corrupted by 5% noise level. The region within the boxes represent the low intensity ROI and the high intensity ROI chosen for calculating the contrast. The original contrast measured is 0.4803.

Table 6.3: Comparison of the denoising techniques based on the similarity metrics computed between the original and denoised T2 weighted axial simulated MR image. The simulated noisy image contains 5% of noise.

	WD-BF (VisuShrink)	Pizurica's method	UNLM	WD-BF (NeighShrink)
RMSE	0.0588	0.0479	0.0417	0.0398
SSIM	0.8636	0.8956	0.9242	0.9278
BC	0.9716	0.9655	0.9738	0.9761
Contrast	0.4804	0.4581	0.4815	0.4819

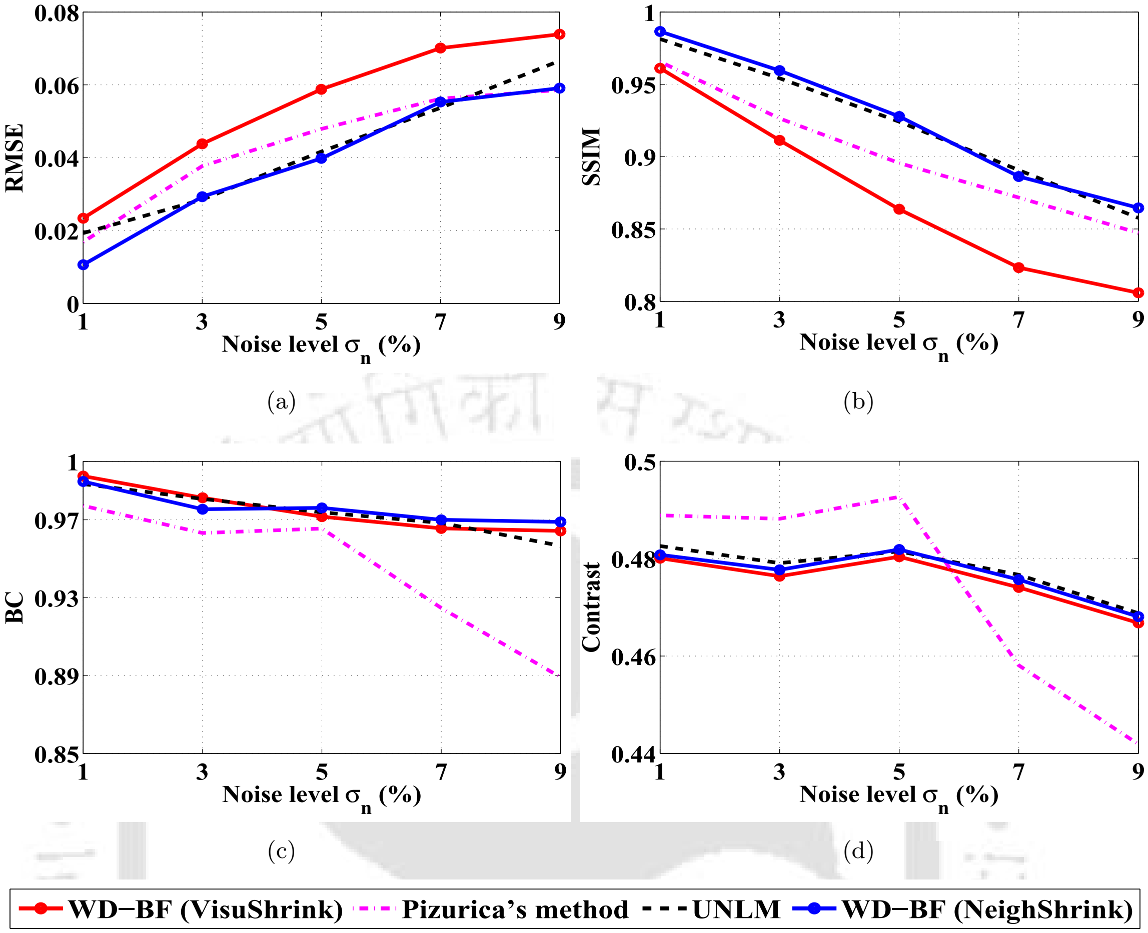

(a) (b)

(c) (d)

Figure 6.8: Comparative plot of denoising results obtained for the simulated T2 weighted axial MR image at varying noise levels. (a) RMSE versus the noise level σ_n (b) SSIM versus the noise level σ_n (c) BC value versus the noise level σ_n (d) Contrast versus the noise level σ_n. Original contrast = 0.4803

The plots in Fig. 6.8 show that for varying noise levels, the performance of WD-BF (NeighShrink) and UNLM are better than other considered methods. The BC value and the contrast of the denoised image obtained using Pizurica's method is comparatively inadequate. The denoising results of a simulated T1 weighted axial MR image corrupted by 7% of noise level is shown in Fig. 6.9. The considered image is pathological data containing severe multiple sclerosis (MS) lesions. The MS lesions are considered as a white matter disease and its imaging characteristics are similar to the characteristics of white matter. This data does consists of structural variations that are of diagnostic importance. Hence, from the results obtained on this image it is possible to review the advantage of these denoising methods in preserving the clinically significant information.

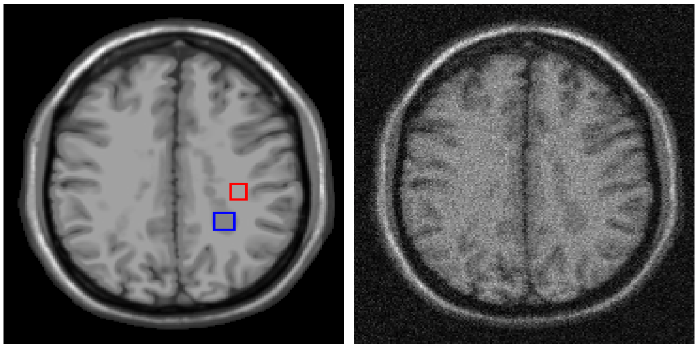

(a) Original image (b) Noisy image

DENOISED IMAGES

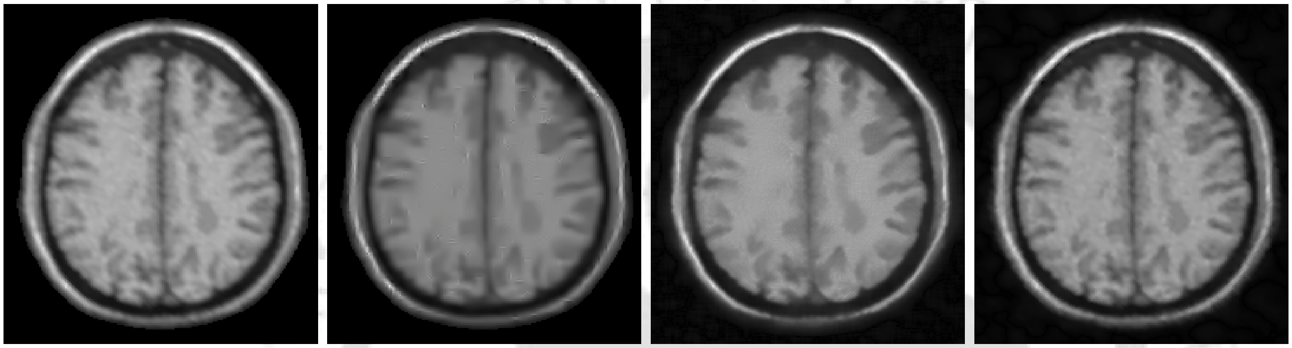

(c) WD-BF (VisuShrink) (d) Pizurica's method (e) UNLM (f) WD-BF (NeighShrink)

RESIDUAL IMAGES

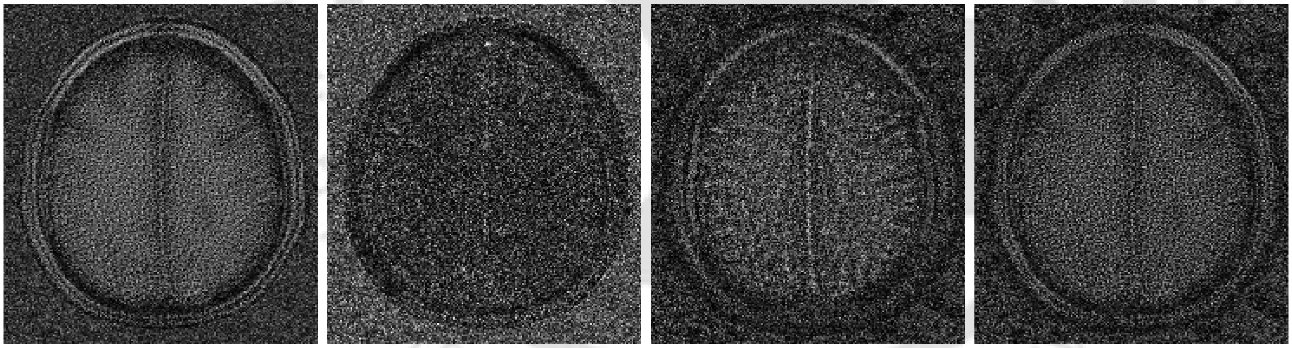

(g) WD-BF (VisuShrink) (h) Pizurica's method (i) UNLM (j) WD-BF (NeighShrink)

Figure 6.9: Denoising results of simulated T1 weighted axial MR image with severe MS lesions corrupted by 7% of noise level. The region within the boxes represent the low intensity ROI and the high intensity ROI chosen for calculating the contrast. The measured value of contrast is 0.0980.

Table 6.4: Comparison of the denoising techniques based on the similarity metrics computed between the original and denoised T1 weighted axial MR image with severe MS lesions. The simulated noisy image contains 7% of noise.

	WD-BF (VisuShrink)	Pizurica's method	UNLM	WD-BF (NeighShrink)
RMSE	0.0424	0.0551	0.0339	0.0268
SSIM	0.9168	0.8787	0.8932	0.9283
BC	0.9249	0.8249	0.8985	0.9367
Contrast	0.0899	0.0781	0.0876	0.0908

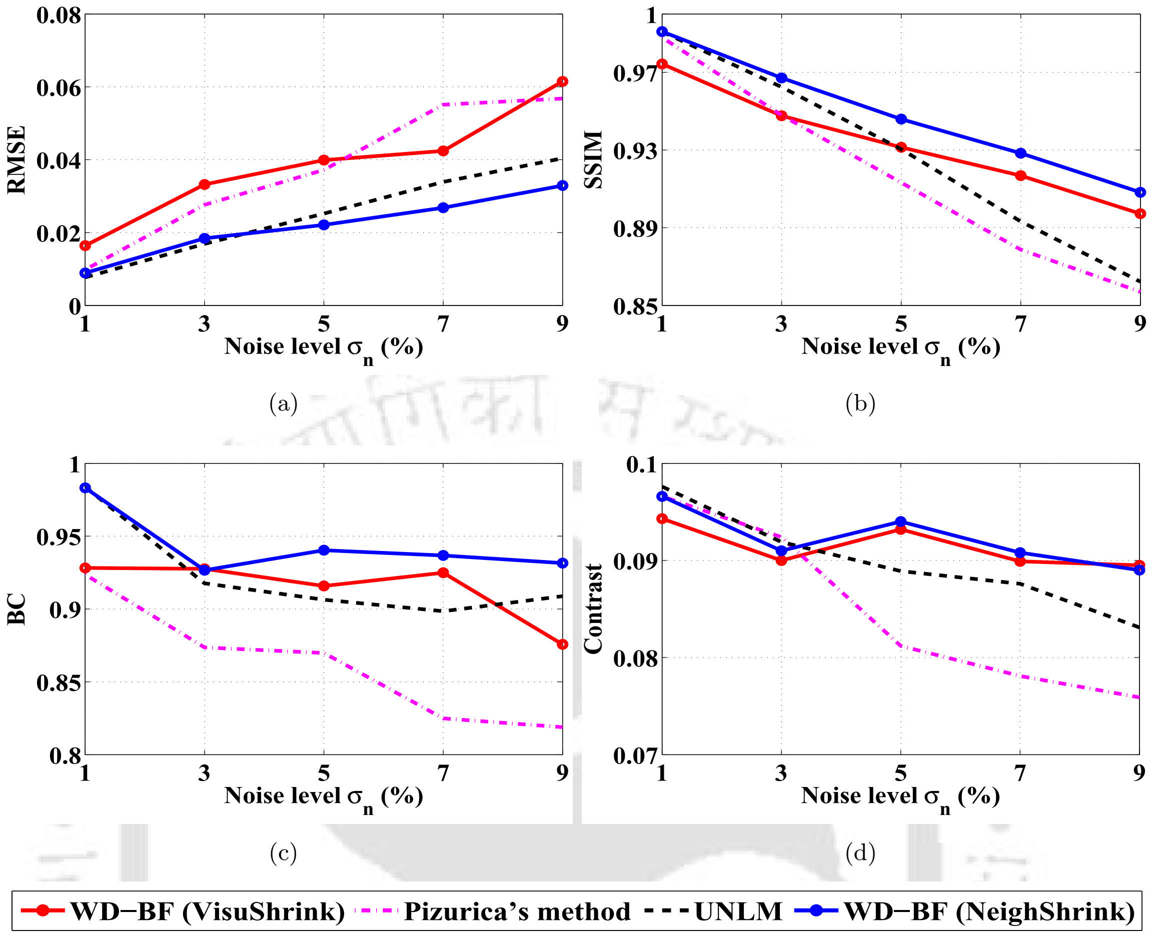

(a) (b) (c) (d)

Figure 6.10: Comparative plot of denoising results obtained for the simulated T1 weighted axial MR image with severe MS lesions at varying noise levels. (a) RMSE versus the noise level σ_n (b) SSIM versus the noise level σ_n (c) BC value versus the noise level σ_n (d) Contrast versus the noise level σ_n. Original contrast = 0.0980.

The values of the quality metrics corresponding to this image are given in Table-6.4. The results obtained for different noise noise levels are shown in Fig. 6.10. At lower noise levels, the UNLM approach is better than the WD-BF (VisuShrink) method. As the noise level increase, UNLM results in more smoothing of the structural features and also, the contrast is not restored. The blip-like artifacts in the Pizurica's method can be observed from the denoised image in Fig. 6.9(d) .

As we refer the BC and the contrast plots in Fig. 6.10, it is evident that WD-BF approaches are efficient in restoring the intensity distributions and thus, the contrast of the denoised image. Thus, these results prove the reliability of WD-BF (NeighShrink) for feature preserved MR image denoising.

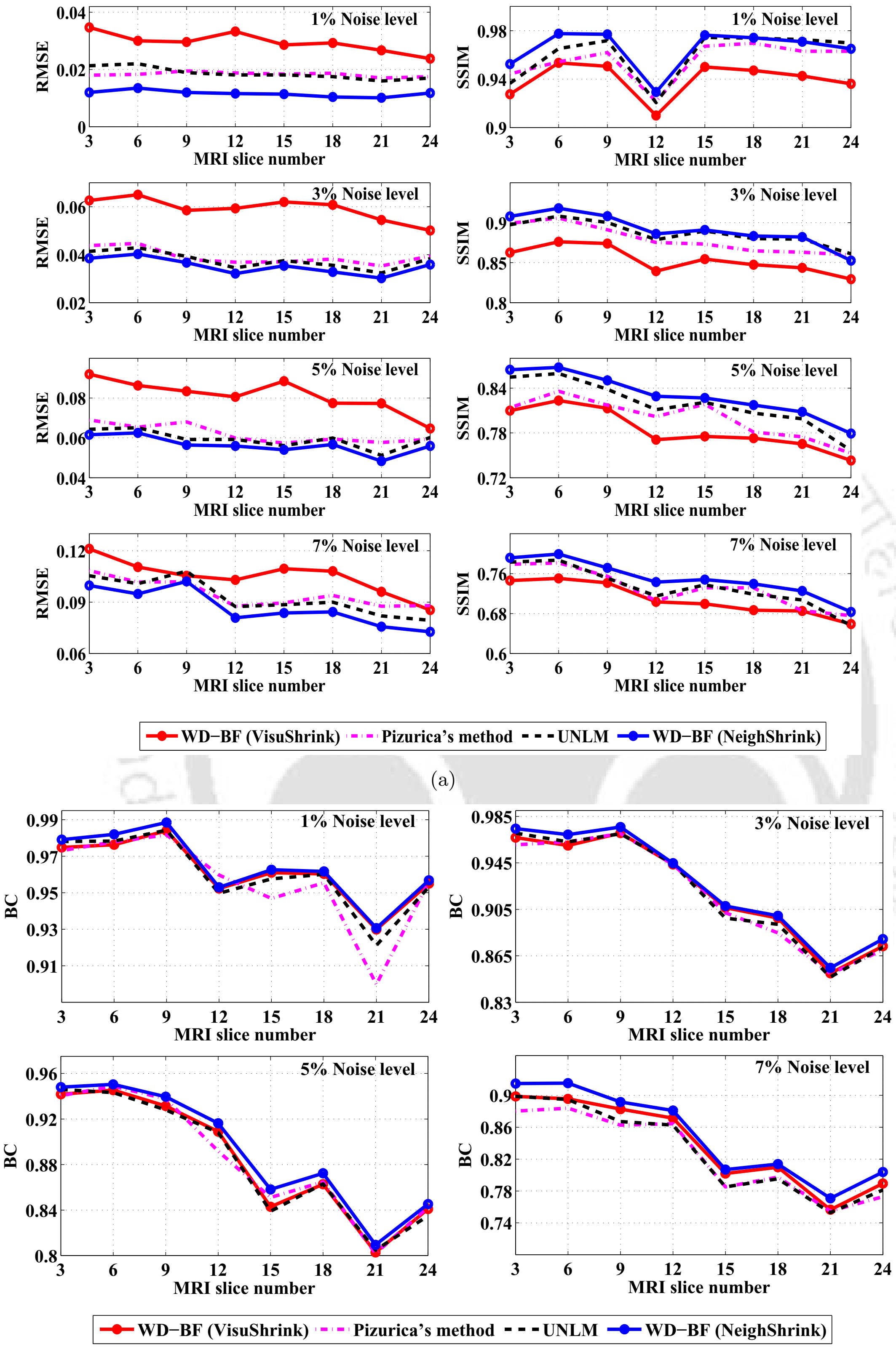

(a)

(b)

Figure 6.11: Results of experiments performed on a sequence of MR images collected from an simulated T2 weighted axial MR volume of slice thickness 1mm. (a) Plot of RMSE and SSIM values obtained at 1%, 3%, 5% and 7% of noise level. (b) Plot of BC values, that represents the statistical correlation between the denoised and the original image.

The performance was also evaluated for the entire sequence of an MRI scan (at specific intervals) in order to take into account the influence of structural variations on the efficiency of denoising methods. The results obtained for denoising MRI slices $(3 - 24)$ interleaved at interval of 3, for four different noise levels are shown in Fig. 6.11. It can be noted that, the performance of WD-BF with VisuShrink is inferior to NeighShrink and UNLM with respect to RMSE and SSIM. The performance of WD-BF with NeighShrink and UNLM in terms of SSIM and BC values are significantly close for low noise levels and at higher noise levels, the performance of WD-BF with Neighshrink is notably better than UNLM. The considered images have large structural details and hence, Pizurica's denoising method is better than WD-BF (VisuShrink). The RMSE plot shows that the prediction error is minimum for WD-BF with NeighShrink and hence, the image characteristics are well preserved. However, in terms of the BC value, WD-BF approaches show improved performance.

6.4.2.2 Evaluation on clinical dataset

Similar to the simulated images, the clinical dataset also includes images with different structural characteristics and pathological importance.

The experiments are include a clinical T1 weighted axial MR image with very low structural features. The denoising results for 5% noise level are shown in Fig. 6.12 and the corresponding values of quality metrics are listed in Table-6.5. The plot in Fig. 6.13 gives the denoising results at different noise levels obtained for this clinical T1 weighted image. Due to the image characteristics, the SSIM values for WD-BF (VisuShrink) is superior to Pizurica's method and UNLM. However, the difference in RMSE values sufficiently characterize the extent of smoothing in the denoising methods. Accordingly, WD-BF with NeighShrink thresholding is superior with respect to RMSE, SSIM and also has the higher BC value and the contrast value representing the similarity between the denoised and the original image. The plots in Fig. 6.13 explain the proficiency of WD-BF (NeighShrink) denoising approach.

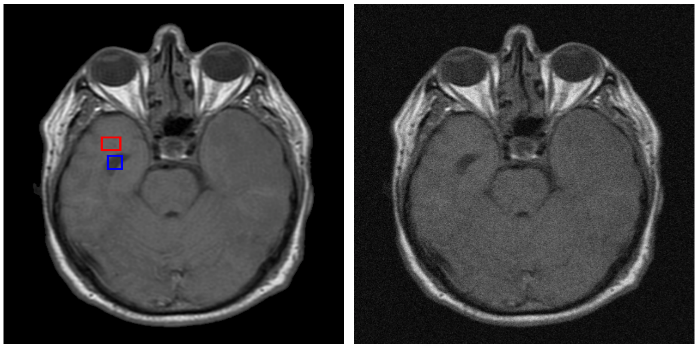

(a) Original image (b) Noisy image

DENOISED IMAGES

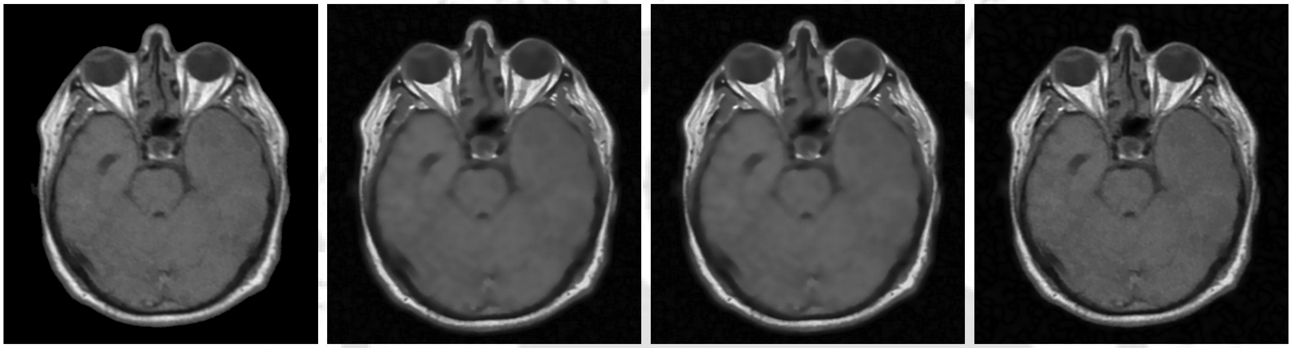

(c) WD-BF (VisuShrink) (d) Pizurica's method (e) UNLM (f) WD-BF (NeighShrink)

RESIDUAL IMAGES

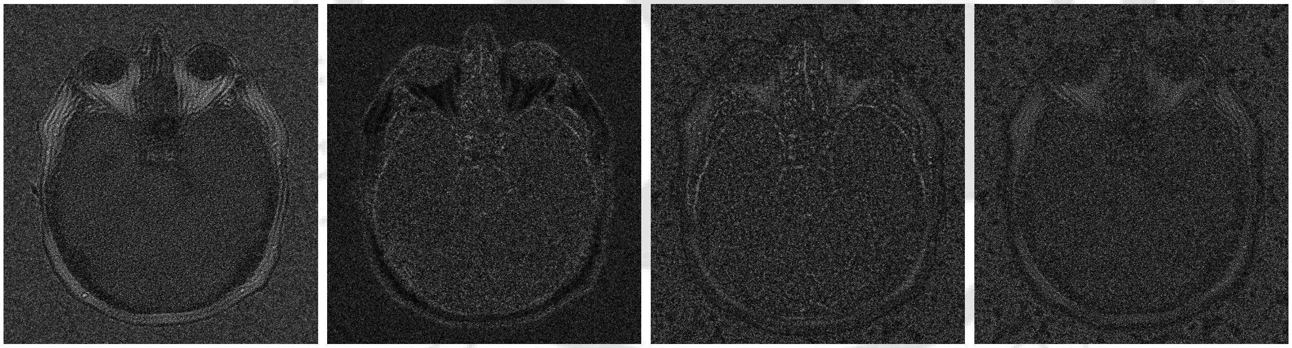

(g) WD-BF (VisuShrink) (h) Pizurica's method (i) UNLM (j) WD-BF (NeighShrink)

Figure 6.12: Denoising results of clinical T1 weighted axial image corrupted by 5% noise level. The region within the boxes represent the low intensity ROI and the high intensity ROI chosen for calculating the contrast. The measured value of contrast in the original image is 0.2677.

Table 6.5: Comparison of the denoising techniques based on the similarity metrics computed between the original and denoised T1 weighted axial MR image. The clinical noisy image contains 5% of noise.

	WD-BF (VisuShrink)	Pizurica's method	UNLM	WD-BF (NeighShrink)
RMSE	0.0245	0.0212	0.0162	0.0128
SSIM	0.9675	0.9567	0.9567	0.9726
BC	0.9467	0.8943	0.9910	0.9942
Contrast	0.2528	0.2300	0.2399	0.2541

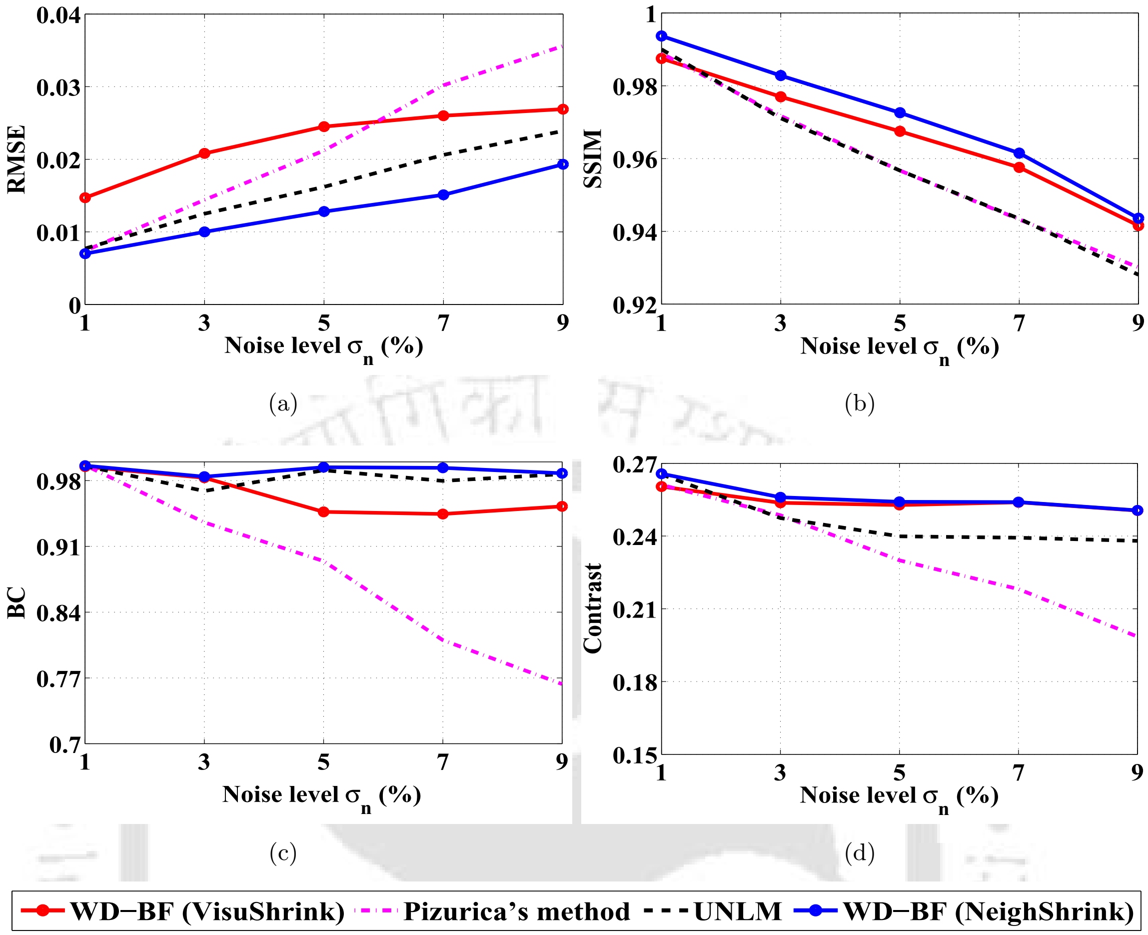

(a) (b)

(c) (d)

Figure 6.13: Comparative plot of denoising results obtained for the clinical T1 weighted axial MR image at varying noise levels. (a) RMSE versus the noise level σ_n (b) SSIM versus the noise level σ_n (c) BC value versus the noise level σ_n (d) Contrast versus the noise level σ_n. Original contrast = 0.2677.

The results obtained for a clinical T2 weighted axial brain image corrupted by 5% noise level are shown in Fig. 6.14. The image contains severe tumor pathology and hence, it shows large structural variations and the structural details in this MR image has large spatial support. As a result, the WD-BF (VisuShrink) does not yield over-smoothened results as in the case of Fig. 6.7. The corresponding values of quality metrics are listed in Table-6.6. The plots in Fig. 6.15 give the denoising results at different noise levels obtained for this clinical T2 weighted image. At low noise levels, the performance of Pizurica's method and the UNLM is better than WD-BF (VisuShrink). From the plots in Fig. 6.15, we can observe that the performances of the Pizurica's and the UNLM methods are comparatively less than the WD-BF approaches. Particularly, in the Pizurica's approach, the noisy coefficients corresponding to the high intensity regions are retained as the signal components.

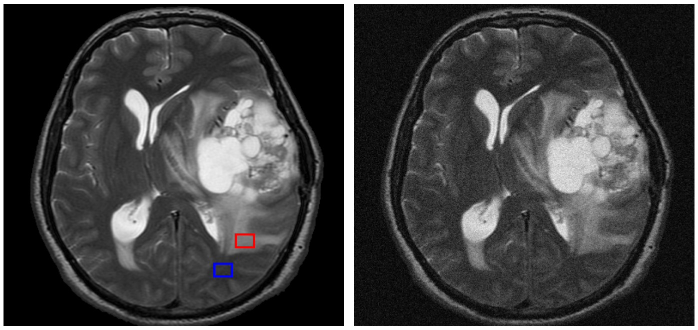

(a) Original image (b) Noisy image

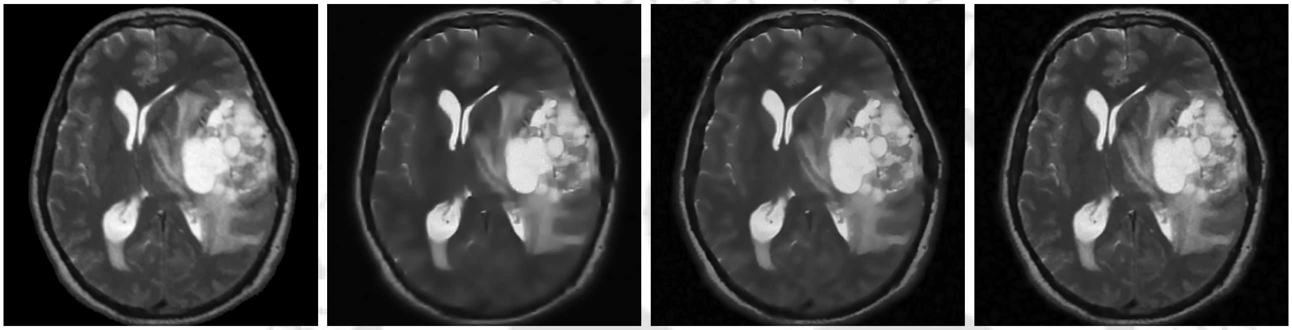

DENOISED IMAGES

(c) WD-BF (VisuShrink) (d) Pizurica's method (e) UNLM (f) WD-BF (NeighShrink)

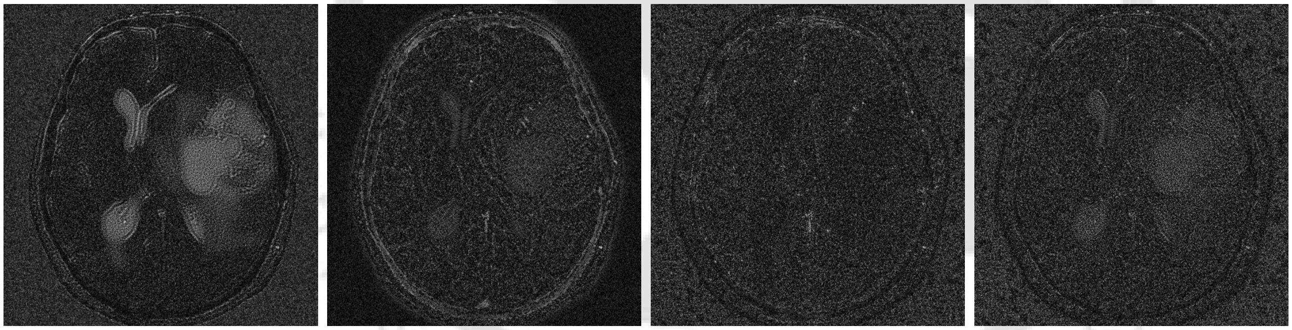

RESIDUAL IMAGES

(g) WD-BF (VisuShrink) (h) Pizurica's method (i) UNLM (j) WD-BF (NeighShrink)

Figure 6.14: Denoising results of clinical T2 weighted axial data containing severe pathology corrupted by 5% noise level. The pathological information corresponds to the area containing high intensity masses. The region within the boxes represent the low intensity ROI and the high intensity ROI chosen for calculating the contrast. The computed contrast value is 0.1957.

Table 6.6: Comparison of the denoising techniques based on the similarity metrics computed between the original and denoised T2 weighted axial MR image with severe pathology. The clinical noisy image contains 5% of noise.

	WD-BF (VisuShrink)	Pizurica's method	UNLM	WD-BF (NeighShrink)
RMSE	0.0253	0.0296	0.0254	0.0177
SSIM	0.9383	0.9049	0.9242	0.9471
BC	0.9702	0.9516	0.9515	0.9738
Contrast	0.2056	0.1939	0.2080	0.2053

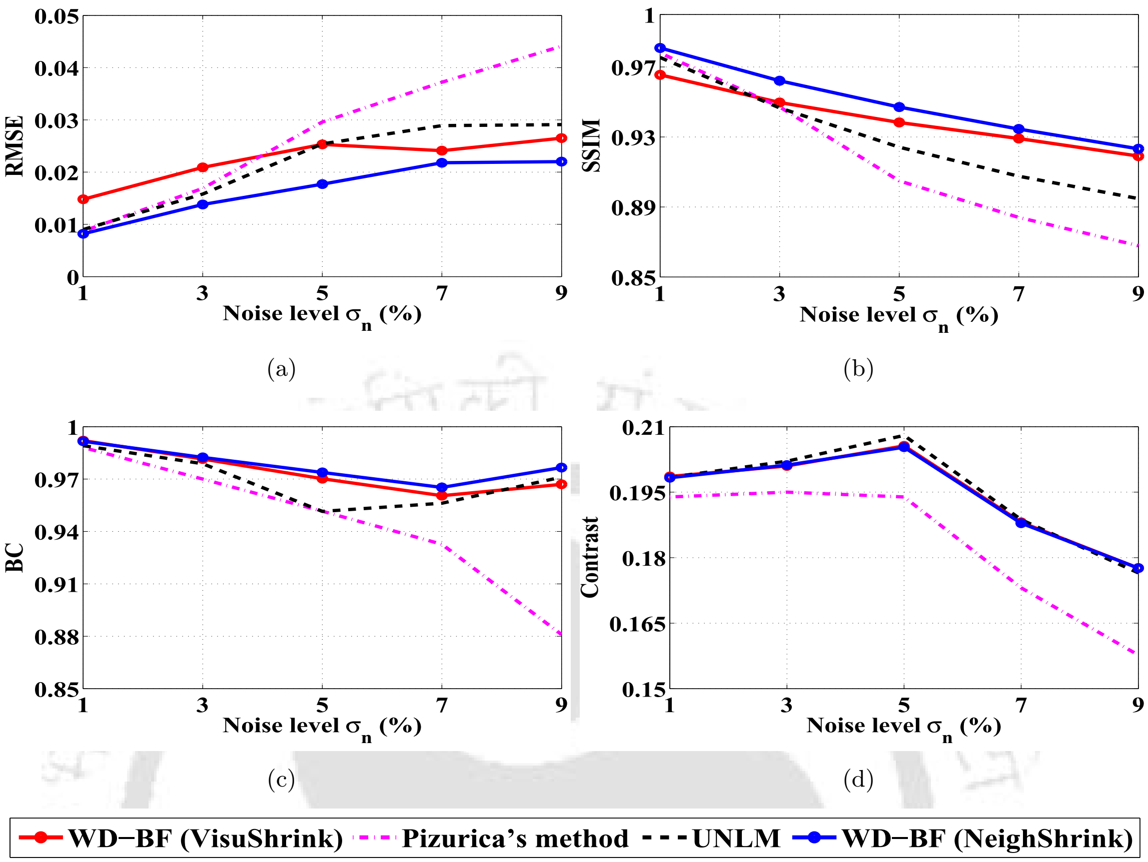

(a) (b)

(c) (d)

Figure 6.15: Comparative plot of denoising results obtained for the clinical T2 weighted axial MR image with severe pathology at varying noise levels. (a) RMSE versus the noise level σ_n (b) SSIM versus the noise level σ_n (c) BC value versus the noise level σ_n (d) Contrast versus the noise level σ_n. Original contrast = 0.1957.

The results obtained for an another clinical T2 weighted axial brain image corrupted by 7% noise level are shown in Fig. 6.16. The image contains large structural variations and the structural details in this MR image has less spatial support. Hence, the WD-BF (VisuShrink) yields over-smoothened results. The corresponding values of quality metrics are listed in Table-6.7. The plots in Fig. 6.17 gives the denoising results at different noise levels. As expected, the UNLM approach performs better than the WD-BF (VisuShrink) technique. But, in comparison with the WD-BF (NeighShrink) method, it is clearly evident that most of the structural information contained in the images are completely lost in UNLM approach. In Pizurica's method, despite the excess smoothing of the structural details significant number of noisy coefficients in the high intensity areas are not completely smoothened. Also, it is evident that the contour between the inter tissue regions are completely smoothened in the UNLM and Pizurica's approach. Instead, these significant details are preserved in the WD-BF methods.

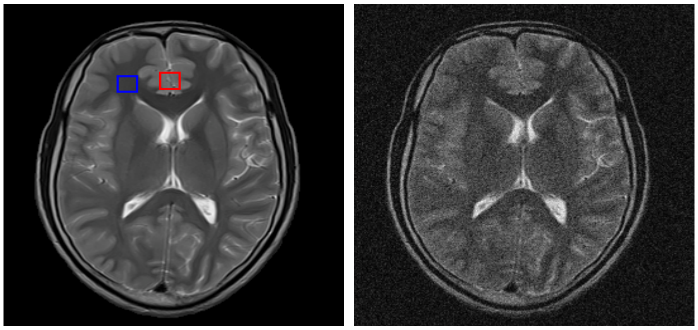

(a) Original image (b) Noisy image

DENOISED IMAGES

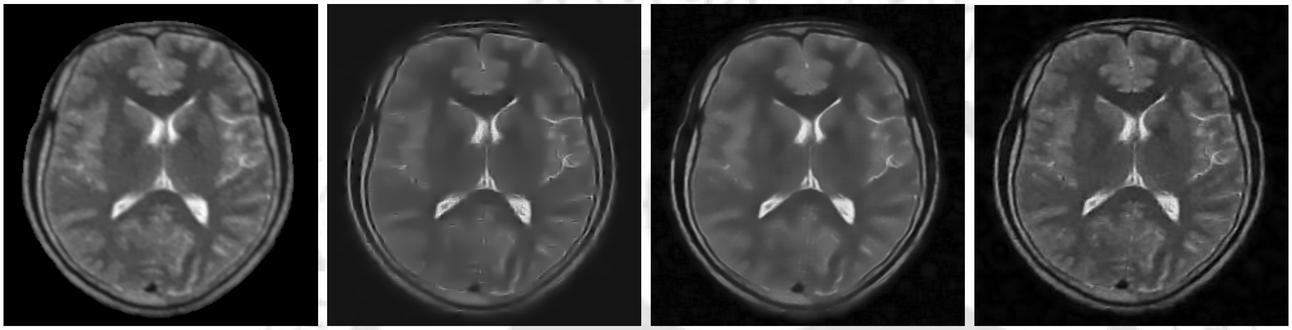

(c) WD-BF (VisuShrink) (d) Pizurica's method (e) UNLM (f) WD-BF (NeighShrink)

RESIDUAL IMAGES

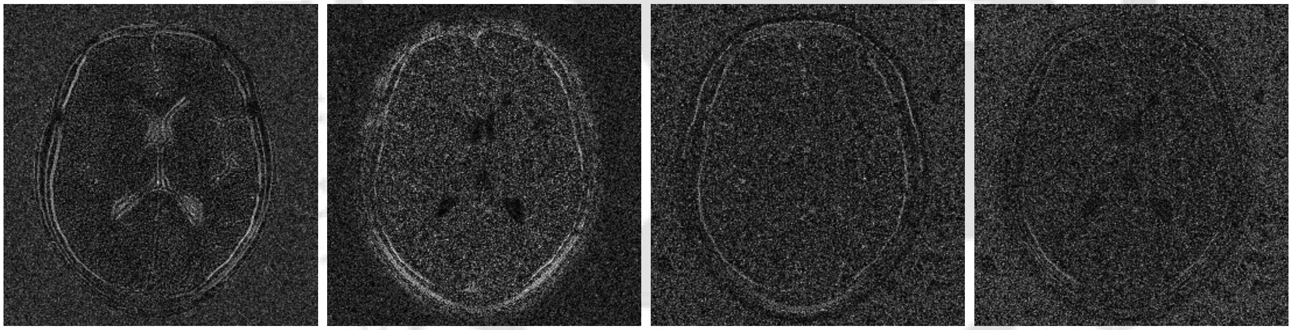

(g) WD-BF (VisuShrink) (h) Pizurica's method (i) UNLM (j) WD-BF (NeighShrink)

Figure 6.16: Denoising results of clinical T2 weighted axial MRI corrupted by 7% noise level. The region within the boxes represent the low intensity ROI and the high intensity ROI chosen for calculating the contrast. Measured contrast value is 0.2964.

Table 6.7: Comparison of the denoising techniques based on the similarity metrics computed between the original and denoised T2 weighted axial MR image. The clinical noisy image contains 7% of noise.

	WD-BF (VisuShrink)	Pizurica's method	UNLM	WD-BF (NeighShrink)
RMSE	0.0506	0.0436	0.0368	0.0316
SSIM	0.8848	0.8768	0.8917	0.9199
BC	0.9740	0.9358	0.9511	0.9665
Contrast	0.2911	0.2547	0.2839	0.2922

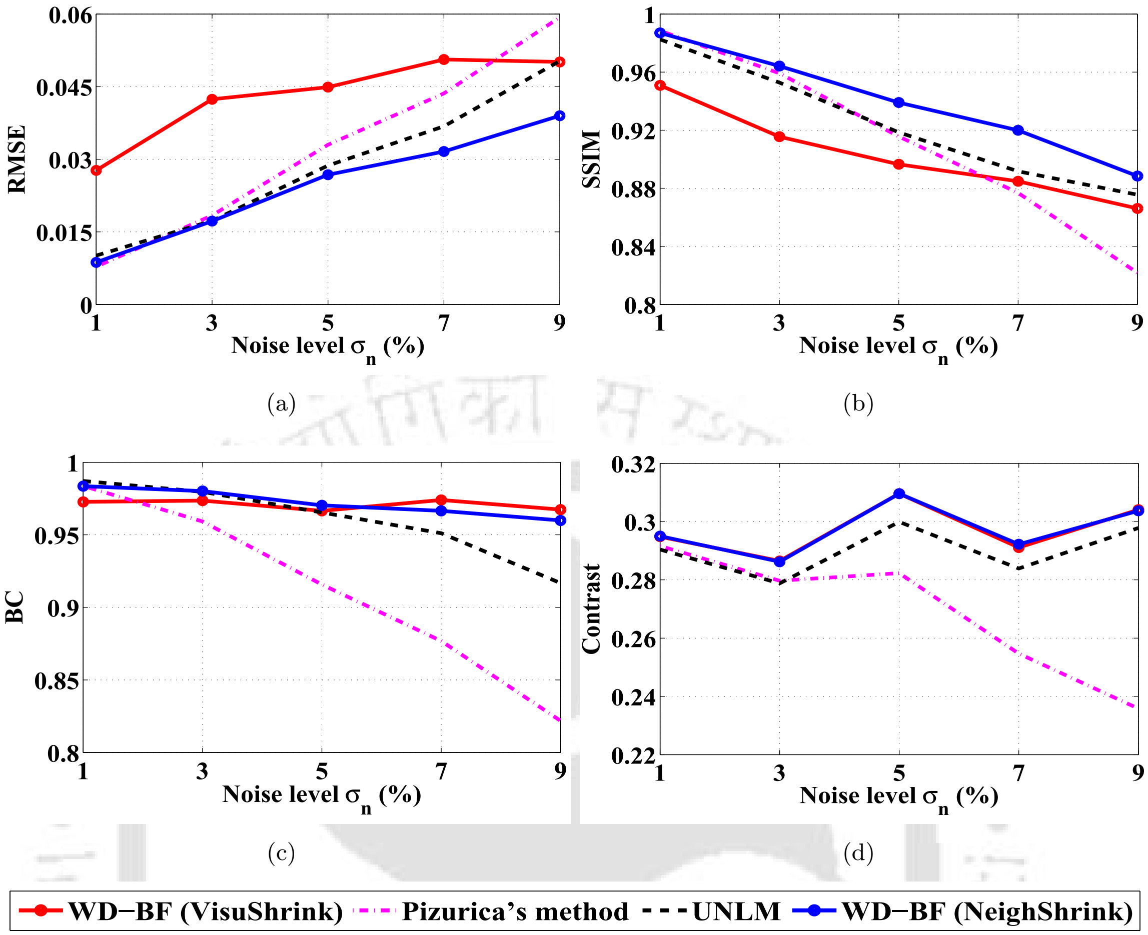

Figure 6.17: Comparative plot of denoising results obtained for the clinical T2 weighted axial MR image at varying noise levels. (a) RMSE versus the noise level σ_n (b) SSIM versus the noise level σ_n (c) BC value versus the noise level σ_n (d) Contrast versus the noise level σ_n. Original contrast = 0.2964.

The results obtained for a high contrast T2 weighted knee MR image corrupted by 5% noise level are shown in Fig. 6.18. The image contains excessive structural variations that include structural details with large and less spatial support. The corresponding values of quality metrics are listed in Table-6.8. The plots in Fig. 6.19 give the denoising results at different noise levels. Due to the high contrast nature of this MR image most of the structural details are preserved by the denoising methods. However, Pizurica's method fails to remove the noise contained in the high intensity regions and creates blips like structures. For higher noise levels, most of these noise structures are passed in to the denoised images and it results in poor performance in terms of the BC and the contrast. In terms of the quality metrics, the WD-BF (NeighShrink) method is comparatively better and at higher noise levels, the approach produced perceptually better denoising results than the other compared techniques.

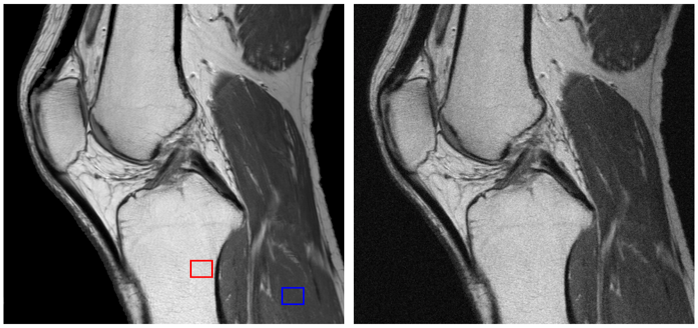

(a) Original image (b) Noisy image

DENOISED IMAGES

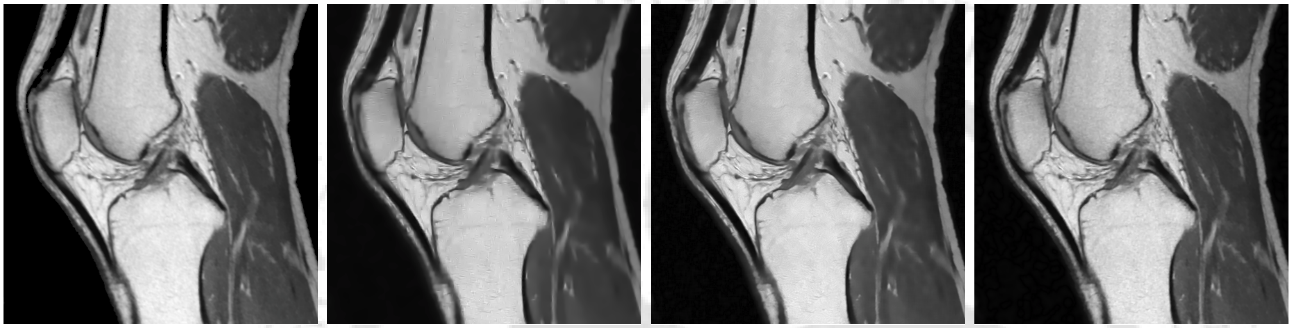

(c) WD-BF (VisuShrink) (d) Pizurica's method (e) UNLM (f) WD-BF (NeighShrink)

RESIDUAL IMAGES

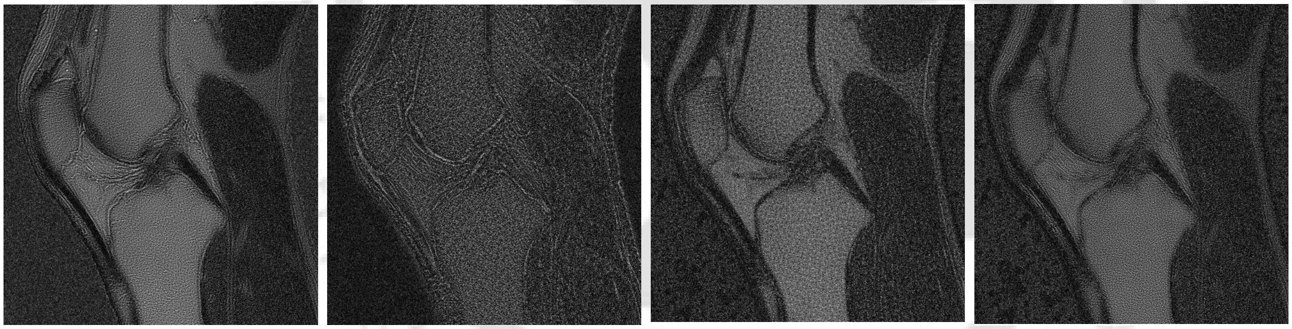

(g) WD-BF (VisuShrink) (h) Pizurica's method (i) UNLM (j) WD-BF (NeighShrink)

Figure 6.18: Denoising results of clinical T2 weighted knee MR image corrupted by 5% noise level. The region within the boxes represent the low intensity ROI and the high intensity ROI chosen for calculating the contrast. The original contrast is 0.4521.

Table 6.8: Comparison of the denoising techniques based on the similarity metrics computed between the original and denoised T2 weighted knee MR image. The clinical noisy image contains 5% of noise.

	WD-BF (VisuShrink)	Pizurica's method	UNLM	WD-BF (NeighShrink)
RMSE	0.0408	0.0353	0.0340	0.0220
SSIM	0.8813	0.8249	0.8431	0.9020
BC	0.9742	0.9696	0.9771	0.9895
Contrast	0.4583	0.4147	0.4587	0.4581

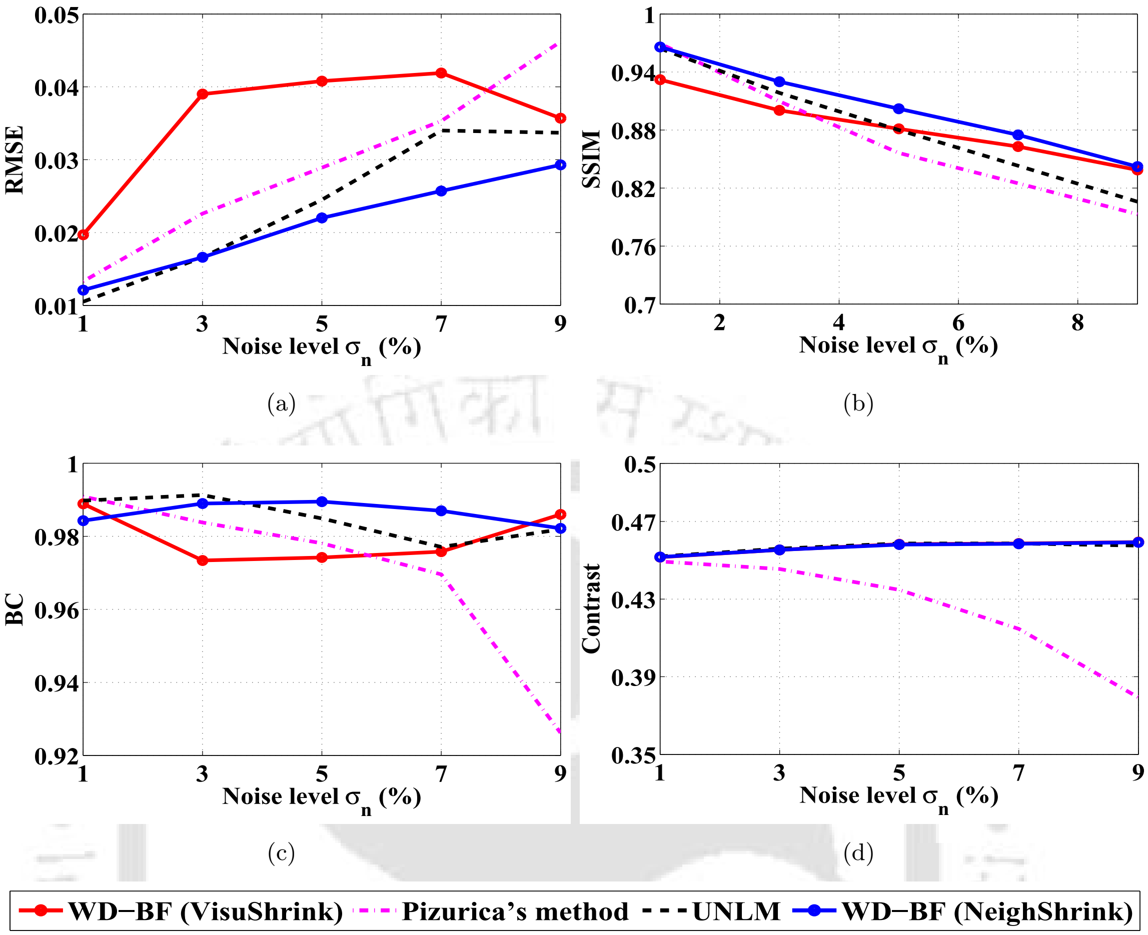

Figure 6.19: Comparative plot of denoising results obtained for the clinical T2 weighted knee MR image at varying noise levels. (a) RMSE versus the noise level σ_n (b) SSIM versus the noise level σ_n (c) BC value versus the noise level σ_n (d) Contrast versus the noise level σ_n. Original contrast = 0.4521.

6.5 Summary

An improved WD-BF approach using the NeighShrink thresholding algorithm is proposed for achieving feature preserved MR image denoising. Through the denoising results presented, we exploited the structural dependency of the denoising methods.

It is evident that the efficient denoising procedures like UNLM and inter-scale dependent wavelet denoising proposed by Pizurica *et al* [66] are particularly well suited for MR images with high structural variations. However, the smoothing parameters in UNLM is not pixel adaptive and so, for higher noise levels the method lacks the sufficient information for differentiating the signal and the noisy coefficients. In contrast, Pizurica's method based on coefficient classification benefits most of the high magnitude noisy coefficients yielding artifacts in the reconstructed images. As the threshold for coefficient classification is increased, large signal details are also removed as noise. Also, the contrast of the denoised MR image is very poor for higher noise levels.

The proposed WD-BF approach is capable of efficiently discriminating the signal and the noisy details. The WD-BF using soft thresholding, preserves the image structures but they are blurred. Therefore, we have the proposed WD-BF with NeighShrink to exploit the neighborhood similarities for improving the denoising of wavelet coefficients. Through experiments, we have successfully verified that exploring the neighborhood similarities in the wavelet domain improves the denoising efficiency by preserving the delicate structural details and not blurring the edge features. RMSE, SSIM, BC and contrast are used as the similarity metrics. The valuation of contrast over the ROI, helps in determining the perceptual quality of the denoised image. The BC values obtained indicate the statistical validity of the proposed method over other considered denoising methods.

7

WD-BF based on Pixel-Wise Adaptation of Bilateral Filter

Contents

7.1 Introduction

One of the main issues identified during the development of WD-BF method for MR image denoising is the optimization of the bilateral filter parameters. As explained in the previous chapter, the width of the domain and the range filters are chosen experimentally to suit the application. It is also shown that the range parameter (σ_r) is more decisive than the domain parameter (σ_d) and its width should be directly proportional to the noise level (σ_n) for better denoising. The best choice of σ_r for MR images is empirically obtained as $1.5\sigma_n$. However, this choice need not be optimum for all the MR images considered. The desired optimal choice can be achieved if σ_r depend on the characteristics of the MR image being filtered.

Therefore, with the incentive to eliminate the experimentation procedures required for choosing the best value of σ_r, a method based on the local variances of the noisy MR image to be filtered is proposed. The choice of σ_r is made proportional to the local statistics and thus, it led to pixel-wise adaptation of the filter parameter σ_r.

In this proposed approach, the range parameter σ_r for each pixel is computed through power-law scaling of the inverse of its local variance. Thus an adaptive range function that is narrow along the edges and wide for smooth regions is obtained. As result, at higher noise levels the smoothing along the edges remains condensed than in the conventional bilateral filter. But, this adaptation of bilateral filter in most of the experiments did not yield very significant improvement in the WD-BF framework. This is because; bilateral filtering in WD-BF is performed on the approximation coefficients at coarsest scale in which the noise level is very less. Therefore, the main advantage it offered in WD-BF framework is the automatic choice of σ_r.

However, this pixel-wise adaptation of bilateral filter in spatial domain performs better than the conventional bilateral filter under Gaussian noise assumption. The evaluations on the standard test images (general images) and the corresponding results are discussed in appendix A.

This chapter explains this proposed approach for pixel-wise adaptivity of bilateral filter based on the local variances and presents the denoising results obtained by employing the pixel-wise adaptive bilateral filter in the WD-BF framework.

7.2 Automatic Parameter Selection

Recalling from chapter 5, the range W_d and the domain W_r components of the bilateral filter are defined respectively as

$$W_d(i;x,j;y) = \exp\left(-\frac{\left|(i-x)^2+(j-y)^2\right|}{2\sigma_d^2}\right) \tag{7.1}$$

and

$$W_r(f\,(i,j)\,;f\,(x,y)) = \exp\left(-\frac{|f\,(i,j)-f\,(x,y)|^2}{2\sigma_r^2}\right) \tag{7.2}$$

The parameters σ_d^2 and σ_r^2 are the variances that specify the width of the domain and range kernels respectively. The optimal performance of the bilateral filter depends on the choice of σ_d and σ_r . Hence, they are considered as the controlling parameters. From the definitions it can be inferred that the domain component is independent of the image content. Its influence depends only on the spatial distance between the pixels and not on their intensity values. Conversely, the range component depends on the intensity values and hence, it decreases the influence of pixels at (i,j) when their intensity values differ from $f\,(x,y)$. This implies that the range component adapts to the structural content of the image and therefore, the extent of filtering is more influenced by the choice of σ_r . It can be inferred that large noise levels require higher values of σ_r and vice-versa. This dependency leads to the proportionality,

$$\sigma_r = \lambda\sigma_n \tag{7.3}$$

λ is the constraint parameter that determines the value of σ_r. Large value of λ will over smooth the image and small values will not suppress noise properly. Generally, the optimal value of λ is chosen experimentally such that there remains a tradeoff between image smoothing and its sharpness. However, this approach has the following setbacks:

(i) It demands several experiments to obtain an optimal λ for image denoising. Since its choice is independent of image characteristics it may not be optimal for all the images corrupted by various noise levels.

(ii) λ is a scalar resulting in a single choice of σ_r. It means that the level of smoothing is uniform over the entire image. Thus it assumes that the influence of noise is independent of the image content. But real images almost always violate this assumption.

The noise in smooth regions is perceptually more dominant than in the edges and coarse texture regions. This requires comparatively less smoothing along the edges and the coarse details [141]. This problem can be handled by varying the control parameter σ_r (and so λ) from pixel to pixel. This is done using the local statistics of the image to be denoised.

The local mean (variance) of a pixel $f(x, y)$ is computed locally over its neighborhood of size $(2R_{neigh} + 1) \times (2R_{neigh} + 1)$. The mean of a pixel m_{xy} is defined as [142]

$$m_{xy} = \frac{1}{(2R_{neigh} + 1)^2} \sum_{i=x-R_{neigh}}^{x+R_{neigh}} \sum_{j=y-R_{neigh}}^{y+R_{neigh}} f(i, j) \tag{7.4}$$

Similarly, the variance of a pixel σ_{xy}^2 is obtained from

$$\sigma_{xy}^2 = \frac{1}{(2R_{neigh} + 1)^2} \sum_{i=x-R_{neigh}}^{x+R_{neigh}} \sum_{j=y-R_{neigh}}^{y+R_{neigh}} (f(i, j) - m_{xy})^2 \tag{7.5}$$

The pixels belonging to the high contrast regions such as edges and coarse texture regions have high variance and those belonging to smooth regions have low variance values [141]. Since the objective is to restrict λ along the high contrast regions it is assumed that

$$\lambda_{xy} = \frac{max(\sigma_{xy})}{\sigma_{xy}} \tag{7.6}$$

The locally computed variance varies directly as its mean and so there exists large variations in the value of λ corresponding to pixels in the low and high contrast regions. Hence, power-law transformation is performed to stabilize the dynamic range and scale the values of λ [42]. Therefore, the value of σ_r for each pixel at (x, y) is obtained as

$$(\sigma_r)_{xy} = (\lambda_{xy})^{\gamma} \sigma_n \tag{7.7}$$

The choice of γ controls the degree of smoothing. The resultant σ_r is a matrix of control values that varies according to the pixel characteristics and is also properly balanced among the pixels belonging to smooth regions, edges and coarse texture regions. The range component in Eq. (7.2) is adapted pixel-wise and can therefore be redefined as,

$$W_r^A(f(i, j); f(x, y)) = \exp\left(-\frac{|f(i, j) - f(x, y)|^2}{2(\sigma_r^2)_{xy}}\right) \tag{7.8}$$

The support of the bilateral filter varies with respect to the pixel characteristics and hence, the adaptivity of the filter is improved. We refer the bilateral filter defined using the pixel-wise range

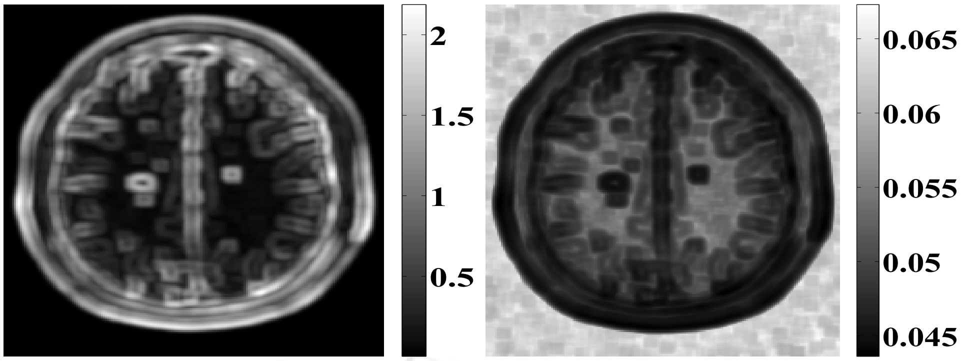

(a) Map of σ_{xy} (b) Map of $(\sigma_r)_{xy}$

Figure 7.1: Pixel-wise choice of σ_r obtained for a simulated T2 weighted MR image corrupted by 5% noise. The $2D$ maps illustrates the pixel-wise σ_r values obtained with respect to the standard deviation σ_{xy} of the pixel. The neighborhood size for computing the σ_{xy} and σ_r is chosen as 7 × 7.

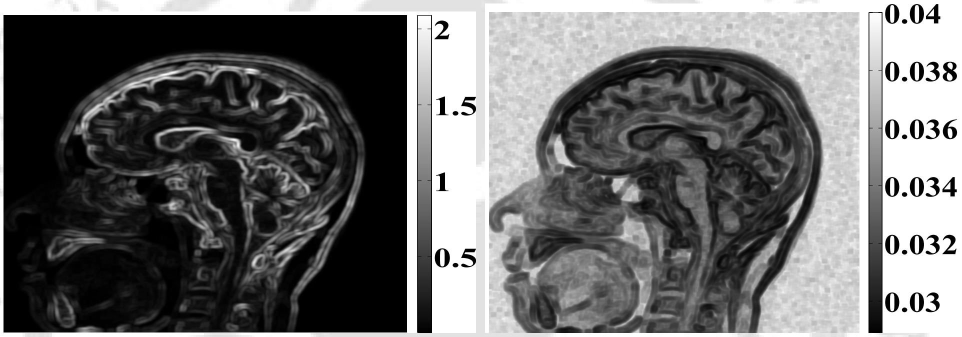

(a) Map of σ_{xy} (b) Map of $(\sigma_r)_{xy}$

Figure 7.2: Pixel-wise choice of σ_r obtained for a clinical T2 weighted sagittal MR image corrupted by 5% noise. The $2D$ maps illustrates the pixel-wise σ_r values obtained with respect to the standard deviation σ_{xy} of the pixel. The neighborhood size for computing the σ_{xy} and σ_r is chosen as 7 × 7.

component W_r^A as *adaptive bilateral filter* (ABF). Accordingly, the WD-BF framework based on ABF will be referred as WD-ABF.

7.3 Results and Discussion

The optimal neighborhood size for computing the local variance and the response of the filter is experimentally determined as 7 × 7. The value of domain parameter σ_d is fixed as 5. The wavelet sub-bands are denoised using NeighShrink thresholding scheme.

The values of the range parameter σ_r computed for each pixel of a simulated noisy T1 weighted axial MR image and a clinical T2 weighted sagittal MR image are shown in Fig. 7.1 and 7.2 respectively. It can be verified that the σ_r values corresponding to the edge pixels are less than the pixels in flat regions and also the range parameter value for each edge pixel depends on its strength. This is because the strong edges are less influenced by noise than the weak edges. As a result the variance of the strong edge pixels is high and weak edges are characterized by comparatively low variance values. Thus the degree of smoothing along the strong edges is relatively less than the weak edges.

From the experiments, it is observed that as the noise level increases the local variance in the flat regions increases substantially than in the edges. For this reason the slope of the power-law transformation should be accordingly chosen such that the range of $(\sigma_r)_{xy}$ values corresponding to the pixels $f(x,y)$ in the flat regions will be expanded to ensure sufficient smoothing. Therefore, γ can be varied to adjust the level of smoothing.

The advantages expected through this adaptive bilateral filter (ABF) strategy are the (i) automatization and (ii) improvement in the denoising performance. Particularly, the improvements are very significant in the spatial domain adaptive bilateral filtering. This is explained through the denoising results obtained by performing experiments on general test images as presented in appendix A.

In the WD-BF method, bilateral filtering is applied on the approximation coefficients at the coarsest scale in which the noise level is very less. As a result, taking in the proposed adaptive bilateral filter in wavelet domain did not yield any significant improvement over the conventional bilateral filter. Thus, the advantage offered by the WD-ABF method is the automatization of parameter selection. However, in the case of MR images for which the choice $1.5\sigma_n$ is not optimum, the WD-ABF strategy has improved the denoising performance. Similar improvements are also observed for MR images with more structural details that is corrupted by high noise levels. Therefore, the validity of the proposed WD-ABF method is confirmed if it yields almost same or even better denoising efficiency than the WD-BF approach in which the value of σ_r is chosen experimentally. Except for the additional computations involved in calculating the local variances, the computational complexity of the adaptive bilateral filter is same as the conventional bilateral filter.

The evaluation of the proposed method for automatic and pixel-wise adaptation of bilateral filter is verified by conducting experiments on simulated and clinical MR images. The empirically suitable value of power variable γ in Eq. (7.7) is estimated as $1.5\sigma_n$ for denoising MR images in the squared magnitude domain. The denoising results of UNLM and Pizurica's method are also included to complete the discussion.

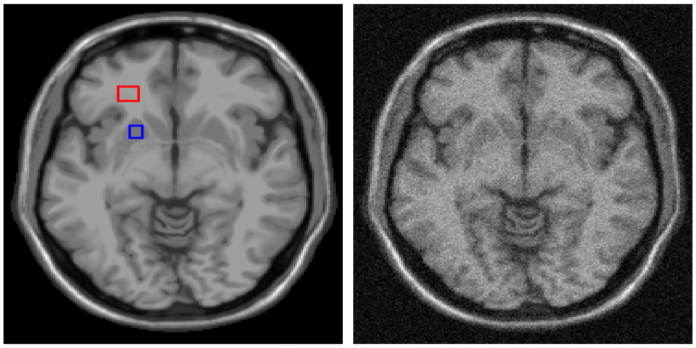

(a) Original image (b) Noisy image

DENOISED IMAGES

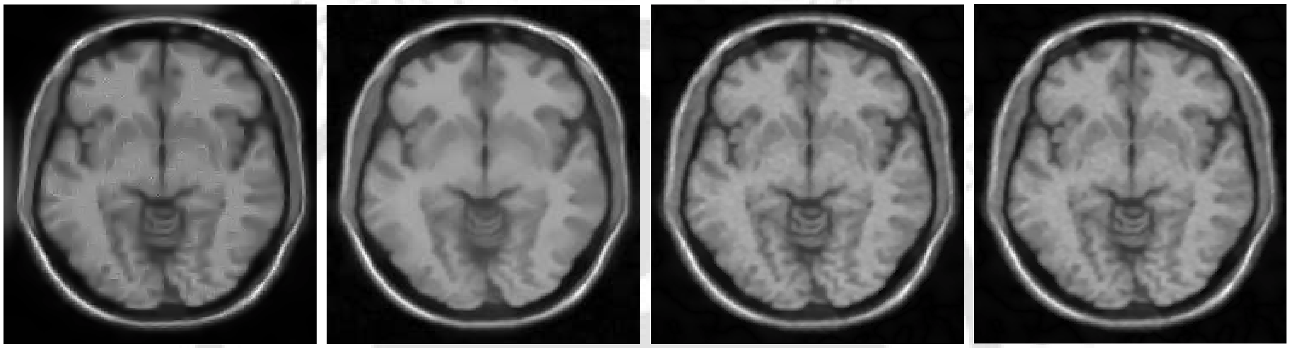

(c) Pizurica's method (d) UNLM (e) WD-BF (NeighShrink) (f) WD-ABF (NeighShrink)

RESIDUAL IMAGES

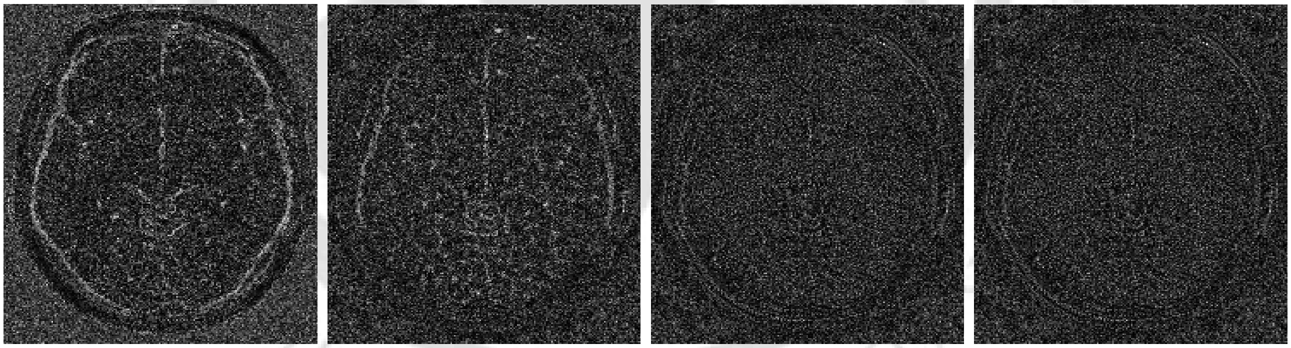

(g) Pizurica's method (h) UNLM (i) WD-BF (NeighShrink) (j) WD-ABF (NeighShrink)

Figure 7.3: Comparison of the denoising results of a simulated T1 weighted axial image corrupted by 5% noise level. The results illustrate the preciseness of the proposed automatic parameter selection approach for bilateral filter. The region within the boxes represent the low intensity ROI and the high intensity ROI chosen for calculating the contrast. The computed value of contrast in the original image is 0.1406.

Table 7.1: Comparison of the denoising results based on the similarity metrics computed between the original and the denoised T1 weighted axial simulated data. The simulated noisy image contains 5% of noise.

	Pizurica's method	UNLM	WD-BF (NeighShrink)	WD-ABF (NeighShrink)
RMSE	0.0329	0.0313	0.03063	0.0305
SSIM	0.8949	0.9022	0.9337	0.9338
BC	0.9310	0.9305	0.9338	0.9352
Contrast	0.1317	0.1345	0.1444	0.1452

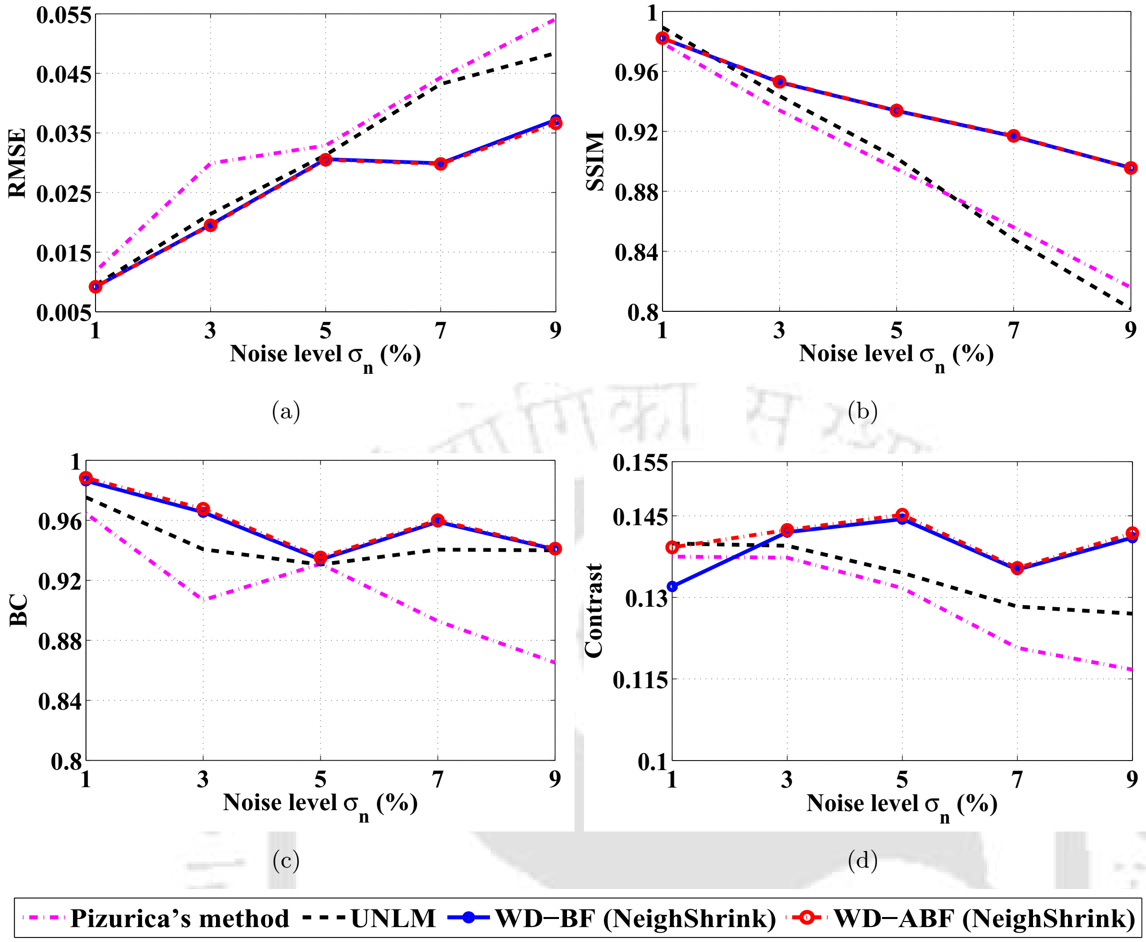

(a) (b)

(c) (d)

Figure 7.4: Comparative plot of denoising results obtained for the simulated T1 weighted axial MR image at varying noise levels. (a) RMSE versus the noise level σ_n (b) SSIM versus the noise level σ_n (c) BC value versus the noise level σ_n (d) Contrast versus the noise level σ_n. Original contrast = 0.1406.

The denoising results of a simulated T1 weighted axial MR image corrupted by 5% of noise level are shown in Fig. 7.3. The values of the quality metrics corresponding to this image are given in Table-7.1. This T1 weighted MR image consists of large structural variations with good spatial support.

From the denoised images, it is evident that the WD-ABF method performs similar to WD-BF which means that the automatically estimated pixel-wise σ_r fits the performance obtained using the empirically chosen optimal value. In the Pizurica's method, the image features especially the inter-tissue boundaries are well preserved. Despite this advantage, some of the high magnitude noisy coefficients appear as blips in the denoised image limiting its extent of smoothing. However, UNLM offers better smoothing but it also results in excessive smoothing of the image structures. The WD-BF approaches succeeds in achieving good smoothing along with preserving the image details. The comparative plots of the denoising results obtained for different noise levels are given in Fig. 7.4.

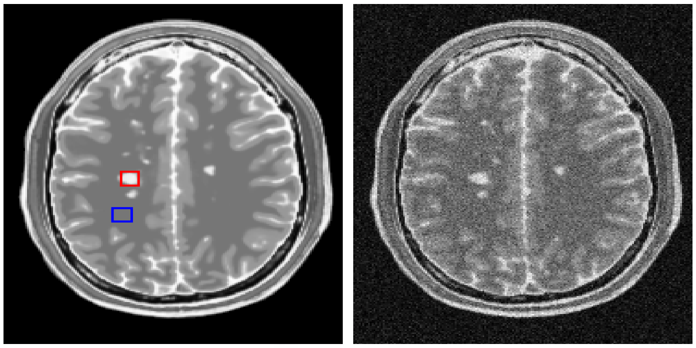

(a) Original image (b) Noisy image

DENOISED IMAGES

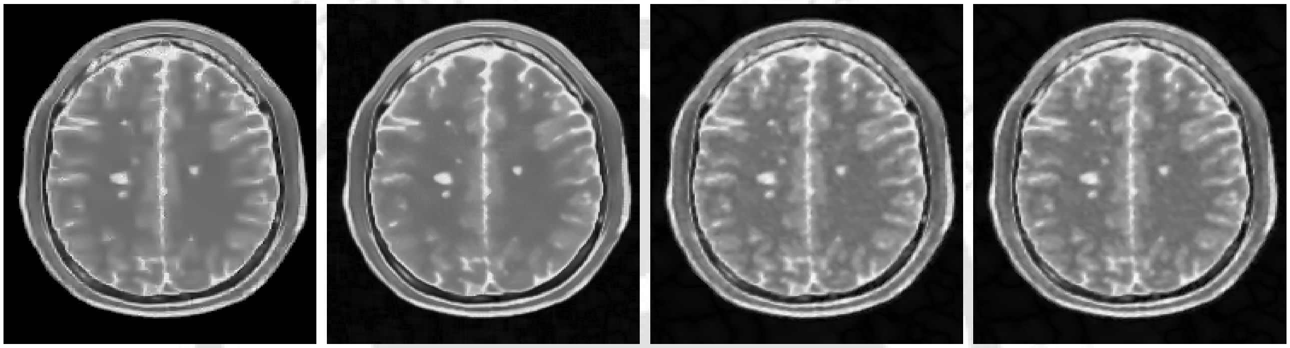

(c) Pizurica's method (d) UNLM (e) WD-BF (NeighShrink) (f) WD-ABF (NeighShrink)

RESIDUAL IMAGES

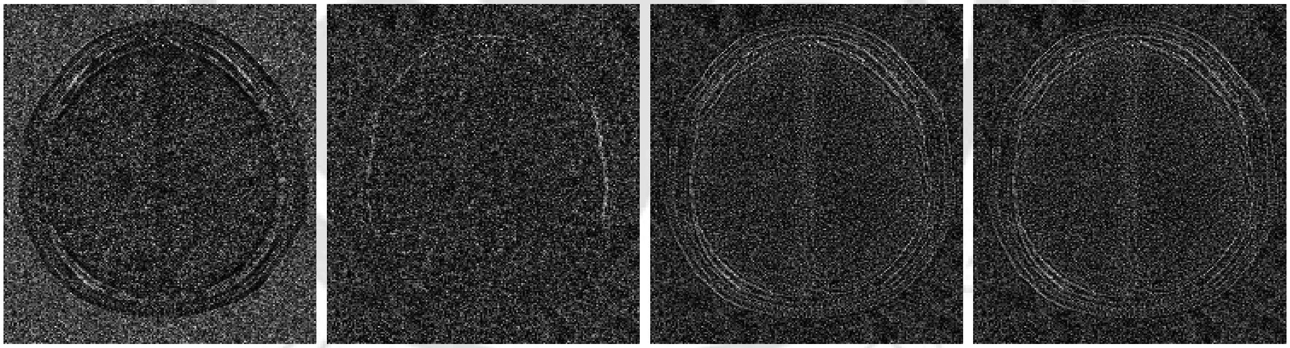

(g) Pizurica's method (h) UNLM (i) WD-BF (NeighShrink) (j) WD-ABF (NeighShrink)

Figure 7.5: Denoising results of a simulated T2 weighted axial image containing lesions and corrupted by 7% noise level illustrating the efficiency of the WD-BF and the WD-ABF methods. The region within the boxes represent the low intensity ROI and the high intensity ROI chosen for calculating the contrast. The computed value of contrast in the original image is 0.3361.

Table 7.2: Comparison of the denoising results based on the similarity metrics computed between the original and the denoised T2 weighted axial simulated data containing lesions. The simulated noisy image contains 7% of noise.

	Pizurica's method	UNLM	WD-BF (NeighShrink)	WD-ABF (NeighShrink)
RMSE	0.0589	0.0528	0.0471	0.0471
SSIM	0.8983	0.9028	0.9118	0.9120
BC	0.8512	0.8533	0.8901	0.8950
Contrast	0.3242	0.3389	0.3387	0.3393

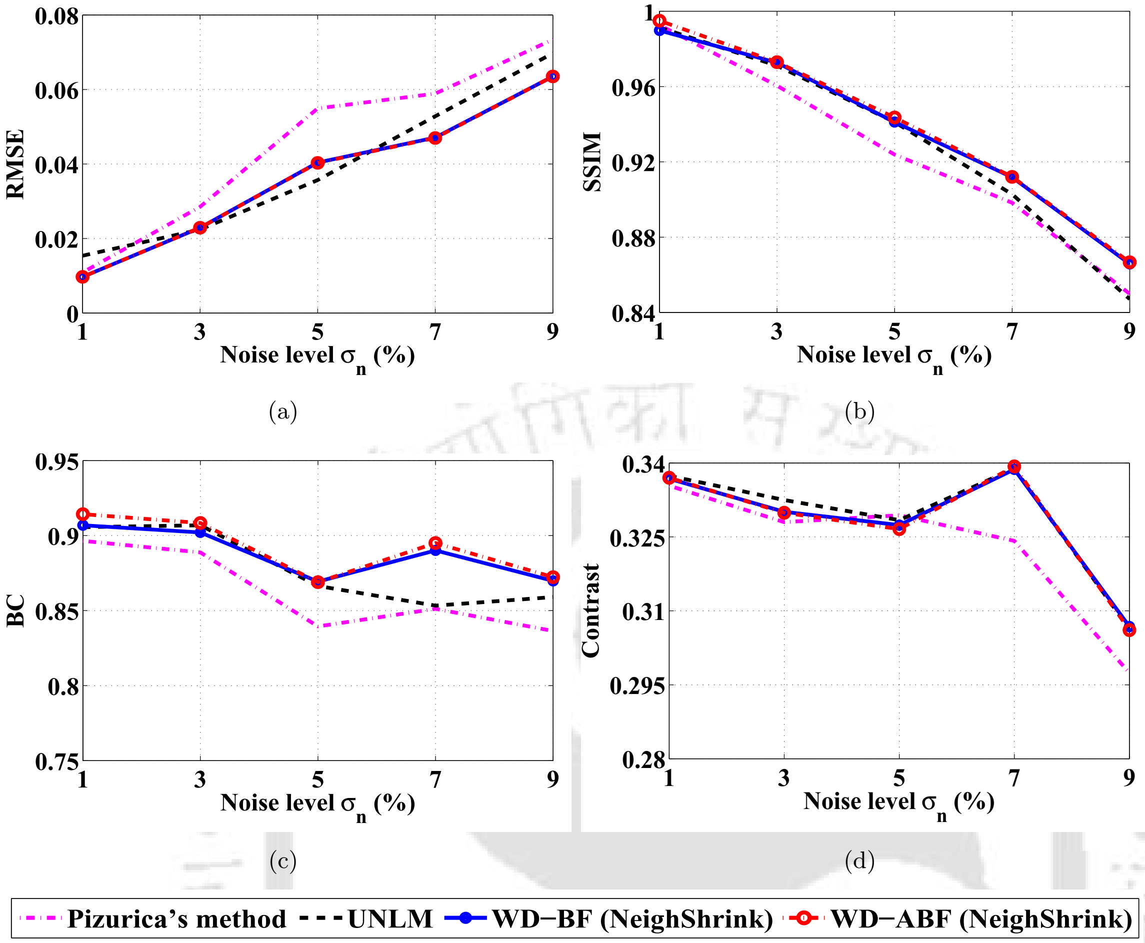

Figure 7.6: Comparative plot of denoising results of the simulated T2 weighted axial MR image containing lesions obtained at varying noise levels. (a) RMSE versus the noise level σ_n (b) SSIM versus the noise level σ_n (c) BC value versus the noise level σ_n (d) Contrast versus the noise level σ_n. Original contrast = 0.3361.

The results of a simulated T2 weighted axial MR image corrupted by 7% of noise level are shown in Fig. 7.5 and the corresponding values of the quality metrics are given in Table-7.2. The image has less structural variations but contains image details including the lesions with high contrast. Some of these lesions have good spatial support and others exhibits poor support. Therefore, the denoising methods should ensure to preserve most of these information while removing noise. From the denoised images it is apparent that WD-BF approaches are superior to the other considered denoising methods. In Pizurica's method, the lesions with small spatial support are completely removed and also the noisy coefficients retained in the high magnitude regions are clearly visible. Alternately, in the UNLM approach the noise in the high magnitude regions are smoothened. But, the details are not completely preserved.

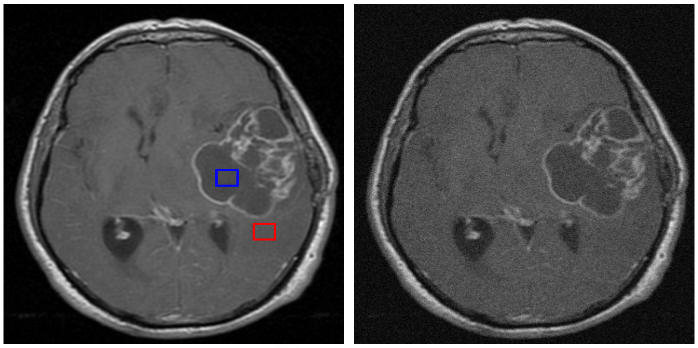

(a) Original image (b) Noisy image

DENOISED IMAGES

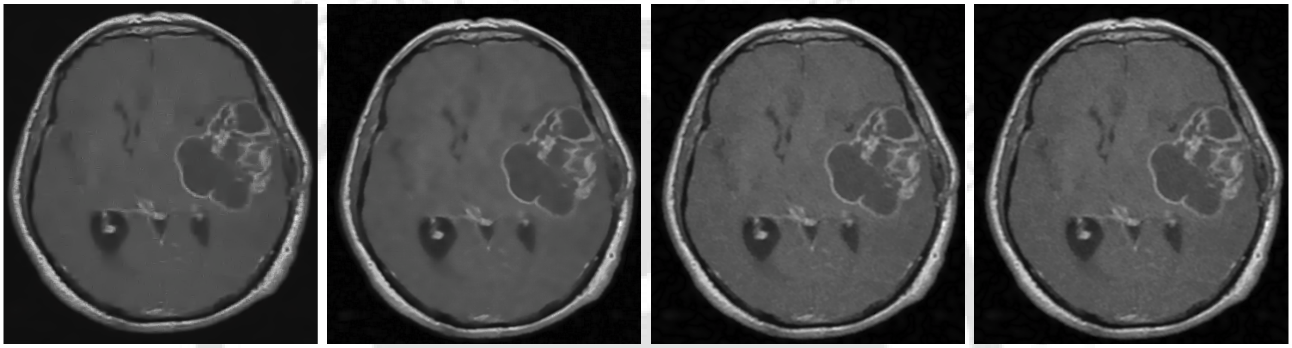

(c) Pizurica's method (d) UNLM (e) WD-BF (NeighShrink) (f) WD-ABF (NeighShrink)

RESIDUAL IMAGES

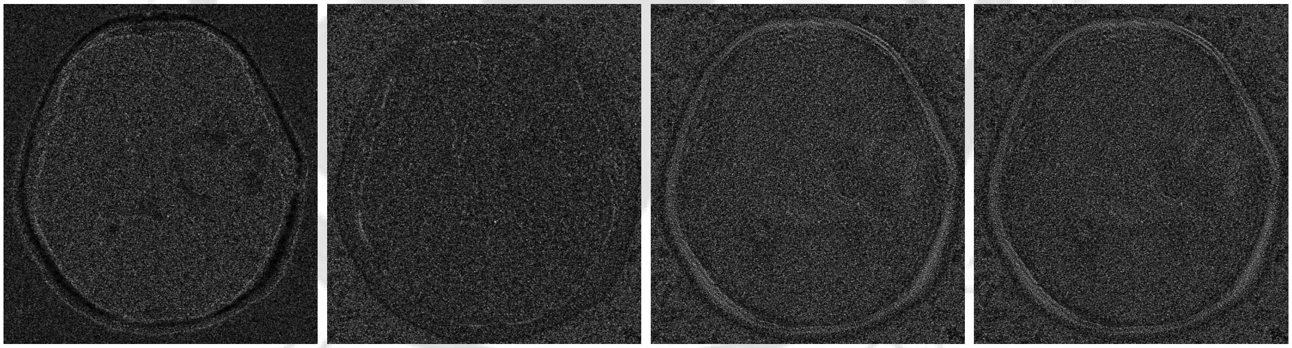

(g) Pizurica's method (h) UNLM (i) WD-BF (NeighShrink) (j) WD-ABF (NeighShrink)

Figure 7.7: Denoising results of a clinical T1 weighted axial image corrupted by 5% consisting of less structural variations. The region within the boxes represent the low intensity ROI and the high intensity ROI chosen for calculating the contrast. The computed value of contrast in the original image is 0.0710.

Table 7.3: Comparison of the denoising results based on the similarity metrics computed between the original and the denoised T2 weighted axial clinical data containing lesions. The clinical noisy image contains 5% of noise.

	Pizurica's method	UNLM	WD-BF (NeighShrink)	WD-ABF (NeighShrink)
RMSE	0.0277	0.0206	0.0128	0.0128
SSIM	0.9473	0.9496	0.9712	0.9702
BC	0.8688	0.9755	0.9872	0.9871
Contrast	0.0720	0.0748	0.0754	0.0753

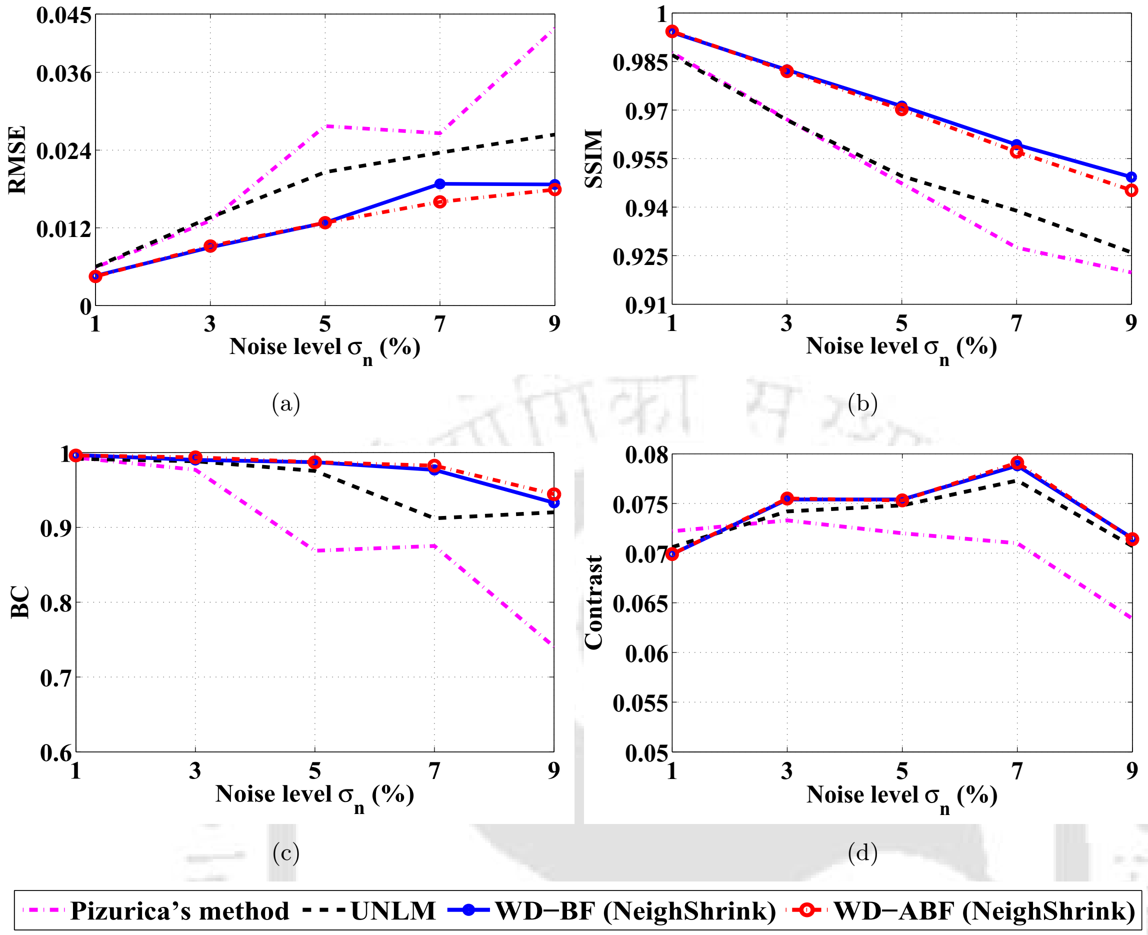

(a) (b)

(c) (d)

Figure 7.8: Comparative plot of denoising results of the clinical T1 weighted axial MR image obtained at varying noise levels. (a) RMSE versus the noise level σ_n (b) SSIM versus the noise level σ_n (c) BC value versus the noise level σ_n (d) Contrast versus the noise level σ_n. Original contrast = 0.0710.

From the residual images in Fig. 7.6, we can infer that the smoothing along the details is slightly more in WD-BF approaches. Despite this excessive smoothing, the details are preserved better in the WD-BF and WD-ABF methods comparatively. The plots of the denoising results obtained for different noise levels are given in Fig. 7.6. It can be observed that the WD-ABF approach has shown slight improvement over the WD-BF method in terms of the BC value.

The denoising results of a clinical T1 weighted axial MR image corrupted by 5% noise level are presented in Fig. 7.7. The obtained values of the image quality metrics is given in Table-7.3. This MR image mostly consists of smooth regions and less structural details. Also, the structural details have less spatial support (like the edges). From the results it is evident that as the Pizurica's method tend to preserve the details, the smoothing along the detail structures is not sufficient.

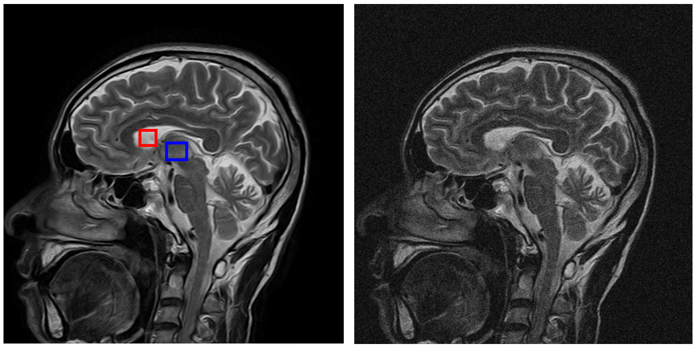

(a) Original image (b) Noisy image

DENOISED IMAGES

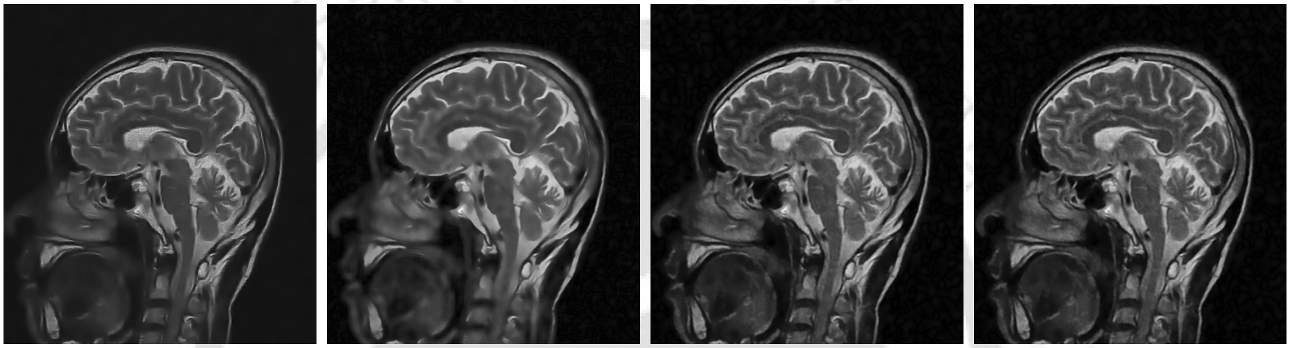

(c) Pizurica's method (d) UNLM (e) WD-BF (NeighShrink) (f) WD-ABF (NeighShrink)

RESIDUAL IMAGES

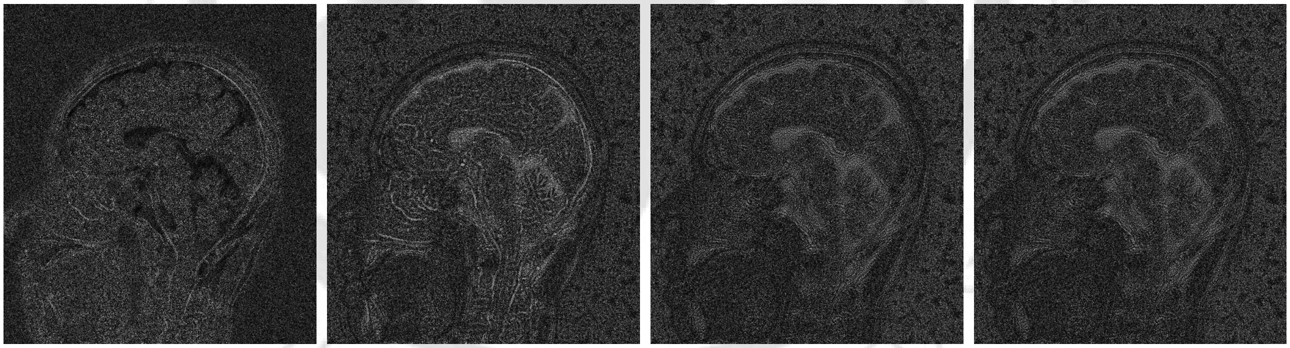

(g) Pizurica's method (h) UNLM (i) WD-BF (NeighShrink) (j) WD-ABF (NeighShrink)

Figure 7.9: Denoising results of a clinical T2 weighted sagittal image corrupted by 7%. The image contains high structural variations and also exhibits good inter-tissue contrast. The region within the boxes represent the low intensity ROI and the high intensity ROI chosen for calculating the contrast. The computed value of contrast in the original image is 0.3323.

Table 7.4: Comparison of the denoising results based on the similarity metrics computed between the original and the denoised T2 weighted sagittal clinical data. The clinical noisy image contains 7% of noise.

	Pizurica's method	UNLM	WD-BF (NeighShrink)	WD-ABF (NeighShrink)
RMSE	0.0422	0.0374	0.0307	0.0270
SSIM	0.8562	0.8511	0.8889	0.9246
BC	0.9367	0.9608	0.9502	0.9613
Contrast	0.3153	0.3352	0.3359	0.3359

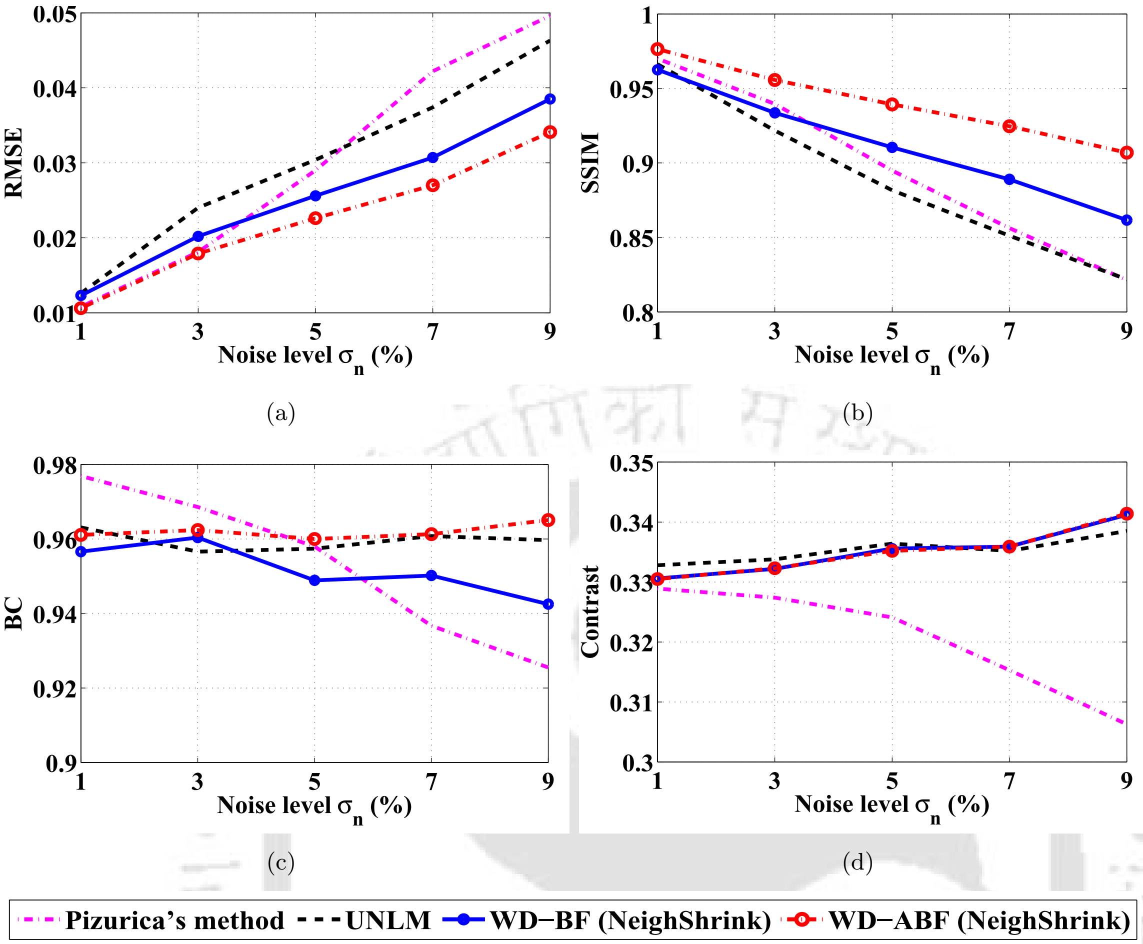

(a) (b) (c) (d)

Figure 7.10: Comparative plot of denoising results of the clinical T2 weighted sagittal MR image obtained at varying noise levels. (a) RMSE versus the noise level σ_n (b) SSIM versus the noise level σ_n (c) BC value versus the noise level σ_n (d) Contrast versus the noise level σ_n. Original contrast = 0.3323.

Hence, the contrast with respect to the edges have reduced. While, the UNLM method yields over-smoothing in the flat regions despite preserving the image structures. The denoising results of WD-BF approaches are comparatively better and clearly, the details are preserved well and sufficient smoothing is achieved in the flat regions. The comparative plots of the denoising results obtained by repeating the experiments for varying noise levels are given in Fig. 7.8.

The results of the experiments performed on a clinical T2 weighted sagittal MR image corrupted by 7% of noise are shown in Fig. 7.9. This image consists of high structural variations and particularly, the image details with low spatial support has high contrast. The denoising results suggests that the denoising efficiency of WD-BF approaches are better than the other techniques. As expected, the Pizurica's method has introduced blips in the denoised image.

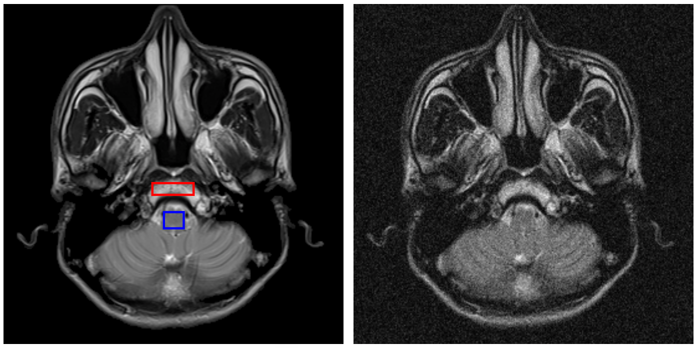

(a) Original image (b) Noisy image

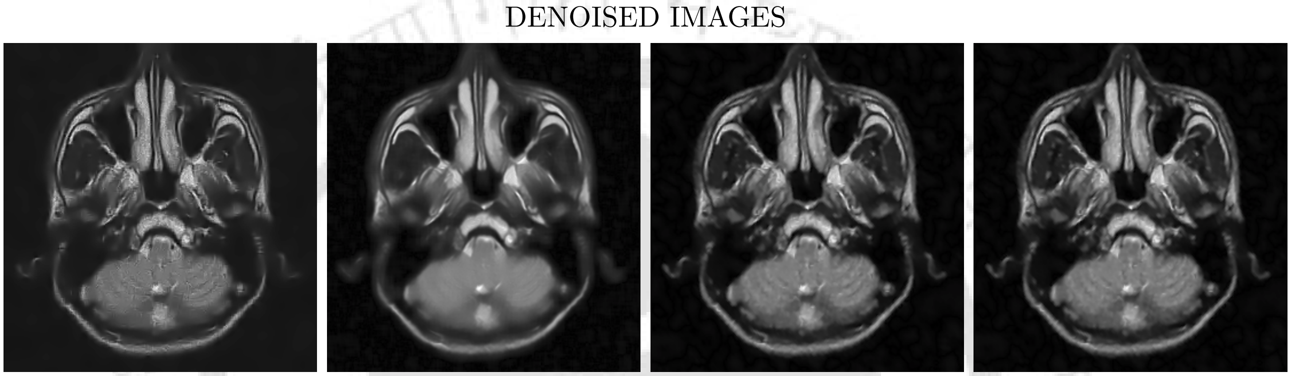

DENOISED IMAGES

(c) Pizurica's method (d) UNLM (e) WD-BF (NeighShrink) (f) WD-ABF (NeighShrink)

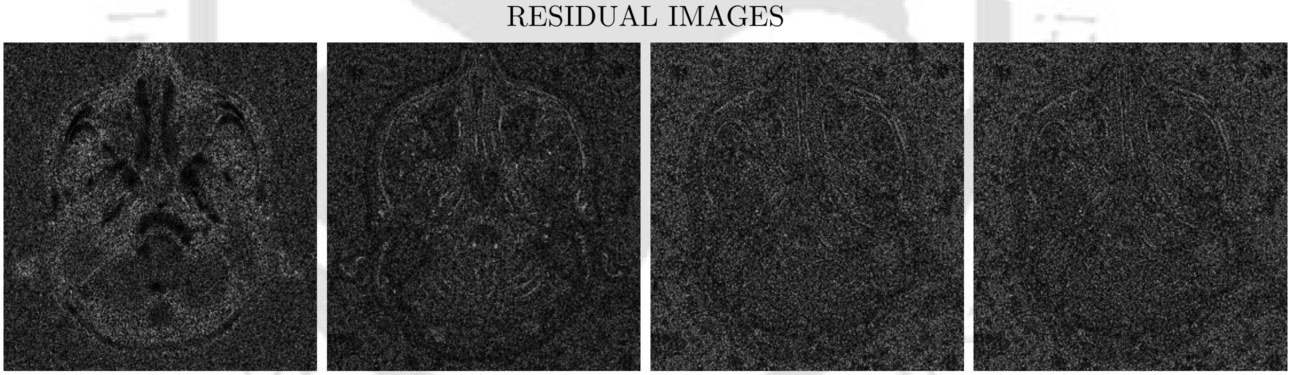

RESIDUAL IMAGES

(g) Pizurica's method (h) UNLM (i) WD-BF (NeighShrink) (j) WD-ABF (NeighShrink)

Figure 7.11: Denoising results of a clinical T2 weighted axial image corrupted by 7% noise level. The region within the boxes represent the low intensity ROI and the high intensity ROI chosen for calculating the contrast. The computed value of contrast in the original image is 0.1786.

Table 7.5: Comparison of the denoising results based on the similarity metrics computed between the original and the denoised T2 weighted axial clinical data. The clinical noisy image contains 7% of noise.

	Pizurica's method	UNLM	WD-BF (NeighShrink)	WD-ABF (NeighShrink)
RMSE	0.0455	0.0438	0.0331	0.0329
SSIM	0.8631	0.8749	0.9198	0.9211
BC	0.9128	0.9518	0.9841	0.9839
Contrast	0.1563	0.1709	0.1684	0.1684

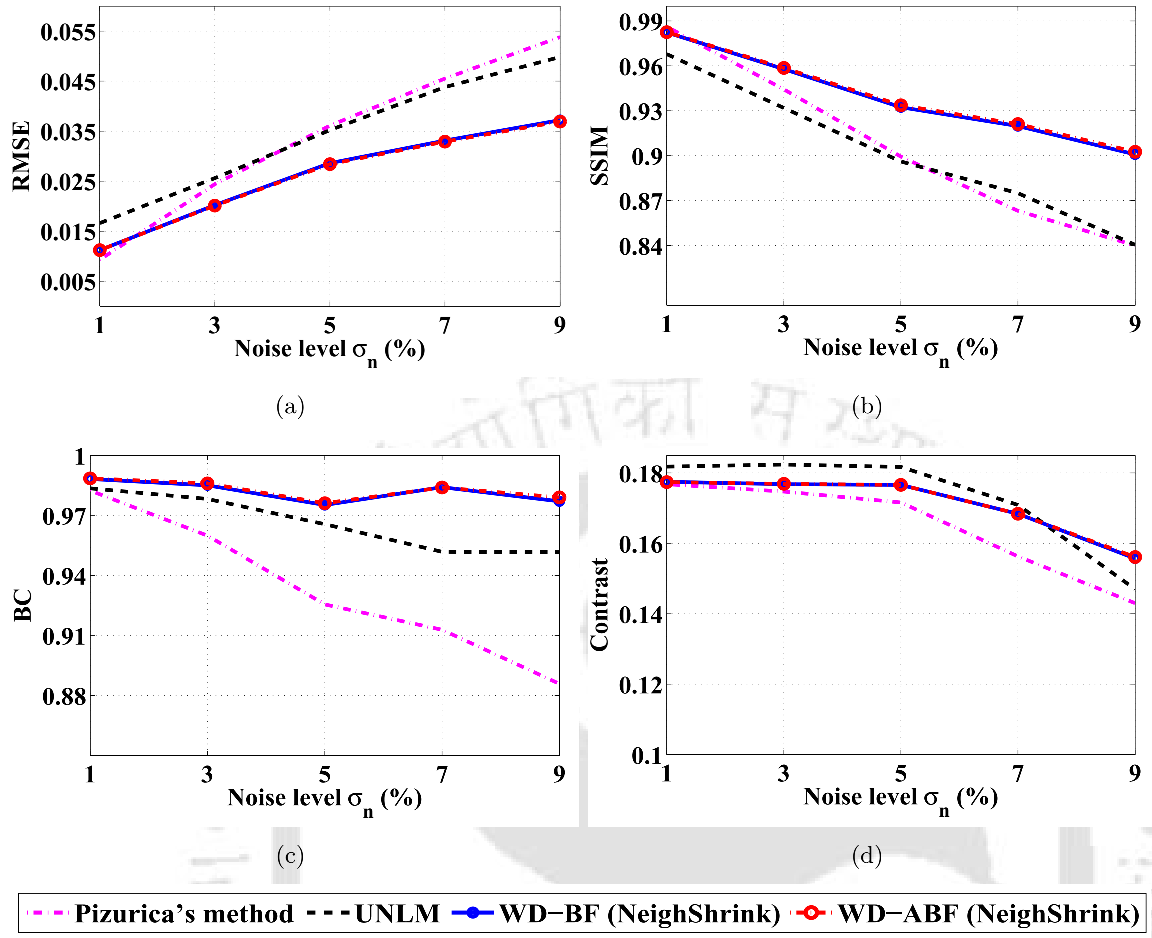

(a) (b)

(c) (d)

Figure 7.12: Comparative plot of denoising results of the clinical T2 weighted axial MR image obtained at varying noise levels. (a) RMSE versus the noise level σ_n (b) SSIM versus the noise level σ_n (c) BC value versus the noise level σ_n (d) Contrast versus the noise level σ_n. Original contrast = 0.1786.

While UNLM resulted in excessive smoothing of some of the image features. From the values of the quality metrics, we can infer the actual advantage offered by the WD-ABF approach over WD-BF method. As mentioned earlier, the empirically determined choice of σ_r will not be the optimal choice for all the MR images. Under such conditions, the value of σ_r may be less resulting in poor smoothing or it would be high yielding excessive smoothing. For this particular MR image, the fixed choice of σ_r was not sufficient to smooth the noise in the high contrast regions. Though the difference between the denoised images obtained from WD-BF and WD-ABF is not perceivable, the advantage can be confirmed from the values of the quality metrics in Table-7.4. The results obtained by repeating the experiments for varying noise levels also proves the improvement in the denoising efficiency achieved by utilizing the ABF in the wavelet domain.

Similarly, an other clinical T2 weighted axial MR image with high contrast and fine structural details is considered in the experiments. The denoising results of this MR image corrupted by 7% noise are given in Fig. 7.11. The corresponding values of quality metrics are tabulated in Table-7.5. The evaluations from the experiments performed for varying noise levels are shown in Fig. 7.12. It is clearly evident that the proposed wavelet domain bilateral filter strategy exhibits good denoising efficiency and the proposed method for automatic parameter selection clearly attains the optimal performance.

7.4 Summary

Fundamentally, the bilateral filter in its standard form itself is an optimal filter for image denoising. Inspite of all the possible modifications of bilateral filter, it should be understood that the conventional bilateral filter will be optimum for a particular choice of its filter parameters. Therefore, any improvements in bilateral filter suggested for noise removal can be attained by properly choosing the filter parameters. This inference is logical in the sense that the standard form of bilateral filter is itself pixel-adaptive due to its dependence on the intensity similarities. Therefore, an important advancement for bilateral filter will be the automatic choice of optimal filter parameter σ_r. Such an advancement will eliminate the need for several experiments in finding the optimal value of σ_r.

In this chapter a very simple and an intuitive approach for automatically finding the values of filter parameter σ_r has been proposed. The computation for automatically tuning the control parameter σ_r based on the local variance has also led to the pixel-wise adaptation of WD-BF. An important advantage offered by the proposed approach along with the automatization is the improvement in the denoising performance. Conversely, in the WD-BF strategy the bilateral filter is applied on the approximation coefficient at the coarsest scale in which the noise level is very low. As a result, there was no plausible improvement in the denoising performance of WD-ABF. However, the objective towards developing an automatic parameter selection procedure turned prolific. Alternately, in spatial domain the proposed adaptive bilateral filter method offer some improvements and hence, its applicability in denoising general images under Gaussian noise assumption is discussed in the appendix A.

8

Applicability of Bilateral Filter in Wavelet Thresholding

Contents

8.1 Introduction

The proposed WD-BF as discussed through the previous chapters has successfully exploited the characteristics of bilateral filter in improving the efficiency of wavelet domain denoising techniques. The WD-BF approach is capable of preserving the image details, while smoothing the noise contained in the image. Therefore, wavelet thresholding in the WD-BF domain has evolved as an efficient feature preserving denoising method for MR images. In WD-BF, bilateral filter is employed for smoothing the approximation coefficients obtained at the coarsest scale. Similarly, we consider that the properties of bilateral filter can also be exploited for denoising the detail coefficients obtained at each scale in wavelet decomposition. Accordingly, we proposed two basic approaches based on the bilateral filter for denoising the detail coefficients.

The first method is named as *Adaptive VisuShrink* and it is formulated by modifying the universal threshold based on the spatial context of the wavelet coefficients. The spatial context information of the coefficient is computed using the range filter $W_r(x, y)$ employed in the formation of bilateral filter. The second approach projects *bilateral filtering as an effective alternative to the wavelet thresholding methods.*

The chapter begins with the formulations of conventional threshold selection and thresholding rules utilized in wavelet denoising. With these fundamentals, the proposed adaptive VisuShrink and wavelet denoising based on bilateral filter are explained. The results obtained through the experiments are included for confirming the significance of these methods.

8.2 Wavelet Thresholding Approaches

The properties of wavelet decomposition forming the basics in wavelet denoising are the (i) sparsity (ii) locality and (iii) multi-resolution [5]. The *sparsity* is the common characteristic of wavelet decomposition and it indicates the singularities of the image represented in the detail sub-bands. *Locality* refers to the spatio-frequency representation achieved in wavelet transforms. The wavelet bases gives exact information on the frequency and the spatial location. Hence, each wavelet coefficient carries a local information. Due to its *multi-resolution* or the *multi-scale* characteristics, it offers several possibilities for noise removal based on the inter-scale correlation of the detail coefficients.

Wavelet denoising through thresholding requires a threshold selection strategy and a thresholding rule. The threshold selection gives an optimal threshold value for differentiating the signal and the noise components. The thresholding rule specifies the shrinkage function that controls the extent of smoothing. Most of the formulations are already presented in chapters 5 and 6. However, those formulations are re-summarized in this chapter to maintain the continuity.

8.2.1 Thresholding rules

Wavelet thresholding is a non-linear technique which removes or shrink the wavelet coefficients based on a threshold. It is basically based on the decorrelating property of the wavelet transform. The magnitude of the wavelet coefficients corresponding to the noise pixels are smaller than the signal coefficients. Therefore, by shrinking coefficients smaller than a particular threshold, the noise pixels can be eliminated while preserving the signal details. The basic thresholding rules are (i) Hard thresholding (ii) soft thresholding and (iii) Neighblock thresholding.

For ease of notation, let us rearrange the $2D$ wavelet coefficients of size $M \times N$ at scale m as a $1D$ vector of length $N_1 = M \times N$, such that $w_m = \left\{W_\psi^m(x, y)\right\}$. The thresholding rules for denoising w_m are summarized as follows

8.2.1.1 Hard thresholding

Recalling from chapter 5, the hard thresholding rule is defined as follows

$$\hat{\theta}^m(n) = \begin{cases} w_m(n) & : |w_m(n)| > \lambda \\ 0 & : |w_m(n)| < \lambda \end{cases} \tag{8.1}$$

Hard thresholding introduces discontinuity between the wavelet coefficients that appear as artifacts in the reconstructed image.

8.2.1.2 Soft thresholding

The formulation for soft thresholding rule is as follows

$$\hat{\theta}^m(n) = \begin{cases} w_m(n) - \lambda & : \ w_m(n) > \lambda \\ 0 & : |w_m(n)| < \lambda \\ w_m(n) + \lambda & : \ w_m(n) < -\lambda \end{cases} \tag{8.2}$$

This thresholding approach removes the noisy coefficients and also shrinks the magnitude of the remaining wavelet coefficients by threshold value. Therefore, it eliminates the discontinuities and results in a smoother reconstruction.

8.2.1.3 Neighblock thresholding

Neighblock shrinks each wavelet coefficient by incorporating the information on its neighboring coefficient. This thresholding operation is performed either for each wavelet coefficient or for the group of adjacent coefficients known as a block. However, coefficient-wise thresholding is better in preserving the important details of the image.

In order to shrink a wavelet coefficient $w_m(n)$, its adjacent coefficients contained within the neighborhood distance d are obtained to form a block. The average energy of this block S is computed as

$$S = \frac{1}{2d} \sum_{r=n-d}^{n+d} w_m^2\left(r\right) \tag{8.3}$$

Given a threshold λ, the coefficient-wise Neighblock shrinkage rule based on this block average energy is formulated as

$$\hat{\theta}_m\left(n\right) = \begin{cases} \left(1 - \dfrac{\lambda^2}{S}\right) & : \; if\, S \leqslant \lambda^2 \\ 0 & : \; \text{Otherwise} \end{cases} \tag{8.4}$$

where, $\theta_m(n)$ is the estimate from the noisy wavelet coefficient $w_m(n)$. The Neighblock thresholding procedure is particularly useful to eliminate blurring of the edges which is prevalent in soft thresholding rule.

8.2.2 Threshold selection

The threshold selection methods can be grouped in to global thresholds and sub-band adaptive thresholds. Global threshold means that a single threshold value is applied for denoising all the detail coefficients obtained at each scale. Sub-band dependent thresholds specifies a different threshold for each sub-band at the scale of decomposition. This threshold is data-driven and obviously, they yield better denoising than the global thresholds. Some of the important threshold selection methods considered are as follows.

8.2.2.1 Universal threshold

As already given in chapter 5, the universal threshold λ_{univ} defined by Donoho and Johnstone [115] is computed as

$$\lambda_{univ} = \sigma_n \sqrt{2 \log\left(N_1\right)} \tag{8.5}$$

where N_1 is the length of the data and σ_n is the estimated noise variance. The universal threshold is a global threshold utilized for denoising all the wavelet coefficients. The universal threshold is made level-dependent by multiplying it with a scale factor and the formulation is given as

$$\lambda_{univ}^{m} = \lambda_{univ} \times 2^{-(J-1-m)} \tag{8.6}$$

where J is the maximum level of decomposition and $m = \{0, 1, \cdots, J-1\}$. Soft thresholding using universal threshold is known as the *VisuShrink*.

8.2.2.2 SURE threshold

Donoho and Johnstone [138] proposed a sub-band adaptive threshold, computed by minimizing the Stein's unbiased risk estimate (SURE). For any particular choice of threshold λ the SURE is computed as

$$\text{SURE}\left(w_m, \lambda\right) = N_1 - 2\#\left\{n : \left|w_m\left(n\right)\right| \leqslant \lambda\right\} + \sum_{n=1}^{N_1} \left[\min\left(\left|w_m\left(n\right)\right|, \lambda\right)\right]^2 \tag{8.7}$$

$\#$ denotes the cardinality. The SURE threshold for level m is obtained as

$$\lambda_{\text{sure}}^{m} = \arg\min_{\{\lambda\}} \text{SURE}\left(w_m, \lambda\right) \tag{8.8}$$

The threshold above assumes that the data has unit noise variance. For data with non-unit noise variance, the coefficients are normalized by the non-unit data variance. The soft shrinkage rule with the SURE threshold is known as the *SureShrink*.

8.2.2.3 Bayes threshold

Bayes threshold proposed in [143] is an adaptive data-driven threshold for image denoising via wavelet soft-thresholding. The formulation is based on modeling the wavelet coefficients as generalized Gaussian distributed (GGD). Therefore with GGD as the *prior*, the average mean square error in a sub-band is approximated by the Bayesian squared error risk estimate.

Let θ_m and χ_m denote the m^{th} scale wavelet coefficients of the noise-free data f and the noise η respectively. Assuming an additive noise model, the wavelet coefficients w_m can be expressed as

$$w_m\left(n\right) = \theta_m\left(n\right) + \chi_m\left(n\right) \tag{8.9}$$

Accordingly,

$$\sigma_{w_m}^2 = \sigma_{\theta_m}^2 + \sigma_n^2 \tag{8.10}$$

The variance of w_m is calculated as below

$$\sigma_{w_m}^2 = \frac{1}{N_1} \sum_{n=1}^{N_1} w_m^2 (n) \tag{8.11}$$

For a known noise variance σ_n^2, the value of σ_{θ_m} is given by

$$\sigma_{\theta_m} = \sqrt{\max \left(\sigma_{w_m}^2 - \sigma_n^2, 0 \right)} \tag{8.12}$$

Therefore, the Bayes threshold for the sub-band m is formulated as

$$\lambda_{bayes} = \frac{\sigma_n^2}{\sigma_{\theta_m}} \tag{8.13}$$

For $\sigma_n^2 \geqslant \sigma_{w_m}^2$, σ_{θ_m} is taken to be 0 and λ_{bayes} is taken as $\max(|w_m|)$. The threshold λ_{bayes} minimizes the Bayesian risk estimate defined as

$$r(\lambda_{bayes}) = E\left(\hat{\theta}_m - \theta_m\right)^2 = E(\theta_m) E_{w_m|\theta_m}\left(\hat{\theta}_m - \theta_m\right)^2 \tag{8.14}$$

where, $\hat{\theta}_m$ is the estimate of θ_m obtained by soft thresholding. Therefore, Bayes threshold with soft thresholding is known as the *BayesShrink*. In practice the Bayes threshold is multiplied by a factor β that is usually assigned to lie between $[1, 5]$. It controls the extent of smoothing and therefore, the Bayes threshold in reference with β is defined as

$$\lambda_{bayes} = \beta \frac{\sigma_n^2}{\sigma_{\theta_m}} \tag{8.15}$$

8.3 Adaptive VisuShrink - Proposed method

The choice of threshold in wavelet denoising is very critical. If the threshold is too large, the thresholding functions tends to remove signal details and hence, underfits the data. Conversely, if the threshold value is too small, noise coefficients remains unfiltered and it means that the thresholding functions overfits the data [144]. The VisuShrink technique aims towards noise-free reconstruction and doing so, it usually underfits the data. The most effective alternatives proposed were the SureShrink and the BayesShrink techniques and it aims towards minimizing the MSE between estimated and the original value. These methods are particularly useful in preventing the blurring of image details. Despite its guarantee towards minimum MSE, it does not ensure noise-free reconstruction as in the universal threshold. Therefore, at high noise levels it introduces few blips in the reconstructed image. In this context, VisuShrink turns advantageous and is optimal when the underlying data is sufficiently smooth.

In recent years, there are several advancements in these wavelet thresholding procedures based on the intra-scale and inter-scale relation of the wavelet coefficients. One such advancement is the NeighShrink procedure and its denoising efficiency was made clearly evident through the discussions in chapter 6. The NeighShrink method exploits the intra-scale correlation between the wavelet coefficients. Alternately, a wavelet thresholding method based on classifying the coefficients through inter-scale correlations proposed in [66] was also discussed. From such improvements, it is understood that employing the spatial context information improves the wavelet denoising methods.

With this motivation, we proposed a simple modification of the universal threshold by incorporating the spatial context information. As a result, the new universal threshold is made adaptive with respect to the characteristics of the wavelet coefficient to be shrinked. The approach is named as *Adaptive VisuShrink*.

The universal threshold as in Eq. (8.5) shows that the threshold is proportional to the data length. It means that the threshold assumes the data to be sufficiently smooth with in its range and aims towards adapting to that smoothness. Hence, universal threshold is optimum in asymptotic sense. For this reason, the universal threshold holds good for smooth regions and strong edge structures like region boundaries. The small and the weak edge structures refutes the asymptotic assumption and so, the threshold remains too high to pass these coefficients.

The basic idea in adaptive VisuShrink is to limit the universal threshold based on the spatial support of the wavelet coefficient to be denoised. The information on the spatial support is obtained by computing the radiometric similarity between the approximation coefficients at the coarsest scale. Therefore, the spatial context of a coefficient is the number of radiometrically similar coefficients within its neighborhood. The radiometric similarity is computed using the range filter defined in the bilateral filtering approach. The advantage of domain component is mimicked by considering a reasonably small neighborhood but sufficiently large for finding the pixels belonging to the same intensity region. The mathematical formulation of finding the spatial context is as follows

Consider the $2D$ approximation coefficient at the coarsest scale m, $W_{\varphi}^{m}(x, y)$ and it is of size $M \times N$ such that $x = \{0, 1, \cdots, M-1\}$ and $y = \{0, 1, \cdots, N-1\}$. For a $2d+1 \times 2d+1$ neighborhood around $W_{\varphi}^{m}(x, y)$ assume, $i = \{x-d, \cdots x+d\}$ and $j = \{y-d, \cdots y+d\}$. The radiometric similarity between the coefficient $W_{\varphi}^{m}(x, y)$ and its neighbor $W_{\varphi}^{m}(i, j)$ is computed as

$$W_r(W_\varphi^m(i,j);W_\varphi^m(x,y)) = \exp\left(-\frac{\left|W_\varphi^m(i,j) - W_\varphi^m(x,y)\right|^2}{2\sigma_r^2}\right) \tag{8.16}$$

Therefore, the spatial context of the coefficient at (x, y) is computed as

$$\varsigma\,(x,y) = \#\left\{(i,j) : W_r(W_\varphi^m(i,j);W_\varphi^m(x,y)) > \varepsilon\right\} \tag{8.17}$$

where # denotes the cardinality and ε is the limiting factor that specifies the maximum permissible value of the radiometric weight for coefficient selection. Using Eq. (8.17), the universal threshold is modified as

$$\lambda_{adap}\,(x,y) = \sigma_n\sqrt{2\log(\varsigma\,(x,y))} \tag{8.18}$$

The threshold defined in Eq. (8.18) is the adaptive universal threshold and soft thresholding of wavelet coefficients based on the adaptive threshold is defined as the adaptive VisuShrink. Additionally, the level dependency of the threshold is improved by assigning

$$\lambda_{adap}^m = \lambda_{adap} \times 2^{-(J-1-m)} \tag{8.19}$$

The empirical value of the range parameter σ_r is chosen as $\beta\sigma_n$. β is the scaling factor and it's value should be > 0. As the noise level increase, the value of β can be adjusted to achieve the optimal performance. Through our experiments β is fixed as 1 and therefore, $\sigma_r = \sigma_n$.

8.4 Bilateral Filtering as an Alternative to Wavelet Thresholding

Another novel approach to exploit the bilateral filter in wavelet domain is the smoothing of wavelet coefficients using the bilateral filter. The classical wavelet thresholding approaches are on the basis of selective reconstruction in which the coefficients less than the threshold are removed [5]. It means that these schemes assume that the wavelet sub-bands consists of purely noise coefficients, that can be well discriminated from signal coefficients. These methods adhere to the decorrelation between the wavelet coefficients. Additionally, it also important that the wavelet thresholding method must be spatially adaptive.

The desired adaptiveness is the inherent characteristics of the bilateral filter and hence, it is capable of varying the degree of smoothing depending on the characteristics of the coefficient. Therefore, for wavelet coefficient corresponding to any image structure like edges the smoothing is limited. In flat regions, the degree of smoothing is maintained sufficiently large to remove the noisy wavelet coefficients.

The proposed idea of using bilateral filter is based on the assumption that, all the wavelet coefficients should be considered to contribute to the unknown signal of interest. Each detail sub-band is explicitly considered as an image with distinct characteristics. The absolute value or the squared value of the wavelet coefficients is correlated [66] and hence, it is possible to find the radiometric weights required for bilateral filtering. Alternately, the radiometric weights can be calculated from the approximation coefficients at the coarsest level and are utilized for weighting the wavelet coefficients. Through experiments, we verified that calculating the radiometric weights using the approximation coefficients yields better results.

For a J-level wavelet decomposition, assume $m = \{0, 1 \cdots, J-1\}$ such that m denotes the high resolution (finest) scale and $m-1$ denotes the low resolution (coarsest) scale. Then, the response of the bilateral filter for a wavelet coefficient $W_{\psi}^{m}(x,y)$ is given by,

$$\hat{\theta}_m\left(x,y\right) = \frac{1}{C}\sum_{i=x-R_{neigh}}^{x+R_{neigh}}\sum_{j=y-R_{neigh}}^{y+R_{neigh}} W_d(i;x,j;y)W_r(W_{\varphi}(i,j);W_{\varphi}(x,y))W_{\psi}^{m}(i,j) \tag{8.20}$$

$W_{\varphi}(.)$ is the approximation coefficient at the coarsest scale. This approach in UDWT domain is named as the wavelet domain all band bilateral filtering and will be referred as WD-all-band-BF. The block diagram representation of the proposed WD-all-band-BF for 3 level decomposition is shown in Fig. 8.1. The important parameter determining the extent of smoothing in bilateral filter is the width of the range kernel σ_r. As mentioned earlier, σ_r is directly proportional to the noise variance σ_n. Since, bilateral filtering is performed on the detail sub-bands its value must be chosen proportional to noise variance of the sub-band.

Yuan *et al* [145] has shown that the noise variances of the wavelet sub-bands at each level follows the exponential function. Accordingly, the noise variance at level m is estimated as

$$\sigma_m^2 = \sigma_n^2\, exp(1 - m^{1.2}) \tag{8.21}$$

where σ_n^2 is the noise variance calculated from the finest scale detail coefficient. In our case, σ_n^2 is estimated from the background regions of the MR image. Therefore, the width of the range filter is made level-dependent by choosing it as

$$\sigma_r = \sigma_m \tag{8.22}$$

Intuitively, application of bilateral filter is similar to spatially adapting the wavelet thresholding through context modeling. However, bilateral filtering approach does not rely on selective recon-

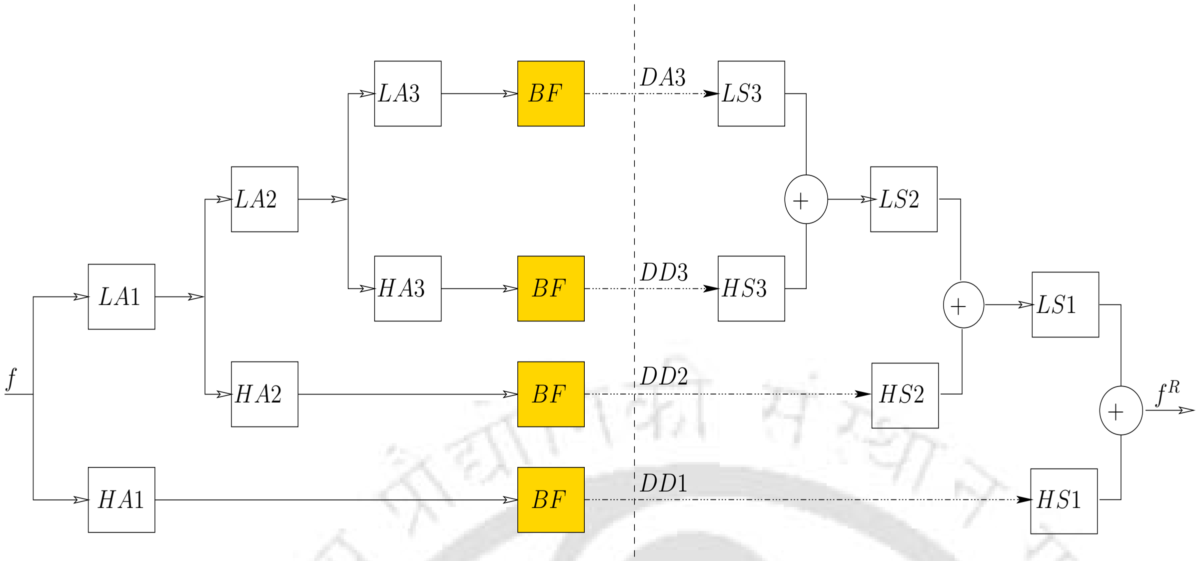

f -Input image
LA -Low-pass analysis filter
HA -High-pass analysis filter
BF -Bilateral filter

$DA3$ -Denoised approximation coefficient
DD -Denoised detailed coefficient
LS -Low-pass synthesis filter
HS -High-pass synthesis filter
f^R -Denoised image

Figure 8.1: Filter bank representation of wavelet domain all band bilateral filtering method

struction and hence, even the noisy coefficients with higher energy are also equally smoothened.

8.5 Experiments and Results

The MR image dataset considered for experimentation includes simulated and clinical images corrupted at different noise levels. The experiments and the denoising results of the adaptive VisuShrink and WD-all-band-BF are presented separately. Denoising of MR images using the above two approaches are performed in the squared magnitude domain.

MR image denoising using the considered thresholding methods is performed in the $WD - BF$ framework. The number of decomposition levels is chosen as 3. The wavelet bases used for decomposition are the Haar wavelets.

8.5.1 Evaluation of adaptive VisuShrink

The extent of denoising in adaptive VisuShrink method depends on the choice of the neighborhood size and the limiting factor ε. The idea in adaptive VisuShrink is to threshold a coefficient based on the spatial support of the region within which the coefficient is contained.

Accordingly, if the value of ε is small it allows most of the wavelet coefficients within the considered neighborhood and so ς increases leading towards more smoothing. Conversely, if the value of ε is high only few coefficients with large radiometric similarity are chosen and so ς decreases to preserve the sharpness of the data. Similarly, the size of the neighborhood $(2d + 1 \times 2d + 1)$ chosen around the coefficient to be denoised also influences the smoothness of the function. If a large neighborhood is chosen then there will be many coefficients that pass the limiting factor and hence ς increases. Within a small neighborhood the number of coefficients passing the limiting factor is less and so ς decreases to control the extent of smoothing.

If the value of ς is very small then the noisy coefficients remains unfiltered, introducing blips in the reconstructed image. On the contrary, large value of ς results in excessive smoothing. Therefore, it is important that the limiting factor ε and the neighborhood size must be chosen appropriately such that there exists a good tradeoff between the smoothness and the sharpness in the denoised image.

8.5.1.1 Choice of ε and neighborhood

The values of adaptive universal threshold calculated for a simulated T1 weighted MR image for different values of ε and neighborhood size are illustrated in Fig. 8.2 and 8.3. From the results in Fig. 8.2, it is evident that for lower values of ε the regions with fine details gets merged and mimics like a flat region. Thereby the value of λ_{adap} becomes large and results in excessive smoothing of the structural details as in VisuShrink.

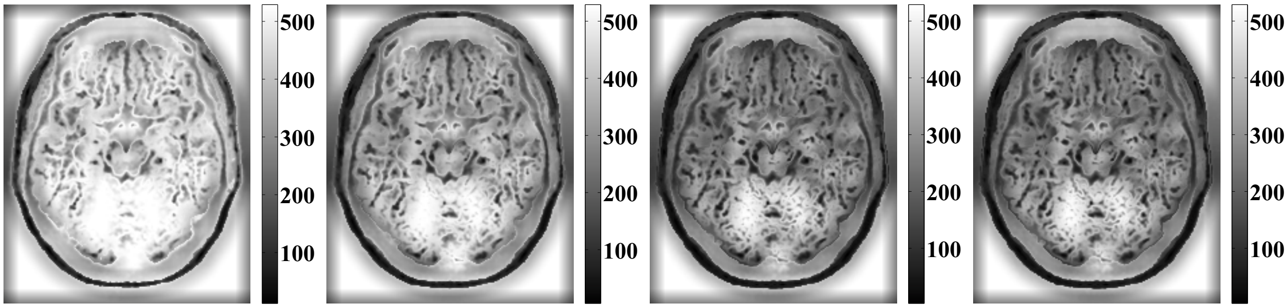

(a) $\varepsilon = 0.05$ (b) $\varepsilon = 0.25$ (c) $\varepsilon = 0.50$ (d) $\varepsilon = 0.75$

Figure 8.2: Coefficient-wise adaptive universal threshold values calculated for a simulated T1 weighted MR image corrupted by 7%. Illustrating the effect of varying the limiting factor ε for a fixed neighborhood size 23×23.

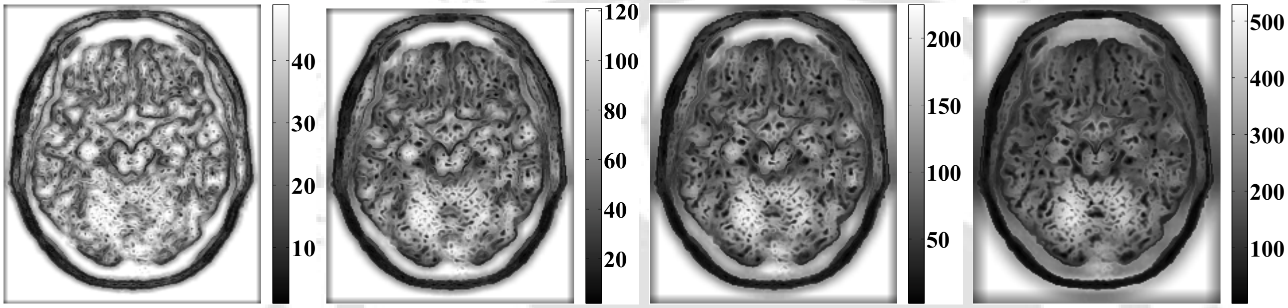

(a) Neighborhood= 7×7 (b) Neighborhood= 11×11 (c) Neighborhood= 15×15 (d) Neighborhood= 23×23

Figure 8.3: Illustration of adaptive universal threshold values computed for the simulated T1 weighted MR image by varying the neighborhood size $(2d + 1 \times 2d + 1)$. The image is corrupted by 7% and the value of ε is fixed as 0.95

Table 8.1: Empirical choice of the limiting factor ε and the neighborhood size $(2d + 1 \times 2d + 1)$ for achieving optimal denoising at different noise levels.

Noise level σ_n in %	Values of ε	Choice of neighborhood
1	0.95	3×3
3	0.85	7×7
5	0.75	15×15
7	0.75	19×19
9	0.65	23×23

From the results in Fig. 8.3, we can understand that large neighborhood size results in large value of λ_{adap}. It should also be noted that increasing the neighborhood size does not result in region merging as in the case of ε. Instead, large value of neighborhood implies that the underlying coefficient is sufficiently smooth over the considered area and this is exactly same as the assumption in the universal threshold. However, the extent of smoothing can be limited by choosing a large ε.

The adaptive VisuShrink method reduces to VisuShrink if neighborhood is large and ε is small respectively. Table-8.1 gives the experimentally obtained optimal values of ε and the neighborhood size for varying noise levels. It can be observed that as the noise level increases the value of ε decreases and neighborhood size increases to ensure sufficient smoothing. This shows that for higher noise levels the number of samples should be sufficiently large for estimation.

8.5.1.2 Denoising results

The performance of the wavelet thresholding methods is evaluated in terms of RMSE, SSIM, BC and contrast. The performance of the proposed adaptive VisuShrink is compared with the conventional VisuShrink, SureShrink, BayesShrink and Neighblock methods. The Neighblock method utilizes the level dependent universal threshold given in Eq. (8.6) for thresholding the wavelet coefficients. Similarly, the VisuShrink and the adaptive VisuShrink methods considered in our experiments utilize the level dependent thresholds defined in Eq. (8.6) and Eq. (8.19) respectively. The optimality of the BayesShrink method is maintained by experimentally choosing the value of β for which the technique gives better denoising.

The denoising results of a simulated T1 weighted axial MR image corrupted by 3% of noise level are shown in Fig. 8.4. This MR image is considered to be highly structural, but not with respect to the high frequency details. The structure in this image refers to the frequent intensity variations that constitutes the flat regions in the image. Therefore, it is important for the inter-tissue contrast to be maintained while denoising.

From the denoised images in Fig. 8.4, it can be observed that the VisuShrink approach has resulted in excessive smoothing and so the image looks blurred. In comparison with the VisuShrink, the extent of smoothing is controlled in the Neighblock thresholding method. But the inter-tissue contrast desired for this image has become less which means that the sharpness between these regions are compensated. The denoised images obtained using the SureShrink and the BayesShrink methods are comparatively sharper. However, due to the limits in the extent of smoothing some of the noisy coefficients remain unfiltered.

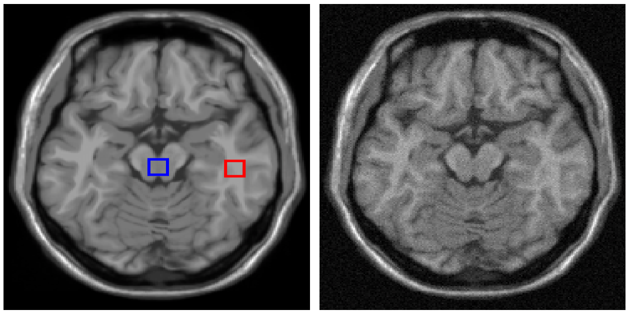

(a) Original image (b) Noisy image

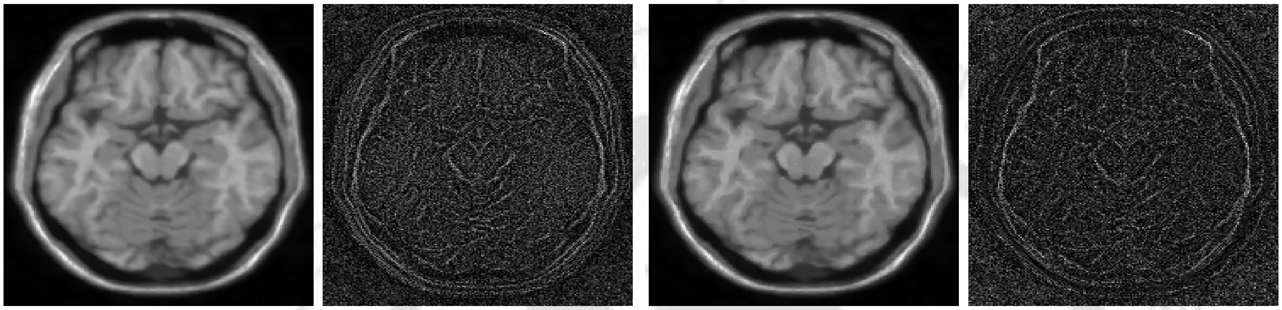

(c) **VisuShrink**-Denoised image and its residual (d) **SureShrink**-Denoised image and its residual

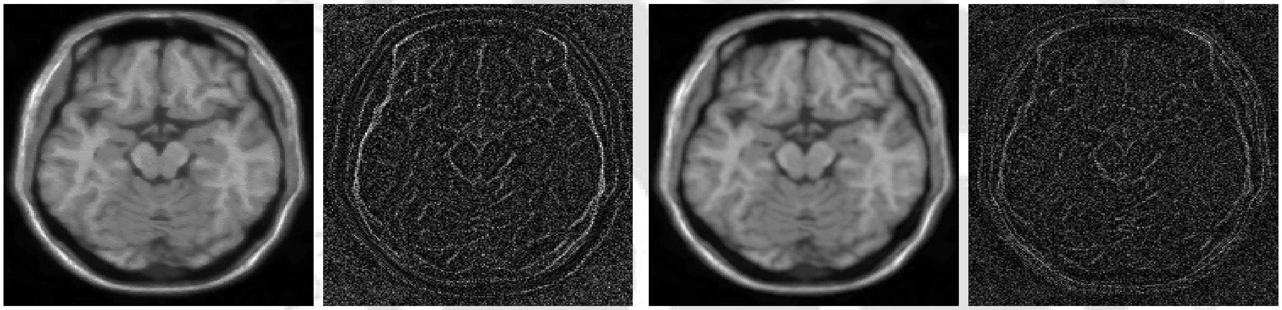

(e) **BayesShrink**-Denoised image and its residual (f) **Neighblock**-Denoised image and its residual

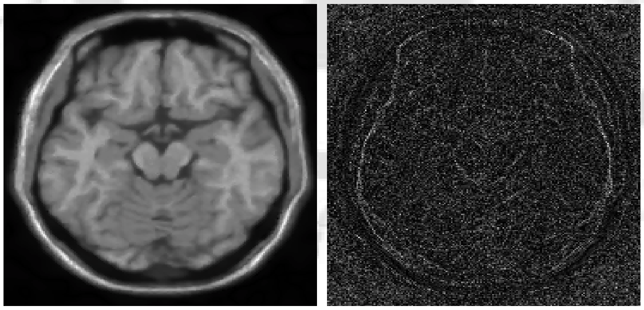

(g) **Adaptive VisuShrink**-Denoised image and its residual

Figure 8.4: Comparison of the results obtained for the noisy simulated T1 weighted axial MR image obtained using wavelet thresholding methods. Original image is corrupted by 3% noise level. The region within the box represents the low intensity and the high intensity ROI's chosen for calculating the contrast. The contrast in the original image is 0.0987.

Table 8.2: Values of the similarity metrics obtained for 3% noise level. The denoised T1 weighted axial MR images are shown in Fig. 8.4.

	VisuShrink	SureShrink	BayeShrink	Neighblock	Adaptive VisuShrink
RMSE	0.0322	0.0216	0.0242	0.0225	0.0188
SSIM	0.9400	0.9467	0.9344	0.9433	0.9522
BC	0.9780	0.9885	0.9887	0.9835	0.9882
Contrast	0.0965	0.0968	0.0964	0.0962	0.0968

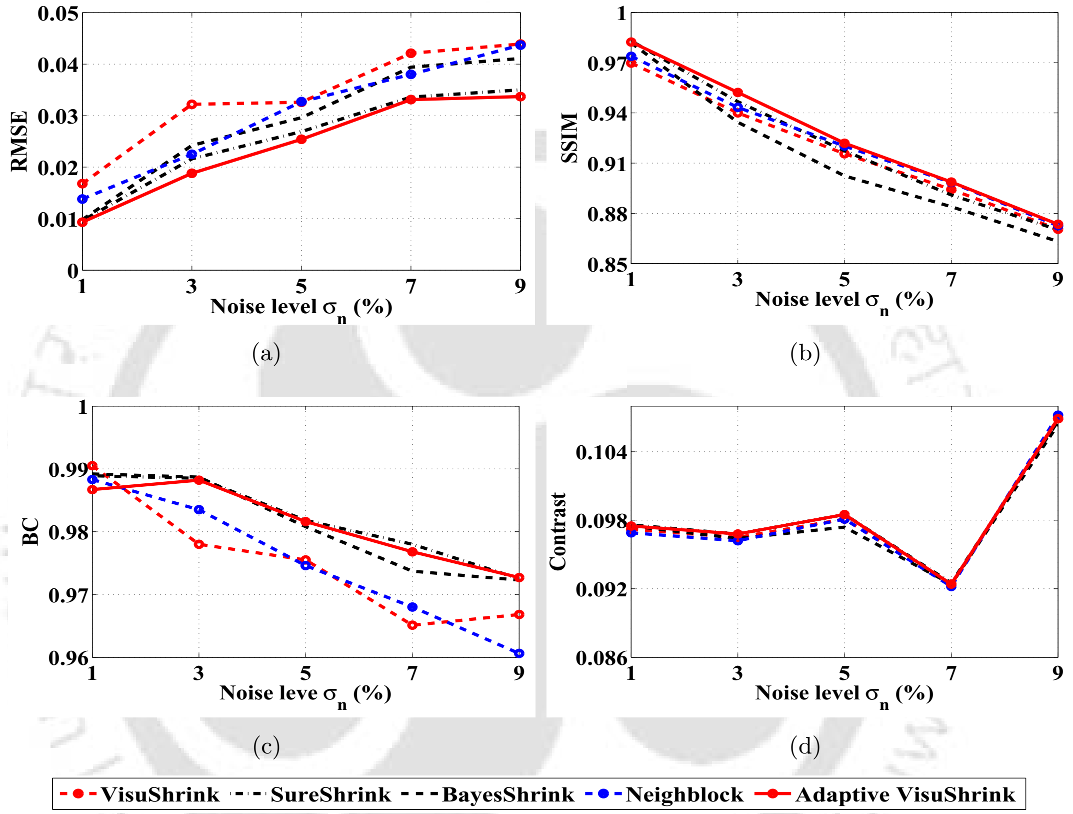

(a) (b) (c) (d)

Figure 8.5: Comparison of wavelet thresholding methods in denoising the simulated T1 weighted axial MR image at varying noise levels. The original image is shown in Fig. 8.4(a). (a) RMSE versus the noise level σ_n (b) SSIM versus the noise level σ_n (c) BC value versus the noise level σ_n (d) Contrast versus the noise level σ_n. Original contrast = 0.0987.

This is particularly more in BayesShrink method and hence, the SSIM value has decreased. The selection of neighborhood in adaptive VisuShrink technique has varied the extent of smoothing in each region and hence, it resulted in a sharp as well as a smooth image. The above can be implied from the values in Table-8.2. The comparative plots of the denoising results obtained for different noise levels are shown in Fig. 8.5. Cumulatively, the performance of adaptive VisuShrink is better than the other considered wavelet thresholding methods.

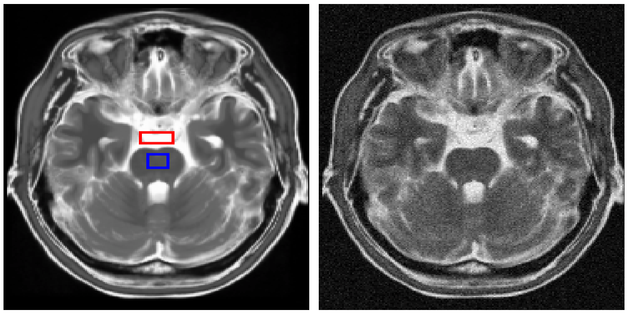

(a) Original image (b) Noisy image

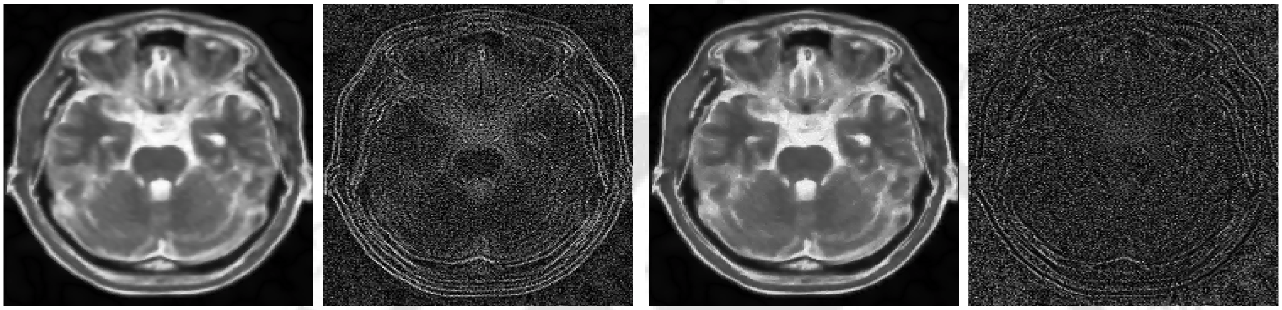

(c) **VisuShrink**-Denoised image and its residual (d) **SureShrink**-Denoised image and its residual

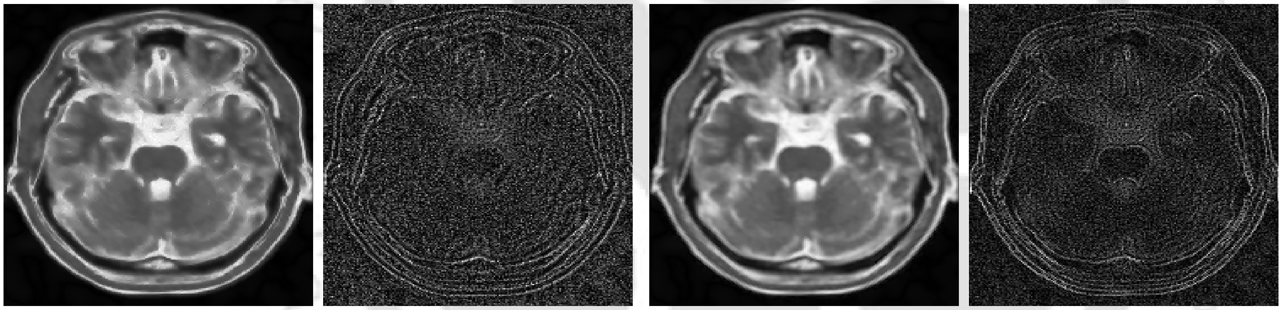

(e) **BayesShrink**-Denoised image and its residual (f) **Neighblock**-Denoised image and its residual

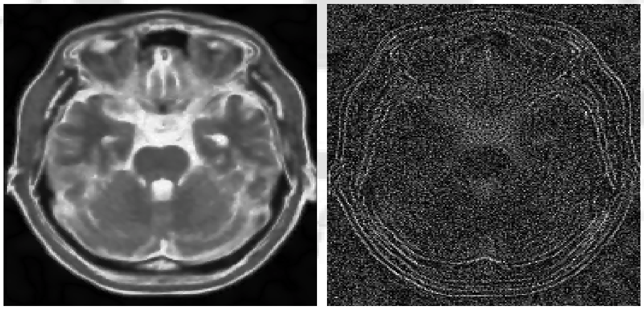

(g) **Adaptive VisuShrink**-Denoised image and its residual

Figure 8.6: Comparison of the results obtained for the noisy simulated T2 weighted axial MR image obtained using wavelet thresholding methods. Original image is corrupted by 5% noise level. The region within the box represents the low intensity and the high intensity ROI's chosen for calculating the contrast. The contrast in the original image is 0.5026.

Table 8.3: Values of the similarity metrics obtained for 5% noise level. The denoised T2 weighted axial MR images are shown in Fig. 8.6.

	VisuShrink	SureShrink	BayeShrink	Neighblock	Adaptive VisuShrink
RMSE	0.0457	0.0438	0.0437	0.0485	0.0406
SSIM	0.8921	0.9171	0.9013	0.8909	0.9137
BC	0.9748	0.9743	0.9773	0.9728	0.9796
Contrast	0.5013	0.5017	0.5012	0.5018	0.5017

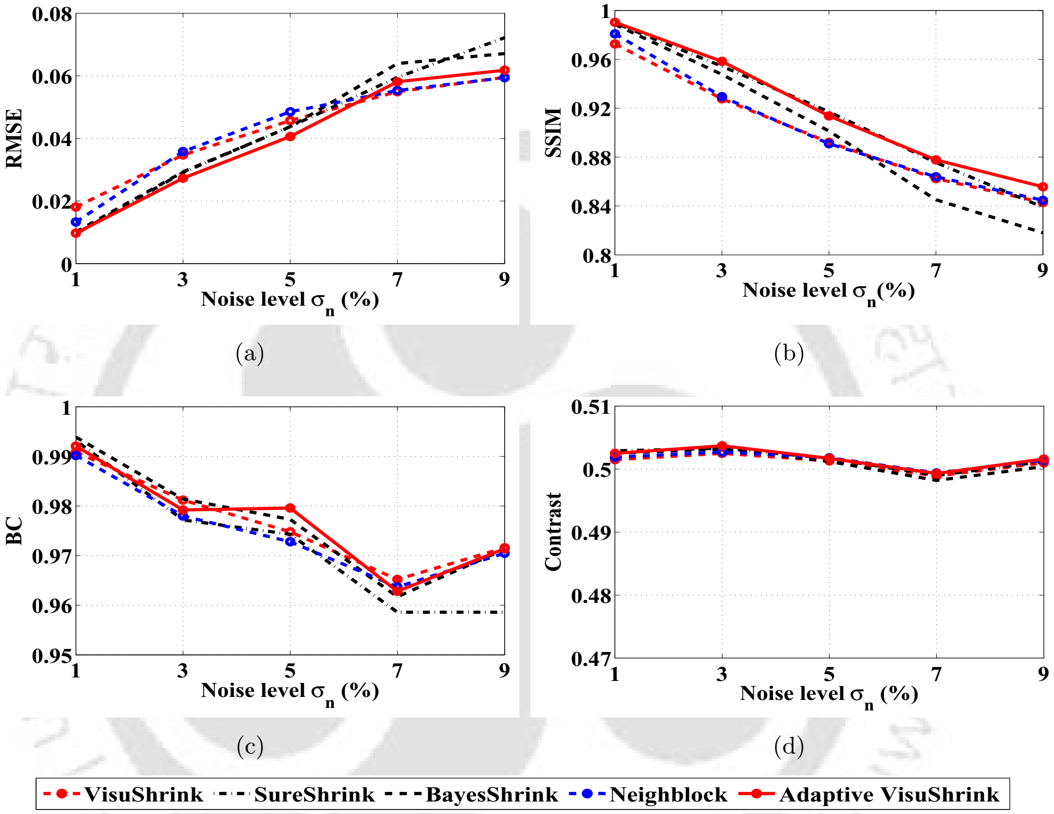

Figure 8.7: Comparison of wavelet thresholding methods in denoising the simulated T2 weighted axial MR image at varying noise levels. The original image is shown in Fig. 8.6(a). (a) RMSE versus the noise level σ_n (b) SSIM versus the noise level σ_n (c) BC value versus the noise level σ_n (d) Contrast versus the noise level σ_n. Original contrast = 0.5026.

The results of a simulated T2 weighted MR image corrupted by 5% of noise level are given in Fig. 8.6. This image consists of high contrast structural details and they can be used as the reference regions to perceive the difference between the denoising results. The excessive smoothing in VisuShrink has blurred the image details.

The SureShrink and the BayesShrink methods performed comparatively better. Particularly, SureShrink method has given good denoising performance and it is due to its suitability to the high structural characteristics of the image. However, some of the noise coefficients with large magnitude contained in the high intensity regions are retained without filtering. In the case of BayesShrink, despite the smoothing in flat regions, noise coefficients in the high intensity regions were not filtered. Alternately, the Neighblock method has also resulted in excessive smoothing. A good compromise is obtained in the adaptive VisuShrink method and it can be observed that the high intensity regions are sufficiently filtered as in VisuShrink and the details are also preserved as in SureShrink. The values of the quality metrics computed for 5% noise level is given in Table-8.3

The experiments are repeated for varying noise levels and the results are given in the plots in Fig. 8.7. From these plots, we can infer that the denoising performance of adaptive VisuShrink is consistent and is better than the other techniques.

Similarly to the simulated images, two clinical MR images with different characteristics are considered for evaluation. The denoising results obtained for the clinical T1 weighted MR image corrupted by 5% of noise level are presented in Fig. 8.8. The values of the quality metrics obtained for this image are tabulated in Table-8.4. Though the values of RMSE show significant difference, the SSIM value obtained for the thresholding methods suggests that the denoised images does not show any perceptual difference. The same can be verified from the denoised and the residual images illustrated in Fig. 8.8. This is expected because; the clinical T1 weighted MR image considered has more flat regions and so, it is sufficiently smooth. Similar to RMSE, the value of BC also shows significant difference. The value of BC is high for adaptive VisuShrink and it implies that the intensity distribution of the denoised image is close to the original noise-free image.

However, as the noise level the performance of adaptive VisuShrink in terms of BC has reduced drastically and is due to the choice of ε and neighborhood size. The image is sufficiently smooth within its range and so the value of ς has to be high. Through experiments, we verified that for large values of ς the value of BC increased almost maintaining the same value of SSIM. The experiments are repeated for varying noise levels and the denoising results are presented through the plots in Fig. 8.9.

The denoising results of the clinical T2 weighted MR image corrupted by 5% noise level are given in Fig. 8.10. This image consists of more structural variations and hence, SureShrink and adaptive VisuShrink methods yields better denoising results.

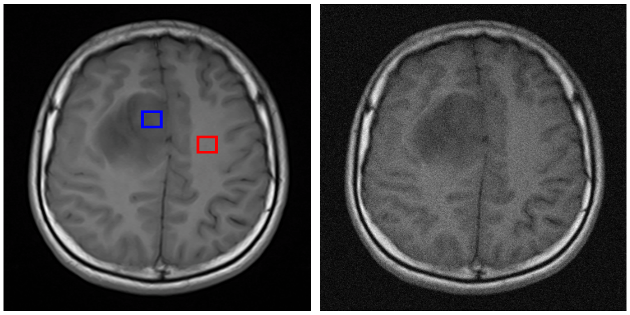

(a) Original image (b) Noisy image

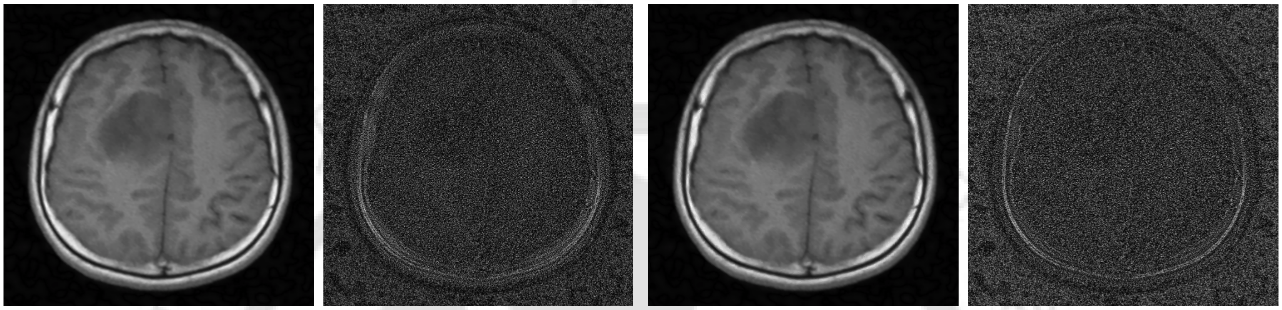

(c) **VisuShrink**-Denoised image and its residual (d) **SureShrink**-Denoised image and its residual

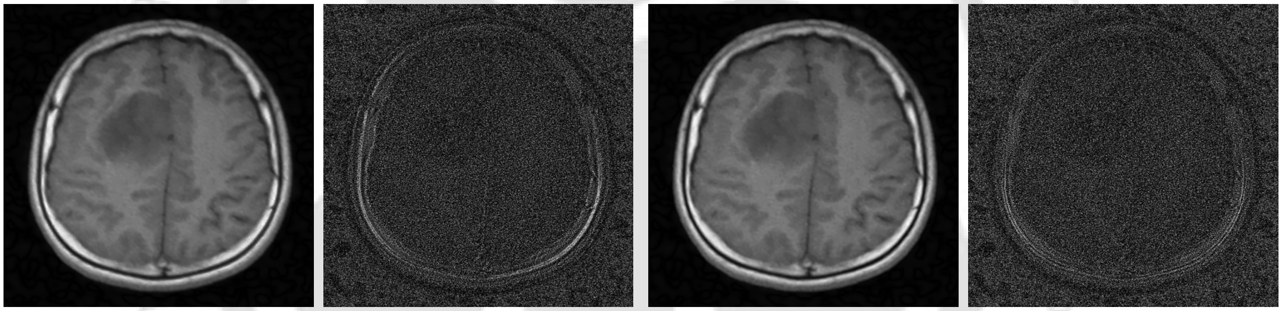

(e) **BayesShrink**-Denoised image and its residual (f) **Neighblock**-Denoised image and its residual

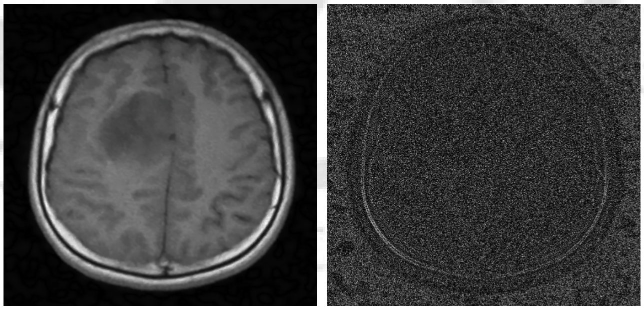

(g) **Adaptive VisuShrink**-Denoised image and its residual

Figure 8.8: Comparison of the results obtained for the noisy clinical T1 weighted axial MR image obtained using wavelet thresholding methods. Original image is corrupted by 5% noise level. The region within the box represents the low intensity and the high intensity ROI's chosen for calculating the contrast. The contrast in the original image is 0.1709.

Table 8.4: Values of the similarity metrics obtained for 5% noise level. The denoised T1 weighted axial clinical MR images are shown in Fig. 8.8.

	VisuShrink	SureShrink	BayeShrink	Neighblock	Adaptive VisuShrink
RMSE	0.0180	0.0157	0.0198	0.0154	0.0143
SSIM	0.9752	0.9752	0.9726	0.9749	0.9752
BC	0.9626	0.9454	0.9601	0.9723	0.9752
Contrast	0.1723	0.1723	0.1724	0.1722	0.1722

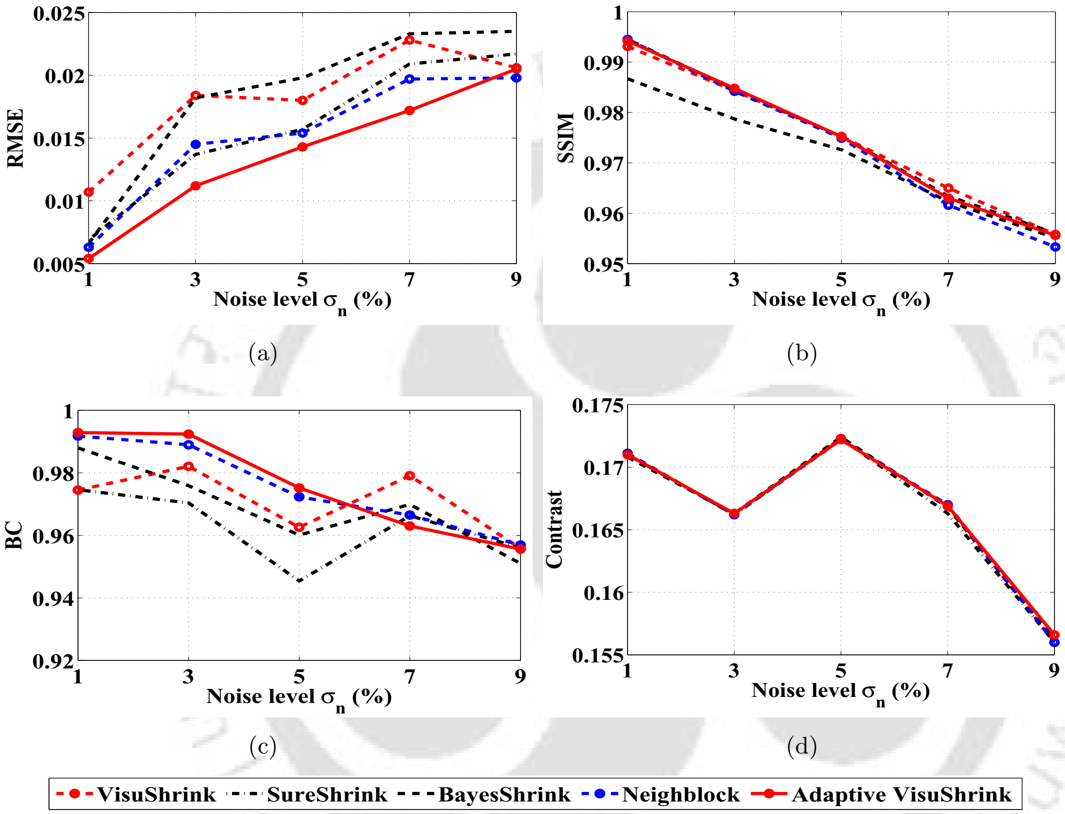

(a) (b)

(c) (d)

Figure 8.9: Comparison of wavelet thresholding methods in denoising the clinical T1 weighted axial MR image at varying noise levels. The original image is shown in Fig. 8.8(a). (a) RMSE versus the noise level σ_n (b) SSIM versus the noise level σ_n (c) BC value versus the noise level σ_n (d) Contrast versus the noise level σ_n. Original contrast = 0.1709.

BayesShrink technique performs well for low noise level and as the noise level increase the Bayes threshold attempts to extent the limit of smoothing. This causes most of high magnitude noisy coefficients to remain unfiltered. The VisuShrink and the Neighblock methods resulted in excessive smoothing.

The denoising results so far confirms the validity of the adaptive VisuShrink method for denoising under different noise conditions. From the discussion, it is clear that the adaptive VisuShrink method performs better than the conventional wavelet thresholding techniques.

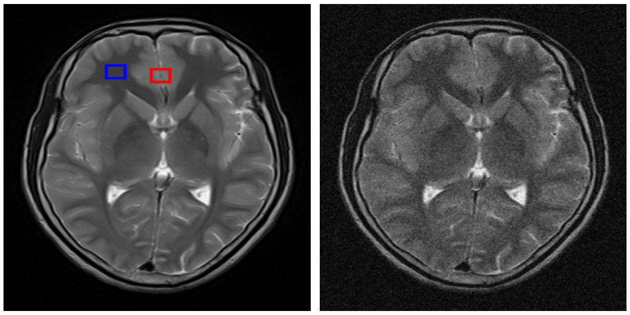

(a) Original image (b) Noisy image

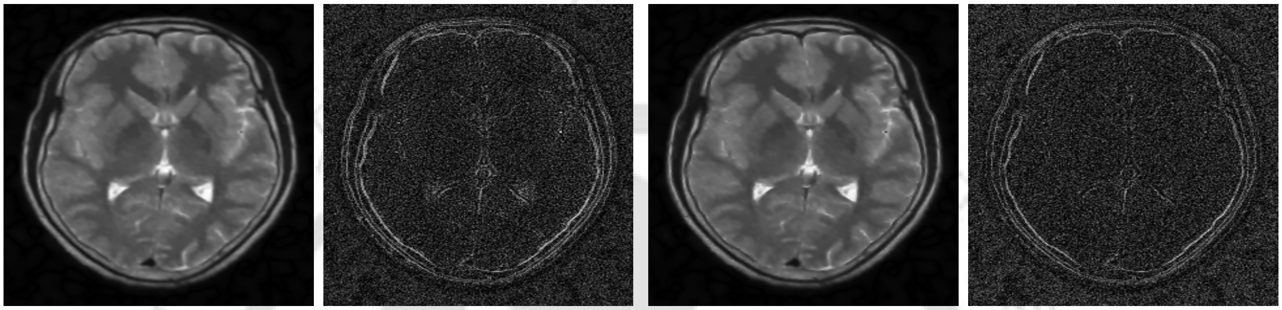

(c) **VisuShrink**-Denoised image and its residual (d) **SureShrink**-Denoised image and its residual

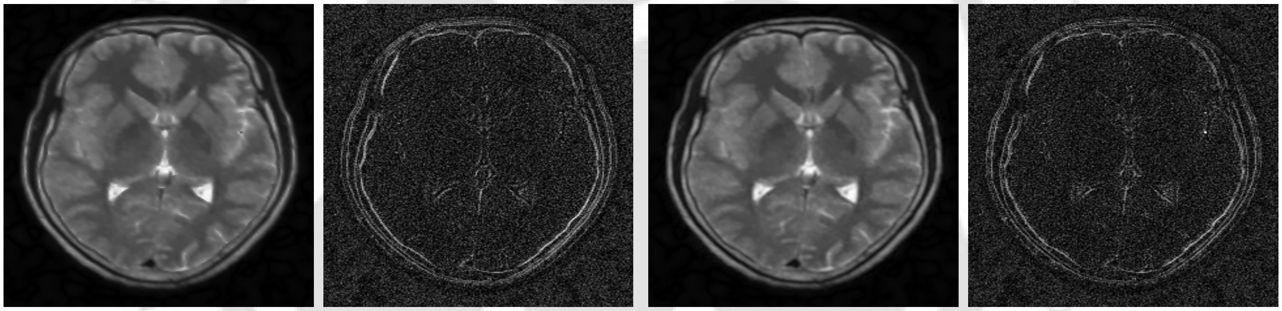

(e) **BayesShrink**-Denoised image and its residual (f) **Neighblock**-Denoised image and its residual

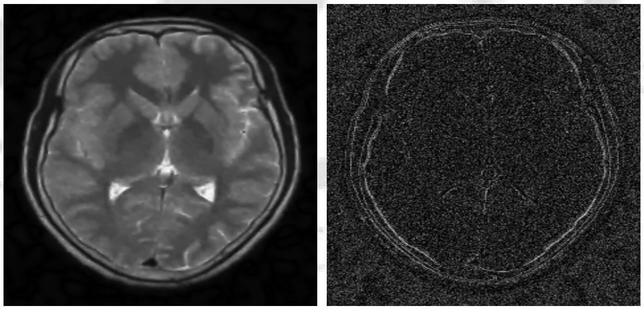

(g) **Adaptive VisuShrink**-Denoised image and its residual

Figure 8.10: Comparison of the results obtained for the noisy clinical T2 weighted axial MR image obtained using wavelet thresholding methods. Original image is corrupted by 5% noise level. The region within the box represents the low intensity and the high intensity ROI's chosen for calculating the contrast. The contrast in the original image is 0.2886.

Table 8.5: Values of the similarity metrics obtained for 5% noise level. The denoised T2 weighted axial clinical MR images are shown in Fig. 8.10.

	VisuShrink	SureShrink	BayeShrink	Neighblock	Adaptive VisuShrink
RMSE	0.0402	0.0336	0.0417	0.0398	0.0326
SSIM	0.9121	0.9216	0.9030	0.9113	0.9240
BC	0.9637	0.9524	0.9567	0.9648	0.9534
Contrast	0.2848	0.2845	0.2886	0.2850	0.2847

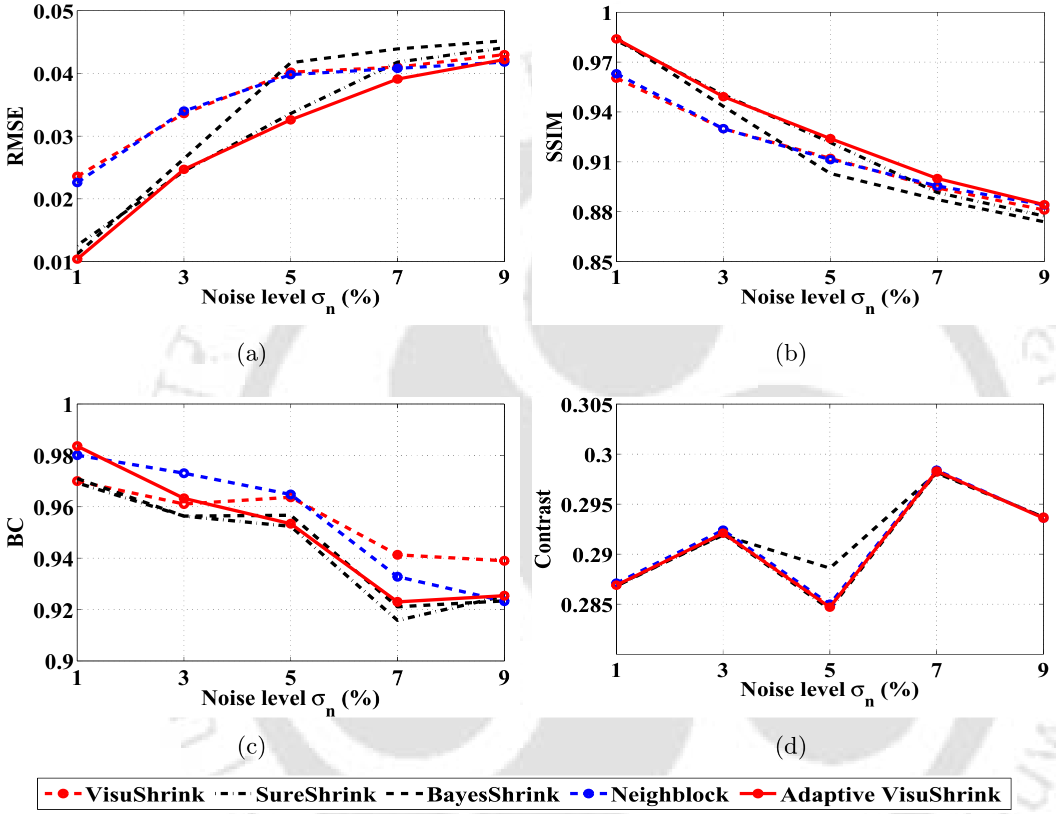

(a) (b)

(c) (d)

Figure 8.11: Comparison of wavelet thresholding methods in denoising the clinical T2 weighted axial MR image at varying noise levels. The original image is shown in Fig. 8.10(a). (a) RMSE versus the noise level σ_n (b) SSIM versus the noise level σ_n (c) BC value versus the noise level σ_n (d) Contrast versus the noise level σ_n. Original contrast = 0.2886.

The method adapts like SureShrink in the case of low noise levels and it is made equivalent to VisuShrink as the noise level increase. Therefore, for lower noise level adaptive VisuShrink is optimal in sense of MSE and for higher noise level it becomes optimal with respect to smoothness.

The other important advantage of adaptive VisuShrink is its simplicity. The extent of smoothing in adaptive VisuShrink can be easily controlled by varying the neighborhood size and the limiting factor ε.

8.5.2 Evaluation of bilateral filtering over wavelet thresholding

This section discusses about MR image denoising using the WD-all-band-BF. The acronym WD-all-band-BF refers to bilateral filtering of all the sub-bands obtained in the undecimated wavelet decomposition. The performance of the method solely depends on the choice of the bilateral filter parameters σ_r, σ_d and R_{neigh}. Also, the optimal values of these parameters are different for the approximation and the detail sub-bands. The choice of these parameter values for approximation and the detail sub-bands and the denoising results are discussed subsequently.

8.5.2.1 Parameter selection

The optimal choice of the bilateral filter parameters for smoothing the approximation coefficients at the coarsest scale was already discussed in detail in chapter 6. Accordingly the filter parameters are chosen as $\sigma_r = 1.5\sigma_n$, $\sigma_d = 5$ and $R_{neigh} = 7$.

The same values cannot be assigned for smoothing in the detail sub-bands, because the detail sub-bands are sparse and obviously the noise contained in the detail sub-bands varies at each scale. The bilateral filter parameter σ_r depends on the amount of noise contained in the sub-band to be smoothened. Hence, a level dependent choice of σ_r based on the statistical model of noise at each scale is chosen according to Eq. (8.21) and (8.22). The neighborhood size is fixed as $R_{neigh} = 7$. The value of the domain parameter σ_d for smoothing the detail sub-bands must be chosen carefully. Due to the sparsity of detail sub-bands, large values of σ_d will result in excessive smoothing and loss of image details. Hence, the optimal choice $\sigma_d = 1$ is employed.

8.5.2.2 Denoising results

The experiments are performed on simulated and clinical MR images with varying structural characteristics and under different noise conditions. The performance of WD-all-band-BF is compared with WD-BF (NeighShrink) and the adaptive VisuShrink thresholding discussed in the previous section. It should be remembered that adaptive VisuShrink thresholding is also performed in the WD-BF framework.

The results of the experiments performed on a simulated T1 weighted axial MR image corrupted by 3% noise level are shown in Fig. 8.12 and the corresponding values of quality metrics are tabulated in Table-8.6. From the denoised images it can be observed that bilateral filtering of detail subbands

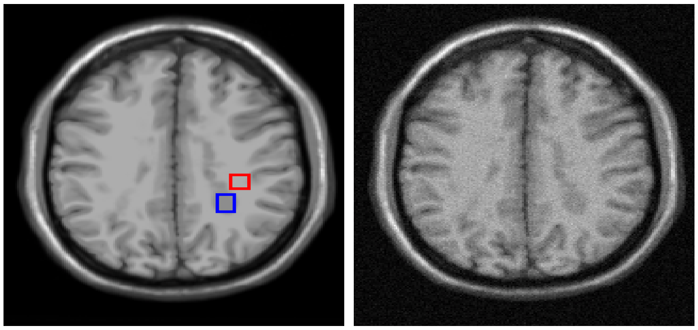

(a) Original image (b) Noisy image

DENOISED IMAGES

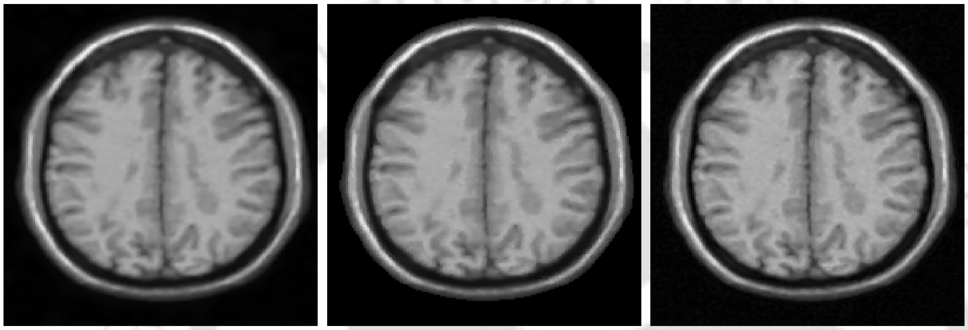

(c) WD-BF (NeighShrink) (d) Adaptive VisuShrink (e) WD-all-band-BF

RESIDUAL IMAGES

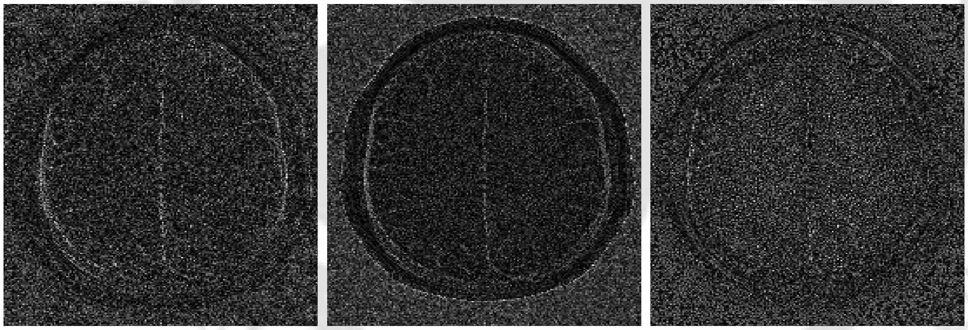

(f) WD-BF (NeighShrink) (g) Adaptive VisuShrink (h) WD-all-band-BF

Figure 8.12: Denoising results of simulated T1 weighted axial MR image corrupted by 3% noise level. The region within the boxes represent the low intensity ROI and the high intensity ROI chosen for calculating the contrast. The original contrast is 0.0940.

Table 8.6: Comparison of the denoising techniques based on the similarity metrics computed between the original and denoised T1 weighted axial MR image. The simulated noisy image contains 3% of noise.

	WD-BF (NeighShrink)	Adaptive VisuShrink	WD-all-band-BF
RMSE	0.0180	0.0172	0.0131
SSIM	0.9701	0.9659	0.9722
BC	0.9255	0.9445	0.9564
Contrast	0.0839	0.0837	0.0865

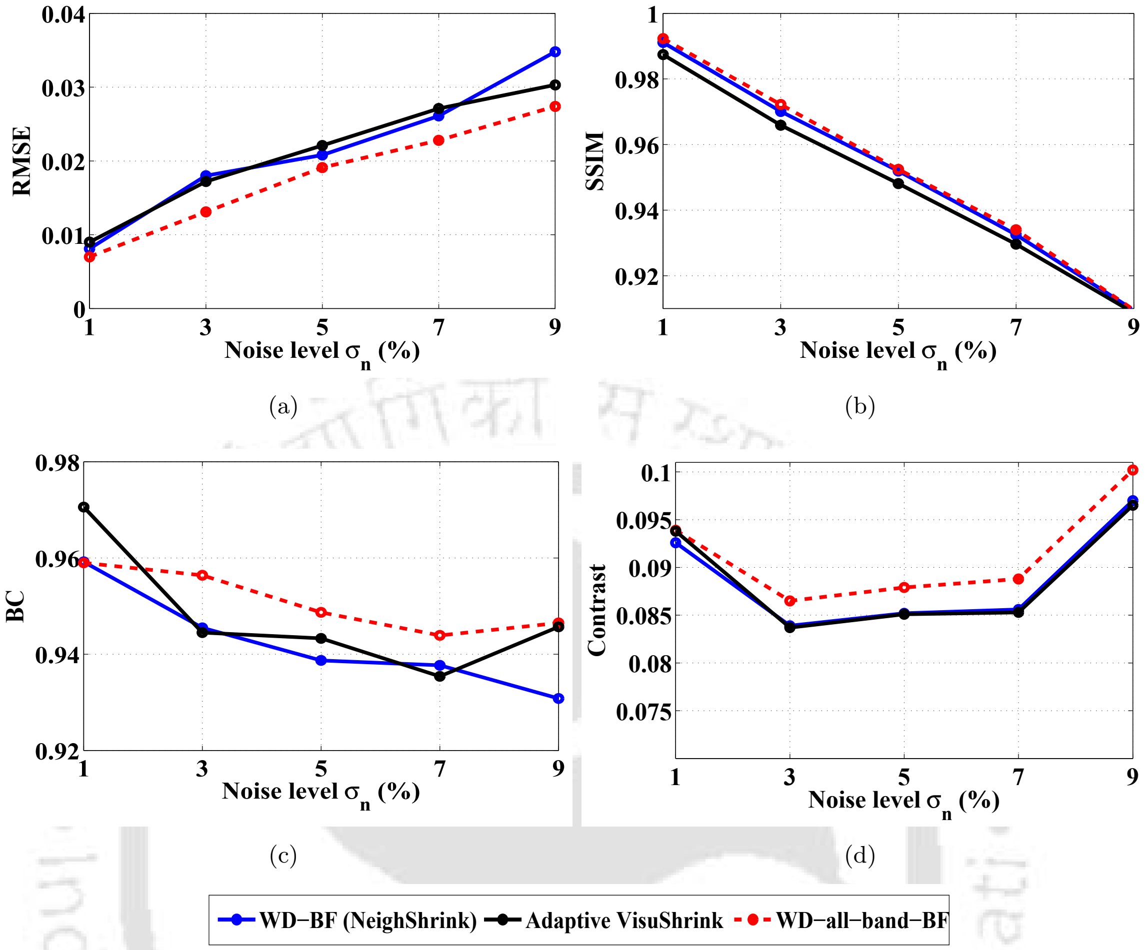

Figure 8.13: Comparative plot of denoising results obtained for the simulated T1 weighted axial MR image at varying noise levels. (a) RMSE versus the noise level σ_n (b) SSIM versus the noise level σ_n (c) BC value versus the noise level σ_n (d) Contrast versus the noise level σ_n. Original contrast = 0.0940.

has preserved the sharpness of the image better than the thresholding based WD-BF approaches. Also, it has ensured smoothing of all the noise coefficients. The residual images illustrates the effects of smoothing on the structural details of the MR image. It is clearly evident that the WD-all-band-BF offers comparatively more controlled smoothing in the high frequency regions. As a result, the structural features of the MR image are better preserved in WD-all-band-BF.

The experiments are repeated on this image by varying the noise level. The plots in Fig. 8.13 give the comparisons of the considered methods. It can be observed that WD-all-band-BF is superior with respect to RMSE. This MR image consists of mostly smooth regions and hence, the values of SSIM obtained for WD-all-band-BF and WD-BF (NeighShrink) are almost same. Also, it should be noted that the performance of the proposed adaptive VisuShrink method is also comparable.

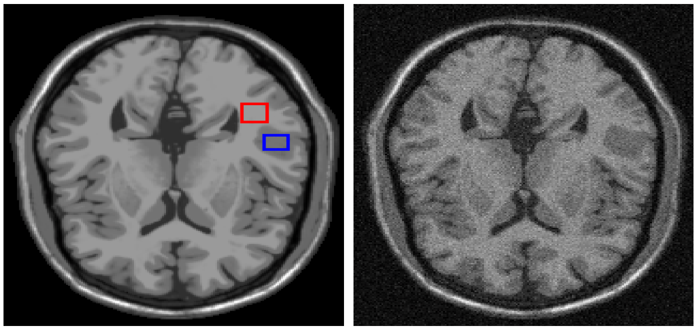

(a) Original image (b) Noisy image

DENOISED IMAGES

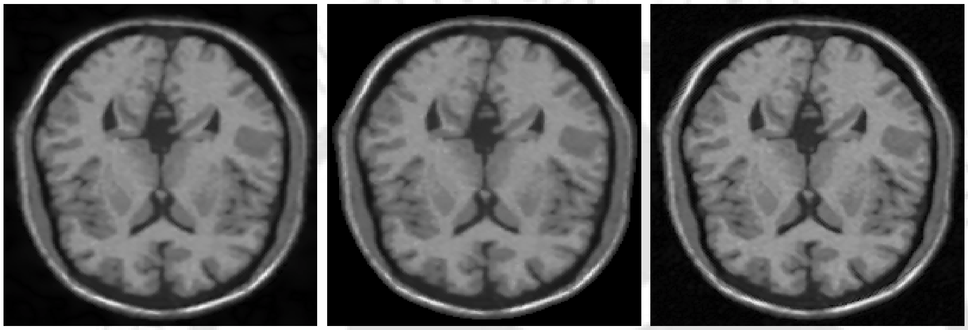

(c) WD-BF (NeighShrink) (d) Adaptive VisuShrink (e) WD-all-band-BF

RESIDUAL IMAGES

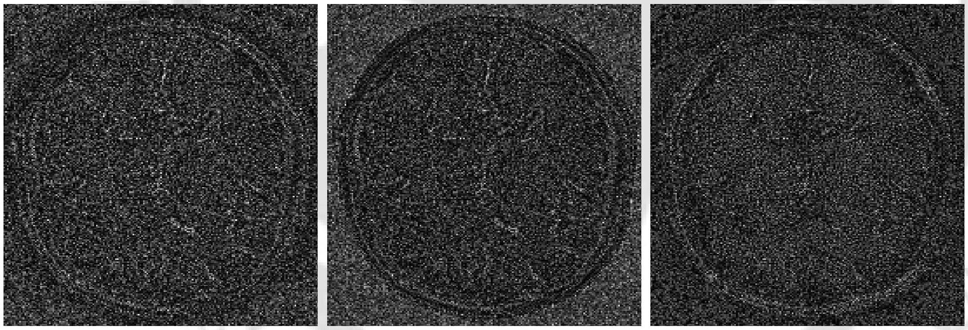

(f) WD-BF (NeighShrink) (g) Adaptive VisuShrink (h) WD-all-band-BF

Figure 8.14: Denoising results of simulated T1 weighted axial MR image corrupted by 5% noise level. The region within the boxes represent the low intensity ROI and the high intensity ROI chosen for calculating the contrast. The original contrast is 0.1435.

Table 8.7: Comparison of the denoising techniques based on the similarity metrics computed between the original and denoised T1 weighted axial MR image. The simulated noisy image contains 5% of noise.

	WD-BF (NeighShrink)	Adaptive VisuShrink	WD-all-band-BF
RMSE	0.0310	0.0317	0.0252
SSIM	0.9230	0.9205	0.9316
BC	0.8841	0.8514	0.9333
Contrast	0.1383	0.1380	0.1396

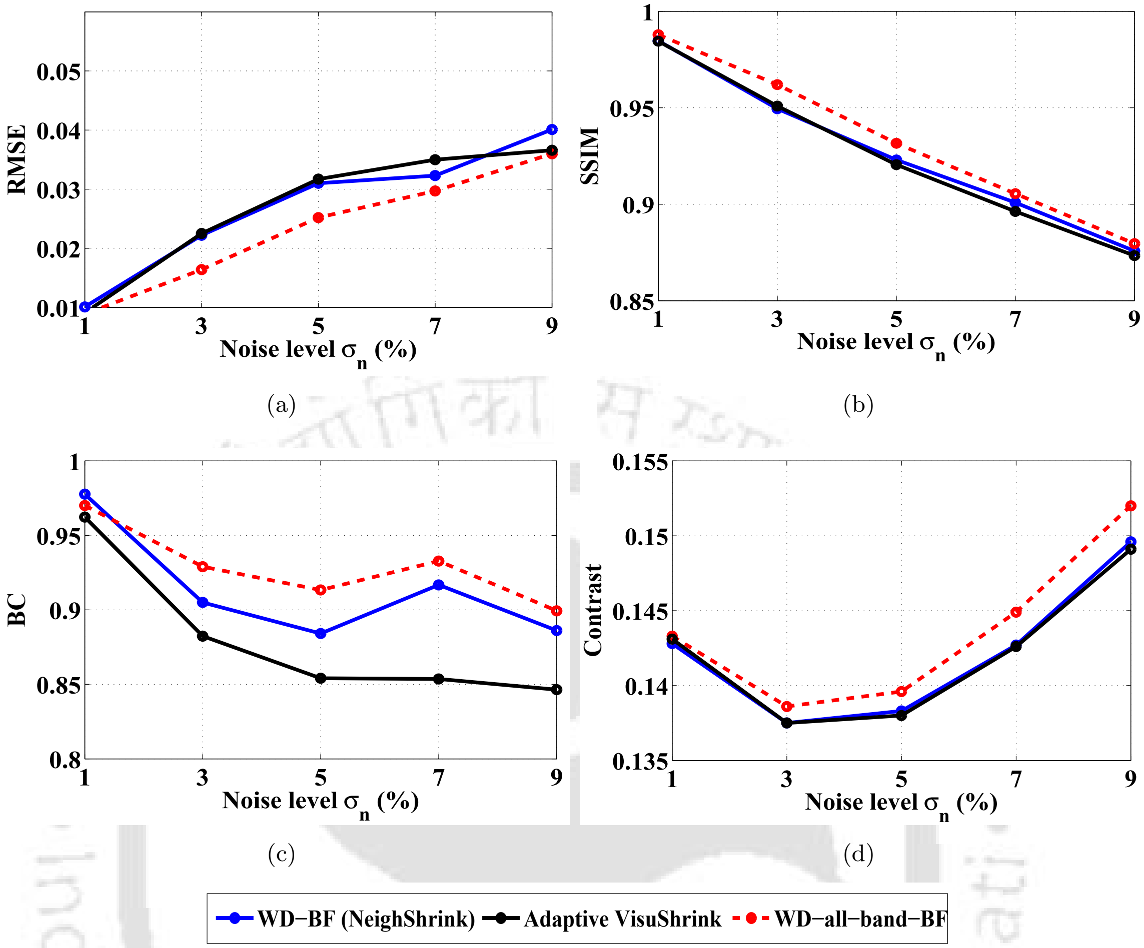

Figure 8.15: Comparative plot of denoising results obtained for the simulated T1 weighted axial MR image at varying noise levels. (a) RMSE versus the noise level σ_n (b) SSIM versus the noise level σ_n (c) BC value versus the noise level σ_n (d) Contrast versus the noise level σ_n. Original contrast = 0.1435.

The denoising results of an other simulated T1 weighted axial MR image corrupted by 5% noise level are shown in Fig. 8.14 and the corresponding values of quality metrics are tabulated in Table-8.7. The considered MR image consists of large structural variations and hence, there is considerable difference in the performance of the denoising methods. Through visual inspection of the denoised and the residual images, it is clear that WD-all-band-BF performs better in preserving the image structures and the inter-tissue contrast.

Except for the decrease in the values of BC, the adaptive VisuShrink method is almost good as WD-BF (NeighShrink). The value of BC is very sensitive to slight variations in the intensity distribution. The variations may be due to excessive smoothing or insufficiency in smoothing. In this case the decrease of BC in adaptive VisuShrink is due to the insufficiency in smoothing for increasing noise levels.

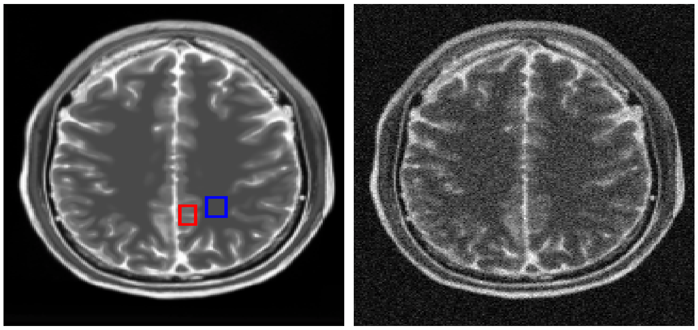

(a) Original image (b) Noisy image

DENOISED IMAGES

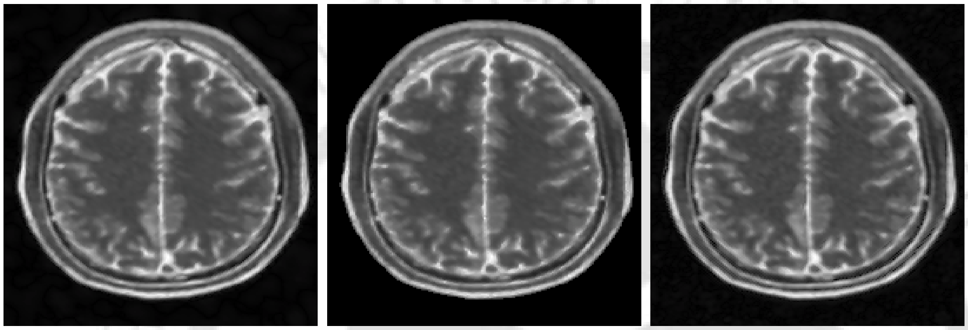

(c) WD-BF (NeighShrink) (d) Adaptive VisuShrink (e) WD-all-band-BF

RESIDUAL IMAGES

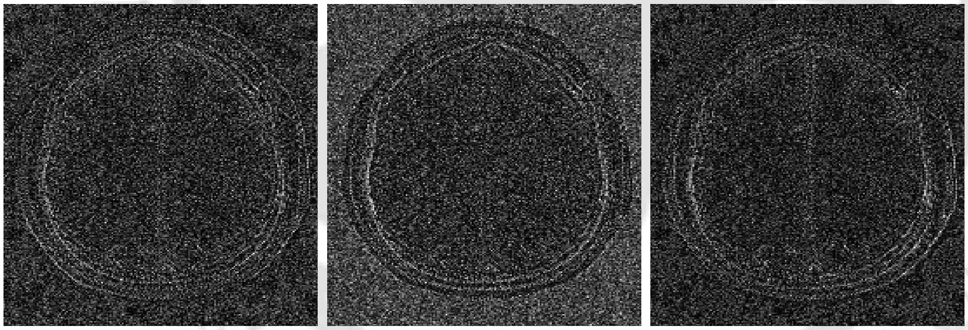

(f) WD-BF (NeighShrink) (g) Adaptive VisuShrink (h) WD-all-band-BF

Figure 8.16: Denoising results of simulated T2 weighted axial MR image corrupted by 7% noise level. The region within the boxes represent the low intensity ROI and the high intensity ROI chosen for calculating the contrast. The original contrast is 0.1981.

Table 8.8: Comparison of the denoising techniques based on the similarity metrics computed between the original and denoised T2 weighted axial MR image. The simulated noisy image contains 7% of noise.

	WD-BF (NeighShrink)	Adaptive VisuShrink	WD-all-band-BF
RMSE	0.0402	0.0448	0.0328
SSIM	0.9304	0.9242	0.9391
BC	0.9139	0.8536	0.9426
Contrast	0.1954	0.1849	0.1942

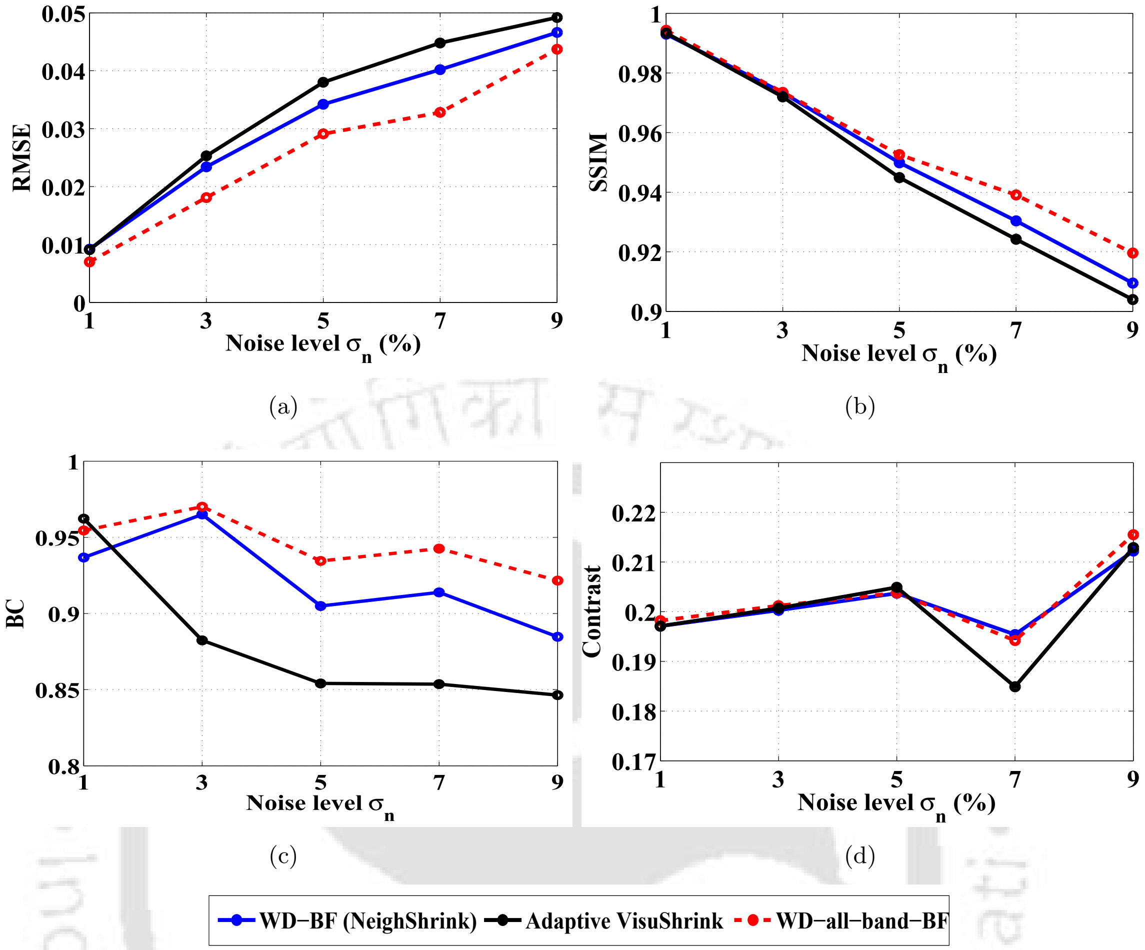

(a) (b)

(c) (d)

Figure 8.17: Comparative plot of denoising results obtained for the simulated T2 weighted axial MR image at varying noise levels. (a) RMSE versus the noise level σ_n (b) SSIM versus the noise level σ_n (c) BC value versus the noise level σ_n (d) Contrast versus the noise level σ_n. Original contrast = 0.1981.

The experiments are repeated on this image by varying the noise level. The denoising results are given in the plots in Fig. 8.15. From these results, we can confirm the supremacy of WD-all-band-BF in feature preserved MR image denoising.

The denoising results of a simulated T2 weighted axial MR image corrupted by 7% noise level are shown in Fig. 8.16 and the corresponding values of quality metrics are tabulated in Table-8.8. This MR image is considerably smooth and it consist of high contrast detail structures that constitutes the high frequency regions. Denoising using WD-all-band-BF is superior to the other two considered approaches. Particularly, for higher noise levels WD-all-band-BF shows the comparatively significant improvement in the denoising performance. Further evaluations are done by repeating the experiments for different noise levels. The plots of the denoising results are shown in Fig. 8.17.

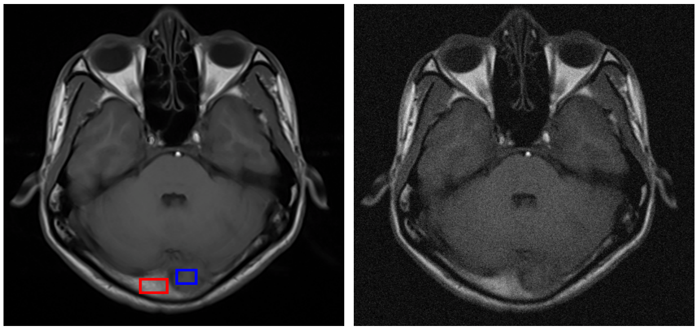

(a) Original image (b) Noisy image

DENOISED IMAGES

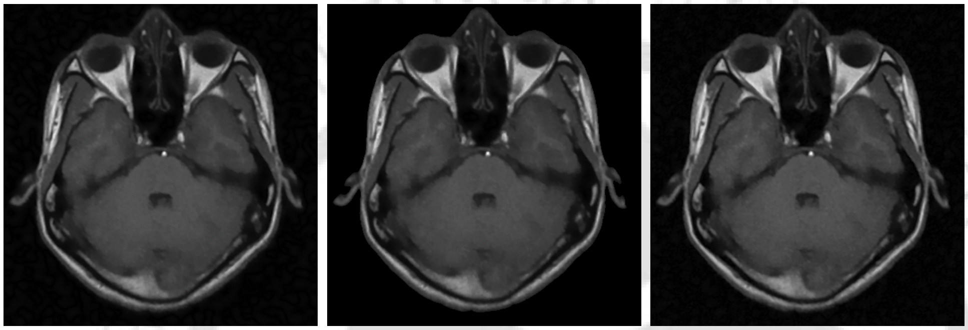

(c) WD-BF (NeighShrink) (d) Adaptive VisuShrink (e) WD-all-band-BF

RESIDUAL IMAGES

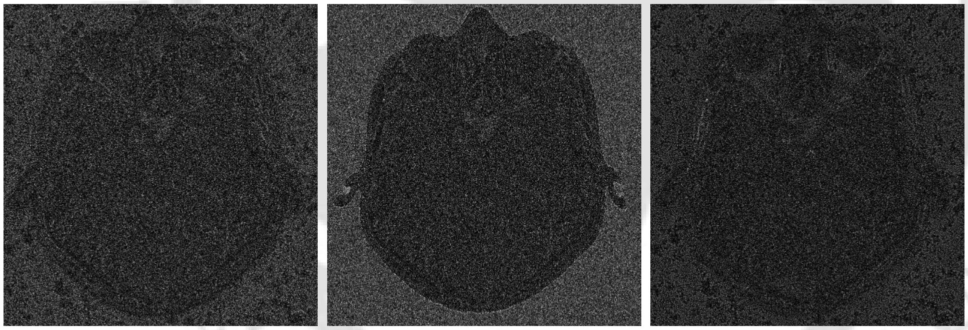

(f) WD-BF (NeighShrink) (g) Adaptive VisuShrink (h) WD-all-band-BF

Figure 8.18: Denoising results of clinical T1 weighted axial MR image corrupted by 5% noise level. The region within the boxes represent the low intensity ROI and the high intensity ROI chosen for calculating the contrast. The original contrast is 0.3156.

Table 8.9: Comparison of the denoising techniques based on the similarity metrics computed between the original and denoised T1 weighted axial MR image. The clinical noisy image contains 5% of noise.

	WD-BF (NeighShrink)	Adaptive VisuShrink	WD-all-band-BF
RMSE	0.0153	0.0154	0.0133
SSIM	0.9602	0.9618	0.9611
BC	0.9855	0.9860	0.9883
Contrast	0.3191	0.3190	0.3196

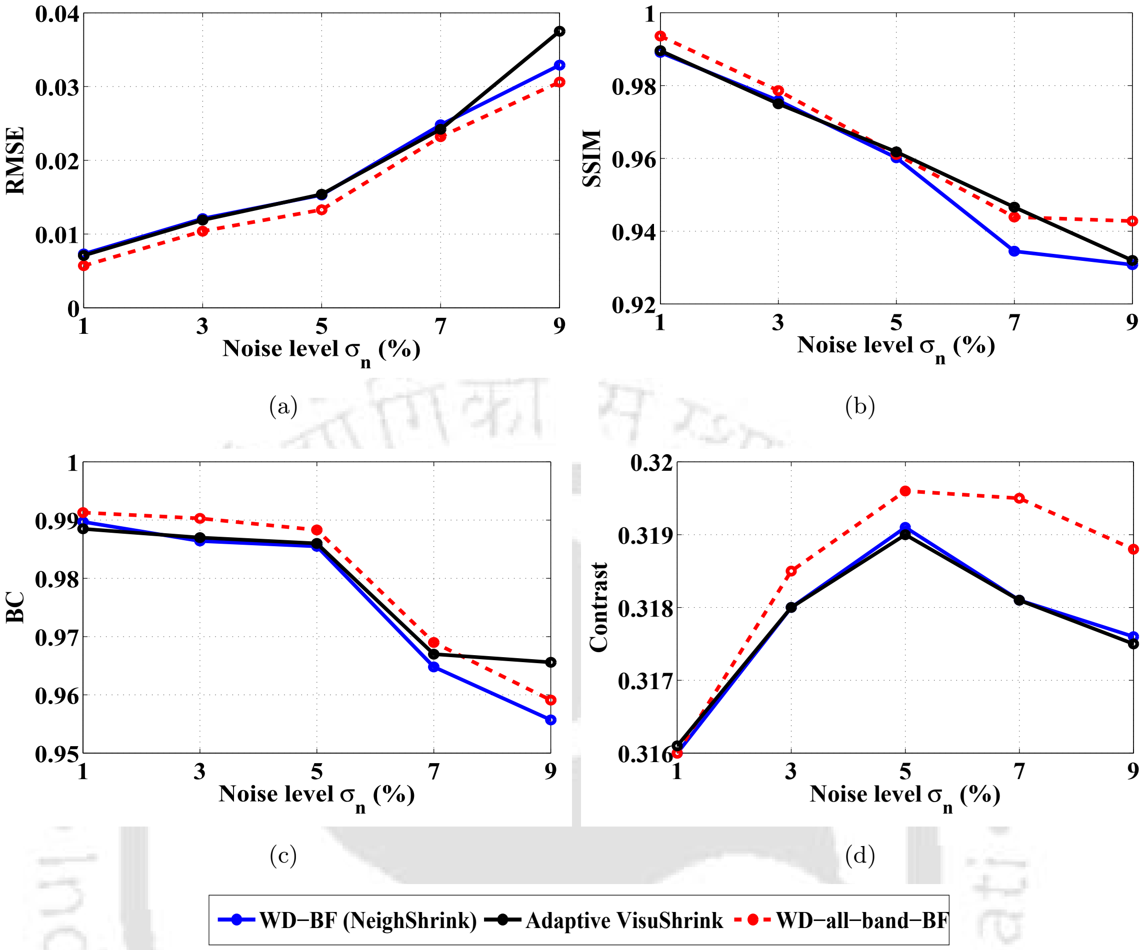

(a) (b)

(c) (d)

Figure 8.19: Comparative plot of denoising results obtained for the clinical T1 weighted axial MR image at varying noise levels. (a) RMSE versus the noise level σ_n (b) SSIM versus the noise level σ_n (c) BC value versus the noise level σ_n (d) Contrast versus the noise level σ_n. Original contrast = 0.3156.

The evaluations of the denoising methods on a clinical T1 weighted axial MR image corrupted by 5% noise level are shown in Fig. 8.18. The values of the quality metrics obtained for these results are tabulated in Table-8.9. This clinical MR image is considerably smooth and hence, the performance of WD-BF (NeighShrink),adaptive VisuShrink and WD-all-band-BF are almost same in terms of RMSE and SSIM. However, for higher noise levels, the performance of WD-all-band-BF is superior. The comparative plots for the denoising results obtained by varying the noise levels are shown in Fig. 8.19.

The denoising results of a clinical T2 weighted coronal MR image corrupted by 3% noise level are shown in Fig. 8.20. The values of the quality metrics obtained for these results are tabulated in Table-8.10.

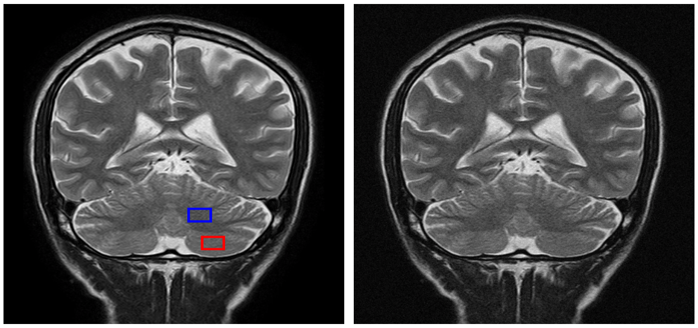

(a) Original image (b) Noisy image

DENOISED IMAGES

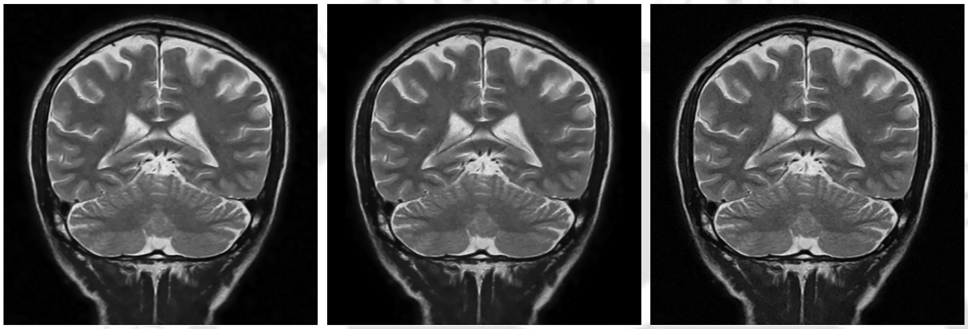

(c) WD-BF (NeighShrink) (d) Adaptive VisuShrink (e) WD-all-band-BF

RESIDUAL IMAGES

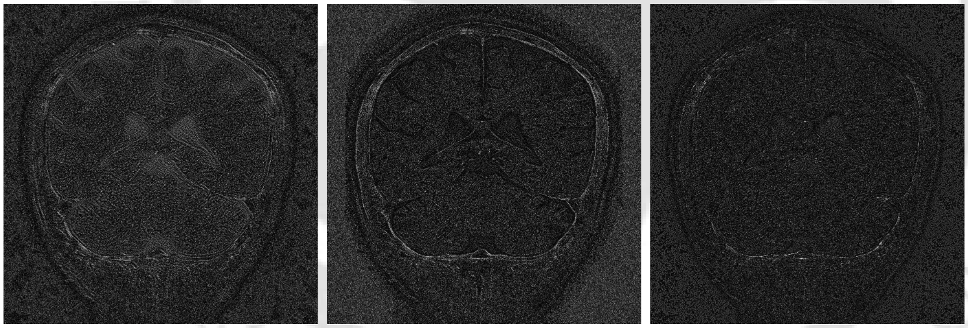

(f) WD-BF (NeighShrink) (g) Adaptive VisuShrink (h) WD-all-band-BF

Figure 8.20: Denoising results of clinical T2 weighted coronal MR image corrupted by 3% noise level. The region within the boxes represent the low intensity ROI and the high intensity ROI chosen for calculating the contrast. The original contrast is 0.4298.

Table 8.10: Comparison of the denoising techniques based on the similarity metrics computed between the original and denoised T2 weighted coronal MR image. The clinical noisy image contains 3% of noise.

	WD-BF (NeighShrink)	Adaptive VisuShrink	WD-all-band-BF
RMSE	0.0188	0.0236	0.0180
SSIM	0.9348	0.9192	0.9562
BC	0.8413	0.8759	0.8570
Contrast	0.4287	0.4286	0.4287

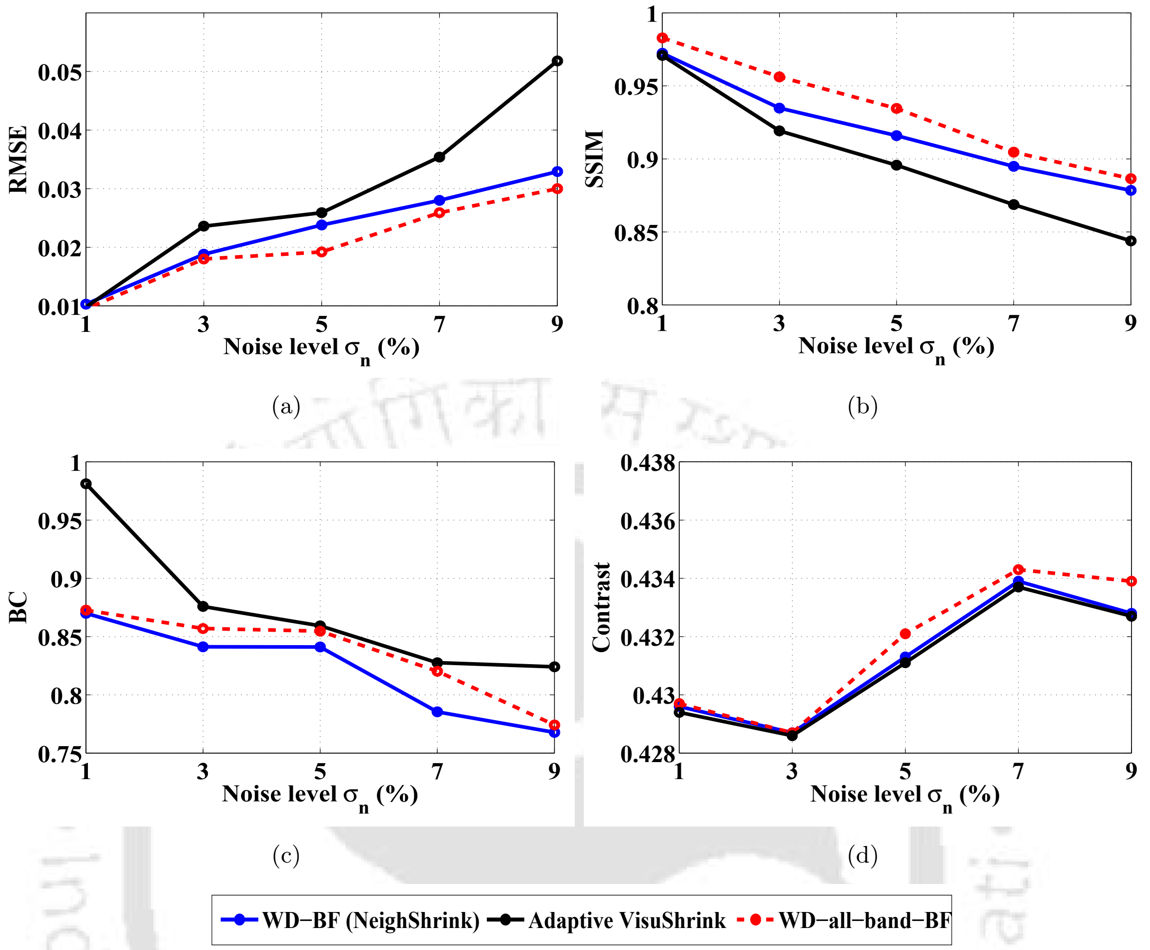

(a) (b)

(c) (d)

Figure 8.21: Comparative plot of denoising results obtained for the clinical T2 weighted coronal MR image at varying noise levels. (a) RMSE versus the noise level σ_n (b) SSIM versus the noise level σ_n (c) BC value versus the noise level σ_n (d) Contrast versus the noise level σ_n. Original contrast = 0.4298.

This clinical MR image has high structural variations and and hence, the performance of adaptive VisuShrink with respect to the RMSE and the SSIM values are comparatively poor.

As expected, WD-all-band-BF performs even better than WD-BF (NeighShrink). From the residual images, it is clearly evident that adaptive VisuShrink and WD-BF (NeighShrink) have resulted in excessive smoothing. While, WD-all-band-BF has preserved the sharpness of the structural details in the MR image. Despite the RMSE, SSIM and contrast obtained, the BC value for adaptive VisuShrink is very much better than the other two methods. Generally, the value of BC favors with respect to the smoothness of the compared distributions. In this case, adaptive VisuShrink provides better smoothing in the flat regions and hence higher the BC value. The comparative plots for the denoising results obtained by varying the noise levels are shown in Fig. 8.21.

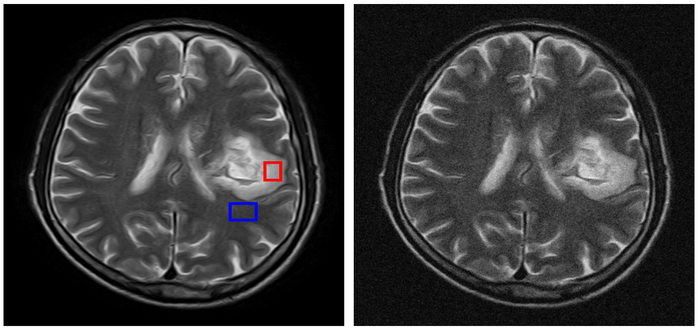

(a) Original image (b) Noisy image

DENOISED IMAGES

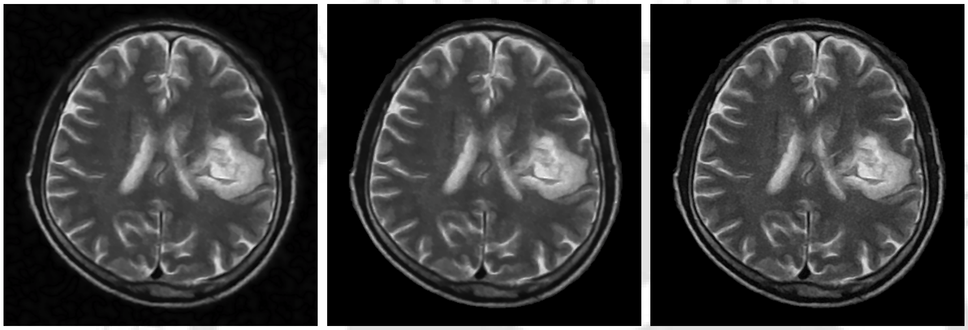

(c) WD-BF (NeighShrink) (d) Adaptive VisuShrink (e) WD-all-band-BF

RESIDUAL IMAGES

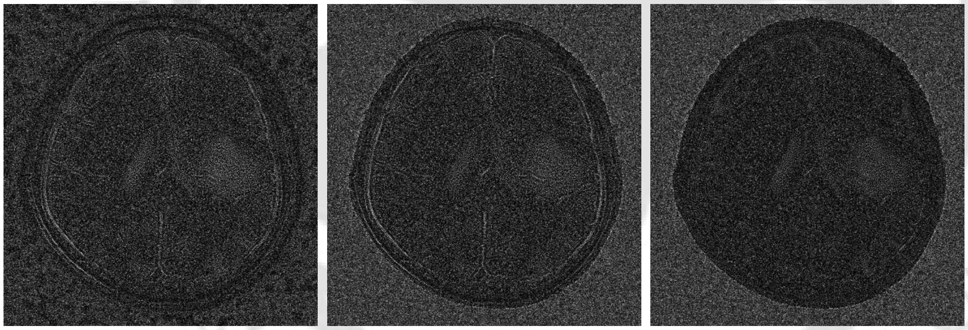

(f) WD-BF (NeighShrink) (g) Adaptive VisuShrink (h) WD-all-band-BF

Figure 8.22: Denoising results of clinical T2 weighted axial MR image corrupted by 5% noise level. The region within the boxes represent the low intensity ROI and the high intensity ROI chosen for calculating the contrast. The original contrast is 0.4148.

Table 8.11: Comparison of the denoising techniques based on the similarity metrics computed between the original and denoised T2 weighted axial MR image. The clinical noisy image contains 5% of noise.

	WD-BF (NeighShrink)	Adaptive VisuShrink	WD-all-band-BF
RMSE	0.0197	0.0202	0.0153
SSIM	0.9561	0.9541	0.9680
BC	0.9496	0.9426	0.9600
Contrast	0.4149	0.4150	0.4161

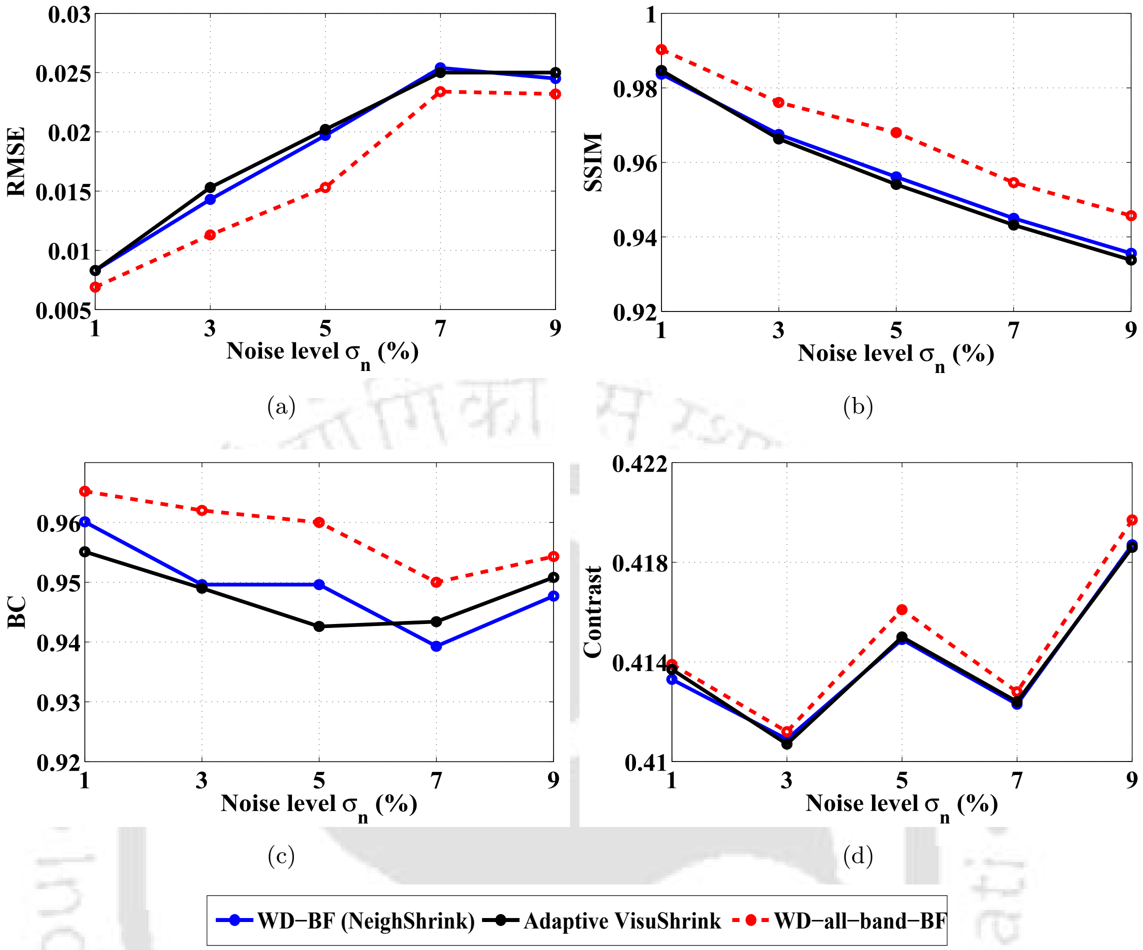

(a) (b)

(c) (d)

Figure 8.23: Comparative plot of denoising results obtained for the clinical T2 weighted axial MR image at varying noise levels. (a) RMSE versus the noise level σ_n (b) SSIM versus the noise level σ_n (c) BC value versus the noise level σ_n (d) Contrast versus the noise level σ_n. Original contrast = 0.4148.

The denoising results of another clinical T2 weighted axial MR image corrupted by 5% noise level are shown in Fig. 8.22. The values of the quality metrics obtained for these results are tabulated in Table-8.11. This clinical MR image has high structural variations and and hence, the performance of WD-all-band-BF is superior to other denoising methods.

The residual images of WD-BF (NeighShrink) and adaptive VisuShrink shows some traces of the details that are excessively smoothed. It can also be observed that the performance of both these methods are almost comparable. Therefore, this aids as an additional validity for adaptive VisuShrink. The comparative plots for the denoising results obtained by varying the noise levels are shown in Fig. 8.23. Clearly, WD-all-band-BF provides the desired smoothing as well as preserves the structural features.

8.6 Summary

In this chapter, we have proposed two novel approaches based on bilateral filter for denoising the detail coefficients of the wavelet decomposition.

The first approach is the adaptive VisuShrink, which is proposed as an improvement of the conventional VisuShrink method. The adaptivity in universal threshold is achieved by computing it in terms of the spatial context of the pixel. The spatial context of a pixel is calculated as the spatial support of the region within which the pixel is contained. The range component as defined in the bilateral filter is used for finding the spatial support in terms of intensity similarities. As a result, the adaptive VisuShrink method provides the advantages of both VisuShrink and SureShrink. At higher noise levels, it behaves like VisuShrink aiming towards the smoothness of the function. Conversely, at lower noise levels, it behaves like SureShrink aiming towards minimizing the MSE. The experimental results validates the efficiency of the proposed adaptive VisuShrink in denoising MR images.

The second approach is the WD-all-band-BF method, in which wavelet thresholding is replaced by bilateral filtering. This approach is a breakthrough in the field of wavelet denoising. The denoising efficiency of the WD-all-band-BF is even superior to WD-BF (NeighShrink) method, which is proved to be efficient than the UNLM spatial filtering and wavelet thresholding based on inter-scale and intra-scale dependencies.

We have proved the efficiency of the proposed methods through sufficient experiments on simulated and clinical MR images. However, we did not derive any mathematical framework for the optimality of these two approaches. Hence, an essential development to mathematically prove the efficiency of adaptive VisuShrink and WD-all-band-BF methods is required and it may possibly lead to its several other advantages.

9

Conclusions and Future Work

Contents

In this chapter, the main contributions of this research work are summarized and a few directions for future research are outlined.

9.1 Concluding Remarks

The main objective of this research was to develop an efficient MR image denoising method that is capable of preserving most of the diagnostically significant structural information. The research work carried out in this thesis resulted in the following contributions:

(i) A novel wavelet domain bilateral filtering framework was developed for improving the efficiency of wavelet denoising techniques. Accordingly, wavelet domain bilateral filtering based on NeighShrink thresholding is proposed for Rician noise removal in MRI.

(ii) An adaptive pixel-wise parameter selection strategy for automatically computing the optimal values of bilateral filter parameters is developed.

(iii) A new strategy for improving the VisuShrink wavelet thresholding is proposed. The universal threshold is made pixel-wise adaptive based on the spatial support of the region within which the pixels are contained.

(iv) Bilateral filtering for denoising the wavelet coefficients is proposed as an alternative to wavelet thresholding schemes.

The performance of the proposed denoising methods are verified by conducting experiments on a large dataset consisting of simulated and clinical MR images.

The study in Chapter 5 shows that the combined features of wavelet transform and the non-linear bilateral filter gives better performance than the traditional wavelet filtering approaches. It is shown that the undecimated wavelet transform adapted in the WD-BF framework provides good denoising results in comparison to the DWT and SWT based filtering approaches.

With this motivation, an improved WD-BF approach using the NeighShrink thresholding algorithm was developed for achieving feature preserved MR image denoising and it is presented in Chapter 6. The proposed WD-BF approach is capable of efficiently discriminating the signal and the noisy details. The NeighShrink thresholding technique exploits the neighborhood similarities for improving the denoising of wavelet coefficients. The optimal choice of bilateral filter parameters in the WD-BF framework is determined experimentally.

Chapter 7 presented the proposed adaptive bilateral filter in which the optimal value of the filter parameter σ_r is chosen automatically. The computation for automatically tuning the control parameter σ_r based on the local variance led to the pixel-wise adaptation of WD-BF. An important advantage offered by the proposed approach along with the automatization is the improvement in the denoising performance. Also, the improvement due to adaptive bilateral filter in denoising general images under Gaussian noise assumption is also discussed in the appendix A.

In Chapter 8, two different denoising approaches based on the bilateral filter are presented. The first approach is the adaptive VisuShrink, in which the universal threshold is made adaptive by computing it in terms of the spatial context of the pixel. The spatial context of a pixel is calculated as the spatial support of the region within which the pixel is contained. The range component as defined in the bilateral filter is used for finding the spatial support in terms of intensity similarities. The adaptive VisuShrink method provided the advantages of both VisuShrink and SureShrink. The second approach is the WD-all-band-BF method, in which wavelet thresholding is replaced by bilateral filtering. The denoising efficiency of the WD-all-band-BF is even superior to WD-BF (NeighShrink) method, which is proved to be efficient than the UNLM spatial filtering and wavelet thresholding based on inter-scale and intra-scale dependencies.

Through this research we have successfully verified and proved that exploring the neighborhood similarities in the wavelet domain improves the denoising efficiency by preserving the delicate structural details and not blurring the edge features. Accordingly, the results obtained for the proposed wavelet domain bilateral filtering strategies validates the same.

9.2 Suggestions for Future Research

In this section we will provide some suggestions for further improvements.

(i) The $3D$ implementation of the WD-BF framework will be an effective tool in dynamic MR imaging systems and in functional MRI.

(ii) The comparison of WD-BF framework is made only at coarse level. A study on the limitations and the advantages of this method in comparison with other redundant decompositions like wavelet packets and complex wavelet transforms is very essential and it may lead to several improvements.

(iii) The adaptive bilateral filter can be further improved by using adaptive neighborhoods of variable size and shape in order to estimate the local variances and the filter response. Also at higher noise levels, the power variable γ becomes ≥ 1. As a result, the power-law transformation reduces the value of σ_r allotted for the edges. Hence, the level of smoothing along the edges is decreased and it retains few noise pixels. This problem limits the advancement of the proposed approach for very low signal to noise ratio images with $\sigma_n > 0.1$. Hence, an improvement in the adaptive strategy is required to make it suitable at high noise levels.

(iv) In WD-all-band-BF method, the values of σ_d and R_{neigh} are chosen experimentally and is kept fixed for all the sub-bands. However, wavelet denoising using bilateral filter is strongly influenced by the choice of the domain parameter σ_d and the neighborhood size R_{neigh}. Hence, more evaluations are required to study the level dependency and find the optimal values of these parameters.

(v) The optimality of the proposed methods was verified through several experiments on the simulated and clinical MR images. However, we did not derive any mathematical framework for the optimality of these approaches. Hence, an essential development to mathematically prove the efficiency of these methods is required and it may possibly expose the concealed advantages of these methods.

A

General Image Denoising Using Adaptive Bilateral Filter

The significance of the proposed adaptive bilateral filter (ABF) based on the automatic parameter selection strategy as explained in chapter 7 is verified for image denoising in spatial domain.

The performance of this ABF as a spatial filter is verified by conducting experiments on the standard test images corrupted by additive white Gaussian noise. The experiments were performed on gray scale and colour images that are shown in Fig. A.1. The evaluations are also performed on magnetic resonance (MR) images in order to validate the application of the proposed method in medical image denoising. The noisy image $\bar{f}$ is generated by adding white gaussian noise of variance σ_n^2 to the original image f and is simulated using MATLAB as follows

$$\bar{f} = f + [\sigma_n \times randn(size(f))] \tag{A.1}$$

The value of σ_n is assumed to lie within the range $[0.01 - 0.1]$. The optimal neighborhood size for computing the local variance and the response of the filter is experimentally determined as 11×11. The optimal value of domain parameter σ_d is evaluated as 3. The empirical value of power variable γ is estimated as $9\sigma_n$ for gray scale images and $4\sigma_n$ for color images.

(a) Barbara (b) Cameraman (c) Pattern (d) MR image

(e) Mandrill (f) Lena (g) Peppers (h) House

Figure A.1: Test images used in the evaluation.

The values of the range parameter σ_r computed for each pixel of the noisy Barbara image is shown in Fig. A.2(a). It can be verified that the σ_r values corresponding to the edge pixels are less than the pixels in flat regions and also the range parameter value for each edge pixel depends on its strength. This is because the strong edges are less influenced by noise than the weak edges. As a result the

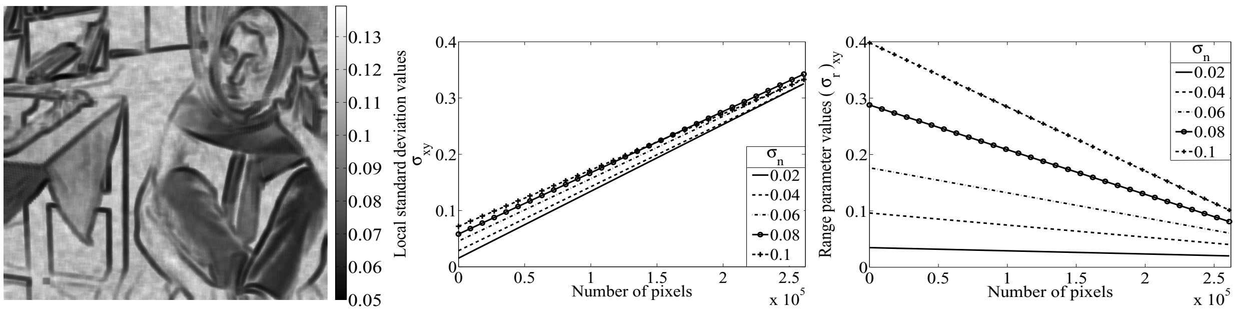

(a) (b) (c)

Figure A.2: Results for Barbara image: (a) Illustration of pixel wise allocation of σ_r values for $\sigma_n = 0.05$ (b) Plot of local standard deviation σ_{xy} estimated for different noise levels. (c) Plot of range parameter values σ_r estimated corresponding to the σ_{xy} values in (b).

variance of the strong edge pixels is high and weak edges are characterized by comparatively low variance values. Thus the degree of smoothing along the strong edges is relatively less than the weak edges.

From the experiments it is observed that as the noise level increases the local variance in the flat regions increases substantially than in the edges. This can also be verified from the plot in Fig. A.2(b). For this reason the slope of the power-law transformation should decrease for high values of σ_n. As a result the range of $(\sigma_r)_{xy}$ values corresponding to the pixels in the flat regions will be expanded to ensure sufficient smoothing. Fig. A.2(c) gives the plot of control values $(\sigma_r)_{xy}$ obtained for the local variances shown in Fig. A.2(b). From these plots it is obvious that for high noise levels the increase in range values $(\sigma_r)_{xy}$ for the edges and coarse texture regions are well regulated. Similarly, the range values for the smooth regions are sufficiently boosted to ensure proper smoothing.

The effectiveness of the proposed technique for improving the bilateral filter is validated using the root mean square error (RMSE) and the structural similarity (SSIM) index. The value of SSIM index lies between $[-1, 1]$. Minimum values of RMSE and large values of SSIM index means high similarity between the compared images.

The results of parameter selection obtained for the experiments performed on the test images for various noise levels are given in Table- A.1. The best choice of fixed σ_r value is determined experimentally for each noisy image. Through the results it can be understood that the values of σ_r (both in fixed and adaptive) increases with the noise level to ensure sufficient smoothing. In the case of fixed σ_r as employed in standard bilateral filter [7], the increase had to be limited to retain the image sharpness. As a result smoothing in flat region will be compensated. Conversely, the adaptive

Table A.1: Fixed and adaptive range parameter (σ_r) values estimated for different test images. $[a, b]$ denote the interval of adaptive σ_r.

Range parameter values for gray scale images								
	Barbara		Cameraman		Pattern		MR image	
σ_n	Fixed σ_r	Adaptive σ_r	Fixed σ_r	Adaptive σ_r	Fixed σ_r	Adaptive σ_r	Fixed σ_r	Adaptive σ_r
0.01	0.015	$[0.01, 0.0137]$	0.0075	$[0.01, 0.0141]$	0.0150	$[0.01, 0.0156]$	0.015	$[0.01, 0.0178]$
0.03	0.0525	$[0.03, 0.0609]$	0.045	$[0.03, 0.0652]$	0.0525	$[0.03, 0.0857]$	0.0675	$[0.03, 0.0741]$
0.05	0.0975	$[0.05, 0.1393]$	0.0975	$0.05, 0.1506]$	0.1375	$[0.05, 0.2194]$	0.125	$[0.05, 0.1827]$
0.07	0.1505	$[0.07, 0.2226]$	0.175	$[0.07, 0.2827]$	0.2100	$[0.07, 0.4562]$	0.175	$[0.07, 0.3215]$
0.10	0.25	$[0.10, 0.4260]$	0.275	$[0.10, 0.5755]$	0.35	$[0.10, 1.0050]$	0.275	$[0.10, 0.7307]$
Range parameter values for color images								
	Mandrill		Lena		Peppers		House	
σ_n	Fixed σ_r	Adaptive σ_r	Fixed σ_r	Adaptive σ_r	Fixed σ_r	Adaptive σ_r	Fixed σ_r	Adaptive σ_r
0.01	0.01	$[0.01, 0.0112]$	0.01	$[0.01, 0.0114]$	0.01	$[0.01, 0.0118]$	0.0125	$[0.01, 0.0119]$
0.03	0.03	$[0.03, 0.0406]$	0.0375	$[0.03, 0.0402]$	0.0375	$[0.03, 0.0449]$	0.045	$[0.03, 0.0408]$
0.05	0.05	$[0.05, 0.0770]$	0.075	$[0.05, 0.0745]$	0.075	$[0.05, 0.0805]$	0.075	$[0.05, 0.0754]$
0.07	0.07	$[0.07, 0.1177]$	0.1225	$[0.07, 0.1305]$	0.1225	$[0.07, 0.1242]$	0.1225	$[0.07, 0.1147]$
0.1	0.1	$[0.10, 0.1930]$	0.2	$[0.10, 0.2024]$	0.2	$[0.10, 0.2022]$	0.2	$[0.10, 0.1767]$

Table A.2: Comparison of RMSE and SSIM values obtained for denoising different test images using fixed and adaptive choice of σ_r.

Results for gray scale images																
	Barbara				Cameraman				Pattern				MR image			
σ_n	Fixed σ_r		Adaptive σ_r		Fixed σ_r		Adaptive σ_r		Fixed σ_r		Adaptive σ_r		Fixed σ_r		Adaptive σ_r	
	RMSE	SSIM	RMSE	SSIM	RMSE	SSIM	RMSE	SSIM	RMSE	SSIM	RMSE	SSIM	RMSE	SSIM	RMSE	SSIM
0.01	0.0098	0.9867	0.0094	0.9863	0.0090	0.9883	0.0084	0.9879	0.0046	0.9968	0.0049	0.9960	0.0076	0.9914	0.0071	0.9909
0.03	0.0268	0.9426	0.0235	0.9422	0.0228	0.9526	0.0194	0.9553	0.0098	0.9860	0.0098	0.9887	0.0201	0.9543	0.0182	0.9550
0.05	0.0408	0.8949	0.0346	0.8995	0.0348	0.9144	0.0287	0.9199	0.0158	0.9697	0.0152	0.9774	0.0296	0.8974	0.0275	0.9005
0.07	0.0555	0.8477	0.0468	0.8579	0.0520	0.8788	0.0385	0.8834	0.0242	0.9544	0.0205	0.9576	0.0385	0.8279	0.0384	0.8280
0.1	0.0678	0.7891	0.0605	0.8084	0.0710	0.8234	0.0549	0.8297	0.0410	0.9209	0.0300	0.9359	0.0594	0.7656	0.0536	0.7776
Results for color images																
	Mandrill				Lena				Peppers				House			
σ_n	Fixed σ_r		Adaptive σ_r		Fixed σ_r		Adaptive σ_r		Fixed σ_r		Adaptive σ_r		Fixed σ_r		Adaptive σ_r	
	RMSE	SSIM	RMSE	SSIM	RMSE	SSIM	RMSE	SSIM	RMSE	SSIM	RMSE	SSIM	RMSE	SSIM	RMSE	SSIM
0.01	0.0098	0.9950	0.0099	0.9949	0.0081	0.9905	0.0081	0.9904	0.0096	0.9900	0.0099	0.9896	0.0093	0.9909	0.0090	0.9914
0.03	0.0248	0.9659	0.0252	0.9643	0.0159	0.9600	0.0158	0.9603	0.0208	0.9541	0.0205	0.9542	0.0188	0.9537	0.0175	0.9601
0.05	0.0351	0.9264	0.0358	0.9216	0.0214	0.9350	0.0211	0.9352	0.0266	0.9285	0.0260	0.9287	0.0231	0.9360	0.0226	0.9367
0.07	0.0433	0.8833	0.0442	0.8752	0.0260	0.9144	0.0253	0.9160	0.0308	0.9099	0.0299	0.9093	0.0281	0.9171	0.0268	0.9174
0.1	0.0543	0.8152	0.0552	0.8064	0.0322	0.8880	0.0308	0.8909	0.0359	0.8860	0.0345	0.8866	0.0355	0.8881	0.0333	0.8885

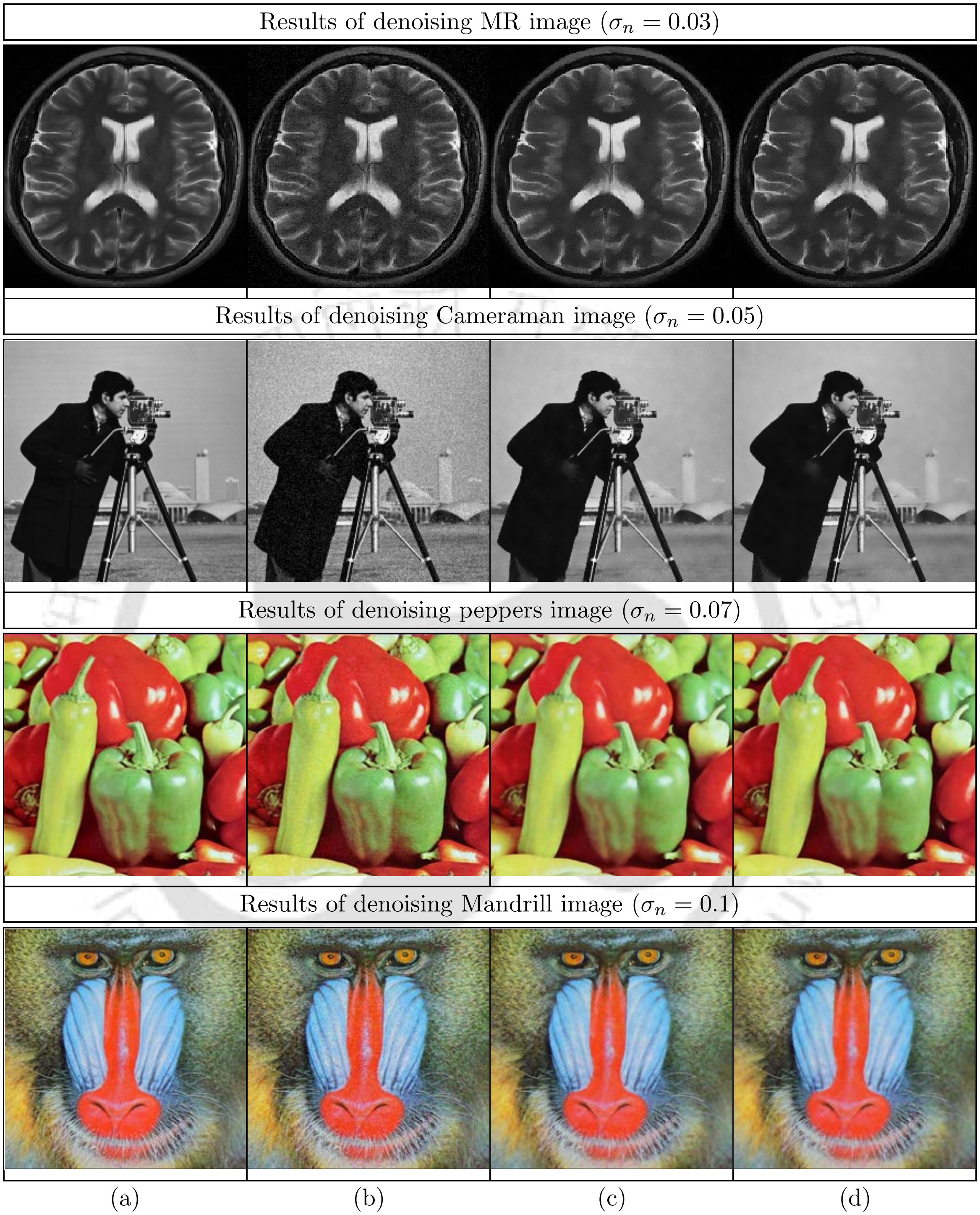

Results of denoising MR image ($\sigma_n = 0.03$)

Results of denoising Cameraman image ($\sigma_n = 0.05$)

Results of denoising peppers image ($\sigma_n = 0.07$)

Results of denoising Mandrill image ($\sigma_n = 0.1$)

(a) (b) (c) (d)

Figure A.3: Illustration of image denoising results. In column: (a) Original images (b) Noisy images (c) Denoising results using bilateral filter with fixed σ_r (d) Denoising results using bilateral filter with automatically estimated pixel wise σ_r values.

choice allocates higher σ_r in the flat regions inspite of limited σ_r in the edges. Thus it achieves good smoothing and retains image sharpness. Also, for low noise levels the range between σ_r for edges and flat regions is well controlled, such that there is no excess smoothing.

This improvement is confirmed by comparing the values of quality metrics RMSE and the SSIM index given in Table-A.2. It can be verified that the proposed adaptive parameter estimation strategy yields better results for most of the test images and is particularly higher for increasing noise levels. In the case of Mandrill image the improvement is not as expected. This is because most of the regions in this image are coarse texture regions. Due to the dependance of the proposed method on local variance values, the estimated σ_r for the pixels in these regions were slightly higher. However, the minimal difference in the values of SSIM indicate that the variations will not be perceptually significant. The image denoising results obtained for some of the test images are shown in Fig. A.3 for visual inspection.

Bibliography

[1] R. E. Hendrick, *Breast MRI: Fundamentals and Technical Aspects.* Springer, 2007.

[2] L. He, "MRI/fMRI noise reduction and data analysis," Ph.D. dissertation, Department of Computer Science and Engineering, University of Connecticut., 2008.

[3] S. P. Awate and R. T. Whitaker, "Feature-preserving MRI denoising: A nonparametric empirical Bayes approach," *IEEE Trans. Med. Imag.*, vol. 26, no. 9, pp. 1242–1555, Sep. 2007.

[4] H. Tanizaki, *Nonlinear Filters - Estimation and Applications.* Springer, 1996.

[5] M. Jansen, *Noise Reduction by Wavelet Thresholding*, ser. Lecturer notes in statistics. New York: Springer-Verlag, 2001.

[6] M. E. Alexander, R. Baumgartner, A. R. Summers, C. Windischberger, M. Klarhoefer, E. Moser, and R. L. Somorjai, "A wavelet-based method for improving signal-to-noise ratio and contrast in MR images," *Magn. Reson. Imaging*, vol. 18, pp. 169–180, 2000.

[7] C. Tomasi and R. Manduchi, "Bilateral filtering for gray and color images," in *Proc. 6th Int. Conf. Computer Vision*, 1998, pp. 839–846.

[8] M. Zhang and B. K. Gunturk, "Multiresolution bilateral filtering for image denoising," *IEEE Trans. Image Process.*, vol. 17, no. 12, pp. 2324–2333, Dec. 2008.

[9] P. Perona and J. Malik, "Scale-space and edge detection using anisotropic diffusion," *IEEE Trans. Pattern Anal. Mach. Intell.*, vol. 12, no. 7, pp. 629–639, Jul. 1990.

[10] A. Buades, B. Coll, and J. M. Morel, "A Review of Image Denoising Algorithms, with a New One," *Multiscale Model. Simul.*, vol. 4, no. 2, pp. 490 – 530, 2005.

[11] Dr. Hans H. Schild, *MRI made easy.* Schering AG, Berlin, 1990.

[12] C. Westbrook and C. Kaut, *MRI in practice*, 2nd ed. UK: Blackwell science Ltd, 1998.

[13] V. Kuperman, *Magnetic resonance imaging - Physical principles and applications.* New York: Academic press, 2000.

[14] C. Westbrook, *MRI at a glance*, 1st ed. Wiley-Blackwell, 2002.

[15] M. A. Brown and R. C. Semelka, *MRI basic principles and applications*, 3rd ed. Hoboken, NJ, USA.: John Wiley & Sons, Inc.,, 2003.

[16] D. Weishaupt, V. D. Kchli, and B. Marincek, *How does MRI work? An introduction to the physics and function of magnetic resonance imaging.* Heidelberg, Berlin: Springer-Verlag , 2006.

[17] D. W. McRobbie, E. A. Moore, M. J. Graves, and M. R. Prince, *MRI from picture to proton*, 2nd ed. Cambridge university press, 2006.

[18] P. Suetens, *Fundamentals of medical imaging*, 2nd ed. Cambridge university press, 2009.

[19] G. Siegel, R. W. Albers, S. Brady, and D. Price, Eds., *Basic neuro chemistry : Molecular, cellular and medical aspects.* Elsevier Academic press, 2006, ch. 1 - 4 : Part 1, pp. 3 – 72.

[20] E. R. Sowell and T. L. Jernigan, *Neuroimaging I: Basic science.* Springer, 1996, ch. "Imaging the developing human brain", pp. 53 – 76.

[21] Robert A. Pooley, “Fundamental Physics of MR Imaging,” *RadioGraphics*, vol. 25, pp. 1087–1099, July 2005.

[22] M. Elmaoglu and A. Celik, *MRI Handbook: MR Physics, Patient Positioning, and Protocols.* Springer, 2012.

[23] J. Hornak, *The Basics of MRI*, 1996. [Online]. Available: http://www.cis.rit.edu/htbooks/mri/

[24] Z.-P. Liang and P. C. Lauterbur, *Principle of magnetic resonance imaging*, M. Akay, Ed. IEEE Press, 2000.

[25] M. Lysaker, A. Lundervold, and X.-C. Tai, “Noise removal using fourth-order partial differential equation with applications to medical magnetic resonance images in space and time,” *IEEE Trans. Image Process.*, vol. 12, no. 12, pp. 1579–1590, Dec. 2003.

[26] D. Parker and G. Gullberg, “Signal-to-noise efficiency in magnetic resonance imaging,” *Med. Phys.*, vol. 17, pp. 250–257, 1990.

[27] J. Sijbers, D. Poot, A. J. den Dekker, and W. Pintjens, “Automatic estimation of the noise variance from the histogram of a magnetic resonance image,” *Phys. Med. Biol.*, vol. 52, pp. 1335–1348, 2007.

[28] J. Sijbers, A. J. D. Dekker, J. V. Audekerke, M. Verhoye, and D. V. Dyck, “Estimation of the noise in magnitude MR images,” *Magn. Reson. Imaging*, vol. 16, no. 1, pp. 87–90, 1998.

[29] H. Gudbjartsson and S. Patz, “The Rician distribution of noisy MRI data,” *Magn. Reson. Med.*, vol. 34, no. 6, pp. 910–914, Dec. 1995.

[30] R. M. Henkelman, “Measurement of signal intensities in the presence of noise in MR images,” *Med. Phys.*, vol. 12, no. 2, pp. 232–233, 1985.

[31] A. H. Andersen, “On the Rician distribution of noisy MRI data,” *Magn. Reson. Med.*, vol. 36, pp. 331–332, 1996.

[32] A. Crdenas-Blanco, C. Tejos, P. Irarrazaval, and I. Cameron, “Noise in magnitude magnetic resonance images.” *Concepts in Magnetic Resonance Part A*, vol. 32(A), no. 6, pp. 409–416, 2008.

[33] J. Sijbers, “Signal and Noise Estimation from Magnetic Resonance Images,” Ph.D. dissertation, Department of Physics, University of Antwerp, 1998.

[34] P. B. Roemer, W. A. Edelstein, C. E. Hayes, S. P. Souza, and O. M. Mueller, “The nmr phased array,” *Magn. Reson. Med.*, vol. 16, pp. 192–225, 1990.

[35] C. D. Constantinides, E. Atalar, and E. R. McVeigh, “Signal-to-noise measurements in magnitude images from nmr phased arrays,” *Magn. Reson. Med.*, vol. 38, no. 5, pp. 852–857, 1997.

[36] S. Aja-Fernandez, A. Tristan-Vega, and C. Alberola-Lopez, “Noise estimation in single- and multiple- coil magnetic resonance data based on statistical models,” *Magn. Reson. Imaging*, vol. 27, pp. 1397–1409, 2009.

[37] R. D. Nowak, “Wavelet-based rician noise removal for magnetic resonance imaging,” *IEEE Trans. Imag. Process.*, vol. 8, no. 10, pp. 1408–1419, Oct. 1999.

[38] G. Gerig, O. Kubler, R. Kikinis, and F. A. Jolesz, “Non-linear anisotropic filtering of MRI data,” *IEEE Trans. Med. Imag.*, vol. 11, no. 2, pp. 221–233, 1992.

[39] E. Bayram, Y. Ge, and C. L. Wyatt, “Confidence-based anisotropic filtering of magnetic resonance images,” *IEEE Eng. Med. Biol. Mag.*, vol. 21, no. 5, pp. 156–160, 2002.

[40] A. Souzaa, J. K. Udupaa, and A. Madabhushib, “Image filtering via generalized scale,” *Medical Image Analysis*, vol. 12, no. 2, pp. 87–98, April 2008.

[41] T. Acharya and A. K. Ray, *Image Processing : Principles and Applications.* New Jersey: Wiley-Interscience, 2005.

[42] R. C. Gonzalez, *Digital Image Processing*, 2nd ed. Pearson Education, 2004.

[43] E. R. McVeigh, R. M. Henkelman, and M. J. Bronskill, “Noise and filtration in magnetic resonance imaging,” *Med. Phys.*, vol. 15, no. 5, pp. 586–591, 1985.

[44] T. Brosnan, G. Wright, D. Nishimura, Q. Cao, A. Macovski, and F. G. Sommer, “Noise reduction in magnetic resonance imaging,” *Magn. Reson. Med.*, vol. 8, pp. 394–409, 1988.

[45] L. Lapidus and G. F. Pinder, *Numerical Solution of Partial Differential Equations in Science and Engineering.* New York: Wiley-Interscience, 1982.

[46] P. Perona and J. Malik, “Scale space and edge detection using anisotropic diffusion,” in *Proc. IEEE Workshop Computer Vision*, Miami, Nov. 1987, pp. 16–22.

[47] J. Weickert, *"A Review of Non-linear Diffusion Filtering", Scale-Space Theory in Computer Vision*, ser. LNCS, B. ter H. Romeny, L. Florack, J. Koenderink, and M. Viergever, Eds. Springer Berlin / Heidelberg, Jul. 1997, vol. 1252.

[48] J. Sijbers, A. J. D. Dekker, A. V. D. Linden, M. Verhoye, and D. V. Dyck, “Adaptive anisotropic noise filtering for magnitude mr data,” *Magn. Reson. Imaging*, vol. 17, no. 10, pp. 1533–1539, 1999.

[49] Y. Wang, T. Lei, W. Sewchand, and S. K. Mun, “MR imaging statistics and its application in image modeling,” in *Proc. SPIE conf. Medical Imaging*, Newport Beach, CA, 1996, pp. 706–717.

[50] G. Z. Yang, P. Burger, D. N. Firmin, and S. R. Underwood, “Structure adaptive anisotropic filtering for magnetic resonance image enhancement,” in *Proc. Computer Analysis of Images and Patterns*, ser. LNCS, vol. 970. Springer Berlin / Heidelberg, 1995, pp. 384–391.

[51] L. L. Cam, “Maximum likelihood: An introduction,” *Int. Statistical Review*, vol. 58, no. 2, pp. 153–171, Aug. 1990.

[52] G. I. Sanchez-Ortiz, D. Rueckert, and P. Burger, “Knowledge-based tensor anisotropic diffusion of cardiac magnetic resonance images,” *Med. Imag. Analysis*, vol. 3, no. 2, pp. 1–25, 1999.

[53] J. H. Elder and S. W. Zucker, “Local scale control for edge detection and blur estimation,” *IEEE Trans. Pattern Anal. Mach. Intell.*, vol. 20, no. 7, pp. 699–716, 1998.

[54] E. Bayram, “Scale selection for medical image segmentation,” M. S. thesis, Wake Forest University, Dec. 2000.

[55] A. A. Samsonov and C. R. Johnson, “Noise-adaptive non-linear diffusion filtering of mr images with spatially varying noise levels,” *Magn. Reson. Med.*, vol. 52, pp. 798–806, 2004.

[56] J. Castellanos, K. Rohr, T. Tolxdorff, and G. Wagenknecht, “Automatic Parameter Optimization for De-noising MR Data,” in *Medical Image Computing and Computer-Assisted Intervention MICCAI 2005*, ser. LNCS, J. Duncan and G. Gerig, Eds., vol. 3750. Springer Berlin / Heidelberg, 2005, pp. 320–327.

[57] K. N. Nordstrom, “Biased anisotropic diffusion: a unified regularization and diffusion approach to edge detection,” *Image and Vision Computing*, vol. 8, no. 4, pp. 318 – 327, Nov. 1990.

[58] J. Weicket, *Anisotropic Diffusion in Image Processing*, ser. ECMI. Stuttgart, Germany: Teubner-Verlag, 1998.

[59] K. Krissian and S. Aja-Fernandez, “Noise-driven anisotropic diffusion filtering of mri,” *IEEE Trans. Image Process.*, vol. 18, no. 10, pp. 2265–2274, Oct. 2009.

[60] Y. Yu and S. Acton, “Speckle reducing anisotropic diffusion,” *IEEE Trans. Image Process.*, vol. 11, no. 11, pp. 1260–1270, Nov. 2002.

[61] S. Aja-Fernandez, C. Alberola-Lopez, and C.-F. Westin, “Noise and signal estimation in magnitude MRI and Rician distributed images: A LMMSE approach,” *IEEE Trans. Image Process.*, vol. 17, no. 8, pp. 1383–1398, Aug. 2008.

[62] S. Aja-Fernandez, M. Niethammer, M. Kubicki, and M. E. Shenton, “Restoration of DWI data using a Rician LMMSE estimator,” *IEEE Trans. Med. Imag.*, vol. 27, no. 10, pp. 1389–1403, Oct. 2008.

[63] K. Krissian, C. Westin, R. Kikinis, and K. Vosburgh, “Oriented speckle reducing anisotrophic diffusion,” *IEEE Trans. Image Process.*, vol. 16, no. 5, pp. 1412–1424, May 2007.

[64] G. McGibney and M. Smith, “Unbiased signal-to-noise ration measure for magnetic resonance images,” *Med. Phys.*, vol. 20, no. 4, pp. 1077–1078, 1993.

[65] C. G. Koay and P. J. Basser, “Analytically exact correction scheme for signal extraction from noisy magnitude mr signals,” *J. Magn. Reson.*, vol. 179, no. 2, pp. 317–322, 2006.

[66] A. Pizurica, W. Philips, I. Lemahieu, and M. Acheroy, “A versatile wavelet domain noise filtration technique for medical imaging,” *IEEE Trans. Med. Imag.*, vol. 22, no. 3, pp. 323 – 331, Mar. 2003.

[67] P. Coupe, P. Yger, S. Prima, P. Hellier, C. Kervann, and C. Barillot, “An optimized blockwise non-local means denoising filter for 3-D magnetic resonance images,” *IEEE Trans. Med. Imag.*, vol. 27, no. 4, pp. 425–441, Apr. 2008.

[68] S. Aja-Fernandez and K. Krissian, “An unbiased non-local means scheme for DWI filtering,” in *Proc. Workshop on Computational Diffusion MRI, MICCAI*, 2008, pp. 277–284.

[69] Z. Wang, A. C. Bovik, H. R. Sheikh, and E. P. Simoncelli, “Image quality assessment: From error visibility to structural similarity,” *IEEE Trans. Image Process.*, vol. 13, no. 4, pp. 600–612, Apr. 2004.

[70] S. Aja-Fernandez, R. San-Jose-Estepar, C. Alberola-Lopez, and C. F. Westin, “Image quality assesment based on local variance,” in *Proc. 28th IEEE EMBC*, New York, Sep. 2006, pp. 4815–4818.

[71] L. I. Rudin, S. Osher, and E. Fatemi, “Non-linear total variation based noise removal algorithms,” *Physica D: Nonlinear Phenomena*, vol. 60, no. 1-4, pp. 259 – 268, 1992.

[72] Y. L. You and M. Kaveh, “Fourth-order partial differential equation for noise removal,” *IEEE Image Process.*, vol. 9, no. 10, pp. 1723–1730, 2000.

[73] H. Soltanian-Zadeh, J. P. Windham, and A. E. Yagle, “A multidimensional non-linear edge-preserving filter for magnetic resonance image restoration,” *IEEE Trans. Image Process.*, vol. 4, no. 2, pp. 147 – 161, Feb. 1995.

[74] J. P. Windham, M. A. Abd-Allah, D. A. Reimann, J. W. Froelich, and A. M. Haggar, “Eigenimage filtering in MR imaging,” *J. Comput. Assist. Tomogr.*, vol. 12, no. 1, pp. 1–9, 1988.

[75] C. B. Ahn, Y. C. Song, and D. J. Park, “Adaptive template filtering for signal-to-noise ratio enhancement in magnetic resonance imaging,” *IEEE Trans. Med. Imag.*, vol. 18, no. 6, pp. 549 – 556, Jun. 1999.

[76] K. Rank and R. Unbehauen, “An adaptive recursive 2-D filter for removal of Gaussian noise in images,” *IEEE Trans. Image Process.*, vol. 1, pp. 431–436, 1992.

[77] H. Robbins, “The empirical bayes approach to statistical decision problems,” *Ann. Math. Stat.*, vol. 35, no. 1, pp. 1–20, 1964.

[78] S. Z. Li, *Markov Random Field Modeling in Computer Vision.* London, UK: Springer-Verlag, 1995.

[79] G. J. McLachlan and T. Krishnan, *The EM Algorithm and Extensions.* New York: Wiley-Interscience, 1997.

[80] S. P. Awate and R. T. Whitaker, “Unsupervised, information-theoretic, adaptive image filtering for image restoration,” *IEEE Pattern Anal. Mach. Intell.*, vol. 28, no. 3, pp. 364–376, Mar. 2006.

[81] M. Martin-Fernandez, C. Alberola-Lopez, J. Ruiz-Alzola, and C.-F. Westin, “Sequential anisotropic wiener filtering applied to 3d mri data,” *Magn. Reson. Imaging*, vol. 25, no. 2, pp. 278–292, Feb. 2007.

[82] N. Wiener, “Generalized harmonic analysis,” *Acta Mathematica*, vol. 55, no. 1, pp. 117–258, 1930.

[83] J. S. Lim, *Two dimensional signal and image processing.* Englewood Cliffs, NJ: Prentice Hall, 1990.

[84] J. H. Luo, Y. M. Zhu, and I. Magnin, “Denoising by Averaging Reconstructed Images: Application to Magnetic Resonance Images,” *IEEE Trans. Biomed. Eng.*, vol. 56, no. 3, pp. 666–674, Mar. 2009.

[85] J. H. Luo and Y. M. Zhu, “MR image reconstruction from truncated k-space using a layer singlular point extraction technique,” *IEEE Trans. Nucl. Sci.*, vol. 51, no. 1, pp. 157–169, Feb. 2004.

[86] J. H. Luo, Y. M. Zhu, P. Clarysse, and I. Magnin, “Correction of bias field in MR images using singularity function analysis,” *IEEE Trans. Med. Imag.*, vol. 24, no. 8, pp. 1067–1085, Aug. 2005.

[87] J. V. Manjon, J. Carbonell-Caballero, J. J. Lull, G. Garcia-Marti, L. Marti-Bonmati, and M. Robles, "MRI denoising using non -local means," *Med. Imag. Analysis*, vol. 12, pp. 514–523, 2008.

[88] M. Mahmoudi and G. Sapiro, "Fast image and video denoising via non-local means of similar neighborhoods," *IEEE Signal Process. Lett.*, vol. 12, no. 12, pp. 839–842, Dec. 2005.

[89] J. V. Manjon, N. A. Thacker, J. J. Lull, G. Garcia-Marti, L. Marti-Bonmati, and M. Robles, "Multicomponent MR Image Denoising," *Int. J. Biomed. Imaging*, vol. 2009, p. 10, 2009.

[90] L. P. Yaroslavsky, *Digital Picture Processing-An Introduction.* New York, USA: Springer, 1985.

[91] P. Coupe, P. Yger, and C. Barillot, "Fast non local means denoising for 3D MR images," in *Proc. Int. Conf. Med. Image Computing and Computer-Assisted Intervention.* Copenhagen, Denmark: Springer, Oct. 2006, pp. 33–40.

[92] I. T. Jolliffe, *Principal Component Analysis*, 2nd ed., ser. Statistics. New York: Springer-Verlag, 2002.

[93] J. V. Manjon, P. Coupe, L. Marti-Bonmati, D. L. Collins, and M. Robles, "Adaptive non-local means denoising of mr images with spatially varying noise levels," *J. Magn. Reson. Imaging*, vol. 31, no. 1, pp. 192 – 203, 2010.

[94] N. Wiest-Daessle, S. Prima, P. Coupe, S. P. Morrissey, and C. Barillot, "Rician noise removal by non-local means filtering for low signal-to-noise ratio MRI: applications to DT-MRI," in *Proc. of Int. Conf. Med. Image Computing and Computer-Assisted Intervention*, New York, 2008, pp. 171–179.

[95] P. Coupe, P. Hellier, S. Prima, C. Kervrann, and C. Barillot, "3D wavelet subbands mixing for image denoising," *Int. J. Biomed. Imaging*, vol. 2008, 2008.

[96] Y. Gal, A. J. H. Mehnert, A. P. Bradley, K. McMahon, D. Kennedy, and S. Crozier, "Denoising of Dynamic Contrast-Enhanced MR Images Using Dynamic Non-local Means," *IEEE Trans. Med. Imag.*, vol. 29, no. 2, pp. 302 – 310, Feb. 2010.

[97] C. K. Chui, *Wavelets: A Mathematical Tool for Signal Analysis.* SIAM, 1997.

[98] S. G. Mallat, "A theory of multiresolution signal decomposition: The wavelet representation," *IEEE Trans. Pattern Anal. Mach. Intell.*, vol. 11, no. 7, pp. 674–693, Jul. 1989.

[99] Alan C. Bovik, *The Essential Guide to Image Processing.* Academic Press, Elsevier Inc., 2009.

[100] Agostino Abbate, Casimer M. DeCusatis, and Pankaj K.Das, *Wavelets and Subbands: Fundamentals and Applications.* Birkhauser Boston, 2002.

[101] Ali N. Akansu and Richard A. Haddad, *Multiresolution Signal Decomposition: Transforms, Subbands, and Wavelets*, 2nd ed., ser. Series in Telecommunications, T. Russell Hsing, Ed. Academic press, 2001.

[102] D. P. Radunovic, *WAVELETS: from MATH to PRACTICE.* Springer-Verlag, Academic Mind, 2009.

[103] M. Jansen and A. Bultheel, "Empirical Bayes approach to improve wavelet thresholding for image noise reduction," *Journal of the American Statistical Association*, vol. 96, no. 454, pp. 629–639, June 2001.

[104] P. Bao and L. Zhang, "Noise reduction for magnetic resonance images via adaptive multiscale products thresholding," *IEEE Trans. Med. Imag.*, vol. 22, no. 9, pp. 1089–1090, Sep. 2003.

[105] J. B. Weaver, Y. Xu, D. M. Healy, and L. D. Cromwell, "Filtering noise from images with wavelet transforms," *Magn. Reson. Med.*, vol. 21, no. 2, pp. 288–295, 1991.

[106] R. R. Coifman and M. V. Wickerhauser, "Entropy-based algorithms for best basis selection," *IEEE Trans. Inform. Theory*, vol. 38, no. 2, pp. 713–718, Mar. 1992.

[107] J. C. Wood and K. M. Johnson, "Wavelet packet denoising of magnetic resonance images: Importance of rician noise at low snr," *Magn. Reson. Med.*, vol. 41, pp. 631–635, 1999.

[108] R. R. Coifman and M. V. Wickerhauser, "Adapted waveform analysis as a tool for modeling, feature extraction, and denoising," *Optical Engineering*, vol. 33, no. 7, pp. 2170–2174, Jul. 1994.

[109] L. Woog, "Adaptive waveform algorithms for denoising," Ph.D. dissertation, Dept. Comp. Science, Yale University, 1996.

[110] R. D. Nowak and R. G. Baraniuk, "Wavelet-domain filtering for photon imaging systems," in *Proc. SPIE Wavelet Applications in Signal and Image Processing V*, vol. 3169, 1997, pp. 55–66.

[111] M. A. T. Figueiredo and R. D. Nowak, "Bayesian wavelet-based signal estimation using noninformative priors," in *Proc. 32nd Asilomar Conf. Signals, Systems, and Computers*, vol. 2, Pacific Grove, USA, Nov. 1998, pp. 1368–1373.

[112] R. L. Gregg and R. D. Nowak, "Noise removal methods for high resolution MRI," in *IEEE Nuclear Science Symposium*, vol. 2, Nov. 1997, pp. 1117–1121.

[113] R. D. Nowak, R. L. Gregg, T. G. Cooper, and J. E. Siebert, "Removing Rician noise in MRI via wavelet-domain filtering," in *Proc. Int. Soc. Magn. Reson. Med.*, Sydney, 1998.

[114] M. E. Alexander, R. Baumgartner, R. L. Somorjai, A. R. Summers, C. Windischberger, and E. Moser, "Denoising of MR images to improve signal-to-noise ratio," in *Proc. Int. Soc. Magn. Reson. Med.*, Philadelphia, 1999.

[115] D. L. Donoho and I. M. Johnstone, "Ideal spatial adaptation by wavelet shrinkage," *Biometrika*, vol. 81, no. 3, pp. 425–455, 1994.

[116] M. E. Alexander, R. Baumgartner, C. Windischberger, E. Moster, and R. L. . Somorjai, "Wavelet domain de-noising of time courses in mr image sequences," *Magn. Reson. Imaging*, vol. 18, pp. 1129–1134, 2000.

[117] S. Zaroubi and G. Goelman, "Complex denoising of MR data via wavelet analysis: Application for functional MRI," *Magn. Reson. Imag.*, vol. 18, pp. 59–68, 2000.

[118] D. L. Donoho, "De-noising by soft-thresholding," *IEEE Trans. Inform. Theory*, vol. 41, pp. 613–627, May 1995.

[119] A. Pizurica, W. Philips, I. Lemahieu, and M. Acheroy, "A joint interscale and intrascale statistical model for Bayesian wavelet based image denoising," *IEEE Trans. Image Process.*, vol. 11, pp. 545–557, May 2002.

[120] ——, "Despeckling SAR images using wavelets and a new class of adaptive shrinkage functions," in *Int. Conf. Image Process.* Thessaloniki, Greece: IEEE, Oct. 2001.

[121] A. Pizurica, "Image denoising using wavelets and spatial context modeling," Ph.D. dissertation, Ghent University, Ghent, Belgium, 2002.

[122] A. Pizurica, A. M. Wink, E. Vansteenkiste, W. Philips, and J. B. T. M. Roerdink, "A review of wavelet denoising in MRI and ultrasound brain imaging," *Current Medical Imaging Reviews*, vol. 2, no. 2, pp. 247–260, 2006.

[123] Y. Xu, J. B. Weaver, D. M. Healy, and J. Lu, "Wavelet transform domain filters: A spatially selective noise filtration technique," *IEEE Trans. Image Process.*, vol. 3, pp. 747–758, Nov. 1994.

[124] B. M. Sadler and A. Swami, "Analysis of multiscale products for step detection and estimation," *IEEE Trans. Inform. Theory*, vol. 45, pp. 1043–1051, Apr. 1999.

[125] S. Mallat and S. Zhong, "Characterization of signals from multiscale edges," *IEEE Trans. Pattern Anal. Mach. Intell.*, vol. 14, no. 7, pp. 710–732, Jul. 1992.

[126] A. M. Wink and J. B. T. M. Roerdink, "Denoising functional MR images: A comparison of wavelet denoising and gaussian smoothing," *IEEE Trans. Med. Imag.*, vol. 23, no. 3, pp. 374–387, March 2004.

[127] M. Lang, H. Guo, J. E. Odegard, C. Burrus, and R. O. Wells, "Non-linear Processing of a Shift Invariant DWT for Noise Reduction," in *Proc. SPIE*, vol. 2491, no. 640, 1995, pp. 640–651.

[128] D. Wei, U. Rajashekar, and A. C. Bovik, *Handbook of Image and Video Processing*, 2nd ed. Elsevier Academic Press, 2005.

[129] G. P. Nason and B. W. Silverman, "The stationary wavelet transform and some statistical applications," Department of Mathematics, University of Bristol, Tech. Rep., 1995.

[130] J.-L. Starck, F. Murtagh, and J. Fadili, *Sparse Image and Signal Processing: Wavelets, Curvelets, Morphological Diversity.* Cambridge University Press, 2010.

[131] J. E. Fowler, "The redundant discrete wavelet transform and additive noise," *IEEE Signal Process. Letters*, vol. 12, no. 9, pp. 629–632, Sep. 2005.

[132] H. Mitchell, *Image Fusion: Theories, Techniques and Applications.* Springer, 2010.

[133] R. Coifman and D. L. Donoho, "Translation-invariant de-noising," in *Lecturer Notes in Statistics : Wavelets and Statistics.* Springer-Verlag, 1995, pp. 125–150.

[134] K. P. Soman, K. I. Ramachandran, and N. Resmi, *Insight Into Wavelets-From Theory to Practice*, 3rd ed. PHI Learning Private Limited, 2010.

[135] Z. Dengwen and C. Wengang, "Image denoising with an optimal threshold and neighboring window," *Pattern Recogn. Lett.*, vol. 29, no. 11, pp. 1694–1697, 2008.

[136] R. K. Kwan, A. C. Evans, and G. B. Pike, "MRI simulation-based evaluation of image-processing and classification methods," *IEEE Trans. Med. Imag.*, vol. 18, no. 11, pp. 1085–1097, Nov. 1999.

[137] G. Y. Chen, T. D. Bui, and A. Krzyzak, "Image denoising with neighbor dependency and customized wavelet and threshold," *Pattern Recognition*, vol. 38, pp. 115–124, 2005.

[138] D. L. Donoho and I. M. Johnstone, "Adapting to Unknown Smoothness via Wavelet Shrinkage," *Journal of the American Statistical Association*, vol. 90, no. 432, pp. 1200–1224, Dec. 1995.

[139] T. T. Cai and B. W. Silverman, "Incorporating information on neighboring coefficients into wavelet estimation," *Sankhya: The Indian Journal of Statistics*, vol. 63, no. Series B, Pt 2, pp. 127–148, 2001.

[140] A. Bhattacharyya, "On a measure of divergence between two statistical populations defined by their probability distributions," *Bull. Calcutta Math. Soc.*, vol. 35, pp. 99–109, 1943.

[141] J. Lee, "Refined filtering of image noise using local statistics," *Computer Graphics and Image Processing*, vol. 15, pp. 380–389, 1981.

[142] J.-S. Lee, "Digital image enhancement and noise filtering by use of local statistics," *IEEE Trans. Pattern Anal. Mach. Intell.*, vol. 2, no. 2, pp. 165–168, March 1980.

[143] S. G. Chang, B. Yu, and M. Vetterli, "Adaptive wavelet thresholding for image denoising and compression," *IEEE Trans. Image Process.*, vol. 9, no. 9, pp. 1532–1546, Sep 2000.

[144] G. P. Nason, "Choice of the threshold parameter in wavelet function estimation," in *In Wavelets and Statistics*, ser. Lecture Notes in Statistics, A. Antoniadis and G. Oppenhim, Eds., vol. 103. Springer-Verlag, 1995, pp. 261–280.

[145] X. Yuan and B. P. Buckles, "Subband noise estimation for adaptive wavelet shrinkage," in *Proceedings of the 17th International Conference on Pattern Recognition (ICPR'04)*, vol. 4, August 2004, pp. 885–888.

List of Publications

Journal Publications

Published Paper:

1. C. Shyam Anand and J. S. Sahambi, “Wavelet domain Non-linear Filtering for MRI denoising”, *Magnetic Resonance Imaging (Elsevier)*, vol. 28, no. 6, pp. 842–861, 2010.
2. C. Shyam Anand and J. S. Sahambi, “Pixel Dependent Automatic Parameter Selection for Image Denoising with Bilateral Filter”, *International Journal of Computer Applications*, Vol. 45, no. 10, pp. 41–46, May 2012.

Manuscripts Submitted:

1. C. Shyam Anand and J. S. Sahambi, “Estimation and Reduction of Noise in Magnetic Resonance Images A Review”, *Medical Image Analysis (Elsevier)*.
2. C. Shyam Anand and J. S. Sahambi, “Spatial Context Based Locally Adaptive Threshold Selection for Image Denoising”, *Signal Image and Video Processing (Springer)*.

Conference Publications

1. C. Shyam Anand and J. S. Sahambi, “MRI denoising using bilateral filter in redundant wavelet domain”, *IEEE Region 10 Conf., TENCON - 2008*, Hyderabad, India, pp. 1–6, Nov 2008.
2. C. Shyam Anand and J. S. Sahambi, “Image Denoising Using Spatial Context Modeling Of Wavelet Coefficients”, *IEEE ICASSP - 2012*, Kyoto, Japan, pp. 1125–1128, Mar. 2012.